ScuDo
Scuola di Dottorato ~ Doctoral School
WHAT YOU ARE, TAKES YOU FAR

Doctoral Dissertation
Doctoral Program in Energetics (33th Cycle)

Conversion of industrial CO_2 to value-added fuels and chemicals via Fischer-Tropsch upgrade

Marco Marchese
* * * * * *

Supervisors
Prof. Andrea Lanzini, Supervisor
Prof. Massimo Santarelli, Co-Supervisor

Doctoral Examination Committee:
Prof. Dr. Thomas Bayer, Referee, Provadis Hochschule
Dr. Stefano Stendardo, Referee, ENEA Centro Ricerche Casaccia

Politecnico di Torino
April 14, 2021

This thesis is licensed under a Creative Commons License, Attribution - Noncommercial - NoDerivative Works 4.0 International: see www.creativecommons.org. The text may be reproduced for non-commercial purposes, provided that credit is given to the original author.

I hereby declare that, the contents and organisation of this dissertation constitute my own original work and does not compromise in any way the rights of third parties, including those relating to the security of personal data.

……

Marco Marchese

Turin, April 14, 2021

Summary

Different solutions can be implemented to reduce the impact of human activities on the environment and target the carbon transition towards a fossil-free society. Carbon capture and utilization (CCU) represents a way to reduce the concentration of CO_2 in the atmosphere, promote a circular economy production scheme, and avoid the extraction of fossil hydrocarbons. As such, mixing anthropogenic CO_2 with hydrogen obtained through electrolysis can generate synthetic carbon compounds that offset their fossil counterparts. In this framework, this doctoral dissertation explores the possibility of converting non-fossil carbon feedstocks (e.g., waste CO_2 and organic digestate) into marketable Fischer-Tropsch (FT) products. It combines Fischer-Tropsch (FT) kinetic model information with process modelling to derive techno-economic considerations on the most effective process route to produce Fischer-Tropsch waxes.

Chapter 1 presents the context and boundaries of this work, with reference to the concept of *circular economy* applied to carbon molecules/sources. An overview of the non-fossil carbon feedstock selected for this analysis, which are biogas, air, and digestate biomass, is provided. Concerning biogas and air, these can be regarded as flows having mildly concentrated CO_2 that can be captured and fed to downstream conversion processes. Digestate can be considered as a feedstock of carbon material coming from the process of anaerobic digestion. Finally, the market potential of Fischer-Tropsch waxes is covered.

Chapter 2 describes the FT technology. Different reactor designs and catalysts information are provided with reference to their *state-of-the-art.* Moreover, the chapter describes the activities carried out within this investigation on Fischer-Tropsch kinetic modeling. A Co-Pt/γ-Al_2O_3 catalyst was tested under several industrial-like conditions. Experimental data were collected using the online gas chromatography technique on the Fischer-Tropsch gas fraction and offline gas chromatography on the liquid and wax fractions. The experimental data were used to feed global and local optimization routines with non-linear least-squared fitting procedures to derive different kinetic models. The final kinetic model represented a detailed mechanistic one, capable of describing the FT product distribution of n-paraffins up to carbon number C_{80} and α-olefins up to carbon number C_{40}. Kinetic information was included in process modeling to find the most suitable plant designs to convert non-fossil compounds into Fischer-Tropsch liquids and waxes.

Chapter 3 and Chapter 4 provide the process modelling methodology and results, respectively. 11 process designs were investigated: 4 for the conversion of biogas, 2 for the conversion of digestate, and 5 for converting direct air CO_2. For biogas, the chemical scrubbing technology fed with MEA solvent was utilized for capturing CO_2. Moreover, the syngas required by the FT reactor was produced inside a reverse water-gas shift reactor coupled with an alkaline electrolyser for green hydrogen generation or in a solid oxide electrolyser working at thermoneutral conditions. Both options operated at either ambient pressure or 25 bar. Additionally, digestate was gasified inside a dual fluidized bed reactor for syngas generation. Afterward, a solution utilizing the Fischer-Tropsch off-gas as fuel for electric generation was compared against recycling the off-gas into the gasifier for higher throughput of synthetic hydrocarbons. Lastly, CO_2 was extracted from the air with the direct air capture (DAC) technology operating at high temperature, coupled with H_2 production via alkaline electrolysers. Within this process route, it was assessed the substitution of fossil hydrocarbon with Fischer-Tropsch off-gas to sustain the capture process. Lastly, an electrified DAC option was investigated. All the process models were evaluated from both a technical and economic point of view. Key performance indicators were assessed to account for the system effectiveness in converting carbon material to FT compounds. Moreover, the cost of FT wax production was determined and compared. The outcomes of the techno-economic analysis show that using digestate as the carbon feedstock provides the least energy-intensive processes to generate FT material. From an economic point of view, biogas as carbon feedstock provides the most economically ready routes to generate FT waxes. On the contrary, using CO_2 from the air is the most expensive solution. Finally, the processes converting CO_2 from biogas and air present a higher variation of the wax production cost depending on the electricity cost than the routes utilizing digestate, given the presence of the electrolysers for H_2/syngas production.

Furthermore, the results of the techno-economic investigation of the biogas-to-FT and digestate-to-FT were engaged to account for the potential production of FT wax at the European level (Chapter 5). Specifically, it was assessed the potential outtake of carbon dioxide and digestate material coming from both biogas and biomethane plants currently operating in Europe. Biomethane plants are the ones with a *ready-to-use* stream of CO_2 derived from the installation of biogas upgrading units. Consequently, the amount of FT wax generated was evaluated. Lastly, it is possible to identify 17 plants with feasible market entry characteristics to produce the FT waxes throughout Europe.

Conclusions and outlooks of this investigation are provided in Chapter 6.

Acknowledgments

This work has received funding from the European Union's Horizon 2020 research and innovation programme under grant agreement No 768543 (ICO2CHEM "From industrial CO_2 streams to added value Fischer-Tropsch chemicals").

This dissertation represents the end of an exciting period of 3.5 years of Ph.D. research activities and advanced education that I carried out at the Department of Energy of Politecnico di Torino. I am extremely grateful for the opportunity that I had, and I will make the most out of all the knowledge that I acquired and the experiences that I had.

First and foremost, I would like to thank my supervisor, Andrea (prof. Andrea Lanzini). This entire journey would not have been possible without his suggestions and directions. I am grateful for the trust and responsibilities that he gave me from day 1 in my research work. I must also thank him for never suppressing my desire to explore the World – literally – and supporting all the activities I proposed to him. Research-wise and personal-wise, I have grown a lot thanks to his valuable knowledge, teachings, and encouragement.

I want to thank my co-supervisor, Massimo (prof. Massimo Santarelli). His technical knowledge has been extremely useful throughout the entire Ph.D., and the passion for what he does is very inspiring.

Obviously, all of this would not have been possible without the constant interaction with my officemates and colleagues, both at work and off-work. A special thank goes to Paolo – with whom we started this journey together – for the continuous interactions, scientific and everyday life confrontations, office time, laughs and challenges we had together, and all that a Ph.D. period brings along. Valeria, for constantly being supportive and ready to help. Giulio, for his critical mind and effortless smile in the office. Marco, for showing me that the Ph.D. is also an opportunity for networking and developing important soft skills. Gabriele, Mohsen, and Salvatore, for all coffee breaks and scientific discussions. Marta, Domenico, and Emanuele for sharing their wise advice and knowledge on both scientific and personal matters.

I would like to thank all the people involved in the ICO2CHEM project; great professionals motivated to change the world.

I thank all the Finnish crew that made my stay in Finland at VTT extremely valuable. Kiitos to Niko, for the daily interaction in the lab, the coffees every 10 minutes, lunches at 10.50, the saunas, and the off-work time. Matti, for his daily support and wise suggestions, not to mention his polite manners and friendly chat about research and life in general. Patrik, for his help in the lab and his brilliant mind. I would also like to thank Pekka and Noora for making my stay possible and memorable.

I want to thank the US crew of Chicago. The research conducted there is not part of this dissertation, but even with bad luck and medical conditions, my stay in Chicago has been a total blast. Thanks to Prof. Scott A. Barnett for having me in his lab and showing great interest in my research. I hope the activities started together will continue in the future. Tim, Travis, and Nicholas, for their friendly, fun, and proactive behaviour and the constant support in the lab. Annalisa, for the fun and the help in time of need. Roberto, a long-known friend, and a bright scientist, full of advice and very supportive. A special thanks also goes to Hailey and Barney for making my stay in Chicago a once-in-a-lifetime experience.

I also want to thank my closest friends outside of Politecnico for their good spirits during the last years: Stefano, Stefano, Andrea, Riccardo, Riccardo, Carola, Arianna, Ilaria, Elena, Angelica, Stefano, Alberto, Giorgia, Francesco, Valeria, Elena, Sara.

I want to thank all my family. My brother and sister, Alessandro and Cecilia, for the support shown in the last years and for celebrating with me my achievements. Thanks to all my nonni, for teaching me that hard work and dedication can take me further than my goals. Zii and cugini, for laughs and encouragement.

Lastly, I want to thank my parents, mamma Rosa and papà Pierpaolo, for selflessly and unconditionally supporting my decisions and always helping me achieving my goals and following the right path.

Contents

Symbols

C_{inv}	Investment cost
C_{op}	Operating cost
E	Activation energy (kJ mol^{-1})
Esp_{CO2}	Specific energy consumption over the CO_2 captured (kWh kg_{CO2}^{-1})
Esp_{wax}	Specific energy consumption over the waxes produced (kWh kg_{wax}^{-1})
F	Faraday constant (C mol_e^{-1})
$f_{i\text{-}th}$	CAPEX cost factors
I	Current (A)
j	Current density (A cm^{-2})
K	Equilibrium constant
k	Kinetic constant
k-year	k-th operational year
$\dot{m}$	Mass flow rate (kg/h)
n	Carbon number
$\dot{n}$	Molar flow rate (mol/s)
$\dot{n}_{i\text{-}th}$	Mole flow rate of component i-th (mol s^{-1})
n_{life}	Plant lifetime
N_{rt}	Repayment time (year)
n_{tot}	Exchange charge
P	Pressure (bar)
P_{el}	Electric power (kW_{el})
Q_{th}	Thermal power (kW)
R	Gas constant (kJ $kmol^{-1}$ K^{-1})
r_d	Discount rate (%)
R_i	Rate of hydrocarbons formation/consumption (mol g_{cat}^{-1} h^{-1})

sf	Scaling factor
S_i	Size of the system component
T	Temperature (K)
V	Voltage (V)
$\dot{V}$	Volumetric flow rate (m^3/h)
W	Power (W)
W_{el}	Electric power (kW)
$x_{i\text{-}th}$	Mass concentration
$y_{i\text{-}th}$	Molar concentration
α	Hydrocarbon probability growth
ΔG	Gibbs free energy ($kJ\ kmol^{-1}$)
ΔH	Enthalpy change
ΔH	Enthalpy change
Δp	Pressure variation
ΔT	Temperature variation
η	Efficiency
η_C	Carbon conversion efficiency
η_{CO2}	Carbon dioxide removal efficiency
η_{Glob}	Plant global efficiency
Θ	Vacancy percentage
ρ	Density (kg/m^3)
X	Conversion

Abbreviations

AF	Annuity factor
AFS	Anderson-Flory-Schultz
ASR	Area-specific resistance (Ωcm^2)
ATR	Auto thermal reactor
BEC	Bare erected cost
BtL	Biomass-to-Liquid
CAPEX	Capital cost
CCU	Carbon capture and utilization
CEPCI	Chemical Engineering Plant Cost Index
CGO	Gallium-doped ceria
CPOX	Partial oxidation
CSP	Concentrated solar power
DAC	Direct air capture
DCF	Discounted cash flow
DFBG	Dual fluidized bed gasifier
FT	Fischer-Tropsch
FTS	Fischer-Tropsch synthesis
GT	Gas turbine
HX	Heat exchanger
KPI	Key performance indicator
LCA	Life cycle analysis
LHHW	Langmuir-Hinshelwood-Hougen-Watson
LHV	Lower Heating Value
LSC	Lanthanum strontium cobaltite
MARR	Mean Absolute Relative Residual
MEA	Monoethanolamine

MSW	Municipal solid waste
NG	Natural gas
NPV	Net present value
O&M	Operation and maintenance
OCV	Open circuit voltage
OF	Objective Function
OPEX	Operating cost
P2G	Power to gas
P2L	Power to liquid
PR-BM	Peng-Robinson, Boston-Mathias modification
PtL	Power-to-liquid
PV	Photovoltaic
RDS	Rate Determining Step
RES	Renewable energy source
RKS	Redlich-Kwong-Soave
RKS-BM	Redlich-Kwong-Soave, Boston-Mathis modification
RR	Recirculation rate
RU	Reactant utilization
RWGS	Reverse water gas shift
SBR	Steam-to-biomass
SMR	Steam methane reforming
SOE	Solid oxide electrolyser
SOEC	Solid oxide electrolysis cell
TN	Thermoneutral
TOF	Turnover frequency
VS	Venture scrubber
WS	Water scrubber
YSZ	Yttria-stabilized zirconia

List of Tables

List of Figures

Chapter 1

Conversion of CO_2 and non-fossil carbon feedstocks to added-value products

Carbon dioxide (CO_2) is addressed as the major contributor to climate change, being responsible for the rise in the Earth's surface mean global temperature [1]. The well-known Paris agreement has set the bases for sustainable development and a reduction of greenhouse gas emissions towards the environment to keep the mean global temperature rise well below 2°C compared to the pre-industrial levels. This means cutting the release of harmful greenhouse gases towards the environment and additionally switching our carbon-based society from fossil to renewable carbon compounds. However, as stated by the Intergovernmental Panel on Climate Change, in the last decades, there has been a constant rise in carbon dioxide emissions from anthropogenic activities towards the atmosphere [2]. According to the data collected by the European Commission, carbon dioxide emissions combining fossil and biogenic sources have risen from about 18 Gt_{CO2}/y in 1970 to almost 45 Gt_{CO2}/y in 2018 (Figure 1) [3,4]. In this context, different applications are being investigated worldwide to reduce the effect of anthropogenic activities towards the environment. Increasing penetration of renewable energy in the electric grid, electrification of the transport sector, utilization of hydrogen into industrial processes (e.g., Power-to-X, iron and steel plants), carbon capping, are some of the solutions that can tackle climate change and cut carbon dioxide emissions from fossil consumption [5,6].

With a direct impact on carbon dioxide concentration in the air, carbon capture storage and utilization solutions are also investigated [7]. On the one hand, carbon capture and storage technologies are being analysed to sequester large volumes of CO_2 into geological reservoirs. On the other hand, carbon capture and utilization solutions are implemented to convert the waste CO_2 molecule into marketable products [1].

Along with this, the utilization of alternative-to-fossil streams like biogas and biomass is intensively studied to favour the concept of *CO_2 circular economy*, shifting the consumption of hydrocarbons from fossil-based to renewable-based ones [8].

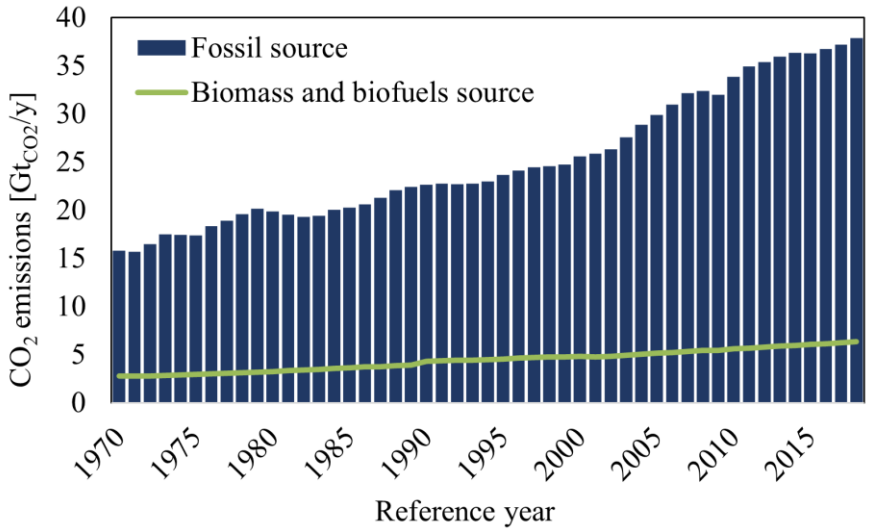

Figure 1. Evolution of the anthropogenic carbon dioxide emissions in the years 1970-2018. Data collected from the EU Commission EDGAR Database (Emissions Database for Global Atmospheric Research). Adapted from [3,4].

1.1 Carbon capture and utilization

The utilization of carbon dioxide, often referred as carbon capture and utilization (CCU) or carbon dioxide utilization (CDU), embodies one viable solution to reduce the concentration of carbon dioxide in the air and the consumption of fossil material, turning waste CO_2 into a market commodity [7]. Carbon dioxide can be captured from different sources. These can be point source emitters (i.e., the flue gas from an industrial process or a power plant burning a fossil fuel), distributed and ultra-diluted sources (e.g., atmospheric CO_2 that is concentrated through direct air capture technology), biological sources (e.g., the off-gas stream of concentrated CO_2 leaving a biogas upgrading plant), or from bio-syngas coming from the gasification of biomass of mixed origin [9,10]. The captured carbon dioxide can then be fed to storage applications, for its underground geological storage, or utilized as the carbon feedstock to supply intermediate compounds of end-products with market value [1] (Figure 2).

When used to produce marketable products, CO_2 utilization opportunities include both direct and indirect applications.

In the first case, the main direct uses of carbon dioxide include food and beverages production, metals fabrication, heat transfer medium in refrigeration and supercritical power systems, yield boosting for biological processes (e.g., algae harvesting and fertilizers production) and injection into reservoirs for either

enhanced oil recovery (EOR) or enhanced gas recovery (EGR). In all the above-mentioned processes, the CO_2 molecule remains unaltered in its chemical form and is embedded in the service production route after impurities elimination [11].

In indirect applications, carbon dioxide is transformed through conversional processes that break its chemical bonds and allow its upgrade to value-added products. Both thermocatalytic conversion, electrochemical reduction, and biological conversion of CO_2 can be applied. Thus, CO_2 is converted into secondary compounds that can substitute their conventional counterparts (e.g., building materials), or substitute fossil-based material with alternative synthetic options (e.g., methane, methanol, Fischer-Tropsch, olefins, ethanol) [12].

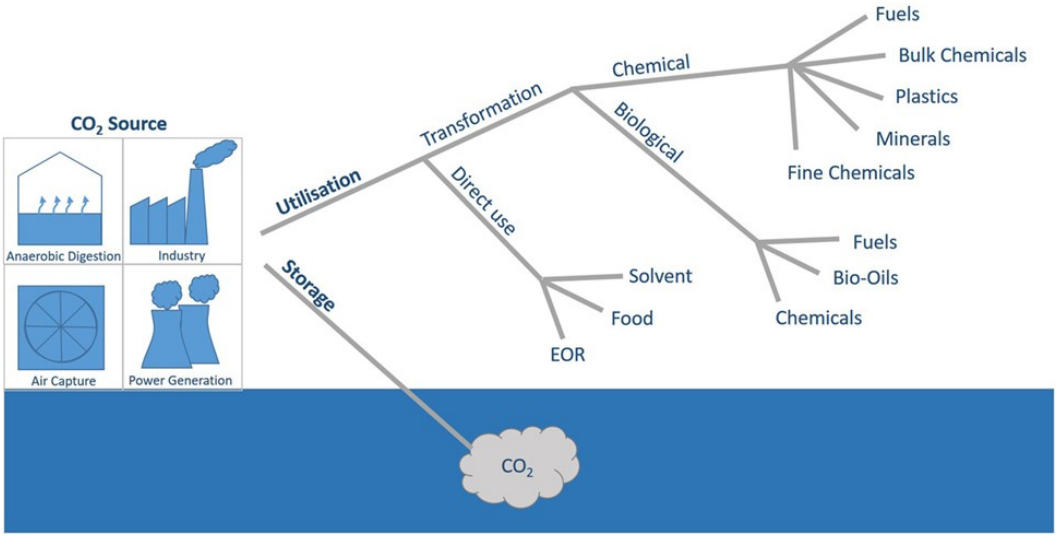

Figure 2. Routes for carbon dioxide storage or utilization solutions [7].

The conversion of carbon dioxide into secondary products may have both advantages and disadvantages. The main drawback of these applications is the relatively high thermal and electric energy demand to obtain the final products, determined by the high stability of the carbon-oxygen bond (-394 kJ/mol) [13]. Furthermore, in applications requiring hydrogen (e.g., methane, methanol, Fischer-Tropsch production – Power-to-X routes), the same must be produced from a low-carbon energy source [14]. However, the great interest of governments and industries for CO_2 utilization rather than carbon dioxide storage solution lies in the possibility of enhancing circular economy, with potential carbon neutral emission provided robust and thorough life-cycle assessments. Furthermore, CCU conversion routes allow for the decentralization of these systems, coupling them with renewable energy at both remote and production plant locations, and allows for the use of pre-existing infrastructure requiring minor adaptation [15,16]. Table 1 lists advantages and disadvantages of CO_2 conversion to fuels and chemicals, bioproducts and mineralization and construction materials [17–19].

Table 1. Advantages and disadvantages of carbon dioxide conversion route. Adapted from [17].

Conversion route	Advantage	Disadvantage
CO_2 to fuels and chemicals	Substitution of carbon fossil feedstock and non-renewable C_1 building blocks; promotion of circular economy; Carbon neutral emissions; minor modification to pre-existing infrastructure; low water footprint compared to conventional synthesis [20]; storage of renewable energy into chemical form.	High amount of energy; bounded to RES intermittency; storage of hydrogen and carbon dioxide; purification of the CO_2 stream needed; required intermediate electro-/thermo-chemical CO_2-to-CO conversion; catalyst development needed; possible CO_2 leakage; short-term CO_2 sequestration; high installation costs (e.g., electrolysis, pressurized gas storage); require low-price electricity.
CO_2 to mineral carbonation and construction materials	Abundant use as raw material; chemical free material; permanent CO_2 sequestration; no CO_2 feed quality requirements; low-energy molecule (carbonate CO_3^{2-});	Slow kinetics of formation; large amount of reagents required; high energy consumption; ash pollution; carbon dioxide transport to plant production location;
CO_2 to biological material	Low CO_2 concentration required; carbon neutral emissions; circular economy promotion; simple process control and reduced land footprint of photobioreactors; possible solar energy storage.	Algae production is bound to CO_2 feed quality and low impurities concentration; costly growth-control and drying process. Large areas for biomaterial production required with open raceway ponds systems.

1.1.1 Conversion f CO_2 into fuels and chemicals

The conversion of carbon dioxide (or gasified biomass) into fuels and chemicals allows for the displacement of fossil-based compounds employed in the chemical, transport, power production, pharmaceutical sectors. For this type of conversion route, the carbon dioxide usually undergoes a one-step or a two-steps hydrogenation process. In the first case, CO_2 directly reacts with H_2. In the latter case, CO_2 is firstly converted to CO by breaking the carbon dioxide C=O bonds and subsequently into end-products by reaction between CO and H_2. The hydrogenation of either CO_2 or CO to end-products usually occurs in chemical reactors, where the reaction is driven on a catalytic bed [21]. Additionally, to make such a route environmentally competitive, the required hydrogen has to be generated utilizing renewable energy sources (e.g., electrochemical conversion of steam to hydrogen via electrolysis technology fed with renewable energy electricity). In this case, the routes take the name of Power-to-X pathways [22].

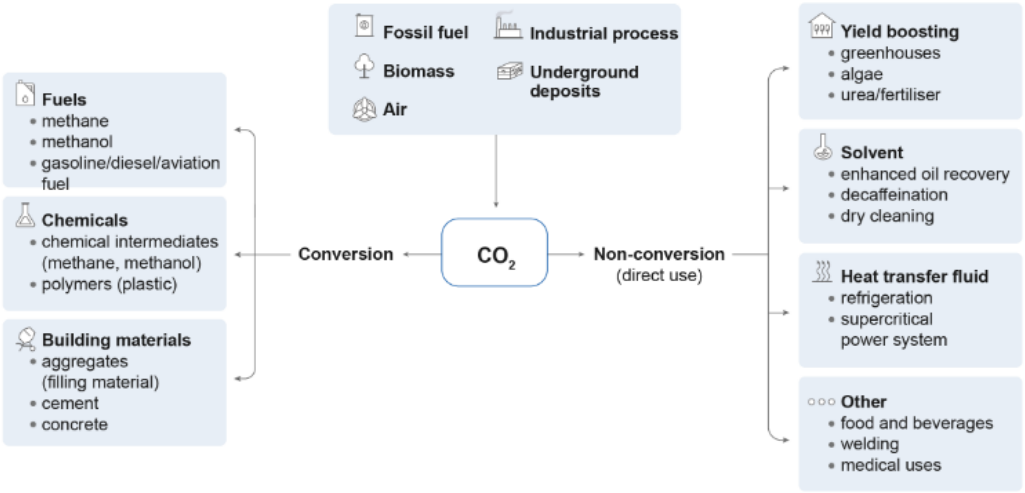

Figure 3. Routes for direct and indirect conversion of carbon dioxide in CO_2 utilization processes and sources of carbon dioxide [1].

Methanol production is one of the most effective and mature CCU routes with hydrogenation of CO_2. It can be employed as feedstock for both fuels, solvents, and the production of industrial chemicals, including dimethyl ether (DME), methyl tertiary-butyl ether (MTBE), formaldehyde, acetic acid, olefins [23,24]. Similarly, great interest is provided by the end-product methane. Natural gas can be synthesized to substitute its fossil-based counterparts for transport, power, and heat generation, with renewable electricity storage into the existing gas grid [25,26]. Additionally, CO_2 can be reduced to carbon monoxide in electrochemically driven conversion routes to generate carbon monoxide, formic acid, ethanol, ethylene [27]. In the case of carbon monoxide, this can be mixed with hydrogen, obtaining the so-called synthesis gas (i.e., syngas), and utilized as the feedstock for the Fischer-Tropsch reaction for alkanes and alkanes fuels and chemicals production [28,29]. With a smaller CO_2 utilization potential, other materials such as cyclic carbonates, polymers, carbon fibers, composites and fine chemicals can be produced from carbon dioxide [13,17]. Lastly, urea can be produced by the reaction of CO_2 with ammonia [12].

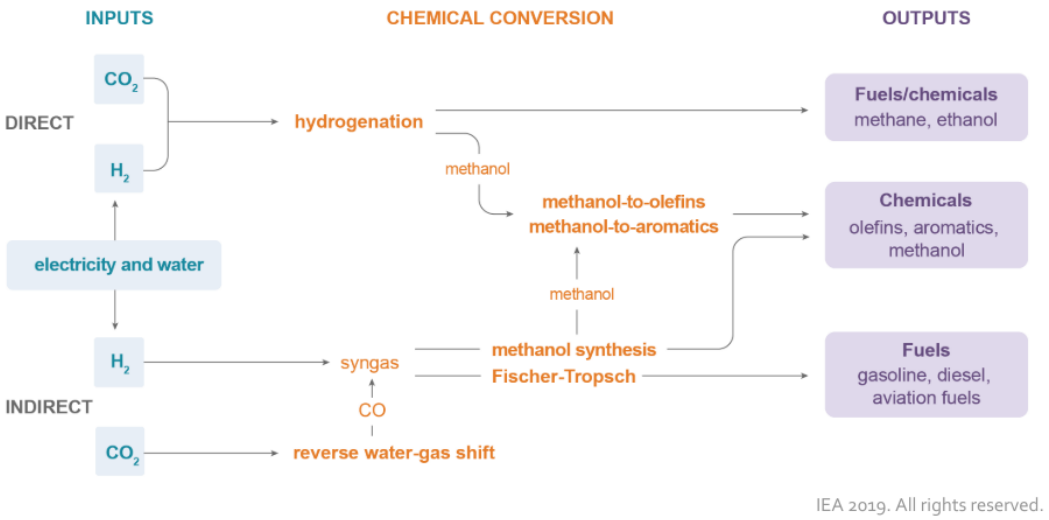

Figure 4. Routes for the conversion of CO_2 into fuels and chemicals [4].

1.2 CO_2 utilization market potential

The current global CO_2 demand for commercially mature CCU applications is estimated at around 250/300 Mt_{CO2}/y [1], which could be considered negligible concerning the CO_2 anthropogenic emissions (>37 Gt/y_{2018}). Moreover, the actual contribution of carbon capture and utilization to climate mitigation might be difficult to assess, reflecting the general early development stages of the available routes (i.e., R&D, demonstration, niche market-scale) and uncertainties in market penetration [30,31]. However, future national and international policies on carbon capping and carbon taxes could boost the development of the carbon dioxide utilization market. Incentives towards carbon capture technologies can determine a higher availability of carbon dioxide feedstocks, resulting in promoting the CO_2 circular economy and increasing CCU mitigation benefits. Additionally, the coupling of CCU routes with alternative-to-fossil carbon feedstocks like direct air capture and biomass allows for carbon negative and carbon neutral emissions [19,32,33].

With detail on conversion routes at the global scale, Table 2 provides the current carbon utilization potential and the market size for different relevant CO_2-derived end-products [12,17,34].

Methane is the most promising product in terms of market size (1.1-1.5 Gt_{CH4}/y) and CO_2 utilization potential (3-4 Gt_{CO2}/y). A commercial-scale production of methane is provided by the Audi e-gas process in Werlte, Germany (plant capacity 6.3 MW) [35]. Additionally, even methanol is a promising CO_2-derived product. The methanol potential accounts for 153 Mt_{CO2}/y for a market size of about 65 $Mt_{methanol}/y$. An already proven application can be found in Iceland through the Carbon Recycling International company, converting CO_2-rich flue gases and exploiting geothermal and hydropower energy [36]. Regarding urea, it represents the chemical with the highest current carbon uptake (130

Mt_{CO2}/y), with a market potential in the range of 180 Mt_{urea}/y. Stemicarbon is one of the few companies that commercialize urea production from anthropogenic carbon dioxide [18,37].

Biological products (i.e., microalgae production) have a slightly lower market size for fuels and chemicals (35 Mt/y), with a CO_2 utilization potential of 63 Mt_{CO2}/y. The Israeli company Seambiotic grows algae from flue gas-derived carbon dioxide, while US company Algenol Biofuels synthesizes ethanol using CO_2-fed algae [35].

Finally, construction materials (i.e., calcium, sodium, and magnesium carbonate utilized in cement and concrete production) account for about 200 Mt/y in market size, with a carbon dioxide utilization potential and latter storage of almost 90 Mt_{CO2}/y. Skyonic Corporation, Carbon8, Solidia Technologies, Carbon Cure, Calera Corporation, and Mineral Carbonation International are the leading companies currently commercializing carbon dioxide conversion into construction materials of different nature [1,38,39].

Table 2. Market size and CO_2 utilization potential for end-products under conversion routes (non-exhaustive), and companies commercializing the route. Adapted from [12,17,18,34,40].

CO_2-based product	**CO_2 Potential [Mt_{CO2}/y]**	**Market size [Mt_{prod}/y]**	**Market price [€/t_{prod}]**
Methane	3000/4000	1100/1500	70-250
Urea	130	180	250-450
Calcium carbonate	50	114	80-300
Ethanol	153	80	480-520
Methanol	90	65	450-500
Sodium carbonate	26	62	80-300
Microalgae [40]	63	35	250-1450
Formaldehyde	31	21	500-950
Magnesium carbonate	5.4	21	500-950
Polyurethane	4.5	15	1900-2200
Dimethyl ether	21.8	11	500-800
Acetic acid	7.5	10	500-800
Acrylic acid	3.5	6.0	1750-2950
Polycarbonates	0.9	5	2950-4000
Dimethyl carbonate	2.3	1.6	950-1300
Formic acid	0.9	1	650-1000
Ethylene carbonate	0.099	0.2	1350-3000
Propylene carbonate	0.086	0.2	1350-3000
Salicylic acid	0.054	0.17	1350-3000

Additionally, to allow for a feasible market entry at commercial level of the CCU routes, the operative cost of CO_2 supply can be evaluated [41]. Depending on the technology used to capture the CO_2, and the source of CO_2 itself, the carbon dioxide feedstock stream has different cost ranges. Utilizing mature technologies (e.g., amine-based chemical scrubbing) coupled with gaseous streams with a high concentration of carbon dioxide (e.g., natural gas processing, ammonia, coal gasification) allows having a price of the captured CO_2 stream

ranging between 15 and 60 €/t_{CO2}. Inversely, capturing carbon dioxide directly from the air can be advantageous from an environmental perspective, but this solution would generate much higher CO_2 stream costs, providing a rise in the final cost of production of the targeted end-use goods.

Table 3. CO_2 sources and capture cost. Adapted from [1,9].

Source of CO_2	CO_2 concentration [mol-%]	Capture cost [€/t_{CO2}]
Natural gas processing	96-100	15-25
Coal gasification	95-100	15-25
Ammonia	98-100	23-35
Bioethanol	98-100	25-35
Hydrogen (SMR)	30-100	15-60
Iron & Steel	21-30	60-100
Cement	15-30	60-120
Biogas	25-45	15-25
Air	400ppm	115-388

1.2.1 Fischer-Tropsch market potential

For Fisher-Tropsch material, the current CO_2 utilization potential is not straightforward to establish. In fact, Fischer-Tropsch conversion routes require the feed of a syngas, which can be obtained from different sources. Additionally, depending on the Fischer-Tropsch catalyst and reaction technology, a different products spectrum can be obtained, determining a variable CO_2 uptake.

Considering the final products, Fischer-Tropsch compounds can be destined to several sectors at once. In the case of transport fuels (i.e., FT-diesel and jet fuels) the reported market potential can be addressed as similar to methanol [42]. In the case of waxes (main interest within this research), Fischer-Tropsch ones have similar applications as of paraffin waxes. In this regard, it is forecasted a rise in the global paraffin waxes market from 5.1 billion € of 2018 to approximately 7.4 billion € in 2025, with a wax price ranging from 0.5 to 2.5 €/kg depending on the carbon number [43–45]. However, there is no global production of waxes coming from CO_2 at commercial level at current date. As a reference, one of the biggest producers of waxes is Sasol, a South African chemical company, which manufactures Fischer-Tropsch paraffin waxes from coal gasification. With respect to the year 2018, they provided sale prices of about 1200 €/t, for market coverage of 252 kt of waxes at Q1 [46,47].

Hence, the potential for carbon dioxide uptake into FT compounds and paraffin waxes demand are quite relevant for alternative-to-fossil routes.

1.3 Circular economy of carbon material

Within CCU applications, the paradigm of circularity of carbon material is currently being promoted as a forecasted solution to reduce fossil fuels consumption, especially in the European Union where circularity becomes a

prerequisite in achieving carbon neutrality (*A new Circular Economy Action Plan for a cleaner and more competitive Europe, November 2020*) [8]. This concept allows shifting from the business-as-usual linear production model to a self-sustained circular pattern where wastes are constantly upgraded to assets.

In the case of linear production, new resources are incessantly utilized for the manufacture of consumer goods. Concerning carbon-based materials, this means extracting crude oil and fossil hydrocarbons from the ground for a one-time use and conversion step, before turning into wastes (e.g., CO_2 waste streams, spent carbon material and marketed products, landfill disposal). This production model has been referred as unsustainable from an economic, ecological, and social point of view, with extensive depletion of limited resources [48].

In the second case, the circular economy promotes the reuse of carbon material, turning waste streams into resource with market potential, as substrate for the production of various other higher value-added products [49]. In this context, the only external inputs come from electricity of renewable source to sustain the conversion processes and mineral raw materials. The only outputs towards the environment become the service or good produced and minimal residual waste, in a net-zero CO_2 emissions boundary (Figure 5).

In a fully established circularity of carbon material, it is paramount that the C_1 molecule comes from biomass, biogas, or directly capturing the CO_2 from the air [50]. For this to happen, a period of carbon transition where fossil hydrocarbons are subsequently substituted by renewable hydrocarbon is vital [51].

1.3.1 Flexible applications

To meet circularity criteria, compact, simple designed, and flexible carbon utilization solutions are preferential with respect to large-scale ones [52]. This solution allows installing the CCU plant close to renewable energy sources (i.e., solar fields and windmills farms). Moreover, the plant can be deployed at the different locations of carbon feedstock, avoiding costs and environmental impacts connected to the transport of feed materials [53]. As stated by Lehtonen et al. [22], this means expanding the regional raw material resource and relying on domestic feedstocks for product generation.

Moreover, small-scale and flexible solutions are also in line with the direction of process intensification in the field of Fischer-Tropsch: novel reactor design are being investigated to reduce their volume, meanwhile increasing the yield of hydrocarbons production [54].

1.3.2 Social acceptance

Social acceptance may also play an essential role as a potential barrier or driver for implementing carbon capture and utilization technologies. With respect to storage applications, carbon dioxide utilization can be regarded as beneficial and less adverse from a public opinion point of view, as CO_2 is turned from waste

to resource [17]. As a result of the available studies specifically developed for CCU products and services [55], it was concluded that the general public deficiencies of technical knowledge and understanding in the field of CCU, but has a condescending attitude towards the concept of recycling carbon dioxide wastes, specifically when considering the benefits of employment provided by novel businesses and reliance on local resource [47]. The main concerns are related to the risk's perception: quality of the end-products, allergies, possible CO_2 leakage, and environmental impacts. These studies suggest delivering clear and comprehensive description of the CCU application, compared with traditional services and end-products from both a quality and safety point of view, and from life cycle assessments results for effective climate mitigation solution [7].

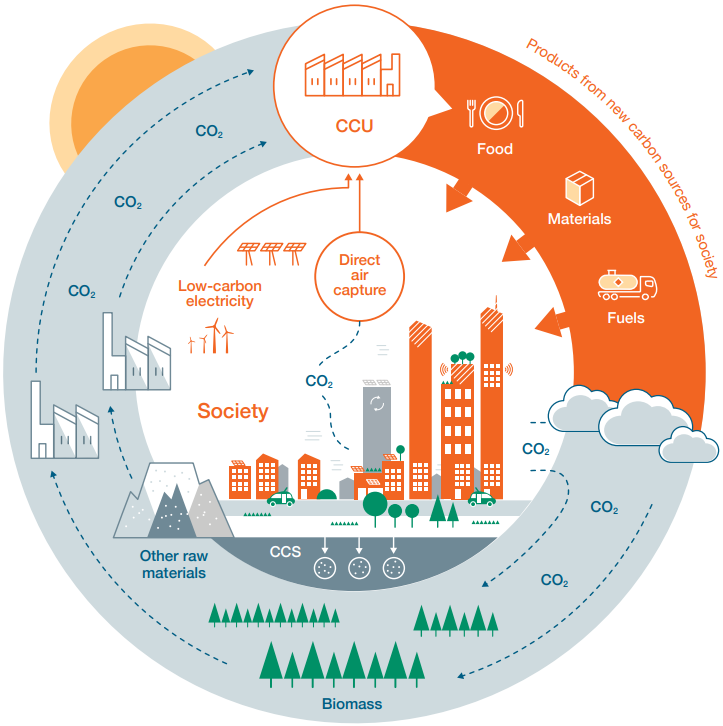

Figure 5. Carbon cycles schematics of a fully developed society under the circular economy paradigm. Courtesy of Lehtonen et al. [22].

1.4 Potential carbon sources

As mentioned, different sources of CO_2 and carbon can be identified to produce carbon-based products. These comprise of biogenic sources such as biomass (combustion or gasification) and biogas, carbon dioxide from the air, and carbon dioxide from flue gases of industrial processes [56].

In the present research, three primary carbon feedstocks were selected to produce Fischer-Tropsch material: biogas from anaerobic digestion, digestate biomass from anaerobic digestion, CO_2 captured directly from the air.

1.4.1 Biogas potential

Biogas represents a valuable resource for the reduction in fossil consumption and is addressed as renewable gas. It can be produced from organic waste feedstocks, such as residues of crops, agricultural wastes, animal manure, organic municipal solid waste, or wastewater sludge. Its generation mainly takes place through anaerobic digestion, which is considered a mature technology. The resulting gas is a mixture of carbon dioxide, methane, and other gaseous species with a concentration in the order of ppm (e.g., H_2S, NH_3, aromatic compounds), which can be directly used in internal combustion engines [51]. Additionally, biogas can be conditioned (i.e., cleaned from its impurities) and upgraded to biomethane for injection and blending into the existing gas grid [57]. The upgrading step consists of separating CO_2 from CH_4 via the application of amine-based chemical scrubbing, physical scrubbing, membranes, cryogenic CO_2 separation, water scrubbing, or pressure swing absorption technologies. This procedure leaves a pure and concentrated flow of carbon dioxide that is generally vented towards the atmosphere. Alternatively, the CO_2 stream can be recovered, mixed with green hydrogen, and fed into conversion processes to synthesize carbon-based hydrocarbons [56].

According to the European Biogas Association [58] and the International Energy Agency [59], there were 18944 biogas plants and 742 biomethane plants operating in Europe at the end 2019, where biomethane plants are intended as biogas plants with an installed upgrading technology, leading to a total CO_2 potential availability of 33.9 Mt_{CO2}/y_{2019} (accounting only for the CO_2 in the biogas, without conversion of carbon content of methane into carbon dioxide in combustion processes). Of this potential, about 10.95 Mt_{CO2}/y_{2019} is CO_2 separated from the biogas, with biomethane plants already connected to the gas grid.

The installation of new biogas plants in Europe is slowly reaching a plateau condition, with a sensible slowdown with respect to the years 2009-2020 (Figure 6). Contrarywise, the installation of upgrading units to separate carbon dioxide from methane has seen a constant (and almost exponentially) rise. Such a trend is connected to governments and European incentives for the injection of renewable methane into the national gas grids [60–62]. In this regard, CCU applications can benefit from the rise in available “ready-to-use” carbon dioxide. Thus, carbon-based products destined to different industrial sectors can be synthetized utilizing an almost pure CO_2 stream, in a condition where local policies already promote the capture of CO_2.

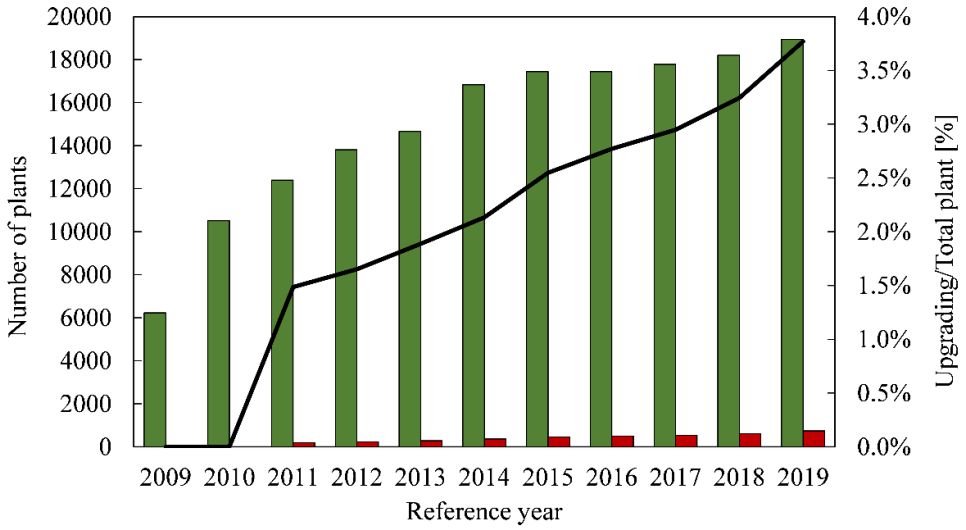

Figure 6. Evolution of the installed biogas and biomethane plants in Europe. Adapted from [58,59].

1.4.2 Digestate potential

The anaerobic digestion (AD) process allows for the generation of biogas, by means of degradation of biomaterial. This process leaves a wet by-product called *digestate*, rich in nitrogen, phosphorous, and stabilized carbon in different concentrations depending on the AD input substate. This material generally undergoes a valorisation step by being utilized as fertilizer for agricultural applications [63]. Additionally, it can be dried and employed in thermochemical conversion routes, as a combustion fuel, or gasified to generate syngas for downstream applications [64]. This last solution of gasification allows recovering the remaining carbon material (i.e., substrate) that did not contribute to the biogas production, increasing the value chain of this compound, provided that an impurities abatement step is included [65]. Moreover, employing digestate as the gasification feedstock reduces land eutrophication and soil degradation provided by the presence of harmful compounds in case of its landfill disposal and avoids its incineration. Finally, using digestate as carbon feedstock promotes circular economy after anaerobic digestion [66].

Regarding existing biogas and biomethane plants installed in Europe, there is a potential amount of wet digestate corresponding to 29.1 Mt_{dig}/y_{2019}. Similar to the CO_2 from biogas upgrading processes, this amount of digestate represents a *ready-to-use* stream of carbon material that can contribute to the offset of fossil hydrocarbons.

1.4.3 Carbon dioxide coming from the air

Extracting CO_2 directly from the air represents another solution to obtain carbon material that offsets the utilization of fossil hydrocarbons [67]. Such a solution requires the implementation of a technology called Direct Air Capture

(DAC), where a stream of air is contacted with a solid sorbent and separates CO_2 (found in the air with a concentration in the range of 400-500 ppm) [68]. Commercialized DAC technologies can be classified upon their regeneration temperature as either high-temperature (HT-DAC) or low-temperature (LT-DAC) solutions. In HT-DAC, CO_2 is continuously extracted from the air. It enters a first absorption reaction cycle where CO_2 reacts with an aqueous alkaline solution. A second regeneration cycle is used to release a stream of pure CO_2 for downstream applications. Carbon Engineering provides a commercial solution with the HT-DAC [9]. Under LT-DAC, solid sorbents are used for the alternating absorption and regeneration cycles. In the first step, a cellulosic filter with solid amines binds the CO_2 from the air. In the second step, carbon dioxide is released with the help of heat. An example of this solution is provided by the company Climeworks [69].

The interest in capturing carbon directly from the air lies in the fact that air can be considered an almost unlimited CO_2 resource, potentially available regardless of the plant location. Additionally, the DAC unit can directly influence and reduce the concentration of CO_2 in the air, increasing the removal rate ensured by the natural sinks in carbon cycles and enhance CO_2 mitigation [70]. The recovered CO_2 from the air can be used for either storage or utilization applications. In this regard, few pilot plants have been installed to demonstrate the feasibility of this concept [71,72].

1.5 The ICO2CHEM concept

One demonstrative CO_2 conversion routes is provided by the H2020 project ICO2CHEM, funded through the public-private platform SPIRE [73].

The ICO2CHEM concept proposes converting captured CO_2 from biogas, and hydrogen coming from a chloro-alkali electrolysis plant, into value-added chemicals. These comprise synthetic hydrocarbons (white oils and linear paraffin waxes) to address the chemical sector and substitute their fossil-based counterparts. Within the project, the conversion of CO_2 to products follows a two-step route. Firstly, carbon dioxide is converted to CO in a reverse water-gas shift reactor by endothermic reaction with hydrogen. Secondly, the resulting CO is mixed with H_2 and fed to a low-temperature Fischer-Tropsch reactor. Finally, synthetic hydrocarbons are collected at the outlet of the second reactor.

The project demonstration plant is located at the Infraserv industrial park of Hoechst, Frankfurt am Main (Germany), and represents the first power-to-liquid unit ever installed at an industrial location, to utilize wasted CO_2. The activities carried out within this research are connected to this project.

1.6 Motivation and research aim

The issue of climate change cannot be solved with just a single solution. Furthermore, the request of carbon-based products from different industrial

sectors will not reduce in the next years. Hence, it becomes paramount to find technological solutions that can promote carbon transition, producing end-products that can substitute fossil-based counterparts meanwhile favouring the penetration of renewable energy.

In this regard, the rising demand for paraffin waxes represents an unresolved issue for the chemical industry decarbonization. These products are utilized as platform chemicals for a wide range of applications: cosmetics, solvents, adhesives, inks, paint thinners, candles, polymer additives [44,46,74]. However, currently, waxes are commercially obtained only from the conversion of fossil hydrocarbons. Fischer-Tropsch applications may provide a feasible solution to meet the requirements posed by the carbon transition agenda, being capable of synthetizing a wide spectrum of synthetic hydrocarbons, among which high molecular weight waxes are the most valuable fraction. Hence, Fischer-Tropsch material can be introduced into the production cycle of the chemical sector. Additionally, the Fischer-Tropsch technology can be coupled with different carbon feedstocks, from industrial CO_2 to biomass. Finally, the need for hydrogen to generate the synthetic compounds allows utilizing electrolysis technology, contributing to the storage of electricity into chemical form [75,76].

Within Fischer-Tropsch, the research has thus far focused on specific topics such as catalyst development, trying to unveil the reaction mechanism evolving over the catalyst surface [77,78]. Parallelly, Fischer-Tropsch reactor engineering has been an important subject matter, investigating the possibility of enhancing thermal exchange and utilizing highly active catalysts [79,80]. Finally, process modelling provides information on the production costs of Fischer-Tropsch material utilizing different carbon feedstocks [75,81]. If catalyst development and reactor engineering are developed tightly together, process modelling involving Fischer-Tropsch conversion generally includes simple kinetics, with lumped hydrocarbon components, focusing on the production route of liquid fuels (i.e., diesel, jet fuels), and seldom including the process of carbon capture.

With the current research work, the aim is to investigate the kinetics of a Fischer-Tropsch catalyst, to extrapolate information about the formation of heavy waxes. Additionally, such detailed information is moved towards process modelling and techno-economic activities, to determine the production costs of Fischer-Tropsch waxes derived from different carbon sources. Biogas, digestate, and CO_2 from the air conversion are included, together with the production of syngas via reverse water-gas shift, co-electrolysis, or gasification, and the generation of green hydrogen via low-temperature steam electrolysis.

Hence, the final objective of this research is to identify the most profitable and effective process schemes that allow for a high outtake of Fischer-Tropsch waxes, promote a circular economy of carbon material by converting existing non-fossil carbon feedstocks through compact and flexible systems, and have a low impact over the environment related to harmful CO_2 emissions.

Chapter 2

The Fischer-Tropsch synthesis and kinetic modelling

The present chapter provides an overview of the Fischer-Tropsch technology and the activities carried out to develop a Fischer-Tropsch kinetic model.

In the first part of the chapter, the Fischer-Tropsch synthesis (FTS) mechanism is described. Additionally, the different technological solutions currently employed for the FTS are provided in terms of catalyst typologies and Fischer-Tropsch reactors, with details on the various process conditions. Lastly, the Fischer-Tropsch products distribution and kinetics are described with reference to literature findings. In the second part of this chapter, the experimental campaign performed on a Fischer-Tropsch catalyst is described. Specifically, a Co/Pt-Al_2O_3 catalyst was experimentally tested to gain information about its performance under several industrial-like operating conditions. The experimental data were used to fit several kinetic models derived from literature utilizing non-linear least-squared fitting procedures. Moreover, one final detailed mechanistic kinetic model was selected to describe the FTS products distribution up to carbon number C_{80}. Such kinetic information has been included into process models involving the FTS reaction for the conversion of non-fossil carbon feedstocks and derive techno-economic considerations of the production of FT waxes. Part of the work provided in this chapter has been previously published in [82].

2.1 Fischer-Tropsch process technology

The FTS is a pseudo-polymerization exothermic reaction, where carbon monoxide reacts with hydrogen under heterogeneous catalyst conditions, converting the syngas to syncrude. Depending on the operating temperature, the FTS refers to High Temperature FT (HTFT) and Low-Temperature FT (LTFT) [83–85]. The HTFT is the preferential application for the synthesis of short-chain hydrocarbons, usually in the gas phase, with the syncrude having a high content of

propane and butane. The typical operating conditions correspond to temperature and pressure ranges of 300-350°C and 20-30 bar, respectively, with a CO-to-syncrude conversion efficiency of 85%. Lastly, Fe-based catalysts are preferred for HTFT [86]. The LTFT implementation yields a generally higher concentration of heavier molecular weight products. The conversion is favoured at the temperature range of 180-250°C, with a pressure of 15-30 bar. The conversion efficiency is typically lower than HTFT, with values of 60-70%. Co-based catalysts are mainly employed in LTFT systems [87].

2.1.1 Fischer-Tropsch stoichiometry and products

The overall stoichiometry of the FTS follows eq. (2.1). The resulting syncrude (i.e., the pool of C_nH_m compounds) represents a multicomponent mixture of synthetic hydrocarbons, whose composition is affected by the type of reactor and the employed catalyst.

$$CO + \left(1 + \frac{m}{2n}\right) H_2 \rightarrow \frac{1}{n} C_n H_m + H_2O \qquad \text{-165 kJ mol}^{-1} \qquad (2.1)$$

The syncrude components can be further identified as different classes of hydrocarbon compounds [88,89].

- Paraffins: these are saturated hydrocarbons simplified to their linear form as n-paraffin. A low concentration of branched paraffin can also be synthetised, decreasing with the increase of the carbon chain length.
- Olefins: these products are mainly considered as α-olefins, olefins in the linear form.
- Other side products: alcohols, aromatic compounds, isomers, esters, ketones. Water is also a major product leaving the FT reactor.
- Side reactions may also take place during FTS reactions. These mainly comprise of the water gas-shift reaction generating carbon dioxide, and the Boudouard reaction leading to carbon deposition.

$CO + 3H_2 \rightarrow CH_4 + H_2O$	Methane	(2.2)
$nCO + (2n+1)H_2 \rightarrow C_nH_{2n+2} + H_2O$	Paraffins	(2.3)
$nCO + (2n)H_2 \rightarrow C_nH_{2n} + H_2O$	Olefins	(2.4)
$nCO + (2n)H_2 \rightarrow C_nH_{2n+2}O + (n-1)H_2O$	Alcohols	(2.5)
$nCO + (2n-1)H_2 \rightarrow C_nH_{2n}O + (n-1)H_2O$	Ketones	(2.6)
$CO + H_2O \rightarrow CO_2 + H_2$	WGS	(2.7)
$2CO \rightarrow C + CO_2$	Boudouard	(2.8)

The syncrude can be utilized as a substitute of crude oil, with offset of fossil-based counterparts by FTS compounds, with the advantage of using syncrude in the same distillation facilities of crude oil [89]. The syncrude is a more reactive feed than crude oil, due to the higher concentration of olefins and oxygenates.

Moreover, syncrude is considered a cleaner product than crude oil, as no nitrogen nor sulphur compounds can be found in it. Consequently, refinery of the FTS products results in a cleaner off gas. The main difference is in the production of FTS syncrude, which requires a syngas source [90]. Moreover, FTS products can be identified as fractions constituents of the syncrude pool at increasing values of carbon numbers: gas (C_1-C_4), liquid (C_5-C_{19}), and wax (C_{20+}) fractions. These are further separated based on their boiling points into methane (C_1) and tail gas (C_2-C_4) at 40°C, naphtha (C_5-C_9) 123°C, middle distillates (C_{10}-C_{20}) 225°C, light waxes (C_{21}-C_{35}) 383°C, and heavy waxes (C_{35+}) 520°C. The FTS end products can be utilized into different sectors:

- Methane and light gases are generally utilized for internal combustion at the plant location.
- C_4-C_{20} products can be utilized to synthesize liquid fuels like gasoline, diesel, kerosene, and jet fuels [91], or for the production of white oils and solvents [89].
- The heavy wax fractions can be hydrocracked to a diesel pool [91], or exploited into the chemical sector as platform chemicals to synthesize wax emulsions, binders, cosmetics, lubricants, food applications [43,74,92].

2.1.2 Fischer-Tropsch reactors

Four main typologies of FT reactors can be utilized to convert syngas into syncrude, either with moving or stationary catalytic beds (Figure 7): fixed-bed multitubular reactors, fluidized-bed reactors, slurry-bed reactors, microchannel reactors [79,85,93,94].

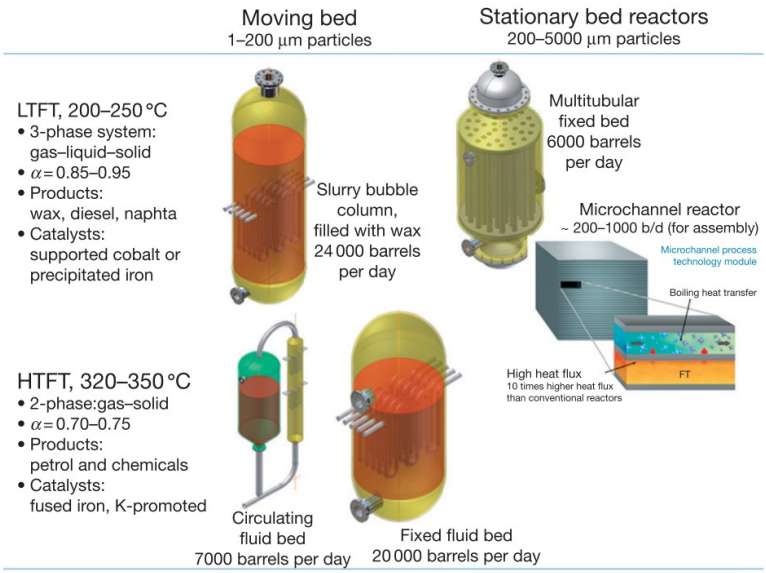

Figure 7. FTS reactor design and preferential operations for the FTS synthesis. Reprinted from [85].

Fixed-bed reactors comprise of a robust multitubular structure where the FT catalyst is loaded inside the reactor shell. These reactors are mainly utilized to

produce heavy hydrocarbons under LTFT conditions. The syngas is fed from the top of the reactor, and the products are collected at the bottom, without any need of separation procedure of the catalyst particles from the FT compounds. The heat removal occurs through steam or thermal fluid flowing in the side around the reactor tubes, with small diameters of the tubes required for effective heat extraction. This solution would also allow the use of highly active catalysts at the expense of narrower tubes. However, a trade-off of the catalyst particle sizes is required. On the one hand, small particles allow reducing possible pressure drops and compression costs using narrow tubes. On the other hand, bigger particles allow a proper flow of the FTS products, with reduced mass transfer and diffusion limitations. From an engineering perspective, these reactors would be preferred for small-scale and compact applications to reduce possible tube blockage and rise in pressure drops. Finally, the substitution of the spent catalyst requires the system to stop its operations [85,93].

Fluidized-bed reactors (either circulating or fixed fluidized) provide a solution where the FTS products are synthetized over a moving catalyst bed. These reactors are usually employed under HTFT operations, aiming at the production of light hydrocarbons. This system allows for the use of small catalyst particles, reducing and avoiding interparticle diffusion limitations, and the fluidization solution provides high gas-solid contact efficiency. Additionally, these reactors have an easy catalyst replacement. However, they require the presence of a separation unit where the catalyst particles are divided from the hydrocarbons, they might be subjected to accumulation and blockage of the circulation lines and reactor degradation due to solid catalyst attrition. Compared to fixed-bed reactors, they can reach higher productions given their higher gas feed, but their design is more complex for operation and scale-up design, and no syngas backflow must be assured [83,95].

Slurry-bed reactors are easier to design than fixed and fluidized bed reactors and are generally utilized under LTFT conditions. The syngas is fed at the bottom of the reactor and bubbled through slurry fluid phase where the catalyst is suspended and dispersed. The gas products exit from the top, while the liquid and catalyst are collected at the reactor side. The main drawback of these reactors is the need for a highly efficient catalyst/liquid phase separator to recover the liquid and wax fractions of the FTS. Additionally, the catalyst must be highly resistant from a mechanical point of view to sustain collisions and attrition. However, the well-mixed system allows for a controlled and constant temperature value inside the reactor [80,85].

Microchannel reactors represent the most recently developed solution for the FTS. They consist of a series of parallel channels of small diameters (around 1 mm), with catalyst loading over a thin layer inside the channel walls. Their design allows for easy thermal management, reaching isothermal operations even when using highly active catalysts, resulting in enhanced FTS productivity. Additionally, their catalyst bed is considerably smaller than other conventional

stationary reactors, which avoids pressure drops and eases FT material throughput. However, their main disadvantage is represented by the complex catalyst loading and replacement [79,94].

2.1.3 Fischer-Tropsch catalysts

In the FT synthesis, a gaseous flow of carbon monoxide and hydrogen interacts with the catalyst activated surface. The type of catalyst utilized for the FTS can affect product distribution. Additionally, the type of catalyst differs depending on the FT application (i.e., reactors and operating conditions).

Four main metals (group VIII) are being utilized for the FTS applications, being active in the dissociation of carbon monoxide [96]: ruthenium (Ru), nickel (Ni), iron (Fe), and cobalt (Co). Dry et al. [19] reported that Ru has the highest activity, followed by Co, Ni, and Fe. Their retail price has a similar trend, being Ru the most expensive and Fe the cheapest one.

Table 4. Advantages, disadvantages, and main applications of the four more active metals used as catalysts in FTS processes.

Metal	Advantages	Disadvantages	Main application
Ru	High activity under LTFT operating conditions High selectivity towards heavy hydrocarbon (liquid and waxes) High conversion	Scarcity of ruthenium High price of ruthenium	Research activities to study the FT synthesis mechanisms
Ni	Activity under LTFT and HTFT operating conditions High availability of nickel Low price of nickel	High selectivity towards light gaseous hydrocarbons and methane Thermal degradation Promotion of solid carbon deposition reactions	Research and industrial applications
Fe	Activity under HTFT conditions Favourable at harsh conditions (high-T, high-p, high flow rates) Low price of iron metal Selectivity towards light hydrocarbons	Not suitable for long-chain hydrocarbons synthesis; Active towards WGS reaction (production of CO_2) Higher amount of oxygenated compounds compared to cobalt catalyst (5%wt and <1 %wt). Prone to sintering and surface poisoning	Commercial applications aimed at light hydrocarbons (gaseous and diesel FT fuels)
Co	Activity under LTFT conditions Need of clean syngas and specific operating conditions Suitable for heavy hydrocarbons and waxes synthesis Negligible/No activity towards the WGS reaction for conversions lower than 85% [97,98].	High price of cobalt Not suitable for short-chain hydrocarbons synthesis High price of cobalt requires regeneration of the catalyst with use of hydrogen Need clean syngas feeds [99] Dispersion of cobalt particles needed over the catalyst support Lower conversion than Fe (60%)	Commercial applications aimed at both light and heavy hydrocarbons (liquid fuels and waxes)

Fe covers the main industrial and commercial applications- and Co-based catalysts [46,54,100].

2.1.4 Cobalt catalyst

The catalyst response can be affected by the preparation process and its composition. Cobalt catalysts are prepared via deposition of the Co material over an oxide support. Such a support can be silica, alumina, titania or zinc oxide, or a further combination of the previous [101].

Catalyst Composition

Co-based catalysts comprise different substrates to favour the FTS process. According to Loosdrecht et al. [85], four main substrates are identified: (i) refractory oxidic support, where cobalt particles are dispersed onto; (ii) cobalt oxide particles, considered the FTS active phase (10-30 wt%); (iii) a metal promoter for the reduction of cobalt (0.05-1 wt%); (iv) a structural oxidic promoter, favouring the stability of the active cobalt phase.

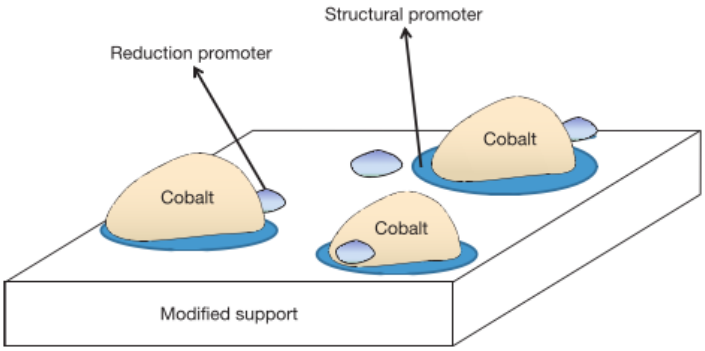

Figure 8. Schematics of the typical structural composition of a cobalt-based catalyst for FTS applications. Reproduced with permission from [85].

Given the high cost of cobalt material (around 1 €/kg for Fe-based catalyst, against 100 €/kg for Co-based ones, estimates by ChemCatBio [102]), metallic cobalt oxide Co_3O_4 is dispersed over support, reaching a high surface area with an amount of active Co phase corresponding to 10-30 wt.%.

Concerning the support material where the active metal is dispersed onto, this must provide high surface area, mechanical strength, thermal stability for the active cobalt particles during the FTS operations. Additionally, the choice of support material influences the amount of Co oxide that is reduced to its metallic form, due to a different Co-to-support interaction. In this matter, it was reported that a strong Co-support interaction increases the dispersion of cobalt particles and reduces the reducibility of Co and the final number of active sites for the reaction, with a reduction of the catalyst activity. Al_2O_3 and TiO_2 are examples of such supports. Similarly, also SiO_2 and ZrO_2 are typical supports for FTS catalysts. Their weaker interaction with Co particles provides superior reducibility

and activity, but agglomeration of cobalt particles might be more likely to occur [103].

Reduction and structural promoters are employed during catalyst manufacturing, too. The first ones aim at increasing the dispersion of the cobalt particles and their further reducibility, allowing for an enhanced formation of active sites for the FTS process compared to unpromoted catalysts [104]. In this regard, noble metals such as Ru, Re, and Pt are generally used as reduction promoters. The second class of compounds (i.e., structural promoters) comprise the element in charge of increasing the number of active sites of the catalyst as well as stabilizing the active Co particles (e.g., avoiding formation of cobalt aluminate in the case of Al_2O_3 supports), thus affecting the catalyst activity and stability [105]. Morales et al. [103] reported a detailed review of the preferential structural promoters involved in the FTS. Additionally, the authors also identified two other classes of promoters: electronic and synergistic. Electronic promoters influence the catalyst activity, stability, and product selectivity, affecting the elementary steps involved in the Fischer-Tropsch synthesis by modifying the chemisorption properties of the active metal. Similarly, synergetic promotion may locally influence the catalytic behaviour of the active metal, catalytically driving parallel reactions under FTS conditions (e.g., water-gas shift, coke burning, H_2S adsorption reactions). Among the elements utilized for promotion, Ru, Re and Pt are the most commonly employed, capable of lowering the reduction temperature (reduction temperature of un-promoted cobalt oxide of about 350°C) [106]:

Rhenium Promotion: Re provides promotion by lowering the reducing temperature of Co oxide. No direct contact of Re and Co is necessary to promote the active phase, making it possible to simply deposit Re on the support rather than on the Co particle. Finally, Rytter et al. [106] reported enhanced C_{5+} selectivity for cobalt-based catalysts doped with rhenium.

Ruthenium Promotion: Ru accounts for both structural and electronic promotion effects. Ru lowers the reduction temperature, increases the conversion of carbon monoxide to FT products [107]. Moreover, Ru promotion favours the selectivity of C_{5+} products at low FTS operating temperatures, possibly by increasing the effect of readsorption of the olefins [103].

Platinum Promotion: Pt enhances the Co dispersion onto the support, decreases the temperature of reduction of cobalt oxide, and enhances cobalt stability during catalyst regeneration procedures [103]. Additionally, Cook et al. [108] reported an increased catalyst activity under Pt promotion.

Considering the size of Co particles, it is reported that the minimum size for effective FTS processes should range around 10±2 nm [109,110]. According to Gavrilović et al. [111], the optimal cobalt particle size varies between 8 nm and 15 nm. Small particles have a low activity under FTS conditions and a higher selectivity towards light and short-chain hydrocarbons. As Mandić et al. [41] stated, small particles are more inclined to sintering during operations, as well as low reducibility due to strong interaction with the metal support. Finally, as

Fratalocchi et al. [42] reported, small cobalt particles might re-oxidize due to interaction with water produced during the FTS, consequently reducing the catalyst turnover frequency (i.e., the activity).

Preparation

Different preparation procedures can be applied when dealing with Co-based catalyst to reach the desired optimal particle sizes and high dispersion over the catalyst support. The main solutions are precipitation and impregnation, with novel techniques like atomic layer deposition currently being implemented [105].

Impregnation: this technique comprises of a liquid carrier (typically water) containing dissolved cobalt precursors (e.g., cobalt nitrate or cobalt acetate) [105]. During the impregnation, the liquid carrier is contacted with a pre-shaped porous solid support, then dried under heat, vacuum and stirring conditions [112]. Finally, the catalyst is calcinated and reduced.

Precipitation: this procedure usually involves the steps of (i) precipitation, (ii) washing and drying, and (iii) shaping. Co particles are obtained by precipitating cobalt-carrier solutions such as hydroxides (e.g., α-$Co(OH)_2$ or β-$Co(OH)_2$), with temperature, precipitation agents, reaction atmosphere, aging time controlling the crystalline size and composition of the precipitates. Filtration and washing is then applied for excess chemicals removal. Finally, for slurry phase reactors, catalysts precursors are re-slurred and spray dried, for fixed bed reactors, the precipitates are extruded or pelletized [85].

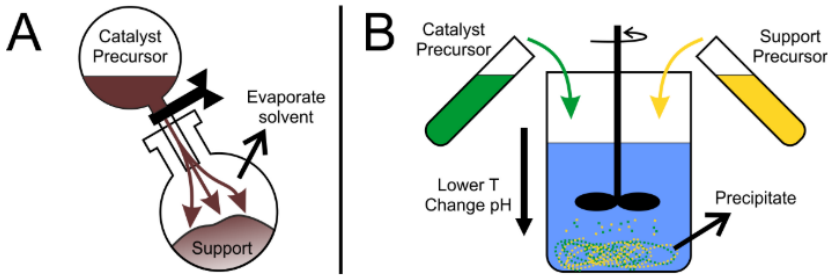

Figure 9. Schemes of the catalyst preparation by impregnation (a) and co-precipitation (b). Reproduced from [112].

Atomic layer deposition (ALD): this method is rather new and unconventional for FT synthesis products. It consists in the sub-sequential deposition of controlled thickness layers of the catalyst (active metals and promoters) over the catalyst support material. The latter is placed into a chamber at a given temperature and pressure, allowing for controlled and surface-limited chemical reactions with the catalyst precursors. Such a procedure enables controlling the Co dispersion and the thickness of the different substrates [112]. However, it is more expensive than conventional techniques [113].

Calcination

A calcination step is generally required to eliminate the water content from the catalyst before reduction and activation. A fast calcination process is required in order to maintain the cobalt distribution and structural composition achieved during the catalyst preparation. This can be achieved with a controlled combination of high heating rates and airflow rates, such that water and NOx are immediately removed from the catalyst matrix. According to Savost et al. [114], calcination temperatures for Co-based catalyst range between 200°C and 500°C.

Activation

The cobalt oxide undergoes a two-steps reduction process from Co_3O_4 to Co using a flow of H_2 to separate oxygen, according to eq.(2.9)-eq.(2.10). The time of reduction depends on the catalyst composition, but for Co-based ones, activation time ranges around 8-10 hours [85].

$$Co_3O_4 + H_2 \rightarrow 3CoO + H_2O \tag{2.9}$$

$$CoO + H_2 \rightarrow Co + H_2O \tag{2.10}$$

Degradation and regeneration

The cobalt catalysts have to ensure high activity, selectivity, and mechanical strength throughout their operational time. However, given their sensitivity to poisoning compounds and possible degradation or reoxidation of the active particles, regeneration procedures might be needed to reduce catalysts-related costs. The cobalt-based catalysts main deactivation causes are considered pore-blocking and sintering. In the first case, active metal sites undergo blockage due to growing hydrocarbons into the wax phase, resulting in mass transfer and diffusion limitations. Additionally, inactive solid carbon may deposit over the catalyst surface [115]. Regarding the sintering process, small and unstable Co-particles might migrate and join under high temperature or high partial pressures of water [116]. Other possible deactivations might take place. These comprise of (i) oxidation of cobalt active sites due to oxygen presence and (ii) metal-support interaction, mainly due to unreduced CoO and surface modification. However, these are less likely to occur under FTS conditions once the catalysts have been suitably reduced, as stated by Loosdrecht et al. [85] and Kocic et al. [115]. Even poisoning substances might deactivate the catalyst. Thus, clean syngas is required at the inlet of the FT reactor. Kim et al. [117] reported that sulfur-based and NH_3 compounds have to be below 1ppm in the feed syngas, halogens, and alkaline metals below 10 ppb, and any dust or organic compounds below the dew point. Finally, catalysts are regenerated with a flow of hydrogen and nitrogen blown over the surface.

2.1.5 Effect of the operating parameters

Operating conditions can influence the production yield and distribution of the FT products. The magnitude of influence over the FTS may vary with the catalyst composition and preparation methods. However, some general considerations can be extrapolated from literature reports. These comprise a change in the operating temperature, pressure, H_2/CO molar ratio in the syngas feed, gas hourly space velocity, and the range of variation in their values depending on the reactor typology and the involved catalyst. As reported by Loosdrecht et al. [85] and Maitlis et al. [83], cobalt-derived catalysts are employed in the LTFT applications, targeting the production of long-chain hydrocarbons (carbon numbers C_{5+}).

Temperature: A variation in the temperature produces a shift of the selectivity towards the distribution of the FT products. Specifically for Co-based catalysts, increasing the temperature value provides a higher synthesis of low molecular weight products, with a rise in the selectivity of C_1-C_4 elements [118]. This suggests that the temperature rise offers a much faster termination of the chain growth mechanism. Finally, an enhanced conversion of CO was reported by Almeida et al. [119] at increasing temperatures.

Pressure: Similarly, a variation in the pressure condition modifies the FTS product distribution and the reaction conversion. Increasing the pressure value during the FTS process positively affects the reaction rate, the selectivity towards high molecular weight molecules, and the CO conversion value [98,119].

H_2/CO ratio: high values of the hydrogen-to-carbon monoxide molar feed ratio at the inlet of the FT reactor leads to an increased yield of light products and to a lower selectivity of high molecular weight products [120,121]. The main reason of this change can be attributed to the decrease in the termination probability (lower primary hydrogenation sites) and an a rise in the re-adsorption of 1-olefins given the rinse in CO partial pressure [122].

Time-on-stream (TOS): Time on stream is directly linked to the activity of the catalyst. Increasing the TOS generally reduces the activity of the catalyst over time. This phenomenon is related to the degradation of the catalyst, specifically sintering, formation of non-active catalyst phases, and accumulation of pore-blocking compounds on the catalyst surface [123–125]. Additionally, a shift of the selectivity towards light hydrocarbons is reported [122].

Conversion level: When considering the conversion level, temperature, pressure, and hydrogen-to-carbon monoxide ratio are kept at constant level, and the effect is studied by means of variation of the gas hourly space velocity (GHSV). Specifically for Co-based catalyst, this results in an increasing value of the selectivity towards longer chains, which can be cause by secondary 1-olefins readsorption onto the catalyst for the chain growth process [123]. The secondary reactions of 1-olefins comprise hydrogenation to n-paraffins, isomerization to 2-olefins and readsorption followed by chain-growth [122].

Water: Depending on the primary carbon feedstock and conversion technology used to generate the required syngas (e.g., coal or biomass gasification, reverse water gas shift reaction, co-electrolysis), a flow of water in gaseous phase might enter the FT reactor together with H_2 and CO. Hence, cobalt catalyst can be affected by water and its partial pressure. Assuming the presence of different sites for CH_4 formation with respect to the other FT compounds, the addiction of water reduces the possibility of hydrogenation and desorption to methane, in favour of C1 species insertion to the hydrocarbon chain growth [121]. This effect can be linked to the capability of water to occupy the catalytic sites of methane [126]. However, specific consensus over the effect of water of the FTS has not yet been achieved. For instance, for Co-based alumina-supported catalysts, Storsæter et al. [127] identified an adverse effect of water over the FTS by deactivating the catalyst due to oxidation. On the contrary, Ma et al. [128] and Rytter et al. [129] reported a positive effect on the kinetics of FTS. Water build-up may enhance the conversion by allowing a more favourable distribution of the reactants and a clean-up from carbonaceous products on the catalyst and lowering the activation energy for CO dissociation.

Fischer-Tropsch kinetic

The Fischer-Tropsch synthesis is a rather complex reaction, which involves several compounds under several phases. Based on the literature, it can be described with a generalized approach like the ASF distribution, or with more detailed kinetic models that will unveil products formation rates of each synthetic hydrocarbon. However, a final consensus on the reaction evolution has not yet been reached [130,131].

2.1.6 Deviations from the ASF model

The FTS products distribution evolves with the carbon number value, with an empirical description following the Anderson-Shultz-Flory (ASF) theory (eq. (2.2)-(2.3)). The ASF describes the formation of the Fischer-Tropsch compounds utilizing a single parameter known as the "*chain-growth probability, α*", assuming that the FTS is a steps-wise reaction where the chain propagation takes place over the catalyst surface [93]. Accordingly, this parameter correlates the rate of chain propagation over the rate of chain termination. The FTS products distribution through the ASF formulation can be represented as a straight line in the logarithmic scale, as follows:

$$log\left(\frac{W_n}{n}\right) = n\log(\alpha) + \frac{\log(1-\alpha)^2}{\alpha} \qquad \text{Mass distribution} \qquad (2.11)$$

$$log(y_n) = \log\left(\frac{1-\alpha}{\alpha}\right) + \log(\alpha)\, n \qquad \text{Molar distribution} \qquad (2.12)$$

W_n and Y_n are the mass and molar fraction of the hydrocarbon having n carbon atoms. Thus, the ASF distribution assumes a constant slope over the hydrocarbons distribution, with the value of alpha independent from the length of the hydrocarbon chain. However, in real FTS applications, the product distribution presents some sensible deviation from the ASF theory, which becomes crucial when studying their formation rates [93,132]. The comparison between the ASF and the actual FTS hydrocarbons distribution is provided in Figure 10 [122].

As visible from Figure 10, some deviations can be identified from the ASF:

(i) A sensibly higher methane selectivity at the carbon C_1 than predicted by the ASF theory.
(ii) A lower-than-expected ethylene selectivity at the carbon number C_2.
(iii) An increasing value of the chain growth probability (α) at increasing carbon numbers, resulting in a positive deviation from the ASF description.
(iv) An exponential decrement of the olefin-to-paraffin ratio for carbon numbers higher than C_3.

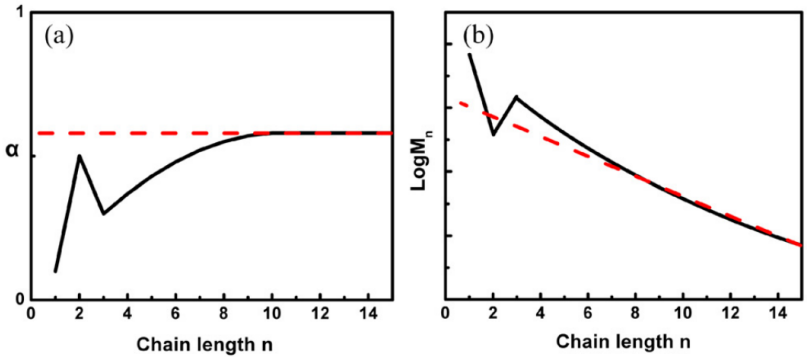

Figure 10 Fischer-Tropsch products distribution: (a) Evolution of the growth probability over the carbon number; (b) direct comparison of the ASF (dotted) and real FTS distribution. Reproduced with permission from [133].

Different explanations have been provided in the literature. Firstly, the existence of varying energies of activation for both methane and ethane from other n-paraffins and α-olefins has been reported, explaining the higher and lower yield, respectively, of these two compounds [134]. In the case of methane, there exist different methanation sites concerning the other paraffins, with a low activation barrier for the CH_4 formation [127]. In the case of ethene, it presents a high activity towards secondary hydrogenation to heavier hydrocarbons (i.e., chain growth), due to strong absorption by the catalyst surface resulting in high activation energy of desorption of C_2H_4 [127,133]. Additionally, the accumulation of heavy compound fractions in the reactor system has been reported as a

deviation explanation. Specifically, long residence time and products hold-up in the reactor can be responsible for the readsorption of olefins to paraffinic compounds [135]. Similarly, the non-ASF behaviour of the FTS distribution has been attributed to the presence of secondary reactions after the termination steps, typically ascribed to two reaction mechanisms of olefinic compounds [136]. Secondary reactions are usually referred to as olefins, given that they are one of the two major products obtained from FT synthesis (excluding the production of water). The proposed mechanisms encompass (i) α-olefin re-adsorption and hydrogenation or (ii) desorption of α-olefins with direct dependency on the chain-length [137,138]. In the first case, olefins are re-adsorbed on the catalyst active sites for further hydrogenation steps to paraffins or are re-inserted in chain growth mechanism, being α-olefins reactive compounds under FTS conditions [139]. In the second case, α-olefins desorption decreases at increasing carbon numbers, possibly due to stronger Van der Waal's attractive forces with the catalyst surface [133]. Sonal et al. [140] tested a bimetallic catalyst (Fe-Co based) inside a fixed-bed FT reactor, deriving mechanistic models based on both α-olefins secondary reactions. Even though both secondary reactions can parallelly occur, the authors established that the principle of chain-length dependency for the desorption of α-olefins firstly suggested by Botes et al. [141] is the most consistent approach to describe the non-ASF FTS behaviour. Finally, some authors also related the non-ASF distribution of the FTS to the existence of local temperature and pressure gradients on the catalyst bed, determining multiple α values along the reactor [142]. However, this explanation is rather debatable [122]: the FTS reaction is generally studied under intrinsic kinetic conditions, ensuring that no gradients, nor mass and energy diffusion limitation exist [143].

2.1.7 Fischer-Tropsch reaction: kinetic modelling

A deep understanding of the actual mechanisms of hydrocarbons formation during the FT reaction is still unknown. Kinetic studies are thus helpful to offer a set of information about the performance of the catalyst and the synthesis yield of hydrocarbons and the reaction evolving over its surface [122]. Additionally, such information can then be applied for process simulation and performance evaluation of a full-scale plant based on the performance of the selected catalyst, tuning the process condition to target specific classes of FT compounds [131].

Kinetic models represent a more detailed description of the FTS products distribution compared to the ASF theory. Several methodologies were carried out for Fischer-Tropsch kinetic activities, with each model classified depending on its nature.

Simple rate models: they represent the class of kinetic laws with the simplest description of the FTS and the lowest amount of information about the product distribution. These models determine the overall rate of FT reaction (ascribed as the rate of CO consumption), considering the partial pressures of the two syngas

reactants, based on empirical expressions to fit the experimental data [144]. These expressions follow the general power-law form provided in eq. (2.13).

$$-r_{FT} = kP_{H_2}^{a} P_{CO}^{b} \tag{2.13}$$

with k being th reaction rate constant, a and b the reaction order of CO and H2, respectively. Examples of this expression are given by Zennaro et al. [145] and Brötz et al. [146], with similar results providing a positive value for a and a negative one for b, suggesting inhibition by absorbed carbon monoxide. Additionally, the description of the overall reaction rate can be provided through Langmuir-Hinshelwood-Hougen-Watson (LHHW) models. As presented by Yates et al. [147], these models assume empirical expression to describe the overall FTS reactions (eq.(2.14)), where the parameters at the reaction rate constant, the driving force, and the absorption equilibrium coefficient.

$$-r_{FT} = \frac{(kinetic\ factor)(Driving\ force)}{Adsorption} = \frac{kP_{H_2}P_{CO}}{(1 + bP_{CO})^2} \tag{2.14}$$

More complex method may also include the dependency over the partial pressures of carbon dioxide (generally existing only for Fe-based catalysts where the WGS reaction takes place) and water [128]. Detailed reviews providing the list of such models are available in the open literature [144,148].

Products selectivity: these models provide a higher amount of information with respect to simple rates models. Specifically, product selectivity models focus on describing the syngas reactants consumption rates through empirical expressions and cluster the FT products into groups of hydrocarbons depending on their carbon numbers. They can include information about the chain probability growth through different α values (i.e., double α models to describe the different curvature of the FTS distribution at low and high carbon numbers), or account for the elementary secondary reactions of the olefins, ascribed to diffusivity, solubility, and physisorption of these compounds (i.e., re-adsorption models, with chain length dependency) [131]. Moazami et al. [149] developed a selectivity model for a Co/SiO_2 catalyst, whose behaviour was described in terms of CO consumption rates, selectivity for CO, CH_4, paraffin and olefins of carbon number C_2, C_3, and C_4, and a single lumped component to include for all the products at C_{5+}., via empirical reaction rate expressions in the form of eq. (2.14). Their model provided useful insights on the CO conversion, and preliminary analysis on the chain-length dependency of the olefinic compounds. However, it failed to describe the FTS products distribution without including data on the FTS probability growth evolution. Similarly, Ostadi et al [144] developed a selectivity approach to describe the formation of FT products up to C_{5+}. The authors utilized Ma et al. [128] empirical model to account for the consumption of CO and included a different reaction rates of methane to predict its higher selectivity

compared to the ASF. Furthermore, they accounted for C_2, C_3 and C_4 paraffin and olefins production utilizing two different α values. Finally, the authors provided information of the C_{5+} output, as the complement to hundred of the C_1-C_4 selectivities. On a general note, the selectivity models tend to work properly under the process conditions for which they have been tested. However, they are considered data-fitting models, rather than being predictive ones, using pseudo-kinetic parameters dependent on the reaction conditions. They do not provide in-depth description of the mechanisms evolving on the catalysts surface, nor catch every non-ASF deviation [122,150].

Mechanistic models: Mechanistic kinetic models are based on detailed reaction description, including elementary FTS steps. These steps include the initial syngas reactants adsorption, followed by chain initiation, chain growth/propagation, re-adsorption of given species, final hydrogenation and termination to FT products. Specifically, they differ from selectivity models by giving comprehensive information about the initiation step depending on the typology of reactant adsorption, and information on the termination step for each of the product analyzed. Additionally, these models show evidence of the preferential reaction mechanism taking place on the catalytic surface. Several mechanistic models have been used to illustrate the FT synthesis, usually including n-paraffin and α-olefins, and oxygenates when produced by the catalyst [92,144,151–155]. The mechanistic models differ depending on the initiation of the chain, the hydrocarbon building units, the chain propagation, and the termination steps. The main mechanistic models considered in FTS Co-based catalysis are the CO insertion [155], the carbide [153], and the enolic [156] mechanism. However, also the alkenyl mechanism has been utilized for kinetic purposes [157]. Such models comprise of both Langmuir (LHHW) and Eley-Rideal steps. The LHHW assumes the involved molecules of a given step as all adsorbed, while the latter considers only one of the molecules adsorbed on the catalytic bed (generally CO) and the other one reacting directly from the gaseous phase without adsorbing (usually hydrogen, when not considered as H-assisted driver). A simplified schematic of the FTS reaction steps is provided in Figure 11.

- **The CO insertion mechanism** model illustrates the chain growth of the hydrocarbons via the insertion of an adsorbed carbon monoxide intermediate building unit. Expressly, it assumes CO insertion of in a metal-methyl or metal-methylene carbon bond (i.e., CO-* into the growing chain). For this to happen, CO and H_2 are adsorbed by the catalyst surface, CO is further hydrogenated, and finally, the C-O is broken for chain propagation. The CO-insertion model is capable of also describing the formation rates of oxygenates [155].
- **The carbide mechanism** (also addressed as carbene, alkyl, or CH_x insertion mechanism) was originally suggested by Fischer and Tropsch [158]. It considers dissociation of adsorbed carbon monoxide and

formation of a metal carbide, with hydrogenation to the CH_x group. CH_x is regarded as the building unit accountable for the development of the hydrocarbon chain, resulting in the formation of C_xH_y species over the catalyst surface [92]. Additionally, it has been proposed that the step of CO dissociation may occur both unassisted (i.e., direct dissociation) and H-assisted, where in the latter case the C-O bonds are broken into CHO before further oxygen elimination. Visconti's group studied both the effect of unassisted and H-assisted CO dissociation as an initial adsorption step, both valid depending on the catalyst [159–161]. The termination steps account for the formation of n-paraffin via chain hydrogenation and α-olefins via β-hydride elimination. The weakness of such mechanism lies in the non-description of alcohols formation, unless a hydroxyl group (*-OH) is involved in the reaction.

- **The enolic mechanism** (also known as hydroxycarbene mechanism) appoints a hydroxycarbene species CHOH for the chain growth responsibility. Such a group is created via hydrogenation of the adsorbed CO molecule with 2 H. Moreover, it considers a double condensation step to eliminate water and include carbon and hydrogen in the chain growth process. This mechanism is capable of giving information to the synthesis of alcohols via hydrogenation, aldehydes via desorption, and hydrocarbons via H-assisted elimination of the OH group [152].

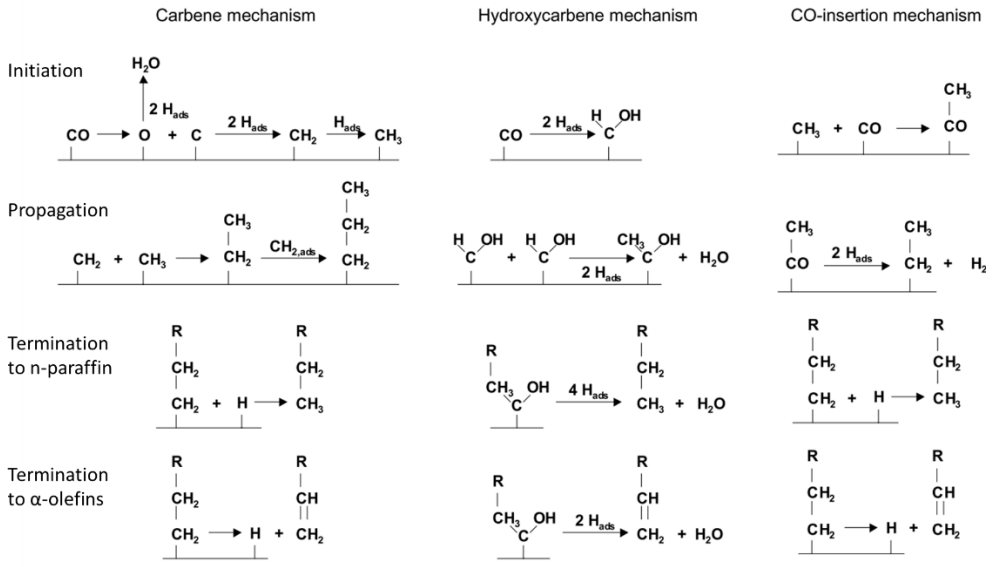

Figure 11. Schematic representation of the most commonly employed and accepted FTS reaction mechanisms: carbide (carbene), enol (hydroxycarbene), CO-insertion. Adapted from [92,162].

- **The alkenyl mechanism** considers the surface methylene species (*=$CH_{2,ads}$) as the building unit for the chain lengthening, coupling with the adsorbed CH_{ads} group via C-C bonds [157]. The termination steps account for the single hydrogenation to α-olefin products [92]. The alkenyl schematic is provided in Figure 12.

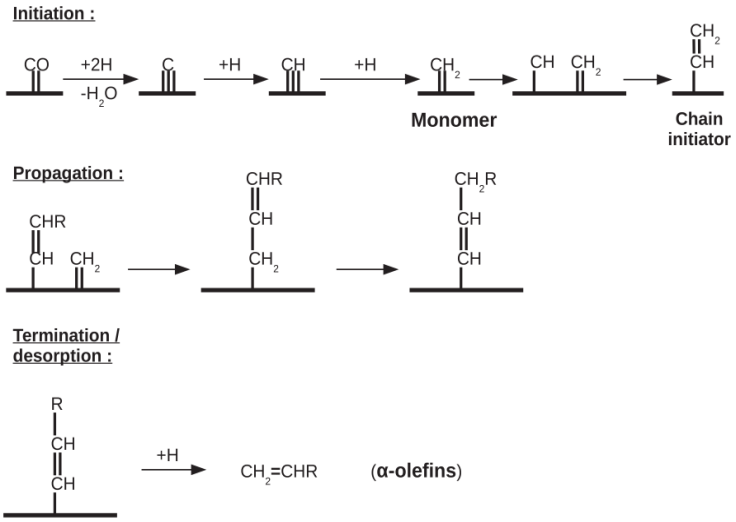

Figure 12. Schematic representation of the alkenyl mechanism for FTS reaction steps. Reproduced from [163]

Once the elementary reactions steps have been defined, computational methods can be applied the extrapolate the kinetic information by regression of kinetic parameters based on the experimental data available. Specifically, for each FTS product its rate of formation can be derived, as well as the consumption of CO and H_2 and the formation of by-product H_2O. Additionally, the surface coverage of each monomer can be found. These models can provide a precise prediction of the FTS distribution at several industrial-like conditions. The main drawback of these models is the high number of kinetic parameters to be regressed. This results in high computational costs [140,164]. Finally, it is worth mentioning that a perfect description of the whole FTS spectrum is not provided by only one model [92]. Depending on the experimental results and the computational methods utilized for kinetic model description, it is likely that one mechanism describes better the catalyst behaviour. However, more than one typology of the monomer may be responsible for the actual evolution of the hydrocarbon [165].

2.2 Fischer-Tropsch experimental activities

During the investigations of the present research activities, a very low/negligible amount of oxygenated compounds was found at the outlet of the FT reactor. Additionally, among the different types of mechanisms, the carbide mechanism is the most commonly accepted for the FTS and used in kinetic modelling, and thus the one with more available comparisons for the results [134,163,166]. In light of this, 11 carbide mechanisms have been derived from the open literature and applied to fit the experimental data. The catalyst preparation, screening, and initial performance evaluation campaign have been performed by VTT, within the framework of the ICO2CHEM project. In this second part of Chapter 2, the catalyst characterization methods are described to provide the

overall catalyst information. However, only kinetic modelling and process modelling are intended as the scope of this research investigation. Finally, part of the results presented in this chapter has been previously published in [82].

2.2.1 Materials and methods

Catalyst preparation and characterization

A Co-Pt/Al_2O_3 (Co-based Pt-promoted, on alumina support) catalyst fabricated via impregnation by the VTT Technical Research Centre of Finland has been tested for the development of the kinetic model. The catalyst was prepared on a γ-Al_2O_3 support, together with 21.4 %wt Co and 0.2 %wt Pt loading. The impregnation method consisted of an aqueous solution of cobalt nitrate and platinum nitrate as Co and Pt carriers, respectively ($Co(NO_3)_2$ $6H_2O$ and $Pt(NO_3)_2$). The catalyst was then dried at 80°C and calcined at 250°C inside of a rotavapor fed with 1000 ml/h/g_{cat} of air. The size of the catalyst particles employed during the experimental campaign was 50–150 μm, with particles of size below 50 μm removed via filter after calcination.

The catalyst was characterized after preparation with H_2-chemisorption, Temperature-programmed reduction (TPR), X-ray diffraction (XRD), and physisorption methods. For details about the characterization techniques, refer to [82]. The catalyst characterization results listed in Table 5 agree with the ones delivered by Karaca et al. [167], and Nabaho et al. [168], considering similar Pt-doped Co catalysts. Additionally, the TPR technique provided a typical profile of the Co catalyst reduction: two main peaks are identified at 290°C and 440°C. The first one at 290°C corresponded to the Co_3O_4-to-CoO transition, the second one to the CoO-to-Co metallic transition [169]. Hydrogen-chemisorption and XRD analyses showed Co0 and Co_3O_4 particles size similar to values from the literature [111,129]. Additionally, the intrinsic catalytic activity (i.e., the turnover frequency, TOF) was calculated. At test settings of 210°C, 30 bar, H_2/CO 2.04, the TOF resulted in $33.6 \cdot 10^{-3} s^{-1}$. This value was in the plateau of the reported results for cobalt catalysts. [110,170]. Thus, the catalyst preliminary characterization and activity evaluation provide evidence that the catalyst manufactured in-house was equivalent to analogous FT investigations and was appropriate for experiments on kinetic model reaction.

Table 5.Catalyst characterization summary results. [a] Dispersion values with catalyst reduced; [b] with catalyst non-reduced; [c] H_2-chemisorption technique; [d] XRD technique. Adapted from [82].

Parameter	21%Co 0.2%Pt/γ-Al_2O_3
Dispersion (%)[a]	8.2
BET surface area (m^2/g)[b]	53.5
Average pore diameter (nm)	11.7
Pore volume (cm^3/g)	0.15
d(Co^0)[c] (nm)	16.6
d(Co_3O_4)[d] (nm)	17.5
Packed bulk density [g/l]	820
Tortuosity [−]	2
Thermal conductivity [W/(m K)]	1.02
Median particle size [m]	7.50×10^{-8}
Characteristic length [m]	1.25×10^{-8}

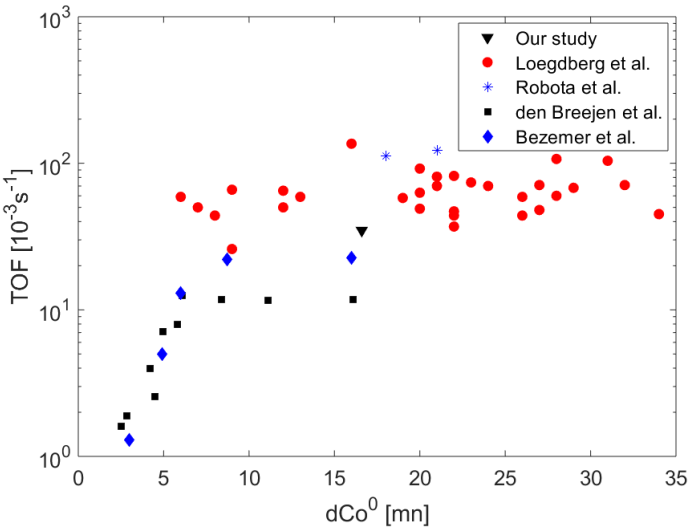

Figure 13. Measure of the TOF (black full triangles) compared with literature reported data: black squares den Breejen et al. [110], blue stars Robota et al. [94], red dots Loegdber et al.[171], blue diamonds Bezemer et al. [109]. Adapted from [82].

Experimental data set

A set of 15 mass balances was collected to determine the catalyst behaviour under different FT operating conditions (Table 6). The packed bed comprised 1 g of catalyst (with particle size 50-150 µm), diluted with 1 g of inert SiC (with particle size 50–150 µm), onto a porous plate. The dilution was used to ensure homogeneous bed temperature conditions and favouring the distribution of the heat generated during the exothermal hydrogenation. A quartz wool layer was positioned over and beneath the catalyst bed. Before data collection, the reduction of the catalyst was made. A steady flow of 50 mlN_{H2}/min was fed for 16 hours at a reactor temperature of 500°C and 1 bar. The reduction temperature was achieved with a 1°C/min ramp-up, starting from ambient temperature. After the reduction, a nitrogen flow was co-fed with hydrogen to the reactor (N_2 and H_2 at 50 mlN/min), while the temperature was cooled down to 220°C. Then both H_2 and N_2 flows were set to the test runs values, and the reactor was set to the required

operating pressure and temperature. Finally, CO flow was slowly fed and increased to its final value. During initial operations, the catalyst exhibited a high activity phase, which decreased over time reaching steady-state conditions (approximately 12 hours after reduction). At stable catalyst activity (i.e., a stable and steady carbon monoxide conversion value), the FT products were accumulated at the outlet of the reactor system for about 45 hours. The conditions tested are presented in Table 6, simulating industrial-like conditions [172]. The temperature was ranged from 205°C to 230°C, the pressure from 15 to 30 bar, the H_2/CO ratio between 1.06 and 2.11. Finally, the conversion of reacting CO was maintained around 10% to ensure the kinetic regime for the present analysis and reduce the selectivity towards methane (unwanted compound if targeting heavy hydrocarbons) [97,173]. Kinetic regime was demonstrated by the calculated negligible mass and energy transfer limitation. This was ensured with a variation of the weighted hourly space velocity from 167 and 720 mlN/min/g_{cat}.

Table 6. Experimental matrix. [a,b]Replicated conditions, not used for the kinetic data regression. Adapted from [82].

RUN	Temp. [°C]	Pres. [barg]	H_2 [%mol]	CO [%mol]	N_2 [%mol]	WHSV [mlN/min/g_{cat}]	H_2/CO [%mol]	X_{CO} [%mol]
1	210	25	60%	30%	10%	166.67	2.00	10.98
2	220	24	65%	31%	4%	146.15	2.10	9.53
3	215	20	59%	28%	13%	177.97	2.11	12.42
4	210	29	51%	25%	24%	196.08	2.04	11.35
5	205	29	54%	26%	20%	188.89	2.08	6.87
6	215	29	51%	25%	24%	190.20	2.04	10.67
7[a]	210	19	46%	22%	32%	304.35	2.09	12.03
8	215	14	63%	30%	7%	285.71	2.10	8.33
9	209	19	50%	24%	26%	370.00	2.08	10.22
10	225	24	58%	28%	14%	682.76	2.07	10.05
11	214	24	60%	30%	10%	400.00	2.00	8.76
12	215	24	45%	36%	19%	322.22	1.25	8.88
13[b]	220	19	33%	31%	36%	606.06	1.06	9.53
14	225	29	40%	36%	24%	475.00	1.11	8.50
15	230	14	50%	25%	25%	720.00	2.00	8.60
16[a]	210	19	46%	22%	32%	304.35	2.09	12.06
17[b]	220	19	33%	31%	36%	606.06	1.06	9.50

The analysis of the FT products was carried out with a Shimadzu GC-2014 on-line gas chromatograph. The sample line was heated to 120°C, avoiding hydrocarbons condensation. CO, H_2, CH_4, CO_2, and N_2 were analyzed with a TCD-detector and two packed columns: a Porapak-Q (1 mm i.d.,×1.8 m) precolumn and a Carboxen-1000 (1 mm i.d.,×2.5 m) analytical column. A 10-port valve was used to inject a sample and facilitate backflush of heavy hydrocarbons from the precolumn. Hydrocarbons from C_1 to C_{14} and C_1–C_9 n-alcohols were analyzed using a DB-1 capillary column (i.d., 0.25 mm × 60 m × 1 μm) and an

FID-detector. The analysis time was ~30 min. Response factors were determined using calibration samples. Additionally, offline analysis was performed for the oil and wax products with a Shimadzu GC-2014 GC-system. Hydrocarbons with a carbon number from C_6 to C_{35} and C_1–C_9 n-alcohols were analysed with an Rxi-5HT capillary column (i.d., 0.32mm×30m×0.10µm df) and an FID-detector. The analysis of the heavy waxes was performed in a different way, as they needed a high-temperature technique (450°C). Hence, a Hewlett Packard 5890 Series II with an on-column sample inlet was employed for this purpose. Hydrocarbons with a carbon number ranging from C_{10} to C_{80} were examined with a CP-SimDist UltiMetal capillary column (i.d., 0.53 mm×10m×0.17µm df, 1 m retention gap) and an FID-detector. This technique allowed for the analysis and collection of experimental data of heavy hydrocarbon (i.e., C_{15+}) that are usually not included in kinetic modelling, given the complexity of analysing these fractions [166].

Experimental test rig

The experiments were performed inside a tubular fixed-bed micro-reactor (PID-Micromeritics Microactivity Effi) available at the VTT facilities. The equipment consists of the reactor tube and a furnace, a hot trap for wax collection and a cold trap for liquid-liquid-gas separation (LLGS). The reactor tube was a Hastelloy-C (9.1 mm, i.d.), with a K-type thermoelement incorporated into the catalyst bed. The reactor and the wax trap were located in a temperature-controlled hotbox, which ensured isothermal conditions at 100°C. The wax trap was attached to the reactor outlet and it was covered by an aluminum housing. The housing contained a type-K thermocouple and a compressed air inlet tube for the trap temperature control. The wax trap operated at 90°C to ensure hydrocarbons collection and avoid the wax runaway and condensation in the unit lines. The other products continued to the LLGS, cooled at 7°C with a Peltier element. Water and oil products were condensed inside the separator, with the water collected in a tank, and the oil products sent to a sampling unit. Light hydrocarbon (i.e., the gas fraction) continued from the LLGS to the gas chromatograph. Calibrated mass-flow controllers (Bronkhorst Ltd, El-flow Select F-211CV) adjusted the gas feed to the reactor. The feeding line was equipped with a check valve to prevent backflow. Figure 14 and Figure 15 provide graphical information of the experimental plant.

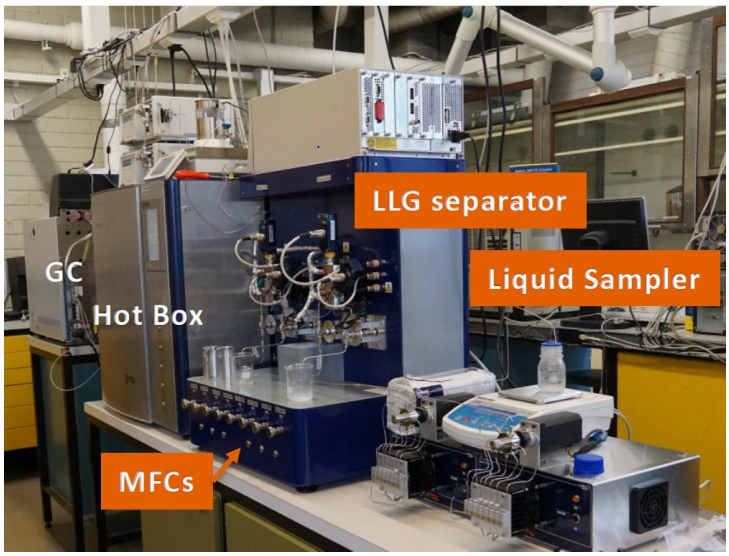

Figure 14. Experimental apparatus.

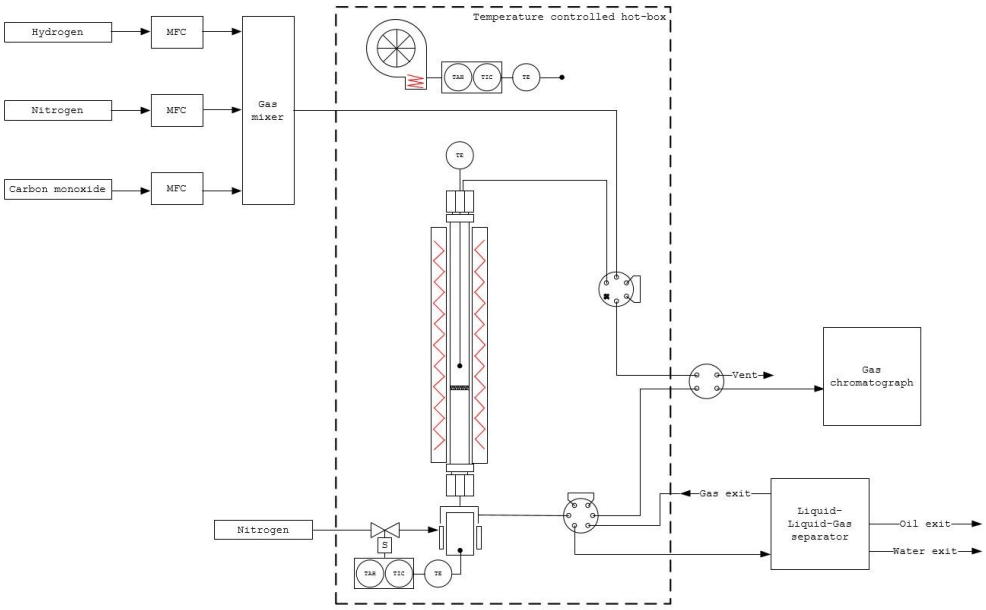

Figure 15. PID-Micromeritics tubular reactor equipment schematics. Reproduced from [82].

2.2.2 Derivation of the reaction rates

11 mechanistic models were derived considering experimental evidence available from literature on the nature of the most commonly found intermediate surface species (e.g., kinetic modelling and Steady State Isotopic Transient Kinetic Analysis) [134,166,174–176]. For each model, hydrocarbons rate equations were obtained based on several assumptions. Firstly, the stream of FT products consisted of n-paraffin, α-olefins, $H_2O_{(l)}$, and unreacted H_2 and CO. Thus, the generation of other products was neglected (alcohols, esters, acids, aromatics had a negligible or non-existent concentration). Additionally, the water

gas-shift reaction is not catalysed over the cobalt-based catalyst, and no carbon dioxide was detected at the outlet of the FT reactor. The FTS reaction followed a carbide mechanism scheme. The total number of active sites on the catalyst surface was assumed constant during the experiments, and the concentration of vacant sites and surface intermediates at a steady state. Moreover, it was considered that methane and ethylene presented different generation rates compared to the other n-paraffin and α-olefins. This assumption allows describing the positive and negative deviations from the ASF at carbon numbers C_1 and C_2. Moreover, the unitary monomer formation and the elementary steps for the formation of n-paraffins and α-olefins (i.e., chain termination) were considered as the rate-determining steps (RDS). In contrast, all the other steps were assumed at quasi-equilibrium conditions. Finally, the chain-length-dependent olefin desorption theory was applied to the rates of formation of α-olefins, to describe the deviations from the AFS distribution (i.e., the decreasing slope of the FT product distribution with increasing carbon numbers). The theory of chain-length-dependency of olefin desorption postulates that the adsorption strength of the olefins on the catalyst surface rises at higher carbon numbers. This results in an incremental value of Van der Waal's forces of attraction of α-olefins at high carbon numbers [101]. Hence, applying the Evans–Polanyi relations [177], the activation energy of olefins desorption at each carbon number comprised of two separate terms: (i) a chain-length *independent* term (E^0_{olef}); (ii) a chain-length *dependent* term (ΔE_{olef}) to account for higher energy of desorption for each CH_2 group. Using the Arrhenius equation, the rate constants for olefins can be found according to eq.(2.15)-eq.(2.18).

$$E^n_{olef} = E^o_{olef} + n\,\Delta E \tag{2.15}$$

$$k^n_{olef} = A_{olef}\, e^{\frac{-E^n_{olef}}{RT}} = A_{olef}\, e^{-\frac{E^o_{olef}+\Delta E}{RT}} = k^0_{olef}\, e^{nc} \tag{2.16}$$

$$k^0_{olef} = A_{olef}\, e^{\frac{-E^0_{olef}}{RT}} \tag{2.17}$$

$$c = \frac{\Delta E}{RT} \tag{2.18}$$

With n being the carbon atom of the hydrocarbon, R the gas constant, T the temperature, A_{ith} the preexponential kinetic factor.

Each model was developed with an LHHW approach. The formation rates of hydrocarbons are related to intrinsic kinetic constants (rate $k_{i\text{-}th}$ and equilibrium $K_{i\text{-}th}$ constants) and the partial pressures of the reactants in the feed gas. Additionally, some of the reaction models included Eley–Rideal-type steps, with one reactant adsorbed and the other one in the gas phase (e.g., model FTS-03 from Appendix A – Catalyst testing and kinetic models).

Here the reaction path and the the derivation of the hydrocarbons rates of formations of the final chosen mechanism are provided (i.e., the one having the

most adequate experimental data regression results) (See Appendix A – Catalyst testing and kinetic models for each model definition and derivation). The reaction steps of this model are presented in Table 7. The model includes a dissociative chemisorption step of hydrogen into H* on the surface of the catalyst, together with a slow adsorption of CO to H*CO species (steps 0 and 1). The latter is then subjeced to subsequent hydrogentations to generate the intermediate C_nH_{2n-1}*, the chain precursor C_nH_{2n}*, and isolate oxygen into OH*. Parallelly, water is released via reaction of the OH* species with adsorbed hydrogen. Furthermore, the monomer responsible for growth of the hydrocarbon chain reacts with the adsorbed hydrogen in the H* form, favouring a lengthening of the chain. Finally, the intermediate C_nH_{2n+1} undergoes hydrogenation to n-paraffins with gaseous hydrogen or desorption to α-olefins.

Table 7. Reaction steps of the most satisfactory carbide mechanism for FTS data regression. With * intended as adsorbed surface species, or vacant site when not connected to any species. Adapted from [82].

Step	Reaction	Constant
0	$H_2 + 2* \leftrightarrow 2H*$	K_H
1rds	$CO + H* \leftrightarrow H*CO$	k_{CO}
	$CO + C_nH_{2n+1}* \leftrightarrow C_{n+1}OH_{2n+1}*$	
2	$H*CO + H* \leftrightarrow CH* + OH*$	K_1
	$C_{n+1}OH_{2n+1}* + H* \leftrightarrow C_nH_{2n-1}* + OH*$	
3	$C_nH_{2n-1}* + H* \leftrightarrow C_nH_{2n}* + *$	K_2
4	$C_nH_{2n}* + H* \leftrightarrow C_nH_{2n+1}* + *$	K_3
5	$OH* + H* \leftrightarrow H_2O + 2*$	K_4
6rds	$CH_3* + H_2 \rightarrow CH_4 + H*$	k_{Meth}
	$C_nH_{2n+1}* + H_2 \rightarrow C_nH_{2n+2} + H*$	k_{Par}
7rds	$C_2H_5* \rightarrow C_2H_4 + H*$	k_{Eth}
	$C_nH_{2n+1}* \rightarrow C_nH_{2n} + H*$	k_{Ol}

During the model development, the rates of the FT products generation and the probability growths depending on the surface species were derived according to eq.(2.19)-eq.(2.27). For probability growth values, the quasi-steady state assumption was included, assuming α as the ratio of the chain propagation rate over the rate of termination of the hydrocarbon chain.

$$R_{CH_4} = k_{Meth} P_{H_2} [CH_3^*] \quad (2.19)$$

$$R_{C_2H_4} = k_{Eth}\, e^{2c} [C_2H_5^*] \quad (2.20)$$

$$R_{C_nH_{2n+2}} = k_{Par} P_{H_2} [C_nH_{2n+1}^*] \text{ , for paraffins at n} \geq 2 \quad (2.21)$$

$$R_{C_nH_{2n}} = k_{Ol}\, e^{nc}\, [C_nH^*_{2n+1}] \text{ , for olefins at n} \geq 3 \tag{2.22}$$

$$R_{CO} = \sum_{j=1}^{n_{carbon}} n\,(R_{Paraf_n} + \mathrm{R_{Olef_n}}) \tag{2.23}$$

$$R_{H_2} = \sum_{j=1}^{n_{carbon}} (2n+1)R_{Paraf_n} + (2\mathrm{n})\mathrm{R_{Olef_n}} \tag{2.24}$$

$$\alpha_1 = \frac{k_1 P_{CO}}{k_{CO}P_{CO} + k_{Meth}P_{H_2}} = \frac{[CH^*_3]}{[H^*]} \tag{2.25}$$

$$\alpha_2 = \frac{k_{CO}P_{CO}}{k_{CO}P_{CO} + k_{Par}P_{H_2} + k_{Eth}e^{c\,2}} = \frac{[C_2H^*_5]}{[CH^*_3]} \tag{2.26}$$

$$\alpha_n = \frac{k_{CO}P_{CO}}{k_{CO}P_{CO} + k_{Par}P_{H_2} + k_{Ol}\, e^{cn}} = \frac{[C_nH^*_{2n+1}]}{[C_{n-1}H^*_{2n-1}]} \text{ n} \geq 3 \tag{2.27}$$

The surface species expressed in squared brachets can be defined using a single coefficiency θ_{vac} (i.e., vacant site). Thus, based on the balance equation of the surface coverages, the vacant sites fraction θ_{vac} was calculated and defined in terms of kinetic parameters and reactants partial pressures.

$$\begin{aligned} 1 = {} & \theta_{vac} + \theta_{H^*} + \theta_{H^*CO} + \theta_{CH^*_3} + \theta_{C_2OH^*_3} + \theta_{CH^*} + \theta_{C_2H^*_3} + \theta_{OH^*} + \theta_{C_2H^*_5} \\ & + \theta_{CH^*_2} + \theta_{C_2H^*_4} + \theta_{\sum_3^N [C_nH^*_{2N+1}]} + \theta_{\sum_3^N [C_nH^*_{2N-1}]} + \theta_{\sum_3^N [C_nH^*_{2N}]} \\ & + \theta_{\sum_3^N [C_nOH^*_{2N-1}]} \end{aligned} \tag{2.28}$$

$$\begin{aligned} \theta_{vac} = {} & 1/\{1 + \sqrt{(K_H P_{H_2})} * \left(1 + \alpha_1 + \alpha_1\alpha_2 + \sum_{j=3}^{n_c}\prod_{n=3}^{j}\alpha_n\right) \\ & + \left(\alpha_1 + \alpha_1\alpha_2 + \sum_{j=3}^{n_c}\prod_{n=3}^{j}\alpha_n\right)\left[\frac{1}{K_3} + \frac{1}{\sqrt{(K_H P_{H_2})}\,K_2K_3}\right. \\ & \left. + \frac{P_{H_2O}}{(K_H P_{H_2})^{1.5}\,K_1K_2K_3K_4}\right] + \frac{1}{K_4}\frac{P_{H_2O}}{\sqrt{(K_H P_{H_2})}}\} \end{aligned} \tag{2.29}$$

The final generation rate of each hydrocarbon was found substituting the probability growths of eq.(2.25)-eq.(2.27) and the sites balance expression θ_{vac} eq.(2.29) into the equations (2.19)-(2.22):

$$R_{CH_4} = k_{Meth}\alpha_1\sqrt{(K_H P_{H_2})}\, P_{H_2}\theta_{vac} \tag{2.30}$$

$$R_{C_2H_4} = k_{Eth}\, e^{2c}\alpha_1\alpha_2\, \sqrt{(K_H P_{H_2})}\, \theta_{vac} \tag{2.31}$$

$$R_{C_nH_{2n+2}} = k_{Par}\alpha_1\alpha_2 \textstyle\prod_{n=3}^{n} \alpha_n\, \sqrt{(K_H P_{H_2})}\, P_{H_2}\theta_{vac} \text{ , for par. at n} \geq 2 \tag{2.32}$$

$$R_{C_nH_{2n}} = k_{Ol}\, e^{nc}\, \alpha_1\alpha_2 \textstyle\prod_{n=3}^{n} \alpha_n\, \sqrt{(K_H P_{H_2})}\, \theta_{vac} \text{ , for olef. at n} \geq 3 \tag{2.33}$$

α_n represents the probability growth of hydrocarbons with carbon number n, k_i, and K_i are the rate and equilibrium constants; P_{H2}, P_{CO}, and P_{H2O} are the partial pressures of H_2, CO, and produced $H_2O_{(l)}$. The rate and equilibrium constants were expressed in accordance to Arrhenius and Van't Hoff formulations:

$$k_i = A_i e^{-\frac{E_{a,i}}{RT}} \tag{2.34}$$

$$K_i = A_i e^{-\frac{\Delta H_i}{RT}} \tag{2.35}$$

$E_{a,i}$ are the activation energies, ΔH_i are the reaction and adsorption enthalpies, A_i are the pre-exponential factors.

Lastly, heat and mass transfer limitations were neglected in the model development. For the mass transport limitations, both the Thiele modulus and Mears' criterion for intraparticle and interphase diffusions were checked, respectively. Considering the energy transport limitations, Weisz-Prater's and Mears' criteria were utilized to evaluate possible internal temperature gradients and verify the presence of interphase heat transport limitation, respectively.

Table 8. Coefficients employed in the verification of the intrinsic kinetic regime, checking mass transfer and diffusion limitations. Adapted from [82].

Intraparticle mass transfer limitation – Thiele modulus [178–180]	
$\emptyset = Lc \sqrt{\frac{\rho_c \, R_{FT}}{D_{e,co} \, C_{co}}} < 1$	(2.36)
$D_{e,co} = \frac{D_{ab} \, \varepsilon_c}{\zeta}$	(2.37)
$\mathrm{D_{ab}} = \frac{\sqrt{\mathrm{T}}}{109} \frac{9.45 \, (\mathrm{V} - 1.230\mathrm{V_0})}{\mathrm{M_1^{0.239}M_2^{0.781}}(\sigma_1\sigma_2)^{1.134}}$	(2.38)
Interphase mass transfer limitations – Mears' criterion [181]	
$M_1 = \frac{R_{FT} \, \rho_c \, r_c \, n}{k_m \, C_{CO}} < 0.15$	(2.39)
$Sh = 2 + 0.552 \, Re^{\frac{1}{2}} Sc^{\frac{1}{3}} = \frac{k_m d_p}{D_{ab}}$	(2.40)
Intraparticle heat transfer limitations – Weisz-Prater criterion [182,183]	
$M_2 = \frac{Ea}{R \, T} \frac{(-\Delta H_{FT}^0) R_{FT} \, \rho_c \, L_c^2}{\lambda_c \, T} < 0.05$	(2.41)
Interphase heat transfer limitations – Mears' criterion [182,183]	
$M_3 = \frac{Ea}{R \, T} \frac{(-\Delta H_{FT}^0) R_{FT} \, \rho_c \, L_c}{h_l \, T} < 0.05$	(2.42)
$Nu = \frac{h_l L_c}{\lambda_l} = 1.31 \frac{Re^{\frac{1}{3}} Pr^{\frac{1}{3}}}{\varepsilon_{PB}}$	(2.43)

Where ΔH^0_{FT} (kJ/mol) and R_{FT} (mol/s/g_{cat}) are the standard enthalpy and the experimental reaction rate of FTS reaction. E_a (kJ/mol) is the activation energy assumed as E_{CO}. ρ_c (kg/m^3) is the catalyst particle density, λ_c (W/m/K) is the catalyst thermal conductivity, L_c (m) is the characteristic length of the catalyst, h_L (W/m^2/K) is the gas-solid heat transfer coefficient, λl (W/m/K) is the thermal conductivity of the gas phase. k_m (m/s) is the mass transfer coefficient. D_e (m^2/s) is the effective diffusivity of carbon monoxide, with D_{ab} considered as the diffusivity of CO into a lumped wax component $C_{28}H_{58}$, ε porosity of the catalyst, and τ tortuosity. M_1, M_2 (g/mol) and σ_1 and σ_2 (Å) are the molar weights and molecular diameters of CO and $C_{28}H_{58}$, V_0 is the close packed hard sphere molar volume (cm^3/mol) [184]. C_{CO} (%mol) is the concentration of carbon monoxide at the inlet of the FT reactor. *Nu* is the Nusselt number, *Re* is the Reynolds number, *Pr* is the Pradtl coefficient, *Sh* the Frossling number.

2.3 Kinetic data non-linear regression

For each experimental set, 48 n-paraffin and 14 α-olefin experimental rates were used to regress kinetic data. The GC analysis provided information up to carbon number C_{82}. However, hydrocarbons higher than C_{48+} were omitted from the data regression procedure, given the constant distribution trend recognized for higher carbon numbers and their marginally lower concentrations, that might negatively influence the computational cost. Nevertheless, the derived model can describe the FTS distribution up to C_{80}. To this, non-reacted CO and H_2 and $H_2O_{(l)}$ were accounted for at the reactor outlet.

2.3.1 Reactor model

The reactor was idealized for the model as a pseudo-homogeneous plug-flow reactor (PFR). The present ordinary differential equation formulation was assumed:

$$\frac{dF_i}{dW_{cat}} = \sum_{j=1}^{n_{react}} \beta_{i,j}\ R_j \quad \text{(i=1,2, 3, …, total number of hydrocarbons)} \tag{2.44}$$

$$W_{cat} = 0, \qquad F_i = F_{i,IN} \tag{2.45}$$

$$W_{cat} = W_{exit}, \qquad F_i = F_{i,exit} \tag{2.46}$$

β is the stoichiometric coefficient of the i-th component in the j-th reaction, F_i represents the molar flow rate pf the i-th hydrocarbon considered, and W_{cat} is the catalyst weight. Moreover, reactants and products partial pressure at the reactor outlet, and the CO conversion value were expressed according to eq.(2.47) and eq.(2.48):

$$P_i = \frac{n_i P_{tot}}{\sum_{i=1}^{N_C} n_i} \tag{2.47}$$

$$\chi_{CO} = \frac{\dot{n}_{CO_{\text{Inlet}}} - \dot{n}_{CO_{Outlet}}}{\dot{n}_{CO_{\text{Inlet}}}} \tag{2.48}$$

The stoichiometric coefficient $\beta_{i\text{-}th}$ for the FT reaction were expressed according to Table 9.

Table 9. Stoichiometric coefficients βith used in the PFR model. Adapted from [82].

Reaction	Paraffins (n ≥ 1)	Olefin (n ≥ 2)
CO	-n	-n
H_2	-(2n+1)	-(2n)
C_nH_{2n+2}	1	0
C_nH_{2n}	0	1
H_2O	n	n

2.3.2 Data regression

For each mechanistic model, kinetic parameters were evaluated employing a non-linear least-squares minimization algorithm minimizing the present objective function:

$$F.Obj. = \sum_{i=1}^{nsearch} \sum_{j=1}^{nexp} \left(\frac{R_{i,j}^{exp} - R_{i,j}^{mod}}{R_{i,j}^{exp}} \right)^2 \tag{2.49}$$

Being n_{search} is the number of observations (n-paraffin and α-olefins), n_{exp} the number of experimental data sets, R_{exp} and R_{mod} the rates of hydrocarbons formation for the experiment and model sets.

Given the strong non-linearity of eq.(2.49) and the possible presence of many minima at local level, the data regression was obtained applying a step of global optimization followed by a second step of local optimization. The regression was performed on MATLAB, with the genetic algorithm followed by the Levenberg-Marquardt algorithm. Specifically, the initial guesses for the kinetic parameters (activation energies, adsorption enthalpies, olefins desorption coefficient) were bounded depending on the reaction steps, with reference to literature studies dealing with FTS kinetics [155,185,186]. Pre-exponential factors A_{ith} were specified between 10^{-10} and 10^{20}. The adsorption enthalpies of CO and H_2 were constrained between -40 and -200 kJ/mol and -1 and -100 kJ/mol, respectively, while activation energies were considered in the range of 40 to 200 kJ/mol. The activation energies for n-paraffins and α-olefins formation, and chain propagation initial guesses were varied between 50 and 150 kJ/mol, 60 and 150 kJ/mol, and 60 and 120 kJ/mol. The coefficient ΔE for olefins chain length dependency was searched between 0 and 10 kJ/mol. The adsorption enthalpies of intermediate

hydrogenation steps were limited between -1 and -100 kJ/mol. Additionally, the genetic algorithm considered an initial population of 200 individuals per searched variable, a maximum number of iterations of 10^9, a cross-over function value of 0.5, and a relative change tolerance of 10^{-10}. The local optimization used the global optimization results as initial guesses, having a maximum iterations value of 10^4, and a step change tolerance of 10^{-10}.

The mean absolute relative residual value (MARR) was evaluated, and utilized to screen between the different mechanistic models, selecting the one with the lowest value, provided that activation energies resulted in $E_a > 0$ and adsorption enthalpies $-\Delta H^0_a > 0$ (being the adsorption an exothermic process).

$$\text{MARR} = \sum_{i=1}^{n_{search}} \sum_{j=1}^{n_{exp}} \frac{\left|R_{i,j}^{exp} - R_{i,j}^{mod}\right|}{R_{i,j}^{exp}} \times \frac{1}{n_{search}\, n_{exp}} \times 100\ \% \tag{2.50}$$

Lastly, the statistical significance of the final mechanism was tested with the F-test, showing a statistically meaningful global fit, and t-test, showing the statistical difference from zero for every kinetic parameter evaluated, at 95% confidence interval.

2.4 Results and discussion

The selected model corresponds to the mechanistic model 2 (Annex A).

2.4.1 Kinetic parameters

The results from the non-linear regression of the kinetic parameters are presented in Table 10.

Table 10. Values of the kinetic parameters found with the regression routine. Fvalue (20,909,0.05) = 133.7 > Fcr. = 1.86; tcr. (0.05,21). The data are adapted from [82]

Parameter		**Unit**	**t_{value}**	
A_H	1.83e-02	MPa−1	88.8	
A_{CO}	9.11e+07	mol/h/gcat/MPa	139.3	
A_{Par}	1.02e+08	mol/h/gcat/MPa	58.7	
A_{Meth}	5.57e+08	mol/h/gcat/MPa	94.1	
A_{Ol}	6.27e+08	mol/h/gcat	739.6	
A_{Eth}	8.63e+08	mol/h/gcat	3.2	
A_1	1.84e+02	-	36.1	
A_2	7.77e+02	-	71.9	
A_3	9.02e+03	-	35.3	
A_4	1.43e+01	MPa	105.7	
A_H	1.83e-02	MPa−1	88.8	
Parameter		**Unit**	**t_{value}**	**Lit. Range**
ΔH_H	–5.97	kJ/mol	133.8	−2.1/−25 [151,164,166]
E_{CO}	82.39	kJ/mol	756.4	80/120 [127,151,155]
E_{Par}	93.65	kJ/mol	767.9	60/100 [151,166]
E_{Meth}	89.97	kJ/mol	138.9	60/100 [151,166]
E_{Ol}	95.24	kJ/mol	565.4	90/130 [134,151]
E_{Eth}	112.82	kJ/mol	112.7	90/130 [134,151]
ΔE	1.249	$kJ/mol_{(CHx)}$	32.7	1.1/2.15 [140,155]
ΔH_1	27.98	kJ/mol	249.3	-
ΔH_2	37.00	kJ/mol	323.1	-
ΔH_3	9.60	kJ/mol	82.5	-
ΔH_4	13.39	kJ/mol	194.3	-
ΔH_H	–5.97	kJ/mol	133.8	−2.1/−25 [151,164,166]

The results of the optimization routine are in line with literature findings utilizing mechanistic models to describe the catalyst behaviour.

By calculating the Thiele modulus and the Mears criteria, no mass or heat transfer limitations occurred during the experiments, ensuring kinetic regime for each of the experimental runs tested. At the highest temperature of the investigations of 230°C, the coefficients presented in Table 8 correspond to Φ 0.055, M_1 0.00152, M_2 0.006, and M_3 0.005.

The activation energy E_1 of the initial CO dissociation step is 82.4 kJ/mol, in the range 80-120 kJ/mol reported by several kinetic investigations on Co catalysts for FT synthesis [119,127,151,187,188]. Keyser et al. identified a value of 79.9 kJ/mol [188]. Similarly, Nikparsaa et al. accounted for an activation energy of 88.4 kJ/mol [189], Todic et al. of 100.4 kJ/mol [166]. The estimated values of the hydrogen heat of adsorption lies in the range of literature results, close to the one listed by Bhatelia et al. (-2.14 kJ/mol) [151]. Energy termination barriers of paraffin and olefins found in this analysis are coherent with studies reporting values similar to those [144,155]. Moreover, CH_4 and C_2H_4 activation energies differ from the other paraffin and olefins, with E_{CH4} lower than E_{paraf} and E_{C2H4} higher than other olefins. E_{CH4} is slightly higher than most kinetic studies results (82.4 kJ/mol from Bhatelia et al. [151], Todic et al. 63 kJ/mol [166], 83.6 from Ghouri et al. [190]). However, this can be related to the low conversion levels of CO, that turns in suppressing the selectivity towards methane at low values [120,179]. The energy barrier for the α-olefin desorption step (ΔE) is 1.25 kJ/mol. This value is comparable with other studies applying the chain-length dependent α-olefin desorption theory [140,155,166]. Moreover, this result provides a rise of the α-olefin termination step from 95.3 kJ/mol to 113.9 kJ/mol at carbon number C_2 and C_{15}, confirming the theory of Cheng et al. [133], which ascribes higher activation energies for α-olefins desorption at higher C_n.

From the kinetic results, it can be unveiled a 0^{th} order dependency on the CO partial pressure and a positive dependency around the unity for H_2, consistently with reported FTS literature values: the reaction orders with respect to CO and H_2 range around −1 to +0.65 and 0.5 to 2, respectively [191,192].

Lastly, with at a confidence level of 95%, the F_{test} corresponds to 133.6 (higher than the critical value of 1.86). Likewise, the lowest absolute value of the t_{test} (equal to 3.2) is higher than its critical value of 1.64.

2.4.2 Fischer-Tropsch products distribution

Results of the hydrocarbons distributions are presented in Figure 16, with the distribution of both paraffin and olefins at the different tested operating conditions. The model provides good fits at different operating conditions, properly accounting for the major deviation from the ASF theory. Additionally, Figure 17 presents the parity plots of the simulated model versus experimental results of reactants consumption and products formation. The dispersed deviations

lie in the range of about ±25%, a range coherent with most mechanistic kinetic studies, having a span of ±15% to ±30% [140,144,151,166,193].

The final model shows a MARR value of 41.2%. This value is slightly higher than most provided literature values for kinetic analyses based on mechanistic models (Bhatelia et al. reported 29.5% [151]. Todic et al. 21.5 to 26% [155,166], Sonal et al. 21.3% and 35.5% [140]). The reason of this outcome can be related to scattering of some experimental values and data exclusion. Ghouri et al. [190] calculated an MARR value of 48.4% for a tested Co/Al_2O_3 catalyst. The authors credited this performance to their small number of experimental observations included in their model. Yang et al. [194] suggested that separation and condensation of high molecular weight compounds may enwrap H_2O molecules into the waxes matrix, providing a small overestimation of such heavy fraction. Finally, Sonal et al. [140] and Todic et al. [166] suggested that the exclusion of some FTS hydrocarbons can negatively affect the final MARR value (i.e., minor compounds were omitted from the data regression due to their marginally small/negligible concentrations found in the outlet flow, and only n-paraffins and α-olefins were included).

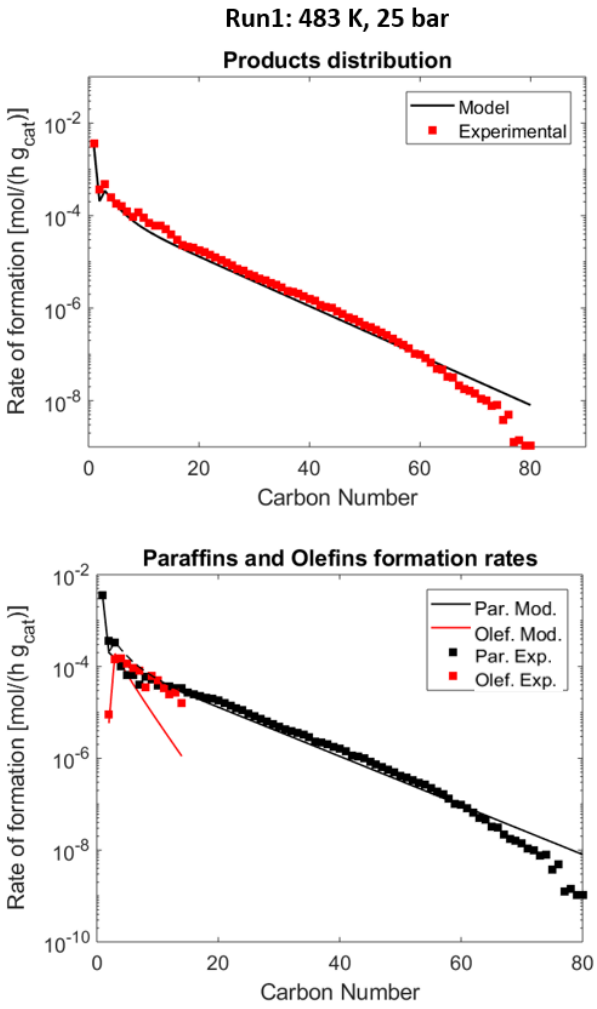

Run3: 488 K, 21 bar

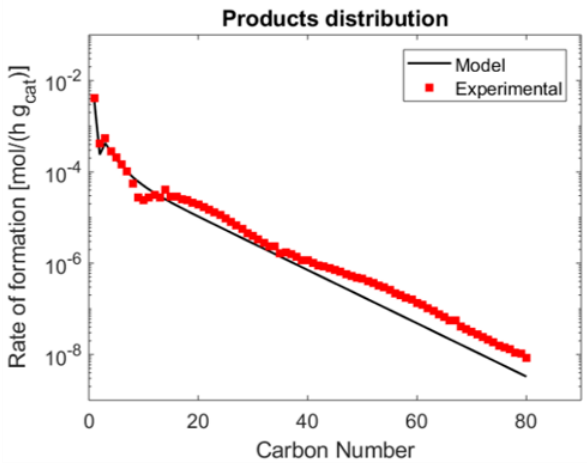

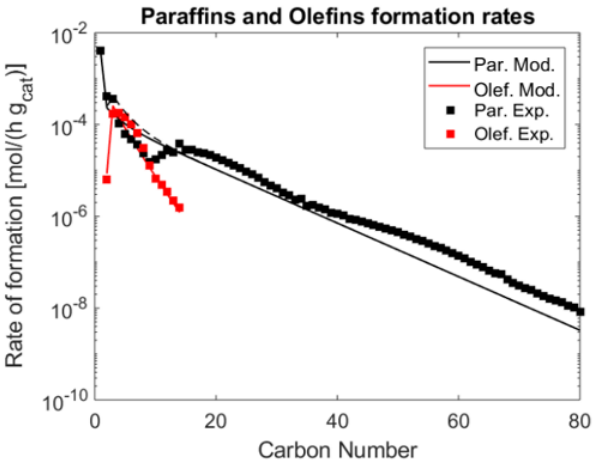

Run6: 488 K, 30 bar

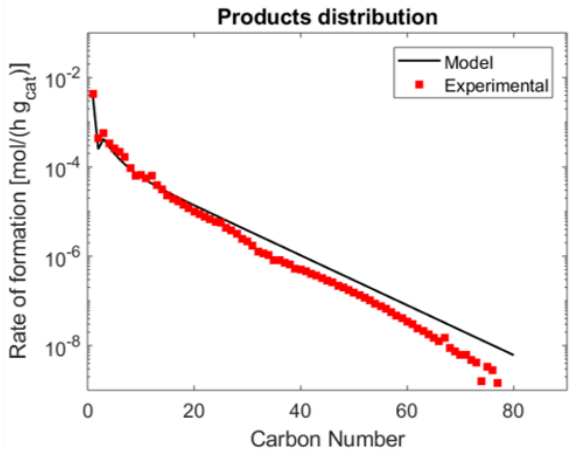

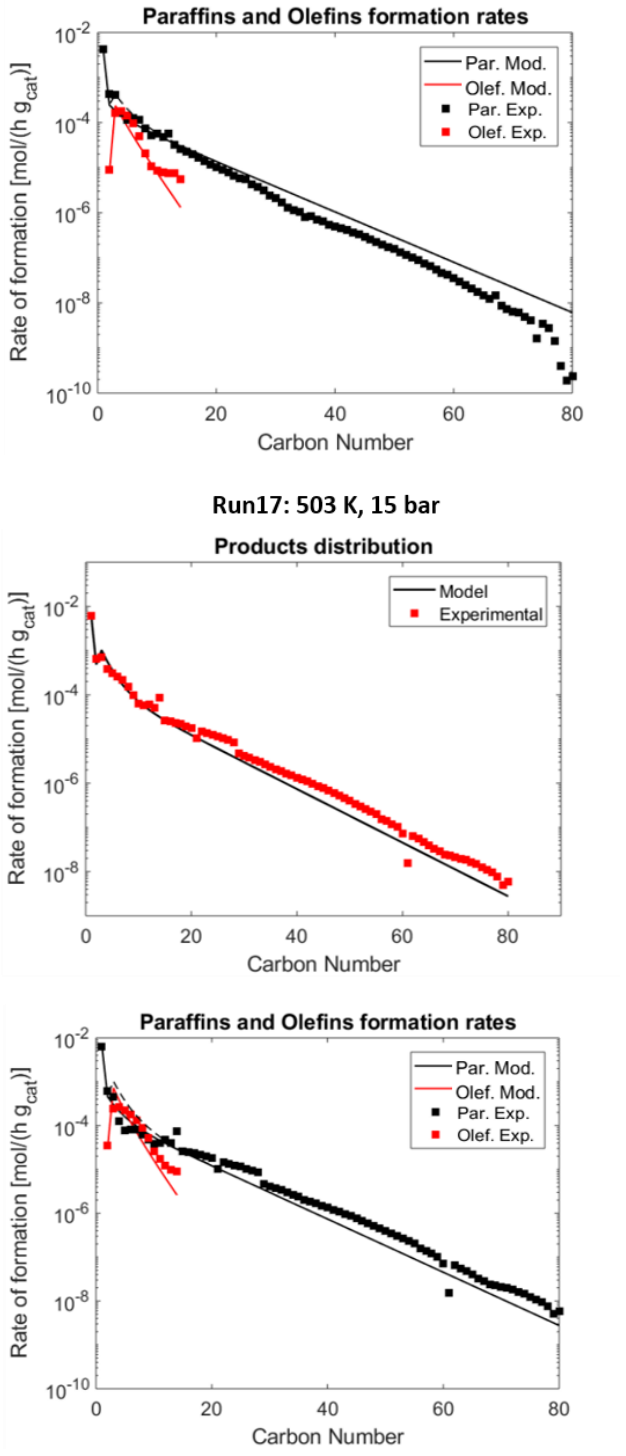

Figure 16. Distribution of FT products, considering both global distribution and contributions of the -n-paraffins and α-olefins (model and experimental results at different operative conditions).

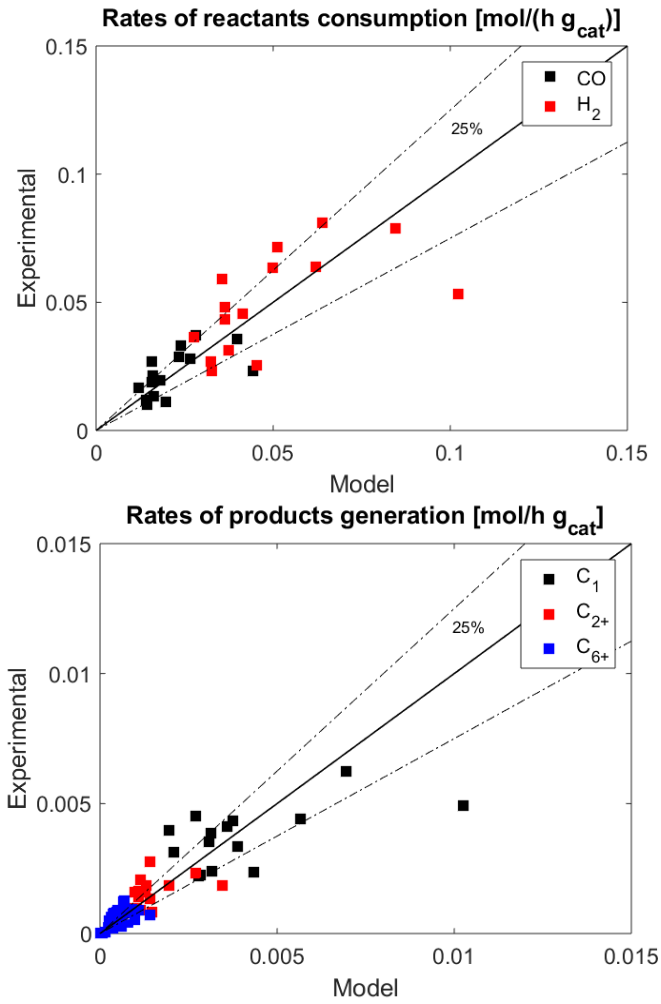

Figure 17. Parity plot of reactants consumption and products generation. Reproduced from [82].

Additionally, the kinetic model provides information about surface coverage values for the different species involved in the FTS. The surface coverage of H_2 spans from 3% to 10% (depending on the reaction data set). The one accounting for all the species comprising CO ranges from 15% to 55%. H_2 and CO surface coverage values from literature are lower than 5–10% and between 20% and 65%, respectively [151,176]. Additionally, the model provided growth probabilities ranging from 0.8 to 0.93, gradually rising to an asymptotic condition around carbon number $C_{25–30}$, after which the α continues constant. This is consistent with the hypothesis of omitting heavy hydrocarbons from the regression steps. Finally, the growth probability evolution clarifies the presence of the positive bend in the FT products distribution.

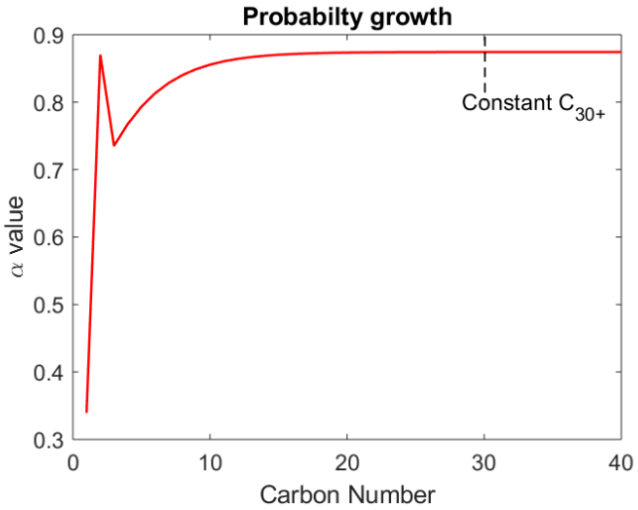

Figure 18. Example of the evolution of the probability growth value α at increasing carbon numbers (run 3).

Optimal Fischer-Tropsch process conditions

Mechanistic models allow for the prediction of the FTS distribution [122]. Thus, based on the kinetic coefficients and regression results, it is possible to extend the kinetic potentiality and determine the optimal process conditions that provide a suitable shift of the hydrocarbons production towards desired product fractions.

As the wax fraction is the targeted one within this research, a multi-objective optimization routine was applied on the kinetic model. Optimal temperature, pressure, and H_2/CO molar ratio at the inlet of the FT reactor were determined. The objective functions included the minimization of the rate of methane production, together with the maximization of the sum of the formation rates of C_{25}-C_{80} paraffins. Based on these conditions, it was found that the preferential operating parameters for this catalyst correspond the 228.5°C, 25 bar, and H_2/CO 1.89 (Figure 19 and Figure 20).

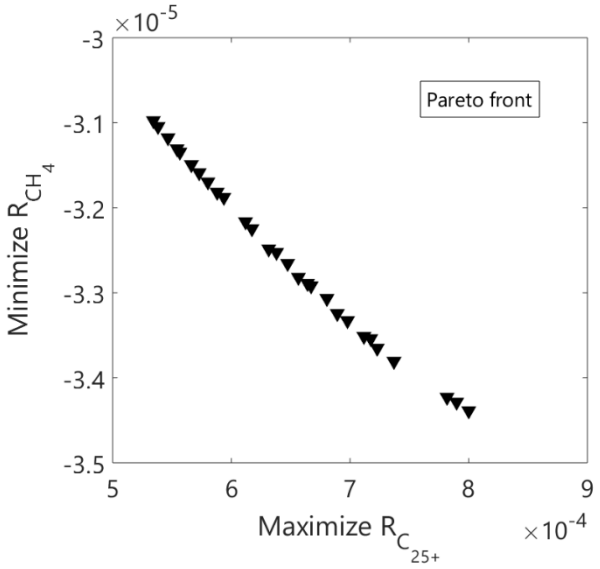

Figure 19. Pareto front of the MOO routine that maximizes the production of waxes and minimizes the generation of methane.

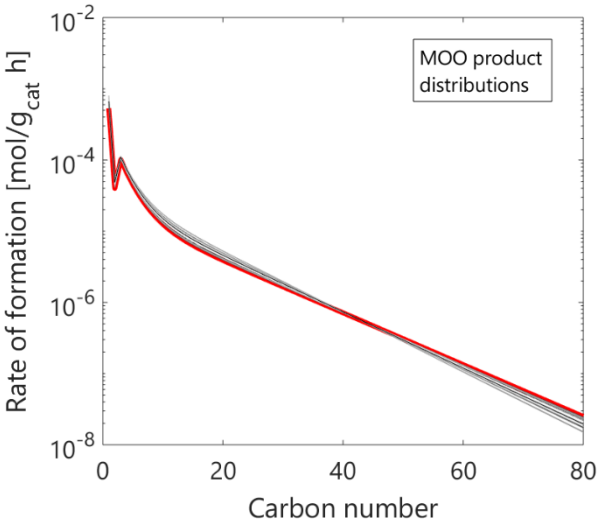

Figure 20. FTS products distribution obtained from the MOO routine that maximizes the production of waxes and minimizes the generation of methane. The red line corresponds to the optimal value of 228.5°C, 25 bar, and H_2/CO 1.89.

Chapter 3

Process modelling – part I

The evaluation of the carbon feedstock conversion into Fischer-Tropsch products was carried through steady-state process modelling of selected plant configurations. The focus is on the conversion of carbon material into paraffins liquids and waxes. The chapter is organized as follows:

- Description of the selected process configurations in this research:
    1. Conversion of biogas from anaerobic digestion to FT products, with CO_2 capture via chemical scrubbing, intermediate low-temperature steam electrolysis for hydrogen production, and *state-of-the-art* reverse water-gas shift reaction for syngas generation.
    2. Conversion of biogas, with the capture of CO_2 via chemical scrubbing, intermediate solid oxide stack for CO_2/H_2O coelectrolysis (SOEC) for syngas generation.
    3. Capture and conversion of CO_2 from the air into FT products, with high temperature direct air capture (DAC), low temperature steam electrolysis, and *state-of-the-art* reverse water gas shift reaction.
    4. Conversion of digestate from anaerobic digestion to FT products, through gasification of the biomaterial for the syngas generation.
- KPIs identification and pinch analysis methodology for energy integration via heat recovery.
- Economic analysis methodology aimed at providing the cost of wax production.

All the processes were modelled on the commercial simulator for mass and energy balances AspenPLUS^{TM}. Chapter 4 will provide the results in terms of process modelling and the direct comparison of the KPIs and economic outcomes for the studied configurations. Finally, part of the work provided in this chapter has been previously published in [28,195,196].

3.1 State-of-the-art

The open literature provides evidence on the effective conversion of non-fossil carbon material to Fischer-Tropsch compounds, with a focus on liquid fractions (i.e., diesel, jet fuels). Indeed, producing lighter hydrocarbons like kerosene and diesel can be a solution to decarbonize the transport sector [197]. However, the Fischer-Tropsch process can be regarded as a valuable solution to produce heavy hydrocarbons (i.e., paraffin waxes in their linear form). This allows addressing the decarbonization of also the chemical industry sector. At present, the synthesis of these compounds comes mostly from fossil sources. An example is given by Sasol, which uses coal in a gasification process [198] followed by syngas upgrade to waxes via Fischer-Tropsch reaction, with production capacities of over 450 kt/y of waxes in 2020 [199].

Concerning the Fischer-Tropsch wax production cost, only few authors addressed it, as it is generally preferred to include hydrocracking of the heavy fraction to synthetise transport fuels. Herz et al. investigated the conversion to FT waxes of either biogas [200] or flue gases [43]. In the first case, the authors analysed the conversion of biogas to Fischer-Tropsch material, interposing either an endothermal or an autothermal reforming reactor to generate the syngas. With a sale price of the wax fraction of 2.00 €/kg, they concluded that the endothermic reformer solution would reach a break-even after 10 years (against 15 of the autothermal one). In the second analysis, they connected the FT reactor to an SOEC unit operating in co-electrolysis, reaching a process efficiency of 68.1% and wax production cost of 69 €/GJ_{wax} when supplying electricity at 100 €/MWh. However, the authors did not include any capture process in their study, nor accounted for a detailed FT products distribution description. They opted instead for the simplified AFS distribution at a fixed probability growth α value of 0.93. Moreover, Kärki et al. [201] studied to production of the FT waxes using CO_2 flue gas. The authors obtained a price range of 1.4-2.4 €/kg_{wax} for waxes heavier than C_{18+}, with production rates of 1.5 kt_{wax}/y. Nevertheless, no data was reported on labour costs, nor experimental validation of their FT model was included.

Hence, studies on the wax production costs are relatively low in number. Contrarywise, the production of lighter FT fuels was examined from different carbon feedstock and with different process routes. Considering the conversion of biogas from anaerobic digestion, Okeke et al. [202] investigated the direct use of clean biogas into steam and partial oxidation reforming processes before synthetising Fischer-Tropsch diesel. The authors used an ASF empirical description, with a probability value α depending on the reactants' partial pressures and the process temperature. Similarly, Hernandez et al. [203] studied the conversion of biogas to Fischer-Tropsch diesel and gasoline with either a low temperature or a high temperature FT reactor, reaching a cost of products of 1.7 $/gal and 3 $/gal, respectively.

Concerning the utilization of biomass material, this is generally limited to applications with high-capacity gasifiers (higher than 100 MW_{th}) to generate the syngas needed by the Fischer-Tropsch. For instance, Dietrich et al. [204] considered woody biomass (gasification capacity of 400 MW_{th}) and synthetised compounds up to C_{36}, with hydrocracking to diesel pool of the C_{20}-C_{36} ones. The authors reached production costs of 2.43 €/kg_{fuel} and an efficiency of the system of 36.3%. Moreover, Hillestad et al. [205] connected a 435 MW_{th} gasifier (wood feedstock) to an SOEC for steam electrolysis and a Fischer-Tropsch reactor for diesel production. The authors reached a plant efficiency of 53% and a cost of 2.6 €/l. Lastly, Spyrakis et al. [206] reached a system efficiency of 28.7%, with a 4.82 MW_{th} gasifier consuming lignocellulosic material.

Accounting for capturing and utilizing carbon dioxide from air, the literature mainly covers LCA analyses and the implementation in future economic scenarios of the DAC-to-FT route. Nonetheless, a detailed mass and energy integration of the two processes is missing. Fasihi et al. [207–209] provided a thorough study of the DAC-FT integration. However, they dealt with the low-temperature version of the DAC technology. Moreover, they used a Fischer-Tropsch product distribution taken from literature, which provided the mass share of clustered FT products. Recirculation of the FT off-gas was included only to generate energy required by an electrified reverse water gas shift reactor. Liu et al. [210] provided the LCA of a high-temperature DAC unit connected to a Fischer-Tropsch reactor to synthetise transportation fuels. Their analysis included literature data for a simplified FT power-law description [211] and the DAC [212]. Nevertheless, the authors emphasized the need for extensive DAC-FT mass and energy integration studies. Vidal et al. [72] investigated the operations of a low temperature DAC with RWGS and FT reactors, achieving 94% of carbon efficiency and 47% of plant efficiency. Graves et al. [213] integrated a DAC with an SOEC and an high temperature FT reactor to produce, mainly, short chain hydrocarbons. They studied a solution where FT heat was fed to the DAC section, but no information about possible mass integration via recirculation of the FT off-gas was provided.

Lastly, studies utilizing a concentrated CO_2 flow are available. Cinti et al. [214] coupled an SOEC in co-electrolysis with an FT reactor. The authors included experimental data for the SOEC and fixed growth probability α of 0.94 for the FT, reaching an efficiency of 40.9%. Rafiee et al. [215] achieved a carbon efficiency of 68.2% when capturing CO_2 from industrial flue gases in a system configuration presenting an autothermal and an FT reactor. Hannula et al. [29] investigated the production of FT compounds based on different configurations to supply heat to the upstream RWGS reactor (i.e., allothermal combustion solution, autothermal partial oxidation, autothermal electric heating). The authors concluded that the optimal configuration corresponded to the electrically heated one, with a CO_2 conversion efficiency as high as 91%. Further studies on the conversion of carbon material to FT hydrocarbons are listed in Appendix A – Catalyst testing and kinetic models.

The production of FT material has been investigated in the open literature. Still, it frequently fails to incorporate experimental information into process modelling, utilizing simplified FT kinetics or avoiding including energy and mass integration solutions. Additionally, the process of carbon capture is often left out from the investigations. Hence, with the present research, the aim is to unveil the production costs of FT waxes from different carbon sources, under the same process hypotheses for direct production route comparison. To this end, carbon capture processes are modelled. Additionally, detailed kinetic information allows describing the Fischer-Tropsch products distribution up to C_{80}. Finally, economic considerations are provided.

3.2 Biogas conversion

As described in Chapter 1, biogas is a valuable renewable gas that delivers as by-product upon upgrading a *ready-to-use* stream of carbon dioxide that can be converted to synthetic products. With respect to the ICO2CHEM project, CO_2 is captured from a clean biogas stream generated from anaerobic digestion [216]. Accordingly, the present analysis investigated different process configurations to capture the carbon dioxide and convert it into FT products – including the one of the ICO2CHEM project (Figure 21).

CO_2 is separated from biomethane utilizing the chemical scrubbing technology with MEA. The captured carbon dioxide is fed to the syngas generation unit. Under option A, CO_2 is fed to a RWGS reactor coupled with an alkaline steam electrolyser. Under option B, CO_2 is mixed with steam and sent to an SOEC unit. The generated syngas is fed to the Fischer-Tropsch reactor, whose product distribution is described by the kinetic model described in Chapter 2. Lastly, the FT compounds are separated, with off-gas recirculation to the syngas generation section. A fraction of the FT off-gas was burnt before ventilation to avoid accumulating inert compounds in the plant lines [83].

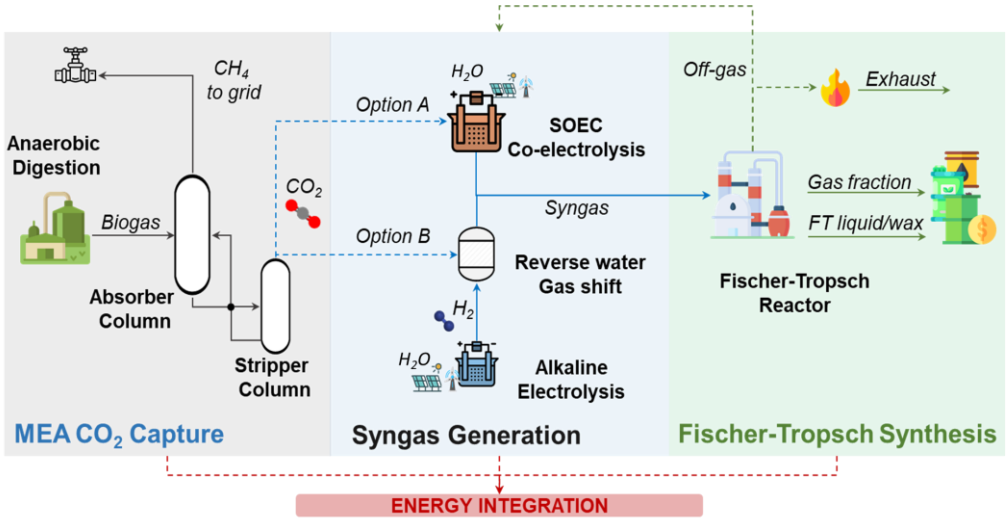

Figure 21. Simplified process schematics for the conversion of biogas. Syngas generation options via low temperature electrolysis and RWGS reaction (option A), or solid oxide co-electrolysis (option B).

3.2.1 Process configurations

Within the ICO2CHEM project, CO_2 is converted into synthetic hydrocarbon by interposing a RWGS reactor operating at high pressure (i.e., > 20 bar) between the carbon capture unit and the FT reactor. This solution allows matching the operating pressure of the downstream FT reactor. Hence, this research investigated two pressurization solutions for the syngas generation sections. In the first case, the RWGS and SOEC operated at ambient pressure. In the second case, the two devices operated at the Fischer-Tropsch pressure.

Low-pressure operations

In the RWGS route (Figure 22), the alkaline electrolyser provided a flow of H_2 that was mixed with CO_2 coming from the biogas upgrading unit. The two reactants were preheated to 560 °C and fed to the RWGS. With the FT off-gas recirculation, heater-H6 ensured the same temperature of the inlet reactants. Moreover, a flow of steam was fed when needed to avoid carbon deposition in the RWGS reactor. The required H_2/CO ratio at the FT reactor inlet was achieved adjusting the water intake of the alkaline unit.

With the SOEC option (Figure 23), water was vaporized and mixed with the CO_2. Moreover, the reactants were heated to the SOEC temperature (800°C). Carbon deposition was avoided modifying the SOEC reactant utilization. The desired H_2/CO ratio was reached with variation of the steam flow rate entering the system.

In both routes, the syngas pressurization occurred before the FT reactor with a 3-stages compression system with intercooling. The pressure ratio was set to 2.924, reaching 25 bar at the outlet of compressor-B5 starting from 1 bar. The intercooling provided a temperature of 100°C at the inlet of each compression stage. These configurations are accounted for as RWGS.LP and SOEC.LP.

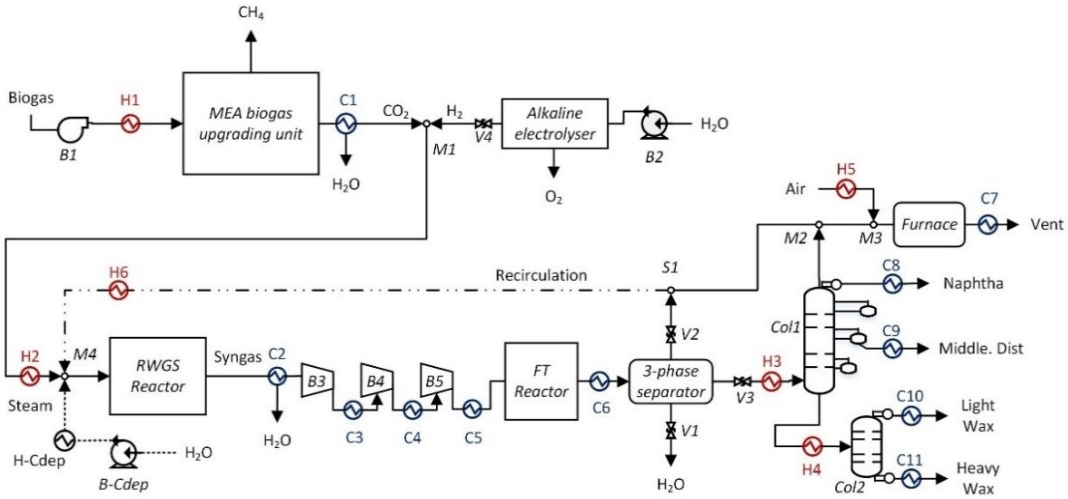

Figure 22. Process scheme of configuration A, with RWGS reactor and LT-electrolyser operating at low pressure. Reprinted with permission from [28].

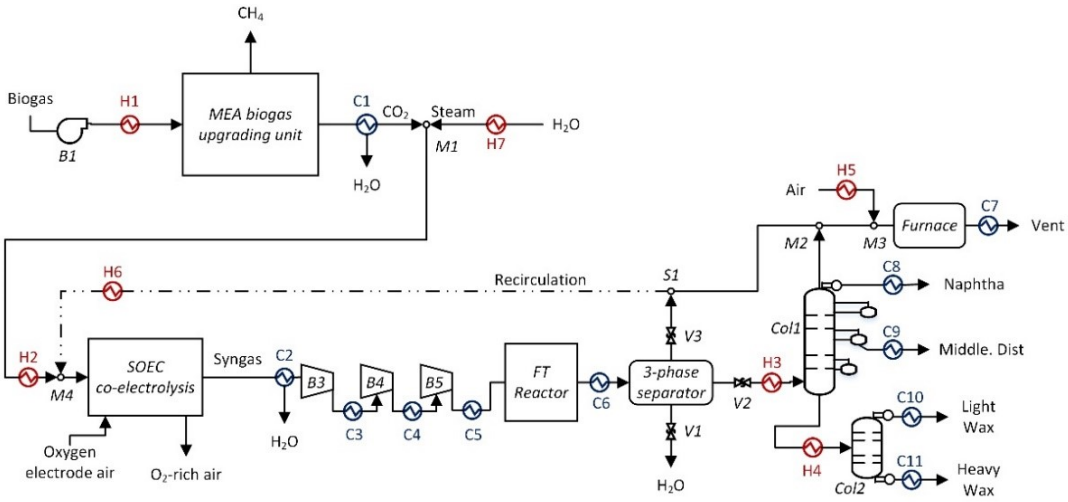

Figure 23. Process scheme of configuration A, with SOEC reactor operating at low pressure. Reprinted with permission from [28].

High-pressure operations

When high pressure operation was selected, the pressurization took place before feeding the reactants to the RWGS or SOEC. In the first case, the alkaline electrolyser operated at 15 bar [217], with further pressurization of hydrogen to 25 bar before mixing with CO_2. With the SOEC unit, water was pumped in the system to 25 bar and vaporized. An intermediate compressor (component B3-HP) was included on the FT off-gas recirculation line.

These configurations are accounted for as RWGS.HP and SOEC.HP.

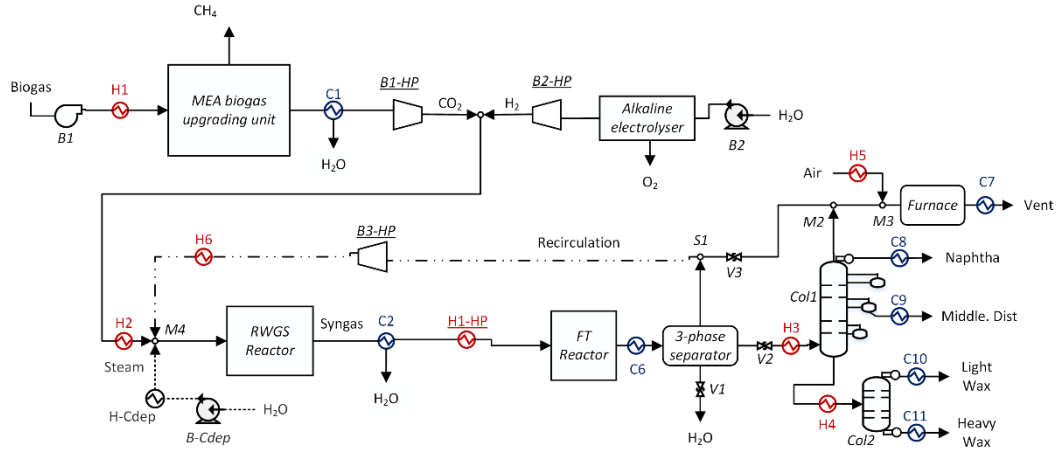

Figure 24. Process scheme of configuration A, with RWGS reactor and LT-electrolyser operating at high pressure. Reprinted with permission from [28].

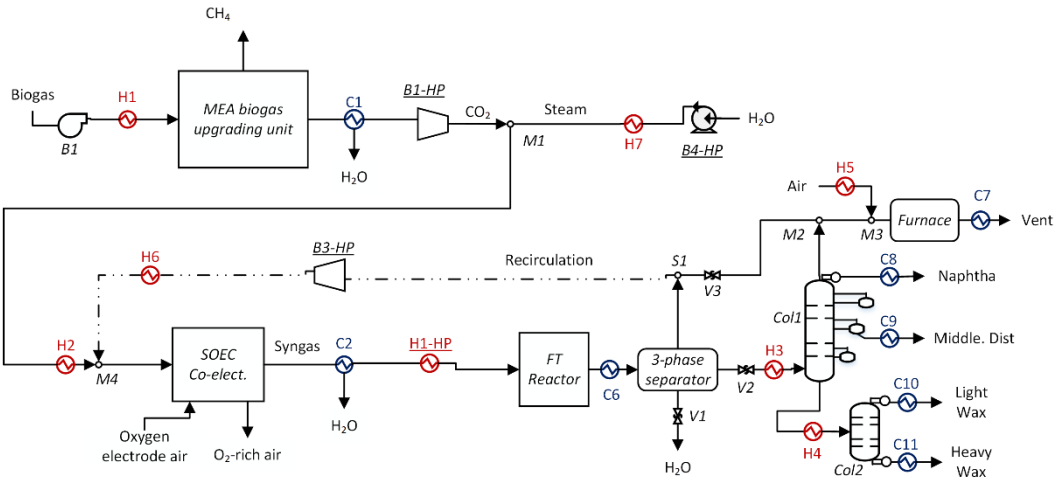

Figure 25. Process scheme of configuration A, with SOEC reactor operating at high pressure. Reprinted with permission from [28].

3.2.2 Biogas upgrading and CO_2 capture

CO_2 was captured from a clean biogas stream (1680 $m^3_{biog.}$/h). The capture unit used monoethanolamine (MEA) for the absorption process (30 %-wt MEA and 70 %-wt water) and separated 1 ton/hr of CO_2. This technology has a capture efficiency in the range of 85-95%, generally referring to the use of flue gases. However, biogas has a higher CO_2 concentration than in flue gases and the only concurrent molecule present in stream is CH_4. Additionally, MEA-based solvents are highly selective towards CO_2. Thus, this component had 98% capture efficiency. For instance, Kasikamphaiboon et al. [218] and Brand et al. [219] reported CO_2 capture values higher than 98%. Additionally, during the European H2020 project "Hydrousa" [220], almost 100% CO_2 recovery from biogas was achieved under high MEA concentration (i.e., 30%-wt). The main drawback of high capture rates is the higher energy consumption of the capture unit.

Nevertheless, its impact could be reduced when matching the upgrading unit with an exothermic FT reactor with heat recovery solutions.

Table 11. Characteristic of the biogas fed to the CO_2 capture unit. Adapted from [28].

Biogas Inlet		**Component**	**[%mol]**
Flow rate [m^3/hr]	1680	CO_2	34.0
Temperature [°C]	25	CH_4	65.0
Pressure [bar]	1	N_2	1.00

The schematics of the biogas upgrading unit is provided in Figure 26. Biogas entering the system was preheated to 40°C. An absorber column ensured methane and carbon dioxide separation. A stripper column ensured CO_2 release via heat transfer from the reboiler bottom stage. The loading value was set to 0.24, being the loading the ratio of the moles of absorbed carbon dioxide per mole of MEA amine in the lean solvent stream. This value is in accordance with the loading parameters reported by Raynal et al. [221] and Li et al. [222] in the range of 0.22-0.25 for optimal extraction of CO_2. Additionally, a cross-heat exchanger preheated the stream entering the stripper and precooled the one leaving the stripper (i.e., CO_2-rich stream and CO_2-lean streams), with 15°C temperature difference between the two flows. Moreover, a make-up flow reintegrated MEA and water lost during the separation process. Lastly, CH_4 was dried, compressed to 10 bars, and injected in the local gas grid. CO_2 was dried and sent to the RWGS/SOEC.

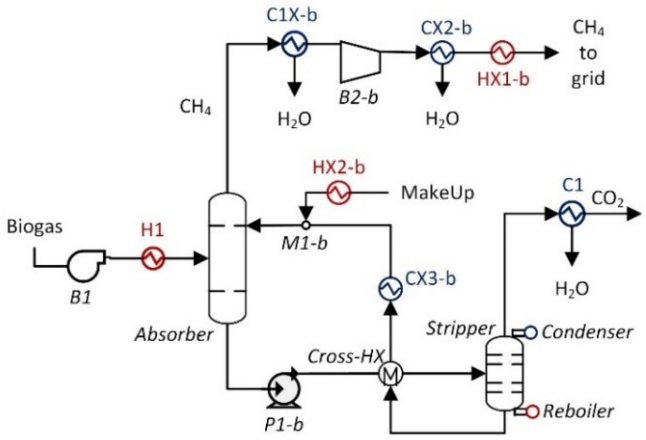

Figure 26. Scheme of the CO_2 capture unit via MEA-based chemical scrubbing. Reprinted with permission from [28].

Both the absorber and the stripper were modelled as rate-based multistage packing columns on AspenPLUS^{TM}. Both columns presented 14 stages, with a pressure drop of 0.5 bar. The absorber column worked at 1.12 bar, with an inlet temperature of 40°C. The stripper column operated at 1.6 bar [223]. It had a kettle-reboiler at the bottom stage and a condenser at the top one. Lastly, the reboiler heat duty was adjusted to reach the desired CO_2 captured rate. Additional information are provided in Table 12.

Table 12. Additional specifications of the biogas upgrading section on AspenPLUS. Adapted from [28].

Absorber	**Reboiler**
Rate-based	Rate-based
1.12 bar (Δp 0.5 bar)	1.6 bar (Δp 0.5 bar)
14 stages	14 stages (condenser and reboiler)
1 m section diameter	1 m section diameter
Mixed Flow model	Mixed Flow model
Interfacial area factor 1.2	Interfacial area factor 1.2
Reaction condition factor 0.9	Reaction condition factor 0.9
Film discretization ratio 5	Film discretization ratio 5
	Distillate to feed ratio 0.04
Preheater outlet	40°C
Cross-HX outlet to absorber	40°C

Moreover, the process of CO_2 separation was modelled with a carbamate formation mechanism with reference to Moioli et al. [224] and Abu Zahra et al. [225] investigations. The model included equilibrium and kinetic reaction steps with water as the base and both molecular and ionic species. The equilibrium reactions correspond to eq.(3.1)-eq.(3.5), with equilibrium coefficients evaluated with the constants listed in Table 13.

$$2H_2O \leftrightarrow H_3O^+ + OH^- \quad (3.1)$$

$$CO_2 + 2H_2O \leftrightarrow HCO^{3-} + H_3O^+ \quad (3.2)$$

$$HCO^{3-} + H_2O \leftrightarrow CO_3^{2-} + H_3O^+ \quad (3.3)$$

$$MEAH^+ + H_2O \leftrightarrow MEA + HCO^{3-} \quad (3.4)$$

$$MEACOO^- + H_2O \leftrightarrow MEA + HCO^{3-} \quad (3.5)$$

Table 13. Reaction coefficients for the chemical reactions of eq.(3.1)-eq.(3.5) .

Reaction	**A**	**B**	**C**	**D**
(3.1)	132.89	-13445.9	-22.47	0
(3.2)	231.46	-12092.1	-36.78	0
(3.3)	216.05	-12431.7	-35.48	0
(3.4)	-3.038	-7008.36	0	-0.0031
(3.5)	-0.52	-2545.53	0	0

$$\ln(K_i) = A_i + B_i/T + C_i \ln(T) + D_i T \quad (3.6)$$

Slower reaction steps correspond to eq.(3.7)-eq.(3.10) [225]. Kinetic constants were evaluated with the parameters listed in Table 14.

$$MEA + CO_2 + H_2O \rightarrow MEACOO^- + H_3O^+ \quad (3.7)$$

$$MEACOO^- + H_3O^+ \rightarrow MEA + CO_2 + H_2O \quad (3.8)$$

$$CO_2 + OH^- \rightarrow HCO^{3-} \quad (3.9)$$

$$HCO^{3-} \rightarrow CO_2 + OH^- \quad (3.10)$$

Table 14. Reaction coefficients for the chemical reactions of eq. (7-10).

Reaction	A_j	E_{act} [cal/mol]
(7)	9.77e+10	9856
(8)	2.18e+18	14138.4
(9)	4.32e+13	13249
(10)	2.38e+17	29451

$$k_i = A_i \exp(-Eact_i/RT_i) \quad (3.11)$$

Lastly, the thermodynamic of the Vapour-Liquid-Equilibrium of this unit was described with Electrolyte-NRTL (Non-Random Two Liquid) method for the liquid phase and Soave-Redlich-Kwong (RKS) state equation for the vapour one.

3.2.3 Fischer-Tropsch

The operating conditions of Fischer-Tropsch reactor consisted of the temperature and pressure provided in Chapter 2 (228 °C, 25 bar), with an H_2/CO molar ratio of 1.9. The reactor was designed as one-through multitubular fixed-bed reactor, with a per-pass CO conversion of 75% (eq.(3.12)). Moreover, recirculation options of unconverted syngas reactants to upstream components were studied, increasing the synthetic hydrocarbons yield. The distribution of the FT products and their rates of formation was described by the kinetic model of Chapter 2, with an external subroutine to include the rates definition of n-paraffins up to carbon number C_{70} and α-olefins up to carbon number C_{40}.

$$Xco = \frac{\dot{n}_{CO_{inFT}} - \dot{n}_{CO_{outFT}}}{\dot{n}_{CO_{in\_FT}}} \quad (3.12)$$

The value of CO conversion at 75% avoided formation of unwanted carbon dioxide under the water-gas shift reaction over cobalt. Similarly, the formation of methane and light hydrocarbons was reduced. As stated by Yang et al. [226], values higher than 80% for fixed-bed FT reactors loaded with cobalt catalysts determine a rise in the CO_2 selectivities. The authors also reported that conversion values over 80% would favour oxidation of cobalt particles, reducing the catalyst activity. Similarly, Tucker et al. [97] reported two regimes depending on the conversion level at constant process conditions (Figure 27). At conversion levels lower than 75%, CO_2 selectivity was close to zero and CH_4 selectivity decreased linearly. At values higher than 80%, both indicators rose exponentially, with additional reduction of the probability growth α and C_{5+} selectivity.

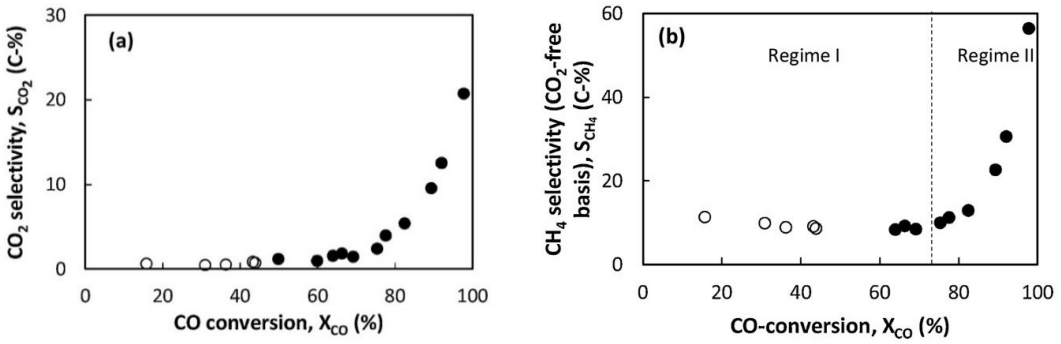

Figure 27. Evolution of the CO_2 and CH_4 selectivity depending on the CO conversion for a Co-Pt FT catalyst, at 20 bar, 220°C, H_2:CO:N_2 4:2:6. Closed symbols (●) changing volumetric flow rate. Open symbols (○) standard volumetric flow rate (1000ml_n/min). Reproduced with permission from [97].

The RKS equation-of-state with Boston-Mathias alpha value modification (RKS-BM) was used, accounting for hydrocarbon and petrochemical problems. Lastly, not all hydrocarbons were available through the AspenPLUS databases. Thus, paraffins of carbon number higher than C_{30} and olefins with odd carbon values greater than C_{21} were manually inserted. The chemical structures of the hydrocarbon compounds were imported from external databases (i.e., ChemSpider [227], PubChem [228]), and critical state parameters and normal boiling point information were included for n-paraffins [229] and olefins [230].

Fischer-Tropsch products distillation

A three-phase separator operating at room temperature and FT pressure split the by-product H_2O from the FT gases and liquids the outlet of the reactor. Water was disposed of, while the FT liquid fractions underwent distillation at ambient pressure dividing naphtha from middle distillates, waxes, and residual gases, depending on the boiling temperature of each product cut inside a distillation tower (Table 15).

The Winn-Underwood-Gilliland method was applied to assess the initial size of the tower, with a generic distillation tower component on AspenPLUS. This allowed finding the theoretical minimum number of stages and minimum reflux ratio necessary for the separation of each fraction from the main flow (i.e., naphtha from liquids, middle distillates from liquids), with partial condensation of the cuts [231]. Consequently, the distillation tower was replaced with a more accurate PetroFrac component in AspenPLUS. This was equipped with a single kettle reboiler at the bottom stage and a condenser at the top one (partial vapour-liquid condensation to separate the remaining gas fraction). Setting the reflux ratio to 1.8, the first distillation tower required 54 stages, with the feed preheated to 250°C and entering at stage 28. A side stripper was included to separate the middle distillate fraction, which consisted of 16 stages, with a draw at stage 18 and overhead return at stage 12. The second distillation column was composed of 58 stages with a kettle reboiler and total condensation to separate light and heavy waxes. The FT products preheated to 455°C and entered at stage 38 [231,232]. All

the products were cooled to room temperature. The off-gas exiting the distillation tower were blended with the flow coming from the 3-phase separator and recirculated to the RWGS/SOEC. The uncirculated fraction was burnt [233].

Table 15. Product classes obtained after FT hydrocarbons distillation. Adapted from [28].

Fraction	Carbon Number	Boiling Temperature [°C]
Gas	C_1-C_4	40
Naphtha	C_4-C_{11}	123
Middle Distillate	C_{11}-C_{20}	225
Light Waxes	C_{20}-C_{35}	383
Heavy Waxes	C_{35}-C_{70+}	520

The LHV of n-paraffin and α-olefins was calculated separately:

$$LHV_{paraffins,m} = \sum_n \left[(608.44n + 213.31)x_{n,paraf}\right] \quad (3.13)$$

$$LHV_{olefins,m} = \sum_n \left[(604.93n + 113.83)x_{n,olef}\right] \quad (3.14)$$

Being n the number of carbon number, x_n the molar yield.

3.2.4 Syngas generation

Alkaline steam electrolysis

For the RWGS routes, the alkaline steam electrolysis technology was utilized, with reference to *state-of-the-art* performance [217]. The electrolyser operated at ambient conditions (or 15 bar for the pressurized RWGS case), with water consumption of 15 L_{H2O}/kg_{H2} and an efficiency of 52 kWh_{el}/kg_{H2} [217]. The electric input to run the electrolysis process came from the grid, assuming a mixed renewable energy source. Oxygen was considered as by-product.

Reverse water-gas shift

CO_2 and H_2 were mixed and heated to 560°C prior to the RWGS. Moreover, by utilizing a suitable Ni-based catalyst Vidal Vasquez et al. [54] reached equilibrium conditions under RWGS reaction for syngas generation. With reference to their results, the RWGS reactor operated at equilibrium conditions at 800°C, loading a Ni-Al_2O_3 catalyst. The conversion of CO_2 to CO followed the endothermic reaction (3.15).

$$CO_2 + H_2 \leftrightarrow CO + H_2O \qquad \Delta H^0_{298K} = 41 \text{ kJ/mol} \quad (3.15)$$

Additionally, side reactions may develop at equilibrium conditions. Vidal Vasquez et al. [54] described methane formation via methanation (eq.(3.16)-eq.(3.17)). Wolf et al. [234] reported solid carbon formation onto the catalyst surface due to the strong interaction between nickel and carbon compounds if no additional oxygen carrier was fed to the unit (eq.(3.18)-eq.(3.19)). Hydrocarbons

decomposition and steam reforming of light compounds can develop due to the FT off-gas recirculation [235] (eq.(3.20)-eq.(3.21)). The main drawback of employing an RWGS is dictated by the equilibrium-constrained conversion of CO_2 (63% at the selected operating conditions).

Table 16. RWGS reactor chemical reactions

Reaction	ΔH^0_{298K} [kJ/mol]	
$CO + 3\ H_2 \leftrightarrow CH_4 + H_2O_{(v)}$	-165	(3.16)
$CO_2 + 4\ H_2 \leftrightarrow CH_4 + 2\ H_2O_{(v)}$	-206	(3.17)
$2\ CO \leftrightarrow CO_2 + C_{(s)}$	-172	(3.18)
$2\ CO + H_2 \leftrightarrow H_2O_{(v)} + C_{(s)}$	-131	(3.19)
$C_nH_m \leftrightarrow n\ C + (m/2)\ H_2$	e.g.+791 for CH_4	(3.20)
$C_nH_m + n\ H_2O_{(v)} \leftrightarrow n\ CO + (n+m/2)\ H_2$	e.g.+206 for CH_4	(3.21)

The RWGS reactor was described with the Redlich-Kwong-Soave (RKS) EoS on AspenPLUS.

Solid oxide CO_2 and steam electrolysis

The SOEC operated at 800°C, at either atmospheric pressure or 25 bar. The SOEC was assumed using *state-of-the-art* materials: Ni/YSZ for the cathode (i.e., fuel electrode), YSZ for the electrolyte layer, LSC/CGO at the anode side (i.e., oxygen electrode) [236]. The electrochemical conversion of CO_2 and steam corresponded to eq. (19-21) [237]. Furthermore, it is reported and accepted that the conversion of the carbon dioxide and steam in this device is determined not only by electrochemical reactions, but also by chemical reactions evolving equilibrium conditions at the cathode side [238]. As reported by Zhang et al. [239], Ni content in the fuel electrode can catalyse the reactions of WGS and reforming of CH_4, caused by the presence of steam, carbon monoxide, carbon dioxide and hydrogen. Additionally, SOEC electrodes are sensible to coke formation, determining the blockage of the three-phase points (i.e., catalyst structure where reactants interacts) and a reduction of their electrochemical properties [240]. Moreover, as reported by Chen et al. [241], oxidation of carbon material may lead to cracking of the electrode. Lastly, FT off-gas recirculation may favour cracking of light hydrocarbons at the stack level (eq.(3.18)-eq.(3.21)). Hence, these reactions were considered for this component.

Global reaction	$n\ CO_2 + m\ H_2O \rightarrow n\ CO + m\ H_2 + (m+n)/2\ O_2$	(3.22)
Cathode Side	$H_2O + 2\ e^- \rightarrow H_2 + O^{2-}$	(3.23)
	$CO_2 + 2\ e^- \rightarrow CO + O^{2-}$	(3.24)
Anode Side	$O_2^- \rightarrow 0.5\ O_2 + 2\ e^-$	(3.24)

The SOEC schematics is provided in Figure 28. Firstly, the electrochemical conversion was modelled with a stoichiometric reactor (EL-S). Secondly, the

reactions taking place at the equilibrium were accounted for with an equilibrium reactor (EQ-2), following the removal O_2 to simulate its transport through the electrolyte layer. Finally, an upstream equilibrium reactor (EQ-1) simulated the chemical reactions between CO_2, CO, H_2 and light hydrocarbons when a recirculation of the FT off-gas was applied.

In the baseline configuration, the reactants utilization (RU) was set to 75% at stack level. This was evaluated according to eq (3.25).

$$RU = \frac{\dot{n}_{react_{in,Stack}} - \dot{n}_{react_{out,Stack}}}{\dot{n}_{react_{in,Stack}}} \tag{3.25}$$

A fraction of the syngas leaving EQ-2 was recirculated at the cathode inlet, reaching a minimum H_2 concentration in the feed of 10%. Such a value corresponds to the minimum amount of hydrogen that guarantees that the nickel of the fuel electrode does not undergoes re-oxidation during operations [240,242]. Lastly, RKS EoS was used for this component.

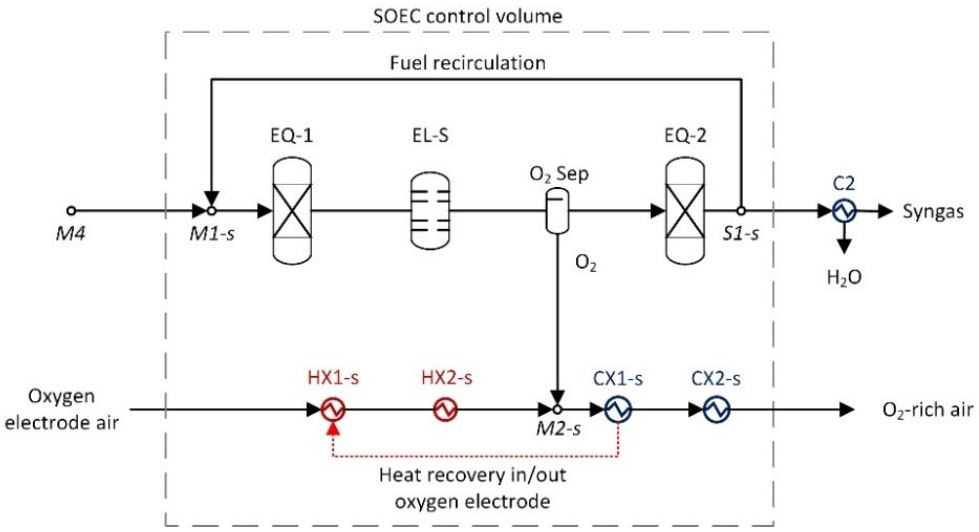

Figure 28. SOEC stack unit schematics. Reproduced from [28].

SOEC operational model

The performance of the SOEC device can be related to its operational voltage. Regarding the voltage, this parameter depends on the open circuit voltage and the overvoltages generated by chemical conversions. These account for ohmic resistance overvoltage, activation overvoltage due to limitation of the kinetic reaction at the electrode side, and mass transport overvoltage. These parameters can be ascribed to a single element called Area-Specific Resistance (ASR) including all the internal losses. The ASR equalled 0.25 $\Omega \cdot cm^2$ at ambient pressure and 0.2 $\Omega \cdot cm^2$ at high pressure [243,244].

$$W_{el} = V_{Operation}\, I \tag{3.26}$$

$$V_{op} = V_{OCV} + V_{losses} = V_{OCV} + ASR\, j \tag{3.27}$$

The value of the open circuit voltage depends on the composition of the feed flow sent to the SOEC, and it can be evaluated as the ratio of the Gibbs free energy variation (Δg) over the current (I). The current value can be expressed through the Faraday's law, referring it to the O_2 component.

$$V_{OCV} = \frac{\Delta g}{2\, F} \tag{3.28}$$

$$\dot{n}_{O_2} = \frac{j\, Atot}{4\, F} = \frac{I}{4\, F} \tag{3.29}$$

where $n_{e,tot}$ is the number of exchanged electrons, F is the Faraday constant (96485 C/mol), j is the current density, and A_{tot} is the total stack area.

Furthermore, the SOEC device generally works at isothermal conditions [245]. To reach this condition, three operational modes can be applied, depending on the value of the operating voltage [246]:

1) Thermoneutral operation: under this condition, the heat generated by the overpotential and equilibrium reactions equals the heat required by splitting of CO_2 and H_2O, thus having a thermally self-sustained device.
2) Exothermic operation: the heat produced by the cell overpotentials is higher than the heat absorbed for the splitting reaction, thus excess heat is removed from the cell. This condition is reached for a value of the operating voltage higher than the thermoneutral voltage.
3) Endothermic conditions: the heat produced by the cell overpotentials is lower than the one absorbed by steam and carbon dioxide for their splitting, thus heat is fed the cell. This condition is reached for a value of the operating voltage lower than the thermoneutral voltage.

The thermoneutral voltage can be evaluated based on the enthalpy variation of the overall reaction. In this study, thermoneutral operations were selected.

$$V_{TN} = \frac{\Delta h}{n_{e,tot}\, F} \tag{3.30}$$

$$j_{TN} = \frac{V_{TN} - V_{OCV}}{ASR} \tag{3.31}$$

3.3 CO_2 conversion from direct air capture

The second process model accounts for the conversion of CO_2 capture from air. High-temperature direct air capture technology (HT-DAC) extracted carbon dioxide from the air based on liquid solvents with calcium loop. Specifically, the DAC unit was modelled after the process proposed by Keith et al. [212] and commercialized by Carbon Engineering [247].

A simplified schematics of the DAC unit principle is provided in Figure 29. It consists of two main loops: the first one accounts for the separation of carbon dioxide from the air, the second one regenerates the solvent and subsequently releases the CO_2 molecule.

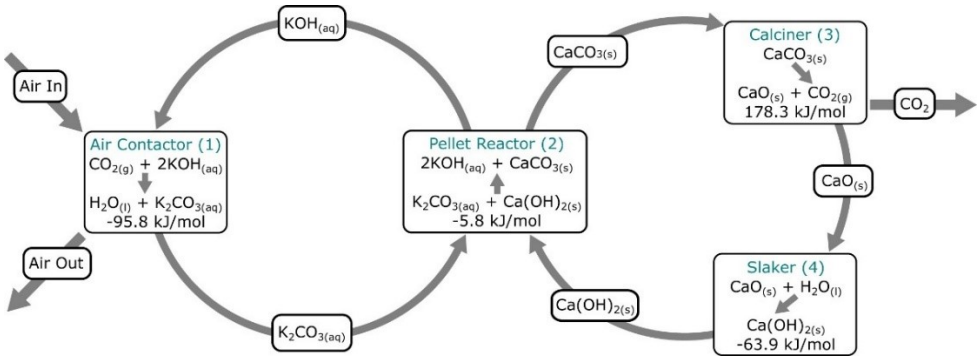

Figure 29. Simplified schematics of the high temperature DAC process. Reproduced from [212].

In the reference process, natural gas burning sustains the thermal and electrical demand of the DAC unit (i.e., calciner reactor and auxiliaries, respectively). However, this solution is not environmentally beneficial when included in the carbon capture and utilization concept, where fossil material would be converted into synthetic hydrocarbons [68,210]. Hence, the present analysis proposes different process configurations to avoid natural gas utilization through recirculation of the FT off-gas or the implementation of an electrified calciner reactor (Figure 30).

3.3.1 Direct Air Capture technology

The reactions included in the AspenPLUS software for the DAC section are summarised in Table 17, including equilibrium, salt precipitation, and dissociation reactions. In Figure 30, the schematic of the process model is provided.

In detail, the model accounted for the extraction of air in the air contactor. CO_2 yielded to K_2CO_3 via reaction with an aqueous alkali solution composed of 1.0 moles OH^-, 0.5 moles CO_3^{2-}, and 2.0 moles K^+ [212]. Parallelly, carbon dioxide coming from the gas turbine (i.e., exhaust gases from the combustion process) was recovered in the absorber column and mixed with air. Subsequently, the alkali solution was regenerated inside a pellet reactor with precipitation of CO_3^{2-} reacting with Ca^{2+} of $Ca(OH)_2$ and formation of $CaCO_3$. The $CaCO_3$ pellets

were washed, dried, heated up and entered an oxyfired calciner (95.6% O_2, 4.4 N_2), releasing CO_2 and CaO. The $Ca(OH)_2$ component was regenerated in a reaction of CaO with water inside a slaker reactor. Unconverted CaO was disposed of. Lastly, the stream of concentrated carbon dioxide exiting the calciner reactor was washed in a water knockout and before entering the RWGS.

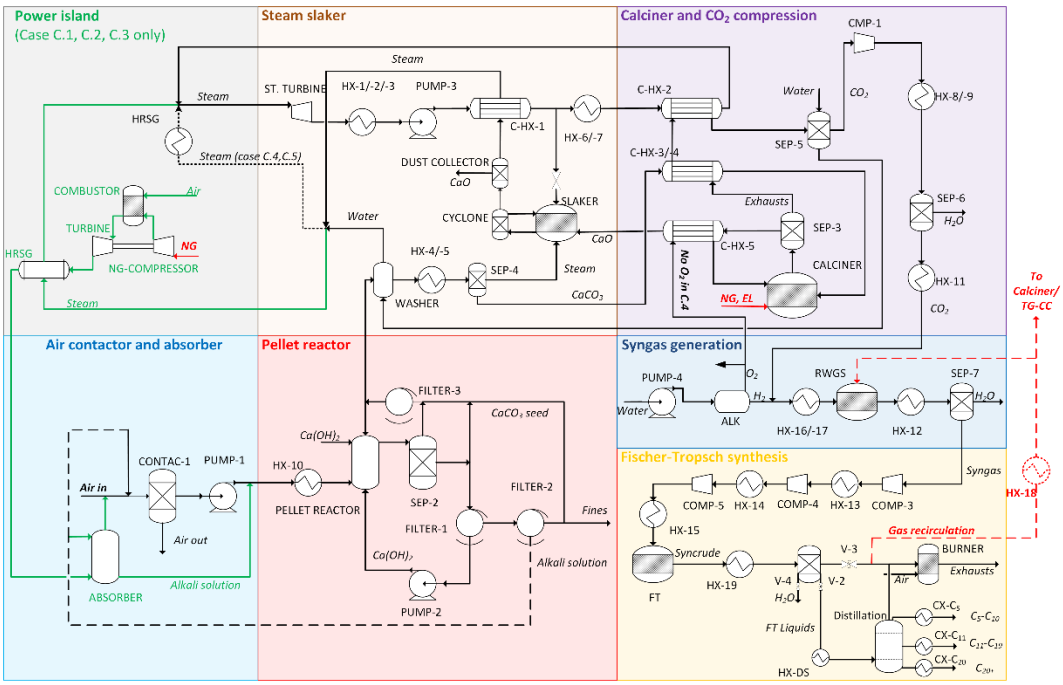

Figure 30. Process layout of the CO_2 from the air plant concept, integrating the DAC technology, with the RWGS and FT reactors. Reproduced from [195].

Table 17. Reactions evolving in the DAC unit.

Reaction	Type	
$H_2O+HCO_3^- \leftrightarrow CO_3^{2-}+H_3O^+$	Equilibrium	(3.32)
$CaOH^+ \leftrightarrow Ca^{2+} +OH^-$	Equilibrium	(3.33)
$2H_2O+CO_2 \leftrightarrow HCO_3^- +H_3O^+$	Equilibrium	(3.34)
$2H_2O \leftrightarrow OH^- +H_3O^+$	Equilibrium	(3.35)
$Ca(OH)_2 \leftrightarrow CaOH^+ +OH^-$	Salt precip.	(3.36)
$K_2CO_{3(S)} \leftrightarrow CO_3^{2-} +2K^+$	Salt precip.	(3.37)
$CaCO_3 \leftrightarrow CO_3^{2-} +Ca^{2+}$	Salt precip.	(3.38)
$KOH_{(S)} \leftrightarrow OH^- +K^+$	Salt precip.	(3.39)
$K_2CO_3 \rightarrow CO3^{2-} +2K^+$	Dissociation	(3.40)
$KOH \rightarrow OH^- +K^+$	Dissociation	(3.41)

Additionally, the model accounted for the following hypotheses [212]:

- CO_2 concentration of 400 ppm_{vol} was considered in the flow of air.
- The capture rate of the pellet reactor was assumed at 75%.
- The absorber recovered 90% of the CO_2 from the turbine exhaust gases.

- The absorption column had an inlet temperature of 93°C.
- The share of injected calcium leaving the calciner reactor as pellets rather than being disposed of as fines (i.e., calcium retention value) was of 90%.
- The calciner reactor operated at adiabatic condition when oxy-combustion was included. If the electric version of the calciner was used, this was sustained with electric heaters [68].
- The conversion of $CaCO_3$ to CaO was assumed of 98%.
- The pellet reactor was modelled as a crystallizer unit [248].
- The slaker recovered 85% of the CaO material.
- In the baseline configuration, the natural gas composition corresponded to CH_4:C_2H_6:CO_2:N_2=89:4:3:4 %-mol.

The model used the electrolyte non-random two-liquid method for the liquid phase, the Redlich-Kwong equation and Henry's Law for the gas phase and Vapor-Liquid Equilibrium. In two-phase blocks, the mass transfer was modelled with a two-film rate-based approach omitting convection mixing [224]. Pressure drops in the heat exchangers were neglected. Additionally, filters (i.e., cyclones) had a solid-to-solid outlet and liquid-to-liquid outlet fractions of 1 and 0.9, respectively, with 0.1 bar pressure drop. Additional specifications about the AspenPLUS components are provided in Table 18.

After carbon capture, the CO_2 was mixed with hydrogen coming from an alkaline electrolyser and fed to a RWGS reactor running at ambient pressure. Moreover, the synthesis gas was compressed and sent to the FT reactor. The alkaline electrolyser, RWGS reactor, and FT reactor operations have been described in previous sections.

Table 18. Specification of the main blocks employed in the DAC section.

Block	Characteristics	Block	Characteristics
Absorber (RadFrac)	Inlet temperature = 93°C p = 1 bar Packing: BERL ceramic (50 mm) Height/Diameter: 12/7.5 m Stages: 16 Reaction condition factor: 0.9 Film discretization ratio: 5 Interfacial area factor: 1.02 Liq. film discret. points: 5	Pellet reactor (Cristallizer)	T = 25 °C p = 1 bar Calcium retention 90%
		Calciner (Rstoic)	T = 900 °C p = 1 bar $CaCO_3$ conversion: 98%
		Slaker (Rstoic)	T = 300 °C p = 1 bar CaO conversion: 85%

3.3.2 Process configurations

The process model accounted for different configuration to assess the optimal conversion of CO_2, the elimination of the need of fossil material (i.e., natural gas) to sustain the electrical/thermal needs of the DAC unit, and the rise in the yield of production of the Fischer-Tropsch wax fraction. These configurations accounted

for the characteristics listed in Table 19. The same configuration schematics is presented in Figure 31.

Table 19. Configurations included in the DAC-to-FT process model.

Configuration	Description
DAC.1	Utilization of natural gas to feed the gas turbine of the DAC to generate power and the oxy-combustion process of the adiabatic calciner reactor, coherently with the design suggested by Keith et al. [212]. FT off-gas leaving the distillation unit were sent to the inlet of the RWGS reactor.
DAC.2	Natural gas use was avoided. The FT off-gas were recycled only to the DAC device, undergoing oxy-combustion in the calciner (adiabatic operations) and combustion in the gas turbine. The remainder of the off-gas were burnt before being released to the environment.
DAC.3	Same process operations as DAC.2 (recirculation of the FT off-gas to the DAC), with additional recirculation of the remaining part of the FT off-gas fed to the RWGS block.
DAC.4	The DAC was assumed as an electrified DAC system, excluding the gas turbine and the absorption column, and including an electrically heated calciner. Off-gas of the Fischer-Tropsch were sent to the RWGS.
DAC.5	The combined cycle and the absorption column were avoided, but the calciner presented oxy-combustion with the FT off-gas. The rest of the off-gas was fed to the RWGS reactor.

Hence, with reference to Figure 30, the gas turbine unit and the connected lines are eliminated (green lines in the figure). The water leaving the washer of configurations DAC.4 and DAC.5 is vaporized with a heater, rather than using the heat recovered from the gas turbine exhausts. Moreover, in the process configurations containing the gas turbine, a fixed electric output of 30 MW_{el} was assumed, covering the DAC electric needs in compliance with the process design suggested by Keith et al. [212]. Additionally, a minimum value of 5% of the FT off-gas was sent to a burner to avoid any accumulation of inert gases [83]. Hence, a maximum recirculation rate towards the RWGS and DAC of 95% was accounted for.

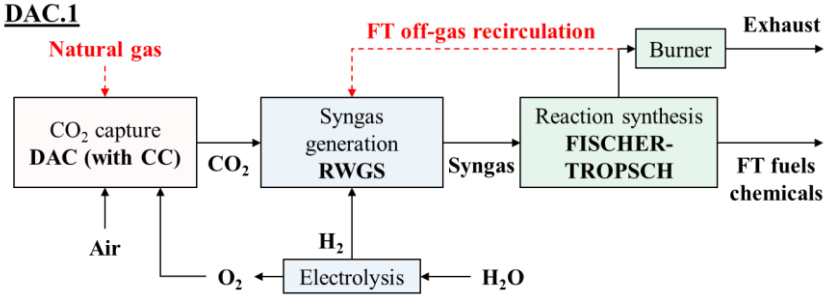

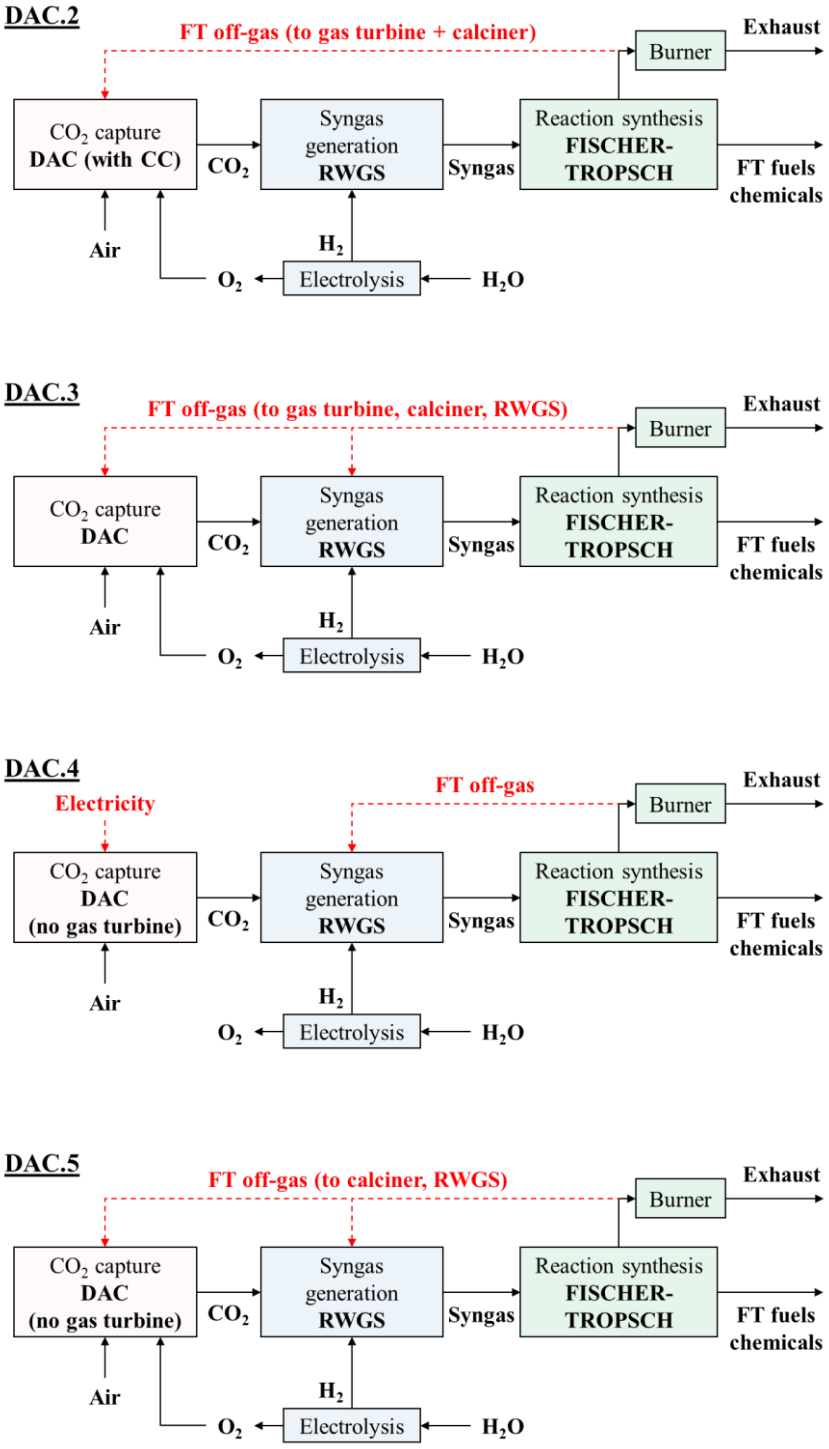

Figure 31. Schematics of the process concepts analysed when converting CO_2 from the air to Fischer-Tropsch material (configurations DAC.1 to DAC.5). Adapted from [195].

3.4 Digestate conversion

The last process model investigated the conversion of gasified digestate into Fischer-Tropsch (digestate coming from anaerobic digestion process).

The gasification of the biomass took place inside a dual fluidized bed gasifier (DFBG). The DFBG consists of two parallel reactor columns: the gasification and the combustion chamber. In the first one, biomass is decomposed and gasified. In the second one, the required heat is generated through combustion and transferred to the gasification column with sand material [249] (Figure 32).

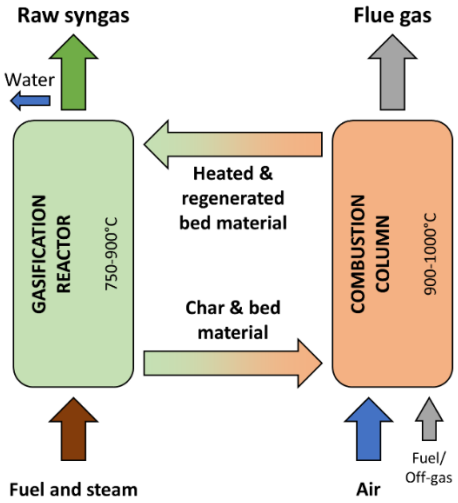

Figure 32. Simplified schematics of the DFBG. Adapted from [250].

3.4.1 Process configurations

After gasification, the raw syngas was cleaned from its impurities inside a conditioning unit composed of cyclones/filters, tar cracker, water scrubber, Venture scrubber, guard bed, and pressure swing adsorption (PSA). The FT products were generated and separated in a system following the considerations provided in previous sections. It was assumed to have a partial recirculation of the FT gaseous fraction at the inlet of the reactor [29]. A reforming unit at 800°C was included on this line to convert light hydrocarbons into Fischer-Tropsch reactants, feeding steam at 450°C for the conversion. Moreover, two process designs were explored, depending on the utilization of the remaining part of the FT off-gas (Figure 33):

- Configuration DIG.A: this configuration presented a gas turbine to produce electricity (1000°C, pressure ratio of 25 bar). The amount of FT off-gas fed to the gas turbine covered the electric energy demand of the system (i.e., auxiliaries). The rest was recirculated to the FT reactor inlet.
- Configuration DIG.B: 90% recirculation was assumed on the reformer line (i.e., outlet/inlet of the FT reactor). Moreover, this configuration included recirculation of the remaining off-gas to the gasification unit, with 90% of this flow to the gasifier and 10% to the combustion column.

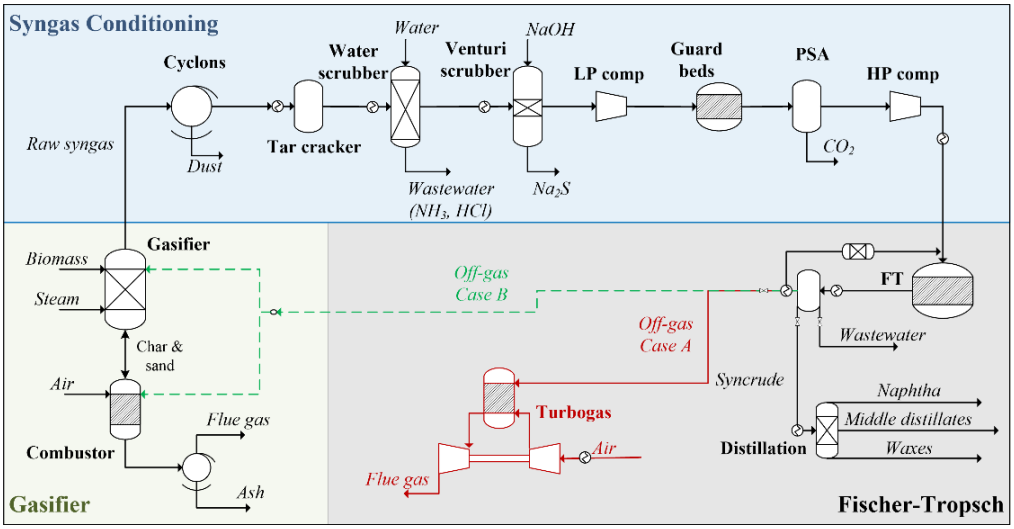

Figure 33. Process configuration for the conversion of biomass (i.e., digestate from anaerobic digestion or traditional lignocellulosic biomass material).

3.4.2 Gasification of biomass

The DFBG gasifier model took reference from the design suggested by Doherty et al. [251], with modification made to allow for the desired syngas composition at the outlet of the unit. The model hypotheses were the following:

- Isothermal and steady-state conditions for the gasification step.
- Instantaneous drying and pyrolysis steps.
- Atmospheric pressure operations, with negligible pressure drops.
- Steam is the gasifying agent.
- S, Cl, and N elements of the biomass are transformed in H_2S, HCl, and NH_3 impurities.
- No SO_x nor NO_x formation is neglected.
- Tars formation is neglected for the gasification temperature (> 800°C).
- There exists the formation of methane in the gasification process due to the co-presence of carbon monoxide and hydrogen.
- The gasifier operates in thermal balance by transferring the required heat from the combustion chamber to the gasifier.
- A flow of N_2 is fed as purge gas, reaching a concentration of 1.4%-mol in the outlet syngas flow (dry basis).

Different blocks were used to simulate the operation of this device on AspenPlus (Figure 34). Information about the main reactors are listed in Table 20.

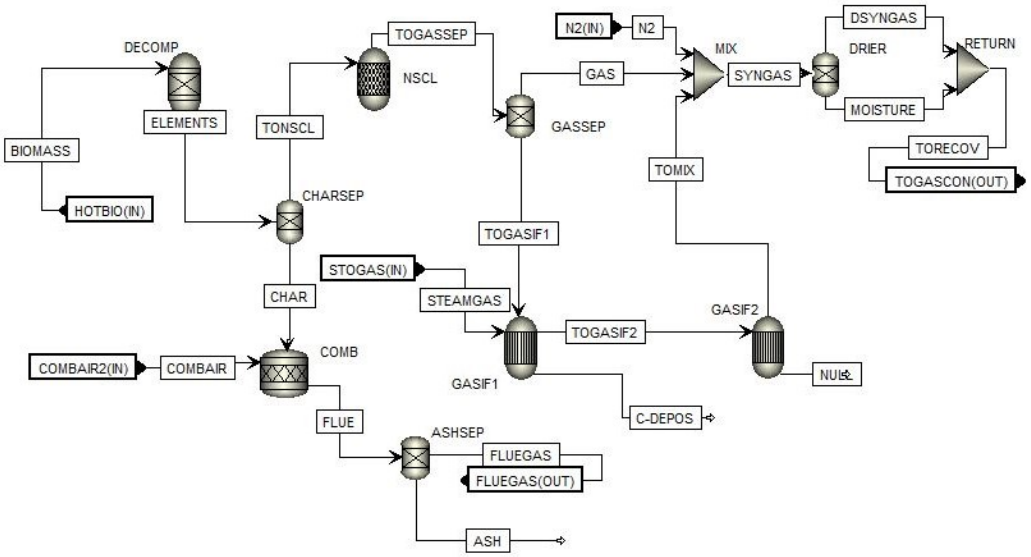

Figure 34. Process schematics of the gasification step.

Table 20. Description of the main components' characteristics for the gasification unit. Adapted from [196].

Block		**Characteristics**
DECOMP	R-Yield	Simulation of decomposition of the biomass material into single components – gases (H_2, O_2, N_2, CO_2, CH_4, steam), char (solid carbon) and ash.
CHARSEP	Sep2	Separation of ash and char.
COMB	RStoic	Combustion of solid carbon material – 1000°C
NSCL	RStoic	Generation of NH_3, H_2S and HCl pollutants
GASIF1	REquil	Process of biomass gasification – Gasification T >800°C
GASIF2	REquil	Adjusts the yield of CH_4, H_2, CO and CO_2 formation [251].
ASHSEP	Sep2	100% ash removal from the flue gas.

Thermal balance between DECOMP, COMB, NSCL, GASIF1, and GASIF2 blocks was ensured adjusting the fraction of char sent to the combustion unit. Biomass entered the unit as-received (1 bar, 25°C). Air sent to the combustor was heated at 450°C. Similarly, water was vaporized and heated to 450°C before entering the gasifier. The gasifier operated at the 800°C. The combustor operated 55°C over the gasification temperature [251]. The required H_2/CO value of 1.9 was reached at the inlet of the FT reactor after syngas generation and clean-up, adjusting the steam-to-biomass ratio (SBR). Steam feed was modified accordingly. The SBR value was expressed considering the moisture content of the biomass (eq.(3.42)).

$$SBR = \frac{\dot{m}_{Biom,Moisture,in} + \dot{m}_{Steam,in}}{\dot{m}_{Biom,dry,in}} \tag{3.42}$$

The model used PR-BM EoS for the gas processing units and RKS-BM EoS for the Fischer-Tropsch. Lastly, biomass properties were expressed with DCOALIGT and HCOALGEN models.

Biomass material

Digestate composition was expressed with both the ultimate and proximate analyses (Table 21) for digestate [65].

Table 21. Ultimate and proximate analyses of digestate.

Ultimate	Digestate		Proximate	Digestate	
C	*35.2*	*wt% dry*	*Ash*	*32*	*wt% dry*
H	*4.00*	*wt% dry*	*Volatile matter*	*55*	*wt% dry*
N	*3.07*	*wt% dry*	*Fixed carbon*	*13*	*wt% dry*
O	*24.6*	*wt% dry*	*Moisture*	*9.9*	*wt% a.r.*
S	*0.87*	*wt% dry*			
Cl	*0.10*	*wt% dry*			
LHV	*12.7*	*MJ/kg*			

Digestate was intended as a by-product of the process of anaerobic digestion of mixed MSW, industrial waste, and sewage sludge. This is similar to the digester existing at the industrial park Infraserv Höchst (Frankfurt, Germany) – partner of the ICO2CHEM project – which yields about 1 ton_{CO2}/h after upgrading of biogas [216]. Such a value agrees with the first process concept (biogas-to-FT), which outputs about 1 t_{CO2}/h. Hence, based on the carbon dioxide flow rate, the amount of digestate leaving the digester was evaluated (eq.(3.43)-eq.(3.46)) [252]. It was assumed a biogas synthesis x_{bio} of 0.85 m^3/kg_{dry}, 60%-mol of CH_4 in the biogas, and a mass conversion of digestate x_{mass} of 65%. The mass flow rate of dry digestate resulted in 881 kg/h (3.11 MW_{th}).

$$\dot{V}_{bio} = \left(\dot{m}_{CO_2}/\rho_{CO_2}\right) \cdot \left(1 - x_{CH_4}\right)^{-1} \tag{3.43}$$

$$\dot{m}_{conv} = \dot{V}_{bio}/x_{bio} \tag{3.44}$$

$$\dot{m}_{in,d} = \dot{m}_{conv}/x_{mass} \tag{3.45}$$

$$\dot{m}_{out,d} = \dot{m}_{in,d} - \dot{m}_{conv} \tag{3.46}$$

Model comparison

The gasification model was validated against the one proposed by Doherty et al. [251], before process optimization for the FT feed. In the validation step, a lignocellulosic biomass whose composition is available at [251] was employed. The same process parameters as Doherty et al. were considered (i.e., wood biomass, 850°C gasification temperature, atmospheric pressure, 450°C feed of air and steam, SBR 0.75). The syngas composition results were compared also with the ones of the Güssing plant, in Austria [253] (Table 22). The lower heating value of the syngas was evaluated according to Fernandez-Lopez et al. [254] formulation:

$$LHV\ \left[{}^{MJ}/_{m^3}\right] = 10.8 \cdot y_{H_2} + 12.6 \cdot y_{CO} + 35.8 \cdot y_{CH_4} \quad (3.47)$$

Where y_{H_2}, y_{CO} and y_{CH_4} are the yield of H_2, CO and CH_4, respectively.

Table 22. Comparison of the molar composition of the syngas leaving the gasification unit.

Component	Model	**Doherty et al.** [251]	**Güssing Plant** [253]
H_2	46.4%	45.8%	45.8%
CO	20.7%	21.6%	21.6%
CO_2	20.2%	20.2%	21.2%
CH_4	11.0%	11.0%	10.0%
H_2S	70 ppm	66 ppm	21.5-170 ppm
NH_3	1600 ppm	1510 ppm	1100-1700 ppm
HCl	158 ppm	150 ppm	100 ppm
LHV	11.6 MJ/m^3	11.3 MJ/m^3	-

The results provided in Table 22 showed great agreement with literature data. Hence, digestate was utilized and the gasifier was connected to the Fischer-Tropsch unit, including intermediate biogas conditioning.

3.4.3 Syngas conditioning

The syngas was fed to a conditioning unit for the impurities elimination. In this regard, Kim et al. [117] reported the poisoning tolerance of FT catalysts: sulphur-based and NH_3 compounds below 1 ppm_{vol}, halogens and alkaline metals at levels lower than 10 ppb_{vol}, and organic compounds below the drew point.

To do so, different solutions were revised from literature and reported in Table 23. In the present work, six devices were employed for the conditioning step. Dust and ashes were eliminated via cyclones. NH_3 and HCl were eliminated with the use of a water scrubber. H_2S compounds were removed in a Venturi scrubber, fed with a water-NaOH solution [255]. Guard beds are inserted for further H_2S and HCl removal. Tars formation was not modelled. However, a tar catalytic reactor (fed with olivine) was considered for further economic evaluations. Finally, a PSA removed the CO_2 generated during gasification. For H_2S and CO_2 removal, the Rectisol or Selexol technologies are generally employed. However, these technologies are utilized for large scale biomass applications, with high complexity and capital costs [256], whereas the present model processes a smaller amount of raw syngas.

Table 23. Syngas conditioning compared against several literature works employing the gasification of biomass material. Cy cyclones, CF ceramic filter, BF bag filters, MES methyl ester scrubbing, WS water scrubbing, PWS pressurised water scrubbing, SB sand bed, SR steam reforming, CC catalytic cracker, RF oxygen/air reformer, AS amine scrubbing, DA dry adsorption, GDC gravity dust collector, PSA pressure swing adsorption, GB guard beds. [1]Electric power output from ICE.

Ref.		Size [MW_{th}]	Feedstock	Dust/Ash	Tars	NH_3	HCl	H_2S	CO_2
[257]	*FTS*	*100*	*Wood*	*Cy + BF*	*CC*	*VS*	*VS*	*VS+GB*	-
[258]	*FTS*	*400*	*Wood*	*Cy + BF*	*CC*	*WS*	*WS*	*GB*	*Selexol*
[206]	*FTS*	*4.8*	*Wood*	*CF*	*CC*	*DA*	*DA*	*DA+BG*	-
[259]	*FTS*	*350*	*Corn stover*	*Cy + WS*	*WS*	*WS*	*WS*	*AS + GB*	*AS*
[260]	*EtOH*	*350*	*Wood*	*Cy*	*CC*	*VS*	*VS*	-	-
[261]	*EtOH*	*150*	*Switchgrass*	*Cy + WS*	*SR*	*SR + WS + PSA*	*WS*	*AS*	*PSA*
[262]	*ICE*	*100*[1]	*Wood chips*	*Cy + BF*	*CC+WS*	*CC+WS*	*WS*	-	-
[263]	*FTS*	*100*	*Forest residues*	*CF*	*RF*	-	-	*MeOH*	*MeOH*
[264]	*FTS*	*393*	*Rice straw*	*SB*	*SR*	-	-	-	-
[117]	*FTS*	*0.2*	*Pine wood*	*Cy + GDC +BF+WS*	*WS*	*WS*	*WS*	*MeOH*	*MeOH*
[265]	*ICE*	*400*	*Wood*	-	-	-	-	*AS*	-
[266]	*FTS*	*750*	*Pine wood*	-	*WS*	*WS*	*WS*	*Selexol*	*Selexol*
[256]	*FTS*	*100*	*Wood Straw*	*Cy + BF*	*RF*	*RF+WS*	-	*DA + GB*	-
[267]	*SNG*	*13*	*Wood chips*	*Cy + BF*	*MES*	*WS*	*WS*	*WS*	*PWS*
This work	*FTS*	*3.1*	*Digestate*	*Cy*	*CC+WS*	*WS*	*WS+VS*	*VS+GB*	*PSA*

Additionally, the following hypotheses were considered:

- The tar cracker employed olivine [262].
- Only the steam reforming reaction took place in the tar cracker for CH_4.
- Interactions between syngas components was neglected.
- The removal efficiency of ammonia and hydrogen chloride of the water scrubber device was considered to be 100% [256,262].
- Syngas left the water scrubber at 40°C. Additionally, no sulphur compounds or carbon dioxide was removed by the WS [267].
- H_2S compound reacted with NaOH in the Venturi scrubber, with 10% excess NaOH in the exiting stream. Additionally, H_2S is completely removed by this device coupled with zinc oxide guard beds [257].
- 100% of Na_2S and unreacted NaOH was retrieved [257].
- CO_2 was not removed by the Venturi scrubber.
- The PSA had a CO_2 removal efficiency of 95%, operating at 6.7 bar [203].
- A pressure drop of 0.45 bar was considered at the PSA system, with an energy consumption of 0.15 kWh/kg_{CO2} [268].

Similar to the other carbon conversion routes, the Fischer-Tropsch products generation is described by the kinetic model derived in Chapter 2.

3.5 Energy integration

Energy integration in the studied process schemes was assessed with the use of the pinch analysis methodology. The pinch analysis methodology aims at reducing the external energy demand of the production process, evaluating the minimum energy consumption and the optimized heat recovery scheme [269]. The methodology allows identifying possible heat exchanges between the cold streams (i.e., heat sinks) and the hot streams (i.e., heat sources) to obtain an optimal energy integration solution. Within this methodology, process data are represented as energy flows as a function of the heat load against the temperature. These data are cumulated and combined for all the streams in the plant to output composite curves, one for all cold flows and one for all hot flows, and a global grand composite curve comprising all the plant streams. A minimum temperature difference value between the composite curves must be specified (usually $\Delta T_{min} \geq$ 10-20°C to ensure heat transfer between hot and cold fluids). The point of minimum distance between the hot and cold composite curves with respect to the temperature axis represents the temperature of pinch point (Figure 35). Heat can be exchanged from higher to lower temperature fluids within the process, where a portion of the hot composite is above the cold composite curve. The portion of the cold composite curve not covered by the hot composite one provides the minimum amount of heat that must be supplied to the plant from the outside. Similarly, the unmatched hot composite curve represents the minimum cold load required by the system to cool down the process fluids.

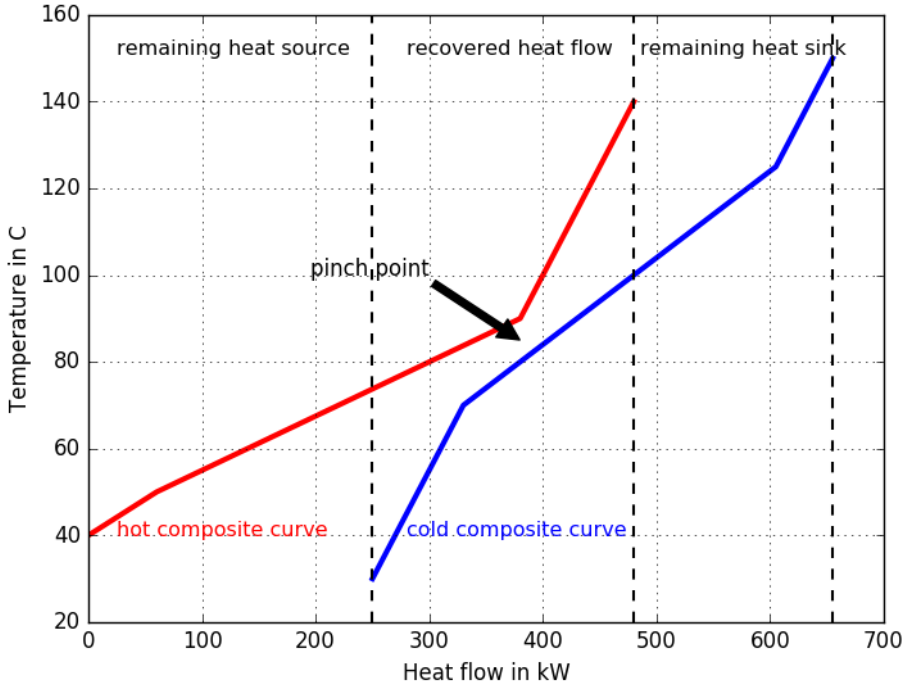

Figure 35. Example of the typical pinch analysis composite curves [270].

3.6 Key Performance Indicators

For each of the process model analysed, different key performance indicators (KPIs) were evaluated to determine the optimal configuration and most suitable non-fossil carbon feedstock when coupled with a Fischer-Tropsch reactor.

Firstly, the conversion of carbon dioxide into Fischer-Tropsch compounds was evaluated (this KPI was neglected for the biomass process route) accordingly to the following formulation:

$$\eta_{CO_2} = \frac{\left[\left(\dot{n}_{CO_2 Feedstock_{in}}\right) - \left(\dot{n}_{CO_2 Feedstock_{out}} + \dot{n}_{CO_2 EXH_{out}}\right)\right]}{\dot{n}_{CO_2 Feedstock_{in}}} \tag{3.48}$$

$\dot{n}_{CO2,Feedstock,in}$ represents the flow rate on molar basis of carbon dioxide entering the plant with biogas or air. Additionally, both the CO_2 leaving the system as non-captured material or the one in exhaust gases is included ($\dot{n}_{CO2,Feedstock,out}$ and $\dot{n}_{CO2,EXH,out}$, respectively).

Secondly, the conversion of carbon material was evaluated and compared for the different processes:

$$\eta_C = \frac{\left[\left(\dot{n}_{C_{Feedstock_{in}}} + \dot{n}_{C_{Extra_{in}}}\right) - \left(\dot{n}_{C_{Feedstock_{out}}} + \dot{n}_{C_{EXH_{out}}}\right)\right]}{\dot{n}_{C_{Feedstock_{in}}} + \dot{n}_{C_{Extra_{in}}}} \tag{3.49}$$

Specifically, the carbon content of the feedstock was evaluated for biogas (CO_2 and CH_4), biomass, and the air. Moreover, additional carbon material entering the plant was included ($\dot{n}_{C,Extra,in}$). This value corresponded to the natural gas flow of the DAC unit. Considering the biomass process route, $\dot{n}_{C,Exh,out}$ accounted for the carbon material leaving the plant through the PSA, the gas turbine flue gases, and the combustor of the FT off-gas.

Moreover, the global plant efficiency was evaluated for each process model as follows:

$$\eta_{Gl_{biogas}} = \frac{\dot{n}_{CH_4} \cdot LHV_{CH_4} + \sum \dot{n}_{FT_{liq}} \cdot LHV_{FT_{liq}}}{W_{el_{in}} + Q_{th_{in}} + \dot{n}_{Biogas} \cdot LHV_{Biogas}} \tag{3.50}$$

$$\eta_{Gl_{DAC}} = \frac{\sum \dot{n}_{FT_{liq}} \cdot LHV_{FT_{liq}}}{W_{el_{in}} + Q_{th_{in}} + \dot{n}_{NG} \cdot LHV_{NG}} \tag{3.51}$$

$$\eta_{Gl_{biomass}} = \frac{W_{el_{out}} + \sum \dot{n}_{FT_{liq}} \cdot LHV_{FT_{liq}}}{W_{el_{in}} + Q_{th_{in}} + \dot{n}_{biom} \cdot LHV_{biom}} \tag{3.52}$$

In all cases the efficiency was evaluated considering naphtha, middle distillates, and waxes flow rates. Moreover, in the biomass route the power output

was included only for process configuration DIG.A (i.e., the one including the gas turbine for electricity generation). Finally, in the DAC route, the term referred to natural gas was included only for the process configuration DAC.1.

Lastly, the specific energy consumption of the systems was evaluated over the net production of the waxes fraction.

$$E_{SP_{wax}}\left[\frac{\text{kWh}}{\text{kg}_{\text{wax}}}\right] = \frac{Power_{net_{in}}}{\dot{m}_{wax_{out}}} \tag{3.53}$$

In the evaluation of the global plant efficiency and the specific energy consumption, the net thermal power required by the system corresponded to the one obtained after the implementation of the pinch analysis methodology.

3.7 Economic methodology

The economic analysis included both capital investment costs (CAPEX) and operational system costs (OPEX). All the costs were referred to the year 2019 by means of the Chemical Engineering Plant Cost Index (CEPCI). Moreover, operations were assumed at the site of production of the non-fossil carbon feedstock (i.e., transportation costs were excluded for biogas and biomass. DAC air was directly connected to the FT).

3.7.1 Capital investment costs

CAPEX accounted for both direct and indirect costs evaluation. Direct costs considered equipment costs estimated by scaling exponent method. Indirect ones included installation, contingencies, site preparation, commissioning costs, plant engineering.

$$TIC_{inv} = \left[\sum_i C_{PI,i}\right] \cdot \left(1 + f_{building}\right) \cdot \left(1 + f_{cont} + f_{eng}\right) \cdot \left(1 + f_{dev} + f_{com}\right) \tag{3.54}$$

$$C_{PI} = \text{C}_{\text{ref,i}}\left(\frac{S_i}{S_{ref,i}}\right)^{sf}\left(\frac{CEPCI_{2019}}{CEPCI_{ref,i}}\right) \tag{3.55}$$

S and S_{ref} are the model and reference size of the i-th component, C and C_{ref} the capital cost of the i-th component. *sf* is the scaling factor. Factors for the cost of building f_{build}, cost of engineering f_{eng} and cost of commissioning f_{com} corresponded to 0.1, contingency cost factor f_{cont} to 0.2, and project development and licenses costs factor f_{dev} was 0.03 [205]. An uncertainty value of ±30% for capital investment costs for chemical plants was assumed [271].

Fischer-Tropsch reactor

For the Fischer-Tropsch reactor technology, a unitary value based on the exchanged thermal power determined by the FT synthesis was utilized, as proposed by Decker et al. [75], with a value of 530 €/kW_{th}. Costs related to the FT technology of the ICO2CHEM are not yet disclosed.

Alkaline and SOC electrolysers

For the alkaline electrolyser, the cost was referred to its nominal power (expressed in kW_{el}) with a function fitting the data available from the work of Proost et al. [272], which included the stack, the power converters, the gas purification unit, the water purification system, and the water recirculation pump (eq.(3.56)). Similarly, a unitary cost over the absorbed electric power was included for the SOEC device, with data fitted from the Store&Go H2020 project [273] (eq.(3.57)):

$$C_{inv_{Alk}}\left[{}^{€}/_{kW}\right] = 1437 \cdot {P_{Alk}}^{-0.095} \tag{3.56}$$

$$C_{inv_{SOEC}}\left[{}^{€}/_{kW}\right] = 2725 \cdot {P_{SOEC}}^{-0.193} \tag{3.57}$$

Biogas upgrading technology

For the biogas upgrading technology, cost curves were extrapolated from the data available through the work of Bauer et al. [274], resulting in a cost curve accounting for the absorber and stripper columns, CO_2 collector condenser, intercooler heat exchanger, stripping reboiler, and expressed as:

$$C_{inv_{Biog}}\left[\frac{€}{Nm^3_{biog}/h}\right] = 252.7 \cdot 10^3 \cdot Flow_{biog.}^{-0.095} \tag{3.58}$$

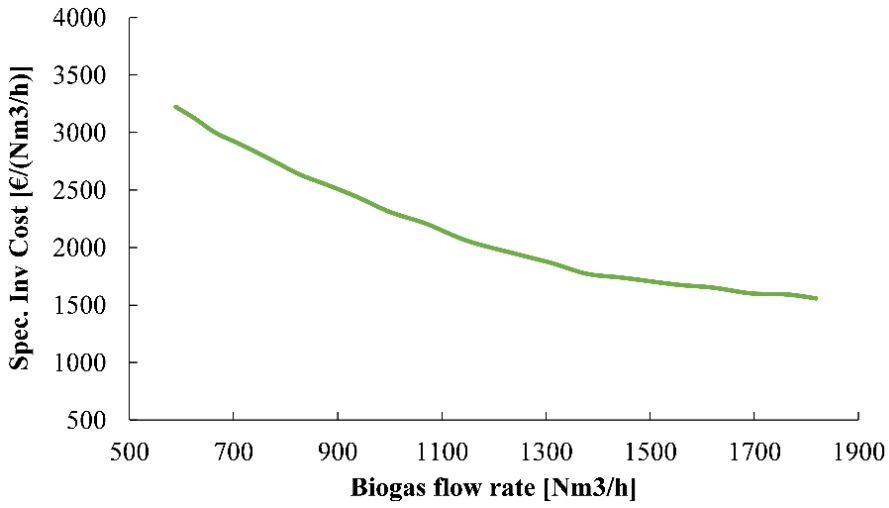

Figure 36. Evolution of the cost function for the biogas upgrading unit utilizing the amine scrubbing technology.

Direct air capture unit

For the DAC technology, the capital cost referred to the unit as a single component (i.e., accounting for a single cost value for the entire capture system). More in detail, a unitary capital cost of 733 €/(t_{CO2} y) was considered for the configurations DAC.1, DAC.2, and DAC.3, including a gas turbine unit [212]. A value of 562 €/(t_{CO2} y) was assumed for the electrified version of the DAC of case DAC.4, and of 549 €/(t_{CO2} y) for the configuration DAC.5 where no gas turbine was included [68]. Moreover, McQueen et al. [275] stated that modular DAC units can be expected to follow a linear scaling law, with the economy of scale factor approaching the unity. Indeed, McQueen et al. utilized a solid sorbet DAC modular unit with similarities with low-temperature DAC systems [68]. Contrarywise, this work referred to liquid solvent DAC modules related to Carbon Engineering one. In this regard, Keith et al. [212] stated that this DAC unit presents both modular component (i.e., air contactor, pellet reactor) and large components (i.e., calciner) that are affected by economy of scale. Hence, a scaling factor for the DAC unit of 0.8 was assumed.

Other components

Other components capital investment costs were expressed as follows.

Table 24. Equipment costs for the CAPEX evaluation.

Equipment	Base cost [k€]	Base size		sf	Ref. year	Ref.
Syngas compr.	490	413	kW_{el}	0.67	2014	[81]
FT Separation	64620	13.25	m^3/s	0.70	2015	[266]
DFBG	5800	500	ton/day	0.60	2010	[260]
Cyclone	50.0	1	m3/s	0.70	2014	[81]
Gas turbine	8470	25	MWe	0.70	2014	[276]
Heat Exchanger	130	150	kW	0.78	2015	[200]
Guard bed	20.0	8	m^3/s	1.00	2014	[81]
Water pump	100	10	m^3/s	0.36	2014	[81]
Wet scrubber	3000	12	m^3/s	0.70	2008	[277]
Burner	1970	20	MW_{th}	0.8	2014	[204]
RWGS	32000	1032	t/day	0.65	2014	[278]
Venturi scrubber	4090	9	m^3/s	0.70	2002	[255]
Tar cracker	3600	34.2	m^3/s	0.70	2002	[258]
PSA	28.0	17.07	kmol/h	0.60	2007	[279]

3.7.2 Operating costs

Total operating costs accounted for cost of operation (direct and indirect, $C_{op,d}$ and $C_{op,i}$), feedstock supplies (C_F), and maintenance (C_{maint}). They were expressed according to the following equation:

$$C_{OP} = C_F + C_{op,d} + C_{op,i} + C_{maint} \quad (3.59)$$

Transportation costs were neglected, assuming installing the plant at location of the biomass and biogas production. Other variable costs considered the disposal of poisoning material, polluted water, fresh water, catalysts, electricity cost, and the sale of the different FT fractions and by-products (i.e., heat and oxygen).

Table 25. Operative costs. [1]37.5 h/(week*operator) 8-hours shifts.

Element	Value		Ref.
Ash disposal	35.9	€/ton	[205]
Biomass (digestate)	30	€/ton	[63,280]
Biogas	50 / 44.3 (DE / IT)	€/MWh	[281–283]
Electric energy price	Varied	€/MWh	[284,285]
NaOH cost	400	€/ton	[286]
Wastewater	2.50	€/m^3	[81]
Demi water	2.00	€/m^3	[81]
Labour[1]	75000	€/y/op	-
Administration & services	1%	of TIC	[205]
Maintenance	2%	of TIC	[287]
Insurance & taxes	2%	of TIC	[75]
Naphtha	0.31	€/l	[205]
Middle Distillates	0.60	€/l	[201]
Oxygen	0.15	€/kg	[288,289]
Residual heat	65.0	€/MWh	[201]
Steam	25.7	€/ton	[81]
Olivine	155.2	€/ton	[260]
RWGS/FTS catalyst replac. (every 3-years)	1%	of TIC	[271]

For the DAC unit, an O&M value of 3.70% was included [68]. Additionally, for the alkaline electrolyser it was assumed a replacement every 10 years. A dependency over the device size was considered [290]:

$$Alk_{Repl.}\left[{}^{€}/_{kw}\right] = \frac{2}{3} 0.4\ Alk_{Capex} \quad (3.60)$$

For the SOEC device, the replacement cost was assumed every 2 years, with a value corresponding to 20% of its initial investment cost [205].

Moreover, it was assumed the availability of statal incentives for biomethane grid injection for biogas routes, with reference to German and Italian policies. In the first case, it was assumed a biomethane sale price of 31.6 €/kWh with 20 years sale credits for 61.6 €/MWh [281,282,291]. In the second case, it was assumed a

sale price of bioCH_4 of 20.9 €/kWh, with credits of 62.7 €/MWh at the first 10 years and 0.305 €/m^3 for subsequent years of plant operations [281,283,292].

3.7.3 Cost of products

25 years of operations were considered. Moreover, it was assumed a repayment period of 10 years (N_{rt}) for the borrow capital investment [205]. Accordingly, the annual expenses for capital payback were accounted for with the annuity method. A nominal discount rate (r_d) of 7.5% was assumed. Finally, the production cost of the FT wax fraction was evaluated considering revenues from profitable material, with a plant capacity factor of 8400 y/h [201].

$$CAPEX_{ANN} = TIC_{inv} * \frac{r_d * (1 + r_d)^{N_{rt}}}{[(1 + r_d)^{N_{rt}}] - 1} \tag{3.61}$$

$$Wax\ production\ cost\ \left[{}^{€}/_{kg_{wax}}\right] = \frac{CAPEX_{ANN} + C_{OP} - Revenues}{FT\ Wax\ Production\ Rate} \tag{3.62}$$

Chapter 4

Process modelling – part II

The present chapter provides the results in terms of mass and energy balances and the economic outcomes obtained for each process configuration described in Chapter 3. Specifically, the thermodynamic analysis is provided for each plant layout, with different sensitivity analyses on the operating parameters affecting the Fischer-Tropsch synthesis. Moreover, a discussion on the economic results is given. Finally, the techno-economic performances of all the modelled plants are compared together. Some of the findings reported in this chapter have been previously published in [28,195].

4.1 Biogas conversion

For the conversion of biogas to FT products, four scenarios were investigated, with either high- or low-pressure operations of the two different syngas generation units (i.e., the RWGS and SOEC units).

4.1.1 Carbon capture unit

The section of carbon capture uses MEA-based chemical scrubbing. This plant section allows capturing about 1 ton/h of CO_2 to feed downstream components, with a stream purity of 98%. The recovered biomethane corresponds to 728 kg/h, with a Wobbe index of 50.6 MJ/Sm^3 and an HHV of 37.9 MJ/Sm^3, suitable for gas grid injection [293].

During the capture process, about 4.75 GJ_{th}/ton_{CO2} are consumed. This thermal input is required by the stripper column to release the captured CO_2 (the average value reported in literature is between 3.5-5 GJ/ton_{CO2} [223,294,295]). Additionally, the cross-heat exchanger recovers 861 kW_{th} from the hot stream leaving the stripping column to the cold entering the stripping unit.

Table 26. Mass and energy balance information of the MEA-based biogas upgrading unit.

Element			
	Mass flow	**Composition [%-mol]**	
Biogas Inlet	1745 kg/h	CH_4: CO_2: N_2 = 65: 34: 1	
Captured CO_2	1003 kg/h	CH_4: CO_2: H_2O = 0.02: 97.96: 2.03	
CH_4 from biogas upgrading	728 kg/h	CH_4: CO_2: H_2O: N_2 = 98.47: 0.02: 0.06: 1.51	
- Wobbe Index	*50.56 MJ/Sm³*		
- HHV	*37.88 MJ/Sm³*		
Make-up flow	1227 kg/h	H_2O: MEA = 97.5: 2.5	
	Energy flow		
Stripper duty (specific)	4.75 GJ_{th}/ton_{CO2}		
Stripper reboiler	1313.2 kW_{th}	Biogas blower	7.44 kW_{el}
Stripper condenser	-227.1 kW_{th}	Ciruclating pump	0.69 kW_{el}
Cross-HX	860.6 kW_{th}	CH_4 compressor (to 10 bar)	103.3 kW_{el}

4.1.2 Mass balances of the simulated processes

The mass balances obtained for the different processes are provided in Table 27. These are provided considering a recirculation ratio of the off-gas of 90% (i.e., 90% of the FT off-gas are sent back to the syngas generation units inlet).

Considering the production of FT compounds, operating the syngas units at low pressure provides a much higher synthesis of useful products compared to high-pressure solutions. Configuration RWGS.LP reaches the highest throughput of synthetic material with 258.8 kg/h, followed by configuration SOEC.LP with just a slightly lower production at 254.1 kg/h (Figure 37). Hence, the two configurations can be considered comparable. Contrarywise, under high-pressure operations, the configuration employing the SOEC device is more effective in converting the carbon dioxide into Fischer-Tropsch material, given the equilibrium-constrained conversion of CO_2 within the RWGS reactor [234]. Lastly, only configuration RWGS.HP requires feeding additional steam to avoid solid carbon deposits in the RWGS unit (840.5 kg/h).

Table 27. Mass balance results for the biogas-to-FT processes. Data are reported with 90% recirculation rate of the off-gas to the syngas generation units.

Mass flow rate [kg/h]	**RWGS.LP**	**RWGS.HP**	**SOEC.LP**	**SOEC.HP**
Biogas Inlet	1745	1745	1745	1745
Captured CO_2	1003	1003	1003	1003
CH_4 from biogas upgrading	728	728	728	728
H_2O inlet feed	2002.0	1858.1	1274.9	2125.4
Steam to avoid C-deposition	-	840.5	-	-
Total Condensed Water	1103.1	1851.8	1185.8	2045.3
Combustion Air	2349.0	4594.2	2437.0	4043.9
Exhaust Gas	2458.7	4859.9	2522.0	4325.5
Syncrude	258.8	184.6	254.1	185.2
- Naphtha C_{5-11}	*79.5*	*52.8*	*77.5*	*58.2*
- Middle distillate C_{11-20}	*93.6*	*72.5*	*93.5*	*67.6*
- Waxes C_{20+}	*85.7*	*59.3*	*83.1*	*59.4*

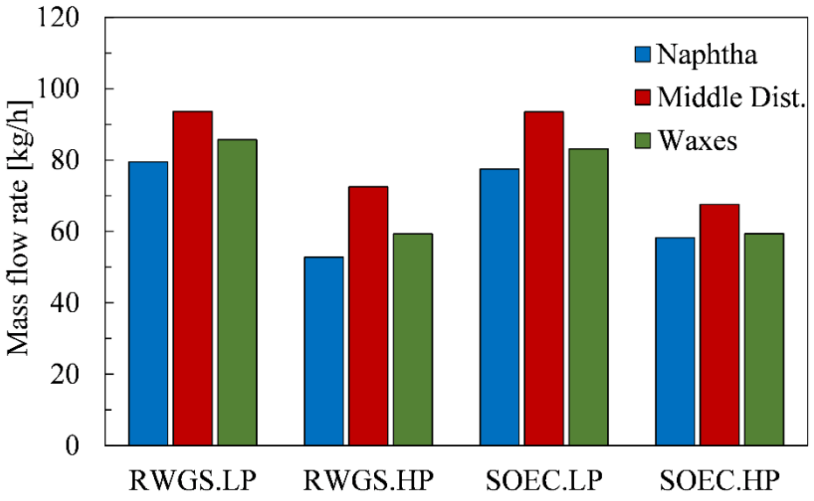

Figure 37. Mass flow rates of the Biogas-to-FT processes.

4.1.3 Energy balances of the simulated processes

The energy balances results are provided in Table 28, accounting for a recirculation of the FT off-gas of 90% to the RWGS or SOEC.

With respect to the electric demand of the plants, the electrolysis units are the most energy-intensive components regardless of the configuration. The energy consumption of these devices corresponds to 6.7 MW_{el}, 6.2 MW_{el}, 5.3 MW_{el}, 4.7 MW_{el} for RWGS.LP, RWGS.HP, SOEC.LP, and SOEC.HP, respectively. At high-pressure operations, the syngas generation units have a lower CO_2-to-CO conversion efficiency. Consequently, a lower amount of hydrogen is needed to reach a constant value of the H_2/CO ratio at the inlet of the FT reactor. Additionally, RWGS and SOEC low-pressure operations determine a rise in the compression needs for the material entering in the FT reactor. For RWGS.LP, the compression of the syngas required 537.1 kW_{el}, for SOEC.LP 613.1 kW_{el}.

Considering the thermal balance, the biogas upgrading unit requires 1347 kW_{th} to extract the carbon dioxide from the biogas, corresponding to 24.1% of the thermal needs in case SOEC.LP and to 40.3% for RWGS.LP. Moreover, SOEC.HP is the most energy-intensive configuration. Its elevated thermal demand is due to the high amount of H_2O entering the system (vaporized before undergoing electrochemical conversion in the SOEC). Furthermore, the extra steam needed in RWGS.HP to avoid carbon deposition provides an extra 0.8 MW_{th} thermal demand.

Lastly, considering the energy content of the syncrude, this is directly dependent on the amount synthetized during operations. Hence, the RWGS.LP and SOEC.LP provide the highest energy contents for this flow.

Table 28. Energy balance results for the biogas-to-FT processes. Accounted for with a recirculation of the FT off-gas of 90%. [a]Operating at thermoneutral conditions. [b]1051.4 kW_{el} related to the compression of sweep-air entering the soec.

Energy balance [kW]	**RWGS.LP**	**RWGS.HP**	**SOEC.LP**	**SOEC.HP**
Electric power supply				
Biogas section	111.5	111.5	111.5	111.5
Electrolysis	6698.7	6217.1	5280.9	4742.9
CO_2 compression	-	69.3	-	69.3
H_2/H_2O compression	-	32.2	-	4.8
Syngas compression	537.1	-	613.1	-
Auxiliaries	2.6	9.5	0.8	1051.7[b]
Thermal energy balance				
Biogas section	1346.6	1346.6	1346.6	1346.6
Steam generation	-	836.3	1245.6	2050.9
RWGS / SOEC[a]	1089.7	1296.5	-	-
FT products separation	98.2	71.6	96.7	75.9
Recirculation heating	233.3	617.4	394.3	938.7
Heat exchangers	572.3	907.4	556.4	1181.7
FT reactor	-1436	-1252.9	-1431.9	-1256.1
Coolers	-4298.5	-6338.2	-4822.4	-6786
Chemical energy content				
Biogas Feed	9868.5	9868.5	9868.5	9868.5
FT Products	-3168.6	-2257.9	-3110.5	-2264.1
Biogas Up. CH_4	-9867.3	-9867.3	-9867.3	-9867.3

The thermal demand of the processes can be reduced applying the pinch analysis methodology. As reported in Table 29 and depicted in Figure 38, optimal energy integration allows reducing the thermal input from the outside. The heat demand reduction is higher than 70% for all the configurations, transferring heat from hot to cold fluids. Residual heat can be provided with electric heaters. Remarkably, SOEC.LP reaches the condition where all the thermal needs are sustained with internal heating, thanks to the thermoneutral operations of the SOEC device. Contrarywise, the RWGS reactor is a highly critical component, with the need of supplying a large amount of heat above the pinch point to sustain its endothermic behavior (i.e., 1.1 MW_{th} for RWGS.LP and 1.3 MW_{th} for RWGS.HP). Moreover, it is noteworthy to observe the adequate matching of the FT section with the highly energy-intensive biogas upgrading unit. For all the configurations, exploiting part or all the heat released by the FT reactor (plateau at 228°C for the hot fluids), together with the cooling of the flue gases, allows covering the heat required by the reboiler of the stripper column (plateau at 116°C for the cold fluids). Finally, for the configurations at high pressure, the cooling of the exhaust gas and RWGS products can provide heat for steam generation for the RWGS and SOEC.

Table 29. Effect of the pinch analysis on the heat demand of each configuration (biogas process).

[kW_{th}]	RWGS.LP	RWGS.HP	SOEC.LP	SOEC.HP
Heat Before Pinch Analysis	3340.2	5075.8	3639.2	5593.8
Heat After Pinch Analysis	1000.0	1000.6	0	153.0
Heat Demand Reduction	*-70.1%*	*-80.3%*	*-100%*	*-97.3%*

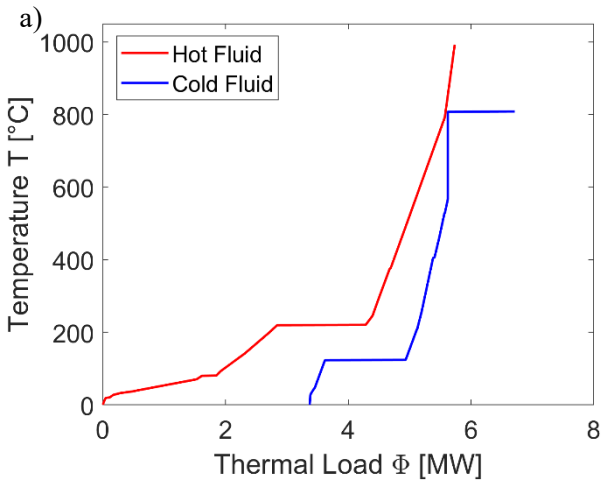

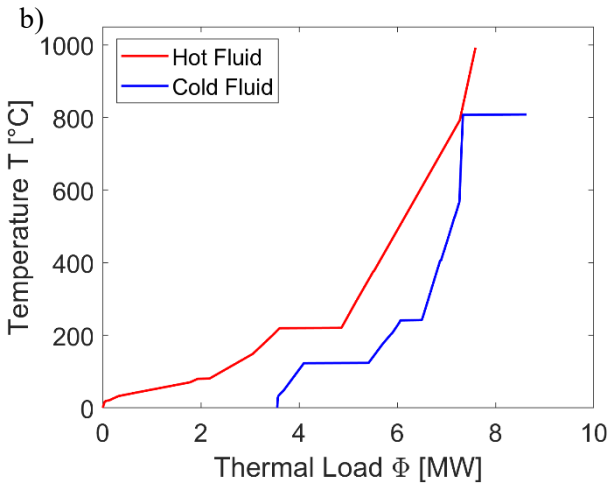

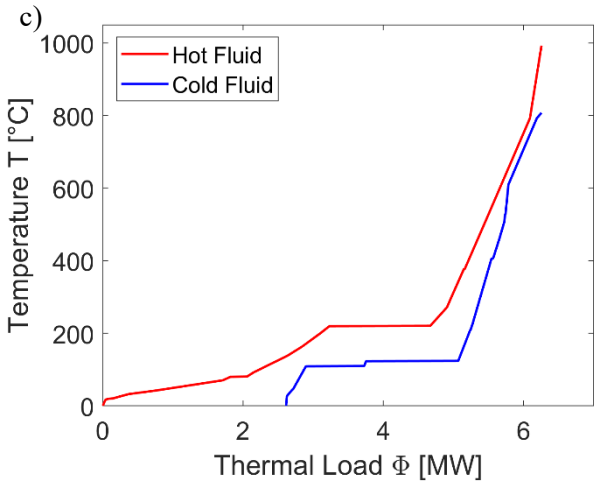

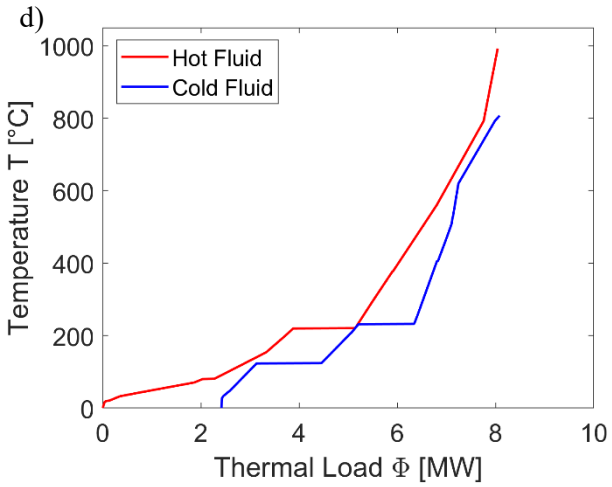

Figure 38. Composite curves the digestate configuration process: a) RWGS.LP; b) RWGS.HP; c) SOEC.LP; d) SOEC.HP.

4.1.4 Key performance indicators

Key performance indicators allow comparing the different processes. The results are listed in Table 30. With respect to energy consumption over the production of wax material, each configuration with the SOEC device reaches a lower value compared to its RWGS counterpart. Moreover, the least energy-intensive solution is SOEC.LP, with 191.0 kWh/kg_{wax}. This configuration is also the one with the highest global efficiency η_{GI} (at 66.5%), thanks to the high output of FT compounds and the net-zero thermal demand derived from the pinch analysis.

The second-best performing configuration is RWGS.LP, penalized by the presence of the RWGS reactor (η_{GI} of 63.4%). However, this configuration has the highest carbon conversion η_C at 27.8%, given a lower amount of CO_2 in the exhaust gas. It is worth mentioning that the low values of η_C for these configurations might be misleading. In fact, the carbon content related to methane entering with biogas leaves the plant with the stream of biomethane. If we were to consider only the η_C related to the carbon entering in the form of CO_2, this value would correspond to η_{CO2}. Lastly, the better production of FT compounds allows reaching considerably higher process efficiencies for the options operating at low pressure of the syngas generators.

Table 30. Key performance indicators of the Biogas-FT processes.

KPI	RWGS.LP	RWGS.HP	SOEC.LP	SOEC.HP
E_{SPwax} [kWh/kg_{wax}]	212.6	291.9	191.0	268.5
η_C	27.8%	20.07%	20.4%	20.14%
η_{CO2}	81.1%	58.4%	79.6%	58.6%
η_{GI}	63.4%	56.7%	66.5%	56.6%

Considering similar applications, Becker et al. [296] reached a plant efficiency of 51%, when coupling a low-T FT reactor to a SOEC operating in co-electrolysis for FT diesel and gasoline production. Similarly, Cinti et al. [214] investigated the conversion of a flow of pure CO_2 into Fischer-Tropsch syncrude connecting an experimentally validated SOEC to the FT reactor. The authors reached a process efficiency of 43.7%. However, no carbon dioxide capture unit was included. Moreover, Vidal Vazquez et al. [72] obtained a CO_2 conversion as high as 94% and a global efficiency of 47% when capturing CO_2 from the air and converting it in a route comprise of a RWGS and an FT reactors.

4.1.5 Effect of process parameters

Effect of the recirculation

As mentioned, the recirculation profile was set to 90%. Such a value allows increasing the conversion of the carbon material regardless of the operating pressure of the syngas generation unit (Table 31).

For the low-pressure processes, if no recirculation were applied, a total of 88.2 kg/h and 105.1 kg/h of syncrude would be produced in RWGS.LP and SOEC.LP configurations. These values are considerably lower than the high recirculation rates counterparts previously presented (Table 28). The slightly higher production in the SOEC.LP case is related to the equilibrium-constrained conversion of CO_2 at the RWGS unit, reaching a maximum value of 63.0%. Contrarywise, the SOEC was operated at a reactant utilization of 75%.

In terms of process efficiency, the lower production of FT compounds is counterbalanced by a lower amount of hydrogen (i.e., smaller electrolysis units), lower thermal demand, and lower compression needs of the syngas compared to the cases at high rates of FT off-gas recirculation. This results in process efficiencies of 64.5% and 67.8% for RWGS.LP and SOEC.LP, comparable with the solution at 90% recirculation rates. Lastly, low recirculation rates mean low CO_2 conversions (27.5% for RWGS.LP and 34.2% for SOEC.LP) (Figure 39).

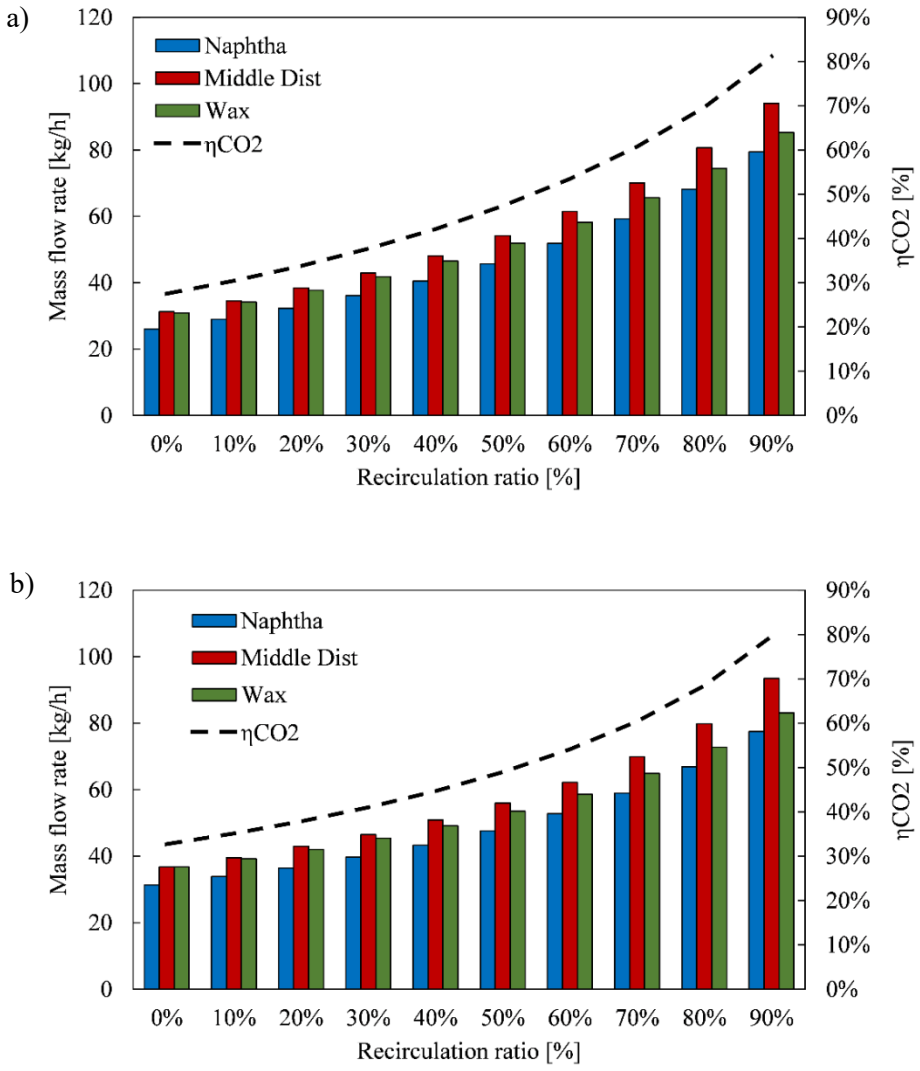

Figure 39. Recirculation effect on the FT syncrude production: a) RWGS option; b) SOEC option.

Similar considerations can be made for the solutions at high pressure of the RWGS and SOEC, with an even lower production of FT material. RWGS.HP would synthetize only 51.6 kg/h of syncrude, against 52.5 kg/h of SOEC.HP. Hence, high recirculation rates are preferable.

Table 31. Mass and energy balances at 0% recirculation rates for the biogas-to-FT processes.

Mass Balance [kg/h]	**RWGS.LP**	**RWGS.HP**	**SOEC.LP**	**SOEC.HP**
Biogas Inlet	1745	1745	1745	1745
Captured CO_2	1003	1003	1003	1003
CH_4 from biogas upgrading	728	728	728	728
H_2O inlet feed	1297.4	1312.6	774.1	786.4
Steam to avoid C-deposition	-	-	-	-
Total Condensed Water	809.0	786.5	761.7	707.9
Combustion Air	5022.1	6539.4	5812.1	7697.0
Exhaust Gas	5549.0	7126.5	6266.3	9060.6
Syncrude	88.2	51.6	105.1	52.5
- Naphtha C_{5-11}	*26.1*	*15.2*	*31.4*	*17.1*
- Middle distillate C_{11-20}	*31.3*	*18.7*	*37.0*	*17.4*
- Waxes C_{20+}	*30.8*	*17.7*	*36.7*	*18.0*
Thermal/Electrical Balance [kW]				
Electricity	319.3	205.4	347.6	1070.3
Electrolysis	4341.1	4391.8	3569.4	3400.5
Heat Needs (Before P.A.)	2432.9	2096.3	2659.5	3005.2
Heat Needs (After P.A.)	0.0	0.0	0.0	0.0
Chemical energy content [kW]				
Biogas Feed	9868.5	9868.5	9868.5	9868.5
FT Products	-1079.3	-631.9	-1285.5	-640.5
Biogas Up. CH_4	-9867.3	-9867.3	-9867.3	-9867.3
Key performance indicators				
E_{SPwax} [kWh/kg_{wax}]	471.7	817.3	375.6	796.6
Total CO_2 Conversion	27.5%	16.1%	34.2%	18.1%
Global Efficiency	64.5%	63.4%	67.8%	60.6%

Effect of pressurized syngas units

As visible from the mass and energy balance results, changing the pressure of the syngas generators impacts the overall plant efficiency and CO_2 conversion into FT material [28]. The main reason is related to the evolution of the chemical reactions inside the RWGS and SOEC. In fact, eq.(3.15) is an equimolar reaction, with no further influence from the pressure. However, eq.(3.16)-eq.(3.17) (i.e., methanation reactions), is shifted towards the products according to the Le Chatelier principle [297].

This behaviour can be seen from the evolution of the yield of CO and CH_4 production (Figure 40). Accordingly, the yield of CO production decreases in favour of a higher generation of CH_4, penalizing the conversion of CO_2. However, CH_4 is an undesired compound for FT synthesis of long chain hydrocarbons. Moreover, for the SOEC device, a further drop of the CO_2 conversion is determined by the reduction in the reactant utilization value needed to prevent coke formation.

Hence, low-pressure operations should be preferred when targeting a higher conversion of carbon dioxide and a reduced production of methane.

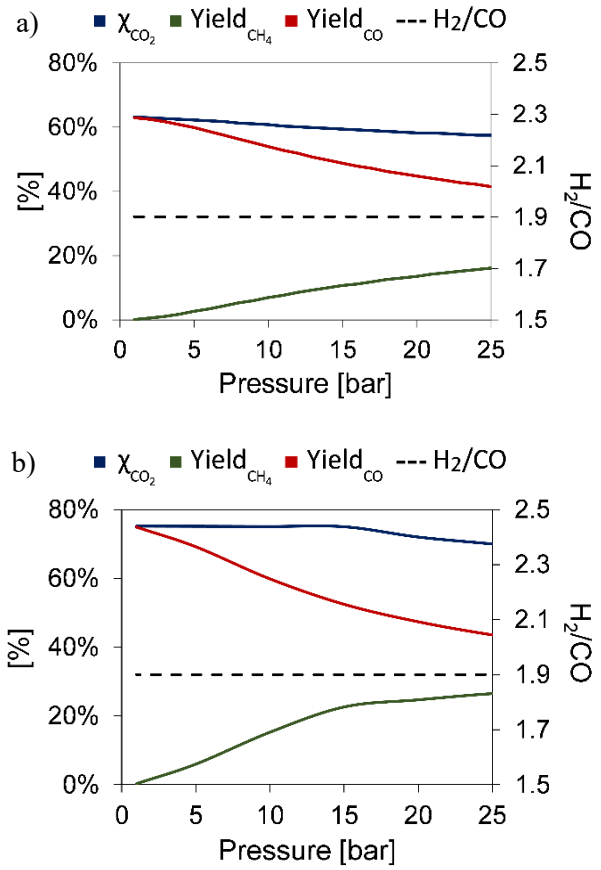

Figure 40. Effect of the pressure over the conversion of CO_2, CO yield, CH_4 yield, and H_2/CO for the biogas-to-FT processes: a) RWGS; b) SOEC [28].

Carbon deposition

Carbon deposition plays an important role in the possible deactivation of the SOEC and RWGS catalysts, consequently reducing their lifetime and conversion efficiencies [234,241]. As such, high recirculation rates and a change in the pressure can favour the cracking of both carbon monoxide and light hydrocarbons dragged in these units with the FT off-gas recirculation, with the Boudouard reaction catalysed by Ni material (present in both the RWGS and SOEC catalysts). To avoid coke formation, steam was added to the RWGS reactor in the case of possible solid C generation. Similarly, for the SOEC the reactants utilization was reduced from its initial value of 75%.

In the case of low-pressure operations, neither the RWGS nor the SOEC devices present any formation of solid carbon based on thermodynamic calculations (Figure 41). From the C-O-H ternary plots it is possible to note that increasing the rates of recirculation (i.e., from 0% to 90%) increases the likelihood of solid carbon deposition. However, even at 90% recycling rate, no modifications are needed for any of the configurations.

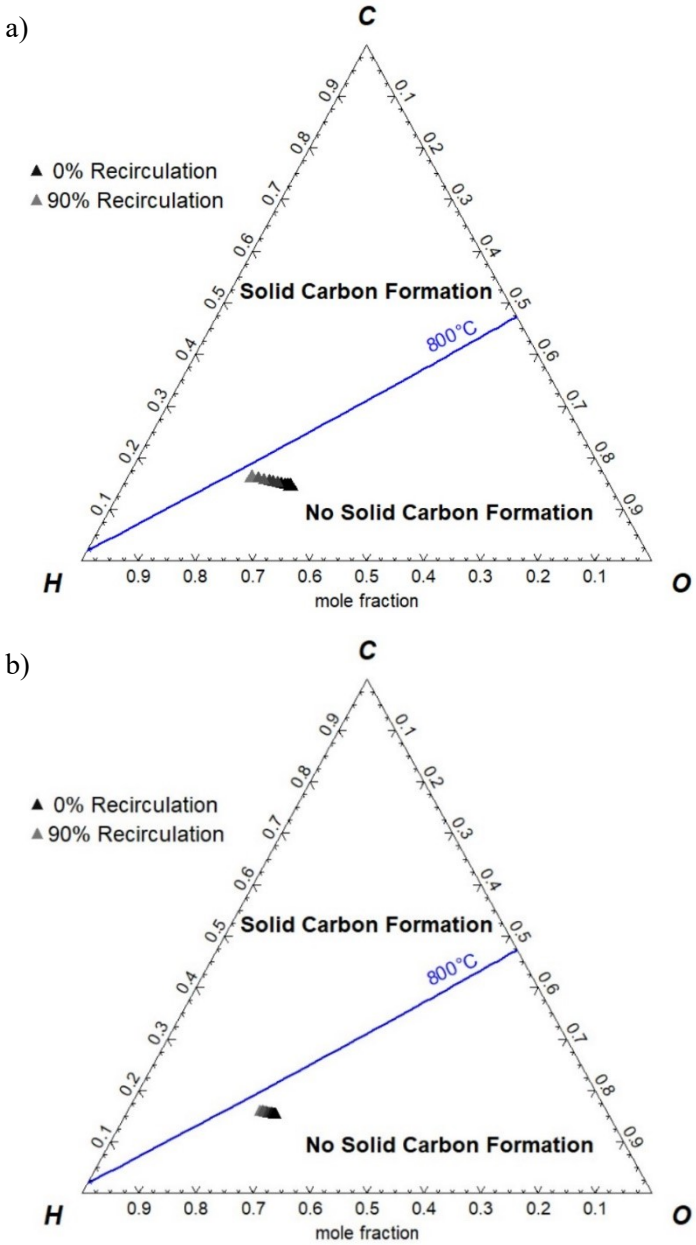

Figure 41. Ternary plots for the coke formation at low-pressure: a) RWGS.LP; b) SOEC.LP [28].

On the contrary, the presence of pressurized RWGS or SOEC provides the need of properly managing coke formation (Figure 42).

In the case of the RWGS, no solid carbon formation is accounted for at 0% recirculation rate. However, when 90% of the FT off-gas are sent back to the RWGS, there exists need of injecting an oxygen carrier. Hence, 840.5 kg/h of steam are required for this configuration. With respect to the SOEC device (Figure 42.b), coke deposition might take place regardless of the recirculation level. Hence, the reactants utilization needs to be reduced at 70% in the case of no recycling of the FT off-gas, and to 40% if 90% recirculation rate is employed.

Even from a carbon formation point of view, the utilization of high-pressure syngas generation units is the least favorable solution.

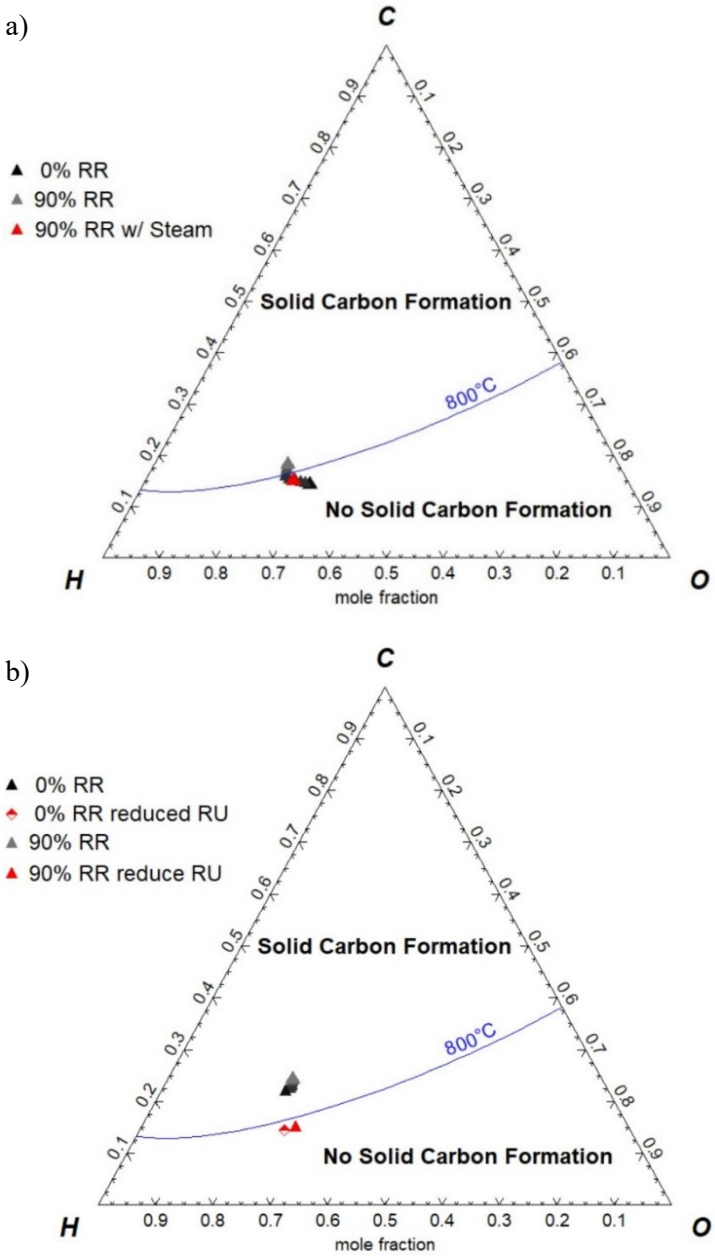

Figure 42. Ternary plots for the coke formation at high-pressure: a) RWGS.HP; b) SOEC.HP [28].

4.1.6 Economic analysis

The economic evaluation results are provided at 90% recirculation rate of the FT off-gas, given the higher FT production and carbon conversion.

Capital costs

The operating costs are presented in Figure 43 and Table 32. The highest total investment cost (TIC) is reached by configuration RWGS.HP at 22.1 M€, while the lowest corresponds to 19.4 M€ of SOEC.HP.

The biogas upgrading section accounts for 3.04 M€, ranging between 13.7% and 15.6% of the capital cost in RWGS.HP and SOEC.HP, respectively.

Moreover, regardless of the pressure level selected, the configurations employing an SOEC device provide a slightly lower capital investment compared to their RWGS counterparts. On the one hand, this can be related to the presence of the SOEC itself. As reported by the Store&Go project consortium [273], the SOEC device shows the highest cost-reduction potential with increasing capacities compared to an alkaline or PEM electrolyser. On the other hand, one less component is present in these plant configurations (i.e., no RWGS reactor needed).

Lastly, only with respect to the compression needs of the system, the CAPEX results show that it would be more cost-effective having a solution where the syngas generation units are operated at high pressure.

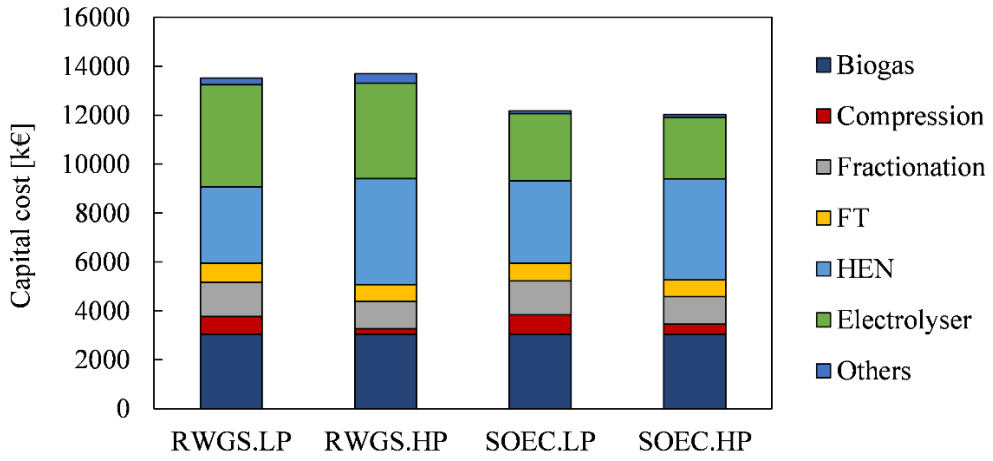

Figure 43. CAPEX breakdown of the Biogas-to-FT processes.

Table 32. CAPEX values for the biogas-to-FT processes.

CAPEX [k€]	RWGS.LP	RWGS.HP	SOEC.LP	SOEC.HP
Electrolysis	4168.5	3896.3	2751.7	2523.6
Biogas section	3038.5	3038.5	3038.5	3038.5
RWGS	190.5	315.8	-	-
FT reactor	777.4	678.3	726.4	680.0
Syngas/CO_2+water compr.	730.5	235.3	798.7	420.6
Thermal integration	3131	4345	3369	4132
FT separation	1399.7	1115.5	1386.5	1126.4
Afterburn combustor	64.4	56.4	56.3	57.8
Auxiliaries	24.2	24.0	53.9	51.6
TIC	21854.6	22145.7	19682.6	19439.4

Operating costs

The OPEX are listed in Table 33, with configuration RWGS.LP being the one with the highest yearly operating expense.

Moreover, the analysis on the OPEX delivers marginally different expenses depending on the assessment location (i.e., Germany or Italy), providing a different cost of labour, cost of biogas purchase, and a different incentive scheme

for the production and grid injection of the recovered biomethane from biogas. Regardless of the plant configuration, the solution accounted for in a German scheme has a slightly higher biogas purchase and labour cost. However, it also provides an overall higher income to the system, provided that the sale of biomethane is more profitable compared to the Italian scheme.

Additionally, under all the configurations, the most impacting elements are the electric-related OPEX, given the high consumption determined by the electrolysers. When accounted at the reference electricity purchase cost of 100 €/MWh_{el}, these range between 5.3 M€/y to 6.9 M€/y.

Lastly, the incomes of the systems are directly dependent on the production of the FT material. Hence, RWGS.LP is the configuration with the greatest inlet cash-flow, while SOEC.HP is the least favourable one.

Table 33. OPEX for the biogas-to-FT processes. aALK replacement every 10 years, SOEC replacement every 2 years.

OPEX [k€/y]	**RWGS.LP**	**RWGS.HP**	**SOEC.LP**	**SOEC.HP**
Biogas cost (DE-scheme)	4173.5	4173.5	4173.5	4173.5
Biogas cost (IT-scheme)	3697.5	3697.5	3697.5	3697.5
Operators (4) (DE-scheme)	332.8	332.8	332.8	332.8
Operators (4) (IT-scheme)	167.1	167.1	167.1	167.1
Demi-water	32.0	45.3	21.4	35.7
Wastewater	23.2	38.9	24.9	43.0
Fresh water	14.6	8.3	5.6	5.8
Maintenance	437.1	442.9	393.7	388.8
Insurance & taxes	437.1	442.9	393.7	388.8
Administration & services	218.6	221.5	196.8	194.4
Electric Opex (@100 €/MWh_{el})	6968.0	6243.5	5263.7	5299.8
Electrolyser replacement[a]	833.7	779.3	550.3	504.7
Catalyst replacem. [k€/3-years]	218.6	221.5	196.8	194.4
Revenues				
Naphtha	350.9	232.2	341.3	256.4
Middle Dist.	591.6	456.8	590.3	425.9
By-products (DE-scheme)	9181.9	9007.8	8763.9	8927.2
- After the year 20	*3852.5*	*3699.0*	*3517.7*	*3682.7*
By-products (IT-scheme)	8369.0	8194.9	7951.0	8114.3
- After the year 10	*5808.2*	*5634.1*	*5390.2*	*5553.5*

Cost of waxes production

The cost of production of the waxes was assessed at the discount rate values of 2.0% (optimistic), 7.50% (realistic), and 12.50% (conservative). The same was evaluated with a variation of the cost of electricity. As reported by IRENA [284], it is possible to assume such a cost depending on the source of production: 41.1 €/MWh for hydropower, 46.3 €/MWh for on-shore wind power, 59.4 €/MWh for

solar PV, 100.4 €/MWh for off-shore wind power, and 158.9 €/MWh for concentrated solar power (CSP).

As depicted in Figure 44, the implementation of these process routes over the German territory seems to be more beneficial compared to their Italian counterparts, having a more favorable financial scheme. In this regard, the sale of the biomethane to the grid allows having a cost-effective wax production route.

Moreover, all the configurations are highly sensible to the cost of electricity. Specifically, RWGS.HP is the one with the greatest electric consumption, which results in a wide range of cost of wax production. With a discount rate of 2%, 7.50%, and 12.50%, respectively, this ranges from 2.81 to 17.72 €/kg_{wax}, from 3.42 to 18.33 €/kg_{wax}, and from 4.04 to 18.95 €/kg_{wax} in the Italian scheme (with the lowest cost obtained if purchasing electricity at 41.1 €/MWh_{el}, and the highest at 160 €/MWh_{el}). In the German production scheme, these costs range from 1.67 to 16.57 €/kg_{wax} at 2% discount rate, from 2.27 to 17.18 €/kg_{wax} at 7.50%, and from 2.89 to 17.8 €/kg_{wax} at 12.50%.

Contrarywise, SOEC.LP configuration is the least affected by a variation in the source of electricity. For the German scheme, the lowest production costs are identified at 0.46 €/kg_{wax}, 0.79 €/kg_{wax}, and 1.21 €/kg_{wax}, at discount rates of 2%, 7.50%, and 12.50%. For the Italian zone, the same costs correspond to 1.54 €/kg_{wax}, 1.70 €/kg_{wax}, and 2.09 €/kg_{wax}.

a)

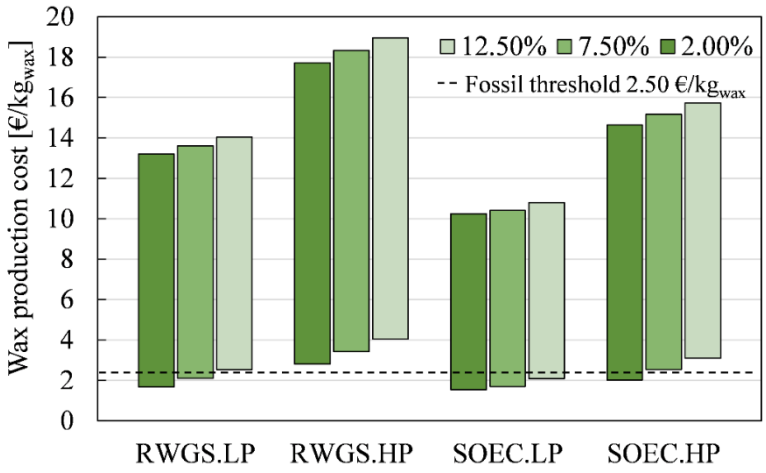

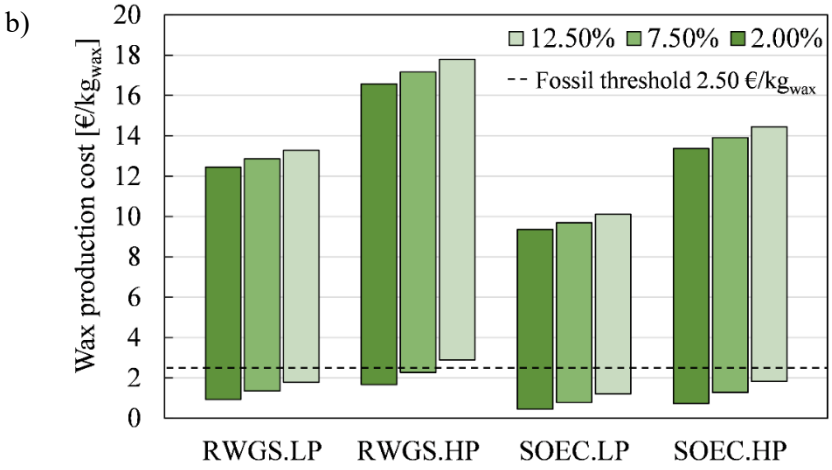

Figure 44. Cost of wax production, depending on the cost of electricity. The low values are obtained with electricity purchase cost of 41 €/MWhel. High values are obtained with electricity purchase cost of 158 €/Mwhel: a) Italian remuneration scheme for biomethane production; b) German scheme for biomethane production.

With respect to the production cost of waxes, it is possible to evaluate the optimal cost of electricity that allows reaching the threshold of wax production from fossil route set at 2.50 €/kg$_{wax}$ [298]. As visible from the data listed in

Table 34, it is of paramount importance to have access to low-price electricity to have a suitable market-entry of these production routes. For instance, in the case of the RWGS.LP configuration, having a middle-range value of the discount factor (i.e., discount factor of 7.50%) requires an electricity purchase cost of 45.9 €/MWh in the Italian case, and of 52.9 €/MWh in the German one. For the SOEC.LP process, the same cost increase to 51.6 €/MWh and 64.9 €/MWh.

Table 34. Preferential cost of electricity in €/MWh needed to reach a wax production cost equal or lower than the upper bound value of fossil route of 2.5 €/kg for the biogas-to-FT processes.

Electricity cost needed to reach a wax cost ≤ 2.5 €/kg$_{wax}$ [€/MWh]	**RWGS.LP**	**RWGS.HP**	**SOEC.LP**	**SOEC.HP**
Italian scheme				
2.00%	50.2	n.a.	55.2	45.9
7.50%	45.9	n.a.	51.6	n.a.
12.50%	n.a.	n.a.	46.8	n.a.
German scheme				
2.00%	57.5	48.0	68.6	57.4
7.50%	52.9	42.5	64.9	53.1
12.50%	48.8	n.a.	57.2	47.5

To produce FT compounds with the process routes, the ICO2CHEM project has the potential to deliver on-field data for the validation of these results, specifically when employing an RWGS reactor to generate the syngas for the downstream FT unit.

4.2 CO_2 from the air conversion

Capturing carbon dioxide from the air provides a valuable solution for synthesizing the Fischer-Tropsch compounds in a carbon-neutral context. Hence, five different process configurations were investigated.

4.2.1 Mass balances of the simulated processes

The mass balance results obtained through process modelling are provided in Table 35.

Considering the DAC section, all configurations present an air inlet flow of 250 kt/h fed to the air contactor unit. Under configurations DAC.1, DAC.2, and DAC.3, the flow entering this component also includes the CO_2 recovered from the gas turbine flue gases in the absorption column. In configurations DAC.4 and DAC.5, only air CO_2 is processed. Finally, the baseline configuration injects natural gas, resulting in an additional carbon flow corresponding to 14.5 ton_C/h.

In terms of Fischer-Tropsch output, the presence of a higher amount of carbon material (i.e., configuration DAC.1) determines the highest FT production, with a corresponding value of waxes of 8.7 t/h. However, this solution has the disadvantage of exploiting fossil hydrocarbons for the generation of synthetic ones. Moreover, high water demand from the electrolyser is required for the H_2 generation, needed in downstream devices of DAC.1.

When substituting the natural gas flow with the FT off-gas, configurations DAC.4 and DAC.5 show a analogous production rate (for the wax fraction). This corresponds to 6.9 and 6.8 t/h, individually, lower than the baseline configuration but higher than cases DAC.2 and DAC.3.

From a mass integration point of view, it is possible to determine that solutions with a recycle loop towards the RWGS (DAC.4) or the DAC-calciner (DAC.5) are equivalent. In the first case, the off-gas light hydrocarbons undergo steam reforming processes. In the second case, oxy-combustion produces carbon dioxide that is further downgraded to CO in the RWGS. However, this second solution's disadvantage is transforming H_2 of the off-gas into H_2O in the oxy-fired calciner (H_2O is then extracted before the RWGS reactor). Hence, recirculation to the RWGS can better manage the hydrogen looping in the system lines.

Furthermore, DAC.2 and DAC.3 present a loss of recycled carbon material due to the capture rate of 75% of the air contactors, with DAC.3 having further carbon loos given the capture rate of 90% in the absorber column [9]. Finally, DAC.2 has the lowest FT material production because no recirculation is provided to the RWGS, determining a final recycling rate of 79.6% against 95% of all the other configurations.

Table 35. Mass balance results for the DAC-to-FT process configuration. Adapted from [195].

Mass flow rate [t/h]	**DAC.1**	**DAC.2**	**DAC.3**	**DAC.4**	**DAC.5**
Air in	250000.0	250000.0	250000.0	250000.0	250000.0
Air out	248354	248379.7	248377.9	248163.1	248163.1
Gas turbine exhausts	232.5	244.1	242.9	-	-
Absorber Column solvent	347.0	290.2	287.3	-	-
Air Contactor solvent	2767.7	2764.2	2761.7	2681.6	2681.6
Water Knockout	531.0	531.0	531.0	531.0	531.0
Natural Gas to gas turbine	12.20	-	-	-	-
Natural Gas to calciner reactor	110.1	-	-	-	-
Air to gas turbine	220.3	223.1	223.6	-	-
Air to off-gas burner	222.4	189.1	92.2	146.9	140.4
Exhausts from burner	233.8	207.7	98.7	152.7	148.7
CO_2 to RWGS reactor	123.9	159.9	149.7	93.9	142.4
Condensed H_2O	130.9	75.1	84.1	74.5	94.3
Water for electrolysis	250.5	211.3	234.4	193.3	256.5
Oxygen from electrolysis	133.5	113.1	124.9	103.4	137.2
to Calciner	*29.5%*	*33.7%*	*29.8%*	-	*25.5%*
FT Products (Total)	240.9	99.0	117.3	114.5	163.2
Gas fraction to burner	*11.4*	*18.4*	*6.5*	*5.8*	*8.3*
Gas fraction recirculated	*195.9*	*67.4*	*92.3*	*82.1*	*128.6*
Liquid/Wax fraction					
- naphtha (C_5-C_{11})	*11.98*	*5.01*	*6.98*	*9.94*	*9.75*
- middle distillates (C_{11}-C_{20})	*12.9*	*4.7*	*6.63*	*9.72*	*9.66*
- waxes (C_{20+})	*8.7*	*3.5*	*4.8*	*6.94*	*6.83*
Gas fraction recirculation					
to RWGS reactor	*95.0%*	-	*37.1%*	*95.00%*	*77.30%*
to Gas turbine	-	*24.9%*	*19.9%*	-	-
to Calciner reactor	-	*54.7%*	*38.0%*	-	*22.70%*

4.2.2 Energy balances of the simulated processes

Concerning the plants' energy balance, the main results are listed in Table 36, considering both electric and thermal power and the energy content of natural gas and Fischer-Tropsch products.

From an electric demand standpoint, the most energy-intensive component is the electrolyser, absorbing an electric power directly dependent on the hydrogen required by the systems. Hence, DAC.5 and DAC.1 are the two most energy-intensive process configurations for the electrolyser unit (858 and 838 MW_{el}, respectively). DAC.4 has the lowest value at 676 MW_{el}. The second most demanding unit is the compression stage before the Fischer-Tropsch reactor. Similarly, configuration DAC.1 is the one that needs the highest amount of electricity (101 MWel). Lastly, only configuration C.4 has an electrified component at the DAC side (i.e., the calciner), which accounts for 128 MW_{el} needed to regenerate the CaO material.

Moreover, both exothermic and endothermic outcomes are included in the thermal balances. The Fischer-Tropsch reactor represents the single component with the highest thermal output of the systems, with the same demand trend as the one of the compression stages (i.e., DAC.1 higher thermal output, DAC.2 lowest thermal output). Moreover, the coolers provide a thermal output that ranges between 58% and 71% of the total cooling power available from the plants. Concerning the endothermic processes, heaters require a thermal input in the range of 293-343 MW_{th}. Moreover, the RWGS is the most energy-intensive single device of each plant. Its thermal demand is directly dependent on the amount of material that is processed inside. Therefore, lower recirculation values as in DAC.2 and DAC.3 determine a lower thermal demand of this unit.

Lastly, material flows exchanged with the environment present an energy content expressed as chemical power. The natural gas enters the system only in the baseline configuration, with 140.5 MW and 127 MW to the gas turbine and the calciner, respectively. Moreover, the FT liquid and wax products account for their energy content. Specifically, the higher the FT material production is, the higher is their energy content value.

Table 36. Energy balance information for each configuration. Adapted from [195].

[MW]	**DAC.1**	**DAC.2**	**DAC.3**	**DAC.4**	**DAC.5**
Electric power					
Electrolyser	838.09	707.16	784.31	646.74	858.14
Auxiliaries	0.92	0.69	0.72	0.63	0.83
Gas turbine compr.	22.06	22.35	22.40	-	-
FT compression	101.05	32.26	43.81	59.09	66.25
Gas turbine	-30.01	-30.00	-30.03	-	-
Calciner	-	-	-	128.47	-
Slake Steam-Turbine	-22.39	-24.92	-24.95	-21.88	-25.06
Energy content					
NG/FT off-gas GT	140.54	-	-	-	-
NG/FT off-gas Calciner	127.55	-	-	-	-
FT liquid products	-419.78	-166.49	-235.84	-337.73	-331.21
Thermal power					
Heaters	343.03	293.80	301.00	334.51	324.75
Coolers	-507.80	-339.40	-339.60	-339.22	-386.63
RWGS	182.12	41.14	69.53	123.67	117.86
FT	-210.36	-80.94	-111.30	-154.80	-159.81
Pellet reactor	-13.14	-6.77	-6.93	-5.47	-5.47
Slaker	-46.31	-41.89	-41.89	-46.31	-41.89
TG Comb	-81.27	-1.97	-11.14	0.00	0.00
Calciner	0.00	0.00	0.00	(Electric)	0.00

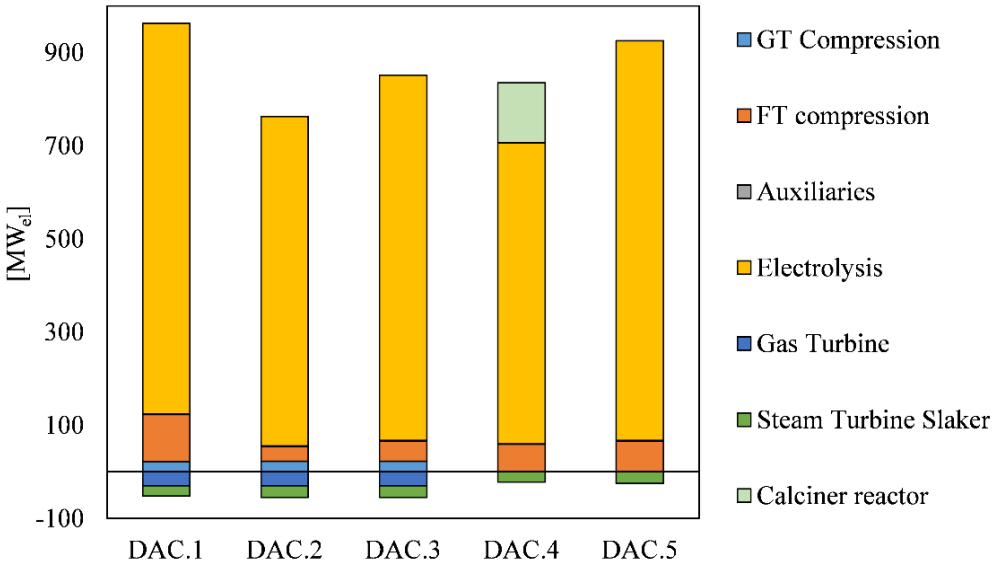

Figure 45. Electric energy balance for the DAC processes.

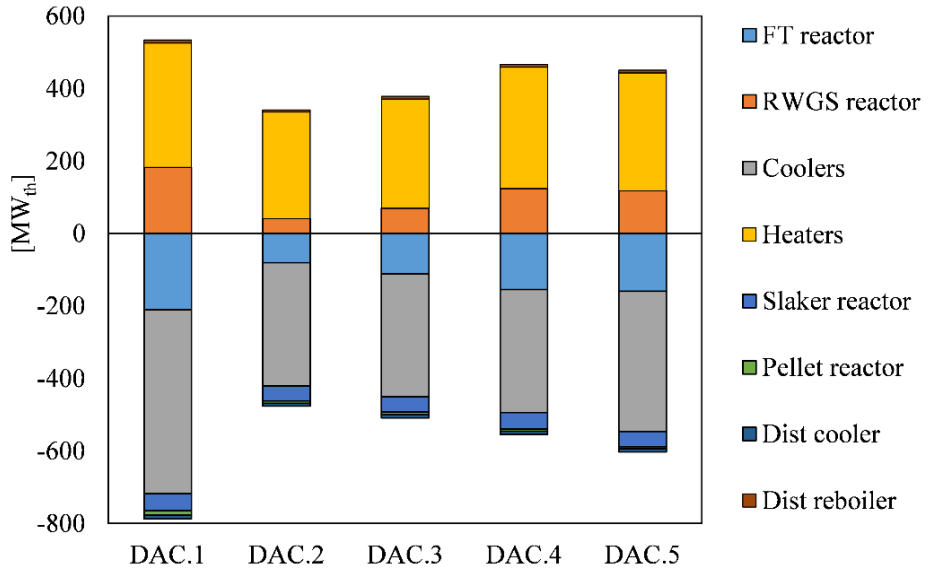

Figure 46. Thermal energy balance for the DAC processes.

Moreover, from an energy balance point of view, the plant flows can be connected through the pinch analysis methodology, exploiting the hot and cold fluids for heat exchange (Table 37 and Figure 47). There is a sensible reduction of the thermal demand for all configurations, ranging from -68% in DAC.1 up to -92% in DAC.2. In terms of thermal sinks (i.e., cold fluids), in all the configurations, the RWGS is again the most critical component, operating at a constant temperature of 800°C. As such, the heat demand that cannot be covered with internal fluids is assumed to be provided with electric heaters. Considering the cold sinks (i.e., hot fluids), three different plateau levels are identified: at 300°C, corresponding to the heat provided by the slaker, at 230°C, corresponding the one released by the FT synthesis, and at 100°C, the phase change of steam entering the steam turbine.

Table 37. Effect of the pinch analysis on the heat demand of each configuration (DAC process).

[MW_{th}]	**DAC.1**	**DAC.2**	**DAC.3**	**DAC.4**	**DAC.5**
Heat Before Pinch Analysis	531.0	342.8	379.0	592.4	487.9
Heat After Pinch Analysis	168.2	28.8	63.7	111.8	109.1
Heat Demand Reduction	*-68.3%*	*-91.6%*	*-83.2%*	*-81.1%*	*-77.6%*

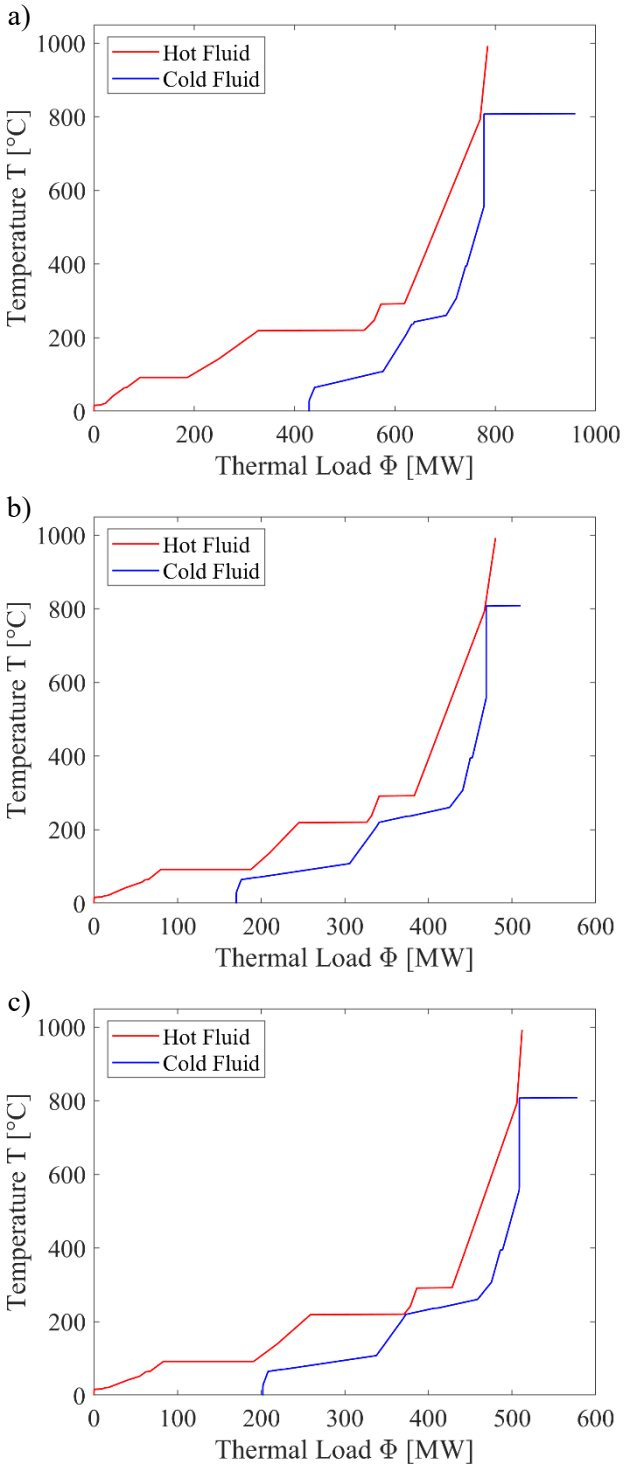

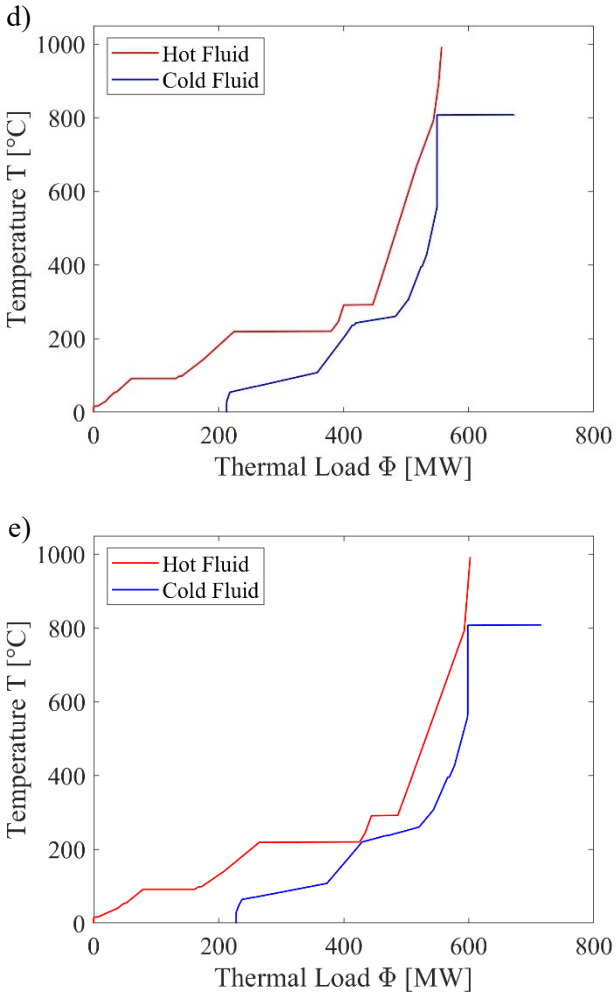

Figure 47. Composite curves: a) DAC.1; b) DAC.2; c) DAC.3; d) DAC.4; e) DAC.5.

4.2.3 Effect of the recirculation

The effect of the recirculation of the off-gas was compared against the same system without any recirculation. In this condition, natural gas is fed to the DAC calciner and gas turbine, with the gas turbine and the slaker steam turbine generating enough electric power to sustain the plant's auxiliaries and compression needs. In this regard, this solution is similar to the one investigated by Liu et al. for their LCA analyses [210].

As visible from Figure 48, thanks to the off-gas recirculation, there is a remarkable shift of the FT distributions towards the higher molecular weight hydrocarbons. For the configuration with no recirculation, the product distribution follows the standard ASF theory for Fischer-Tropsch, with a curve peak on molar basis at the carbon number C_3. Contrarywise, the recirculation allows accumulating heavy compounds and reducing the light ones (i.e., CH_4 and gas fraction), with a consequent shift of the curve peak around carbon number C_6-C_7. Only for configuration DAC.2, the peak remains at carbon number C_3, with a lower magnitude of change in the product distribution than configurations DAC.3,

DAC.4, and DAC.5. Configuration DAC.1 has a peak at C_7 (the highest among the configurations), which results in a tail at C_{45}-C_{70} in the direction of DAC.2.

In this context, the reforming of light hydrocarbons is not the only one responsible for the change in the distribution. Also dragging inert N_2 in the recirculated flows might influence the concentrations of reactants in both the RWGS and the FT reactor, shifting the selectivity in favour of the heavier hydrocarbons [43,299]. Same results and considerations could be given if the curves were provided as mass distribution (Figure 49).

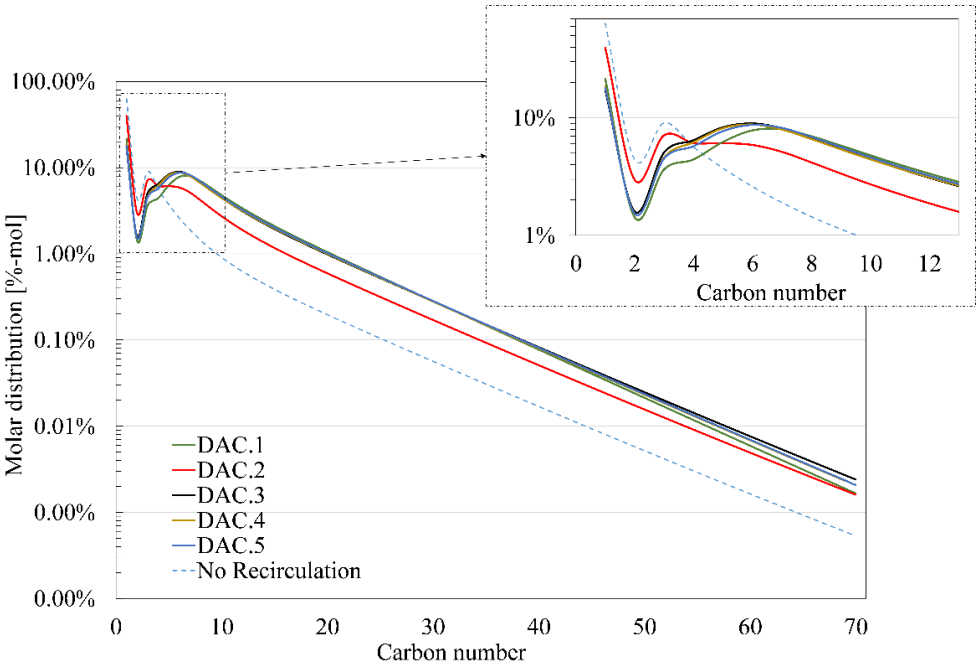

Figure 48. FT off-gas recirculation in the DAC process of the FT distribution (%-mol). Dashed blue line represents the configuration with no recirculation.

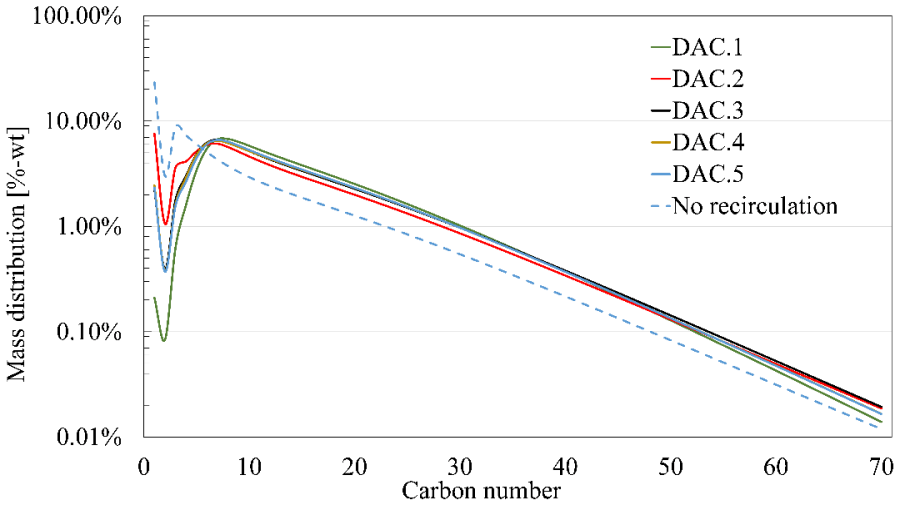

Figure 49. Mass distribution of the FT production with effect of the off-gas recirculation.

Moreover, coke deposition in the RWGS reactors should be avoided, similar to the other processes investigated. For the DAC processes, zero solid carbon formation was found in any of the configurations. Hence, additional oxygen carrier feed to this device was avoided. As presented in Figure 50, configurations DAC.1 and DAC.4 are the two most critical ones, but still in a safe area with no coke formation. This can be related to the off-gas, that in these configurations are recycled to the RWGS reactor. Hence, there is a lower oxygen content with respect to the cases with a recirculation towards the DAC: in this unit, the carbon content of the off-gas is converted into CO_2 in the gas turbine or calciner.

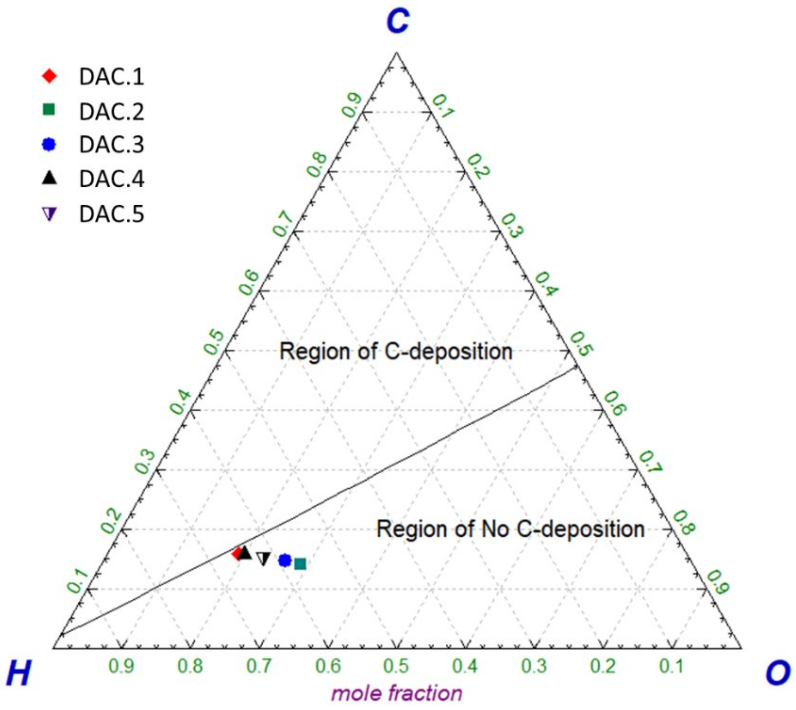

Figure 50. Carbon deposition region for the DAC-FT processes.

4.2.4 Key performance indicators

The KPIs are accounted for after the integration through the pinch analysis and summarized in Table 38. For configurations DAC.2 to DAC5, the carbon dioxide conversion η_{CO2} and the carbon conversion η_C are the same, as the only source of carbon material is the CO_2 from the air.

Moreover, DAC.2 is the most energy-intensive solution (210.5 kWh/kg_{wax}). This configuration is also the least beneficial one considering the plant efficiency (η_{GI}), η_{CO2}, and η_C. Contrarywise, C.1 has the highest carbon conversion thanks to the high production of FT compounds (73.7%). However, it is also the second least performing solution in terms of η_{CO2}, meaning that the addition of natural gas is penalizing the conversion of CO_2 from the air into FT material. Finally, configurations DAC.4 and DAC.5 have the two highest values of η_{CO2}.

Table 38. Key performance indicators of the DAC-FT processes.

KPI	DAC.1	DAC.2	DAC.3	DAC.4	DAC.5
E_{SPwax} [kWh/kg$_{wax}$]	154.7	210.5	179.2	133.4	147.8
η_{CO2}	64.4%	58.1%	68.3%	67.2%	66.4%
η_{C}	73.7%	58.1%	68.3%	67.2%	66.4%
η_{GI}	31.2%	22.6%	27.2%	36.5%	32.8%

4.2.5 Economic analysis

The cost of the different processes are provided as CAPEX and OPEX.

Capital costs

Capital costs are depicted in Figure 51, with their breakdown in Table 39. The most expensive configuration is DAC.1, at 1.8 G€, while the least expensive is DAC.4, at 1.4 G€. Cases DAC.4 and DAC.5 allow having a lower CAPEX thanks to the avoidance of the gas turbine unit for power generation. Moreover, regardless of the configuration, the most expensive unit is the DAC, possibly due to its relatively low technology readiness level [68]. Furthermore, the electrolysis stage ranges between 14% and 18%, and the FT section 6-15%.

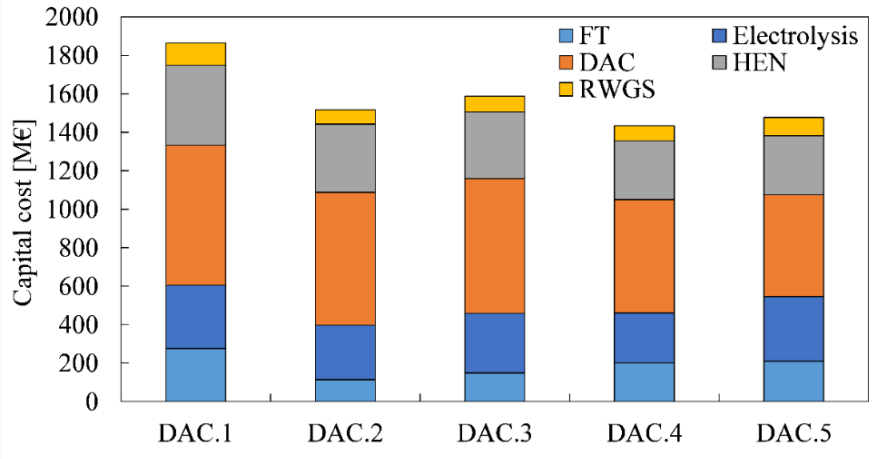

Figure 51. CAPEX for the DAC-FT processes. The FT section includes compression, distillation and afterburn of the off-gas.

Table 39. CAPEX breakdown for the DAC-FT processes.

CAPEX [M€]	DAC.1	DAC.2	DAC.3	DAC.4	DAC.5
Electrolysis	330	283	310	261	337
DAC section	727	691	700	590	530
RWGS reactor	115	75	82	79	96
FT reactor	223	86	118	164	169
Syngas compression	32	15	18	22	24
Thermal integration	416	355	347	305	306
FT separation	14.76	7.80	9.03	9.62	11.46
Afterburn combustor	6.0	5.5	3.0	4.3	4.2
TIC	1864	1517	1588	1435	1478

Operating costs

Operating costs of each system accounted for both electric and non-electric ones (Figure 52 and Table 40).

The cost of the electric ones was referred to at the reference value of 100 €/MWh_{el}. The most impacting operating cost is related to the purchase of electricity for the system, accounting for about 85% to 89% of the cash flow seen as expenditures. This is mainly due to the presence of the alkaline electrolyser for hydrogen production. Considering only the non-electric OPEX, the FT section is the most impacting one.

Moreover, if electric OPEX were excluded, the sale of the system by-products allows covering the expenses related to the non-electric OPEX, besides for configurations DAC.2 and DAC.3.

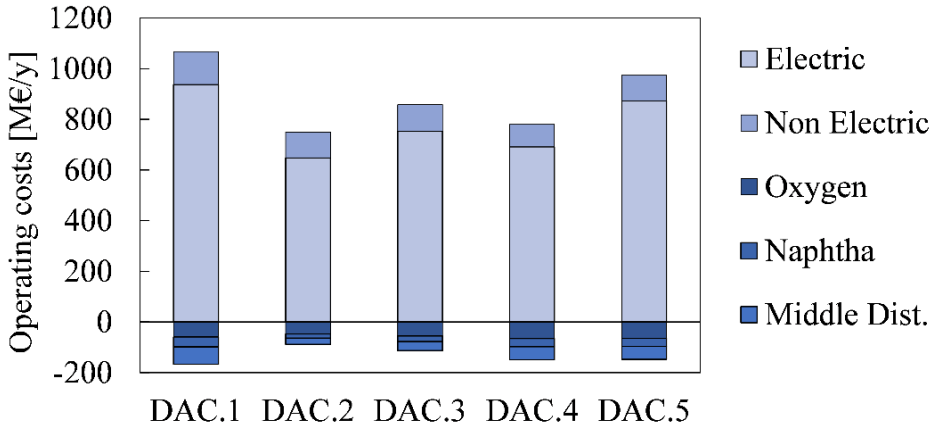

Figure 52. OPEX of the DAC-FT processes. Electric OPEX reported at an electricity purchase cost of 100 €/MWh_{el}.

Table 40. OPEX breakdown for the DAC-FT processes. [1]Includes syngas compression, off-gas burner, and hydrocarbons distillation.

OPEX [M€/y]	**DAC.1**	**DAC.2**	**DAC.3**	**DAC.4**	**DAC.5**
Non-electric OPEX					
Electrolysis	13.6	11.7	12.8	10.7	13.9
DAC section	52.7	26.0	26.3	22.2	20.0
Thermal integration	52.7	26.0	26.3	22.2	20.0
RWGS	9.7	7.3	7.8	7.1	7.8
FT[1]	41.8	46.0	47.0	39.5	48.9
Electric OPEX					
100 €/MWh_{el}	937.55	648.70	753.4	691.3	873.7
Revenues					
O_2 sale	59.3	47.2	55.3	65.1	64.4
Naphtha (C_5-C_{11})	38.9	16.3	22.7	32.3	31.7
Middle Distillates (C_{11}-C_{20})	68.6	25.0	35.3	51.7	51.4

Cost of wax production

The cost of wax production was evaluated from the combination of CAPEX and OPEX. The production cost was assessed at discounting factor of 2.0%, 7.5%,

and 12.5%. Similarly, a variation of the cost of wax production can be obtained with respect to the purchase cost of electricity. This was varied between 40 €/MWh and 160 €/MWh, with reference to the cost of electricity from renewable energy sources reported by IRENA [284] (Figure 53). Among the different configurations, case DAC.4 is the most economically feasible, followed by DAC.1. The least favourable configuration corresponds to DAC.2. Hence, configuration DAC.2 shall be avoided from both a thermodynamic and economic point of view. For configuration DAC.4, the wax production cost from the air CO_2 ranges between 4.91 and 18.8 €/kg_{wax} at 2.0% discount rate, 5.25 and 19.17 €/kg_{wax} at 7.5% discount rate, and 5.59 and 19.51 €/kg_{wax} at 12.5%. Hence, it is vital to access low-price electricity for a reliable market entry of this specific process route.

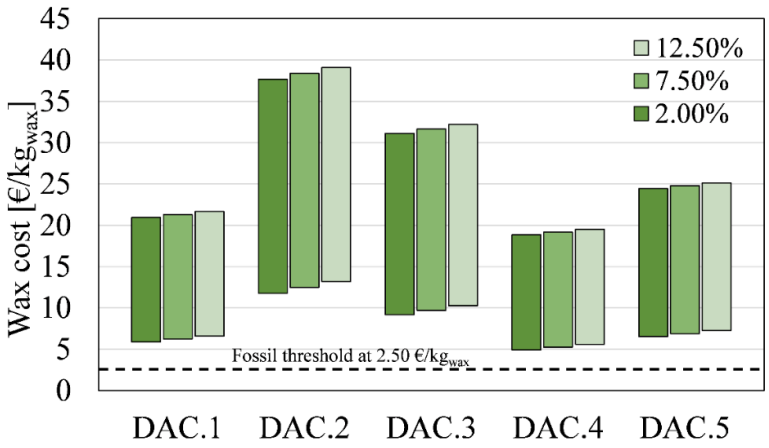

Figure 53. Wax production cost for the DAC-FT processes. Low values obtained with electricity purchase cost of 41 €/MWhel. High values obtained with electricity purchase cost of 160 €/MWhel.

4.3 Digestate conversion

The results of the process integration of the gasification unit with the Fischer-Tropsch reaction are provided here, ranging from the mass balance to the evaluation of the cost of waxes production.

4.3.1 Mass balances of the simulated processes

From a mass balance point of view, the results are provided in Table 41. Considering the production of Fischer-Tropsch products, configuration DIG.A provides a lower amount of hydrocarbons with respect to configuration DIG.B. In the first case it is produced 137 kg/h of syncrude (71.3, 44.1, 21.9 kg/h of naphtha, middle distillates, and waxes). In the second case, a total 185 kg/h of syncrude leaves the plant, corresponding the 74.4 kg/h of naphtha, 80.3 kg/g of middles distillates, and 30.2 kg/h of waxes (Figure 54). Moreover, DIG.B requires a higher amount of steam entering the system to allow for the conversion of biomass and sustain the process of reforming of the recirculated material. Lastly, configuration B has a higher flue gas discharge from the combustion column compared to DIG.A (969 kg/h and 790 kg/h, respectively). However, the latter has an additional 3.8 t/h of flue gases leaving the gas turbine unit.

Such results can be linked to the typology of configuration. Under case A, the FT off-gas generate electricity inside the gas turbine to cover the plant's electric demand. This means that light hydrocarbons are not looped back to the system, providing a lower accumulation of the heavier compounds. Moreover, in this configuration, net-zero electricity demand is obtained with 70.7% recirculation of the FT off-gas to the reforming unit, with the rest employed in the gas turbine. For DIG.B, 90% of the off-gas are recycled to the reformer, with the rest being sent to the gasification unit. Similarly, Im-Orb et al. [264] identified a value of 40% of recirculation for maximum diesel production when converting rubberwood into Fischer-Tropsch.

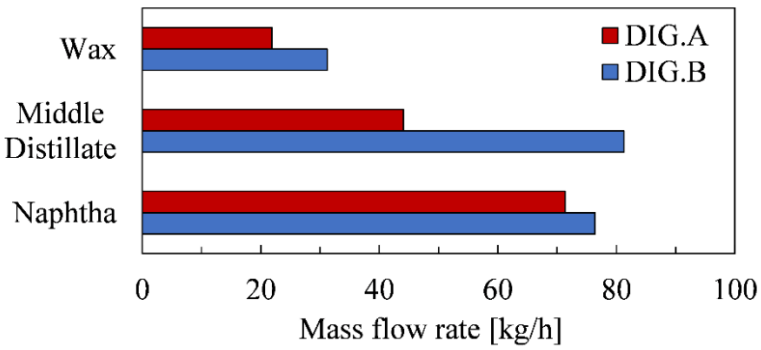

Figure 54. Mass flow rates of FT fractions for the biomass-to-FT process route.

Table 41. Mass balance results for the Biomass-to-FT process configuration.

Mass flow rate [kg/h]	**DIG.A**	**DIG.B**
$Biomass_{a.r.}$	979.00	979.00
Syncrude	137.24	184.87
- *Naphtha*	*71.34*	*75.40*
- *Middle Distillate*	*44.05*	*81.28*
- *Wax*	*21.85*	*31.19*
FT Off-gas *(% to Reformer)*	370.13 *(70.7 %)*	2641.4 *(90%)*
Steam for the gasifier	209.58	221.25
Air for combustor	731.80	877.10
Air for GT	3806.30	-
Flue gas from combustor	790.20	969.46
Flue gas from GT	3916.74	-
Char to combustor column	340.32	347.72
Raw syngas from the gasifier	859.90	1093.54
Wastewater from the FT	219.26	306.90
Steam for the reformer	52.06	100.33
PSA CO_2	317.37	320.50
Ash flow	281.92	281.92
NaOH consumption	21.03	21.03
NaOH → Na_2S out	41.02	41.02
NaOH → H_2O out	9.47	9.47
Wastewater	147.42	162.13
NH_3 out	9.93	9.93
HCl out	0.91	0.91
Fresh olivine [ton/h]	0.07	0.07

Moreover, the temperature of gasification can influence the production of the Fischer-Tropsch material. In this regard, the gasifier temperature was varied between 800°C and 950°C. Higher values of this parameter might promote the melting of ash material, with its latter agglomeration in the gasifier lines [251]. The evolution of the Fischer-Tropsch liquid hydrocarbons is depicted Figure 55. For both configurations, a rise in the gasification temperature is detrimental on the production of FT compounds, providing a lower rate of production of naphtha, middle distillates, waxes. In case DIG.B, high temperatures increase the biomass-to-syngas conversion, resulting in a rise of the FT gas content (2.82 t/h at 900°C against 2.64 t/h at 800°C). In case DIG.A, this behavior could be linked to the requirement of keeping a net zero electric demand. This determines a reduction of the recirculation rate to the reformer (e.g., 70.7% at 800°C, 46.5% at 900°C), consequently reducing the amount of unconverted material going in the reformer.

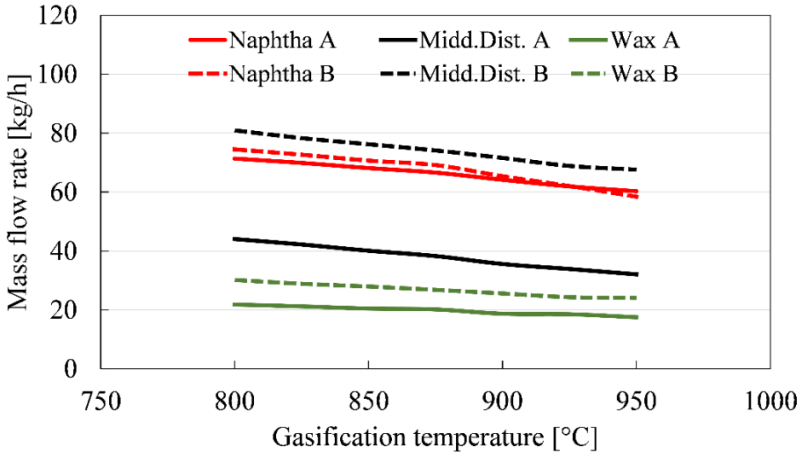

Figure 55 Effect of the gasification temperature on the production of the FT material.

4.3.2 Energy balances of the simulated processes

The results in terms of energy balance are provided in Table 42. Concerning the electric demand of the system, the presence of the gas turbine covers the electric need of compression, PSA, and auxiliaries for DIG.A. In contrast, for DIG.B the overall electric input required by the system corresponds to 195 kW_{el}.

Considering the energy content of the Fischer-Tropsch compounds, case B has a higher value than case A, at 2.2 MW and 1.7 MW, respectively. This is directly dependent on the higher production of FT material from case B.

Accounting for the plants' thermal energy, the FT provides 527.1 kW_{th} and 742.7 kW_{th} for case A and B, respectively. Similarly, the reformer unit has a higher thermal demand for its operations in case B.

Table 42. Energy balance results for the biomass-to-FT process.

Energy balance [kW]	**DIG.A**	**DIG.B**
Chemical energy content		
FT product	-1717.2	-2223.5
Inlet biomass	3107.9	3107.9
Electric power supply		
Air blower	3.70	4.46
Water pump	0.09	0.12
LP compressor	70.92	90.66
HP compressor	38.25	51.47
PSA system	47.61	48.08
Gas turbine (net out)	-160.55	-
Net electricity	0.0	194.79
Thermal energy balance		
Fischer-Tropsch reactor	-527.1	-742.7
Reformer	239.7	639.0
Heat exchangers	446.7	892.6
Coolers	-997.7	-1425.9

Moreover, applying the pinch analysis methodology, the thermal needs of the plants can be reduced (Figure 56). As visible from

Table 43, it is possible to reduce the thermal demand by 66.4% and 59.3% for case A and B, respectively. Excess heat could be supplied with electric heaters. The higher thermal demand of case B can be linked to the higher production of FT material and the reforming unit's thermal needs.

Table 43. Effect of the pinch analysis on the heat demand of each configuration (biomass process).

[kW_{th}]	**DIG.A**	**DIG.B**
Heat Before Pinch Analysis	686.4	1531.6
Heat After Pinch Analysis	230.2	624.0
Heat Demand Reduction	*-66.4%*	*-59.3%*

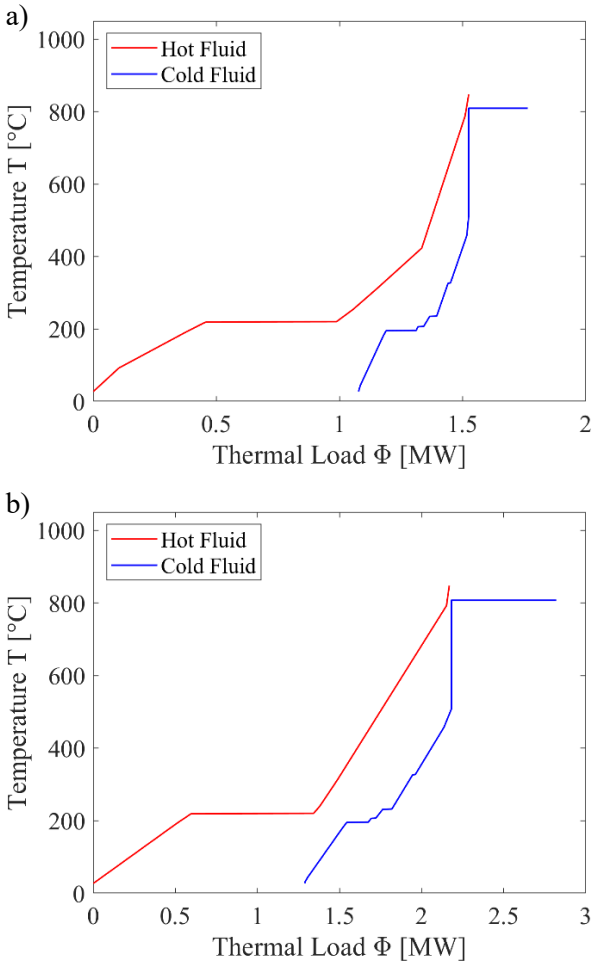

Figure 56. Composite curves the digestate configuration process: a) case A; b) case B.

4.3.3 Key performance indicators

KPIs obtained from the process of converting digestate into Fischer-Tropsch material are summarized in Table 44. Similar to the previous processes, these were accounted for after the integration through the pinch analysis.

Considering the unitary energy demand over the waxes production, case A shows a value of 160.1 kWh/kg_{wax} against 132.1 kWh/kg_{wax} for case B. Even though there is a net-zero electric demand for case A, together with a lower thermal need after energy integration, case B outputs a more significant amount of valuable waxes. Moreover, DIG.B reaches a carbon conversion of 50.4% and a plant efficiency of 56.1% (higher than DIG.A). Hence, it is more efficient to convert the carbon material of digestate into Fischer-Tropsch hydrocarbons rather than utilizing it to produce electricity for internal purposes. For comparison, Hillestad et al. [205] reached a plant efficiency of 53%, with a carbon conversion of wood biomass into FT products of 37.8% for their Biomass-to-Liquid process. Snehesh et al. [300] had a process efficiency ranging between 30.6 and 53.5%. Finally, Albrecht et al. [81] converted 24.9% of the carbon of generic woody biomass into Fischer-Tropsch, with a plant efficiency of 36.3%.

Table 44. Key performance indicators of the DAC-FT processes.

KPI	DIG.A	DIG.B
E_{SPwax} [kWh/kg_{wax}]	160.1	132.1
η_C	38.88%	50.41%
η_{Gl}	50.91%	56.13%

4.3.4 Economic analysis

Capital costs

The breakdown of the capital costs is provided in Figure 57 and Table 45. A total cost of 8.11 M€ and 9.54 M€ are found for DIG.A and DIG.B, respectively. The gas turbine unit is present only in configuration A, with a capital value of 477.5 k€. However, case B has a higher throughput of synthetic material generated by the system, providing a higher installation cost (i.e., rise in the FT reactor cost, reformer, products separation, and syngas compression). Lastly, the gasification unit accounts for 19.8% of the price in case A, and 16.8% in case B.

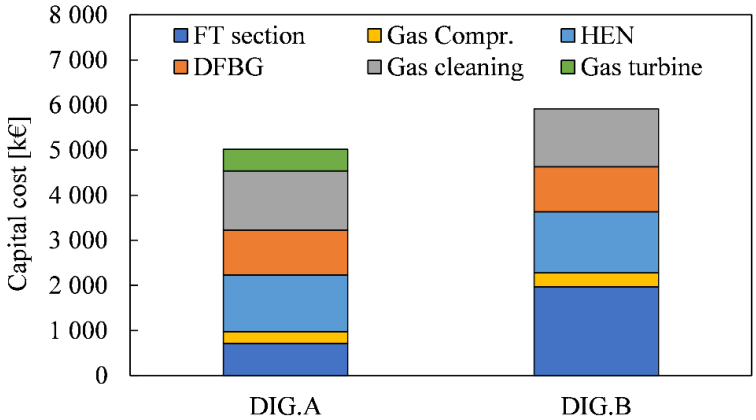

Figure 57. CAPEX breakdown of the Biomass to FT processes. The FT includes the products distillation and the reforming unit of recirculated material.

Table 45. CAPEX breakdown for the biomass-to-FT processes.

CAPEX [k€]	DIG.A	DIG.B
FT	243.4	393.6
DFBG	994.3	994.3
LP compressor	155.8	184.1
HP compressor	102.4	125.3
Cyclone syngas	62.4	61.3
Gas turbine	477.5	0.0
Guard bed	0.4	0.5
Water pump	0.0	0.0
Wet scrubber	571.9	529.0
Venturi scrubber	159.6	178.3
Tar cracker	468.1	459.5
PSA	52.0	57.7
FT Separation	42.3	99.3
Reformer	637.0	1471.8
HEN	1258.9	1359.2
TIC	8107.1	9539.3

Operating costs

The operating costs of the systems are presented in Table 46, providing the costs of the systems in terms of expenses and incomes. The total annual costs are 1.23 k€/y and 1.81 k€/y for case A and case B, respectively. Under configuration A, the most impacting yearly fee is represented by the personnel cost (300 k€/y). On the contrary, the electricity fed to the system in configuration B is the most expensive element, representing 37.6% of the annual expenses (679.4 k€/y when purchased at 100 €/MWh_{el}). Regarding the revenues, these are connected to the plant output. As a result, DIG.B presents a higher income rate compared to DIG.A.

Table 46. OPEX for the biomass-to-FT processes.

OPEX [k€]	DIG.A	DIG.B
Digestate feed	41.1	41.1
Ash disposal	103.9	103.9
NaOH cost	70.3	69.8
Wastewater	7.4	9.5
Freshwater	0.9	1.2
Olivine	93.0	92.9
Operators (4)	300.0	300.0
Maintenance	162.1	190.8
Insurance & taxes	162.1	190.8
Administration & services	81.1	95.4
Electric Opex (@100 €/MWh_{el})	185.1	679.4
Catalyst replacem. [k€/3-years]	81.1	95.4
Revenues		
Naphtha	273.9	311.7
Middle	277.5	537.7
By-product heat	367.1	524.0

Cost of waxes production

The cost of production of the waxes was evaluated at different values of the discounting rate (Table 47). For the baseline configuration at 7.5%, the wax production cost corresponds to 3.44 €/kg_{wax} and 3.48 €/kg_{wax} for A and B. Remarkably, the two configurations are comparable from an economic point of view. The extra CAPEX and OPEX of DIG.B are counterbalanced by its higher conversion to Fischer-Tropsch material of the digestate (i.e., higher income).

Moreover, the wax production cost was evaluated with a purchase value of digestate of 5 €/ton. However, as stated by Corden et al. [63], its price can also be considered at 0 €/ton when this material is accounted for as waste or when public investments for the upstream anaerobic digestion unit are included. This situation would reduce the cost of wax production by about 20 cent€ for every condition.

Table 47. Waxes production costs for the digestate to FT processes. Values in brackets would represent the cost of production if the digestate was purchased at 0 €/kg.

Cost of waxes [€/kg_{wax}]	**DIG.A**	**DIG.B**
2.00% (if 0 €/ton for digestate)	2.83 (2.61)	2.98 (2.83)
7.50% (if 0 €/ton for digestate)	3.44 (3.22)	3.48 (3.33)
12.50% (if 0 €/ton for digestate)	4.06 (3.83)	3.99 (3.84)

The cost of production of the FT waxes can also be investigated by means of variation in the electricity price. Depending on the electricity source, a change in the wax production cost can be observed. Figure 58 presents such evolution, with a digestate purchase cost fixed at 5 €/ton. Similar to the other processes analysed, the cost of electricity ranges from 41.05 €/MWh (corresponding to hydropower according to IRENA [284]) and 158.9 €/MWh (corresponding to CSP).

As visible from Figure 58, case A reaches a scenario where the cost of wax production is lower than the fossil threshold of 2.50 €/kg_{wax} only when a low discount rate is applied (i.e., optimistic solution 2.00%). In this case, the electricity price should be equal to or lower than 65.5 €/MWh, corresponding to either hydropower, on-shore wind, or solar PV energy source. Contrarywise, case B reaches a cost of waxes lower than the fossil threshold regardless of the discount rate value. The energy purchase cost should be equal to or lower than 82.1 €/MWh, 63.2 €/MWh, 42.0 €/MWh at a discount rate of 2.00%, 7.50%, and 12.50%, respectively (Table 48).

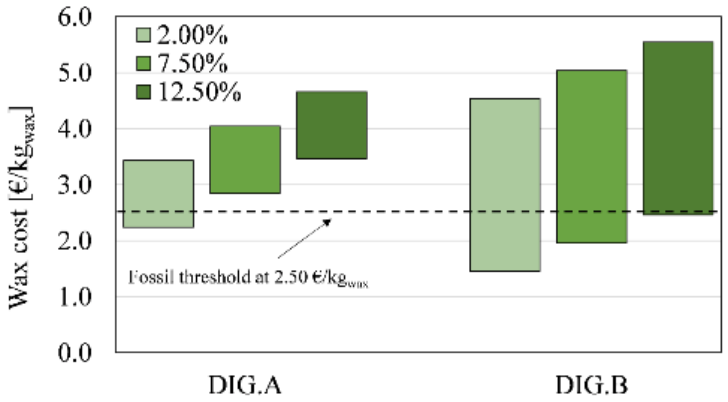

Figure 58. Cost of wax production, depending on the cost of electricity. The low values are obtained with electricity purchase cost of 41 €/MWh$_{el}$. High values are obtained with electricity purchase cost of 158 €/MWh$_{el}$.

Table 48. Preferential cost of electricity to reach a wax production cost equal or lower than the higher value of fossil route.

Electricity cost for wax production ≤ 2.5 €/kg$_{wax}$	**DIG.A**	**DIG.B**
2.00%	65.5 €/MWh	82.1 €/MWh
7.50%	n.a.	63.2 €/MWh
12.50%	n.a	42.0 €/MWh

Considering the most economically feasible route (i.e., DIG.B), the cost of wax production can be broken down depending on the CAPEX, OPEX, and revenues of the system. As such, considering an electricity cost of 41.1 €/MWh and a discount rate of 7.50%, the weight of each model component is provided in Figure 59, reflecting the share of CAPEX, OPEX, and revenues on the cost of waxes.

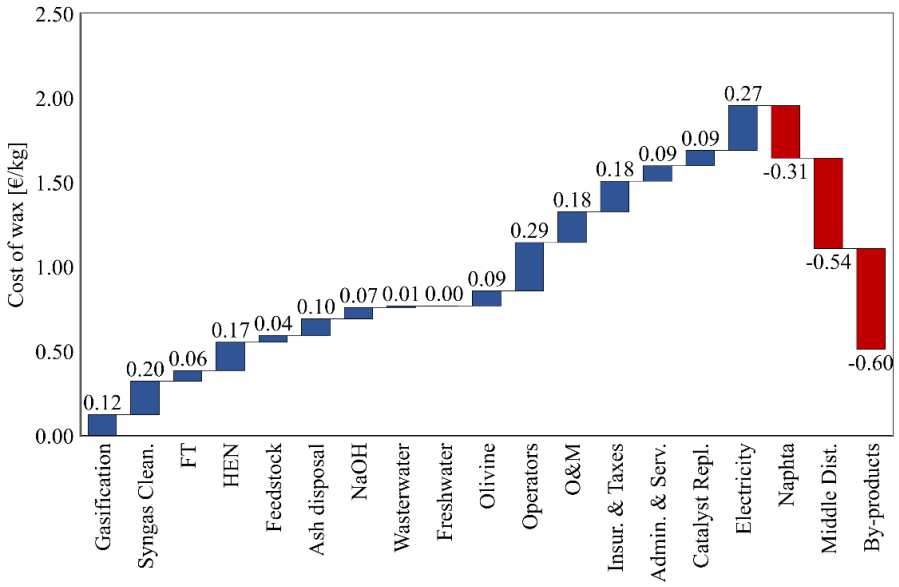

Figure 59. Cost of wax break-down provided for DIG.B.

4.4 System performance comparison

The three separate production routes can be compared one to the other, accounting for key performance indicators and wax production cost.

Key performance indicators

The process routes' KPIs are compared and provided through Figure 60 for Esp, Figure 61 for η_C and η_{CO2}, and Figure 62 for η_{gl}.

As visible from the values of Esp_{wax}, the most energy-intensive processes correspond to the one converting carbon dioxide from biogas into FT material. Such an outcome can be correlated to different reasons. Firstly, the evaluation of the factor Esp accounts for all forms of energy entering the system. Thus, biogas injects about 9.8 MW when entering the control volume of this route. Secondly, there is the presence of highly energy-intensive units like the biogas upgrading and the electrolysers. Compared to the other processes, a solution with digestate injects an additional expense of 3.1 MW. In the case of DAC routes, only configuration DAC.1 has a mass flow entering the system (i.e., natural gas).

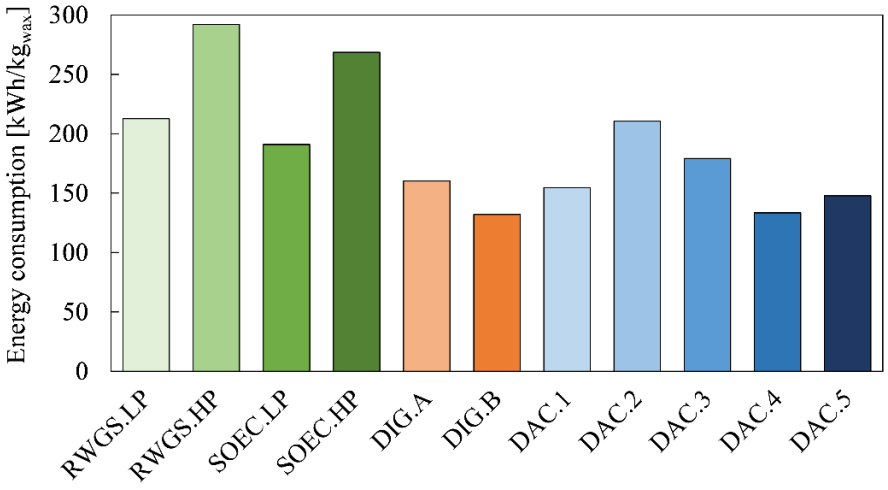

Figure 60. Comparison of the specific energy consumption over the wax production.

Considering the conversion of carbon material and carbon dioxide into FT compounds, these are directly dependent on the process configuration and system throughput of FT material. Specifically, the highest carbon conversion efficiency is reached for DAC.1 (η_C 73.7 %). However, this configuration injects a higher amount of carbon into the system (i.e., natural gas) than the other DAC layouts. Moreover, in the biogas configurations, a significant amount of carbon entering the plants is retained within the biomethane stream, hence providing a low value of η_C. Concerning the conversion of carbon dioxide (η_{CO2}), a solution with low-pressure RWGS and SOEC units allows reaching the highest values (i.e., 81.1% and 79.7, respectively), immediately followed by the solution extracting carbon dioxide directly from the air.

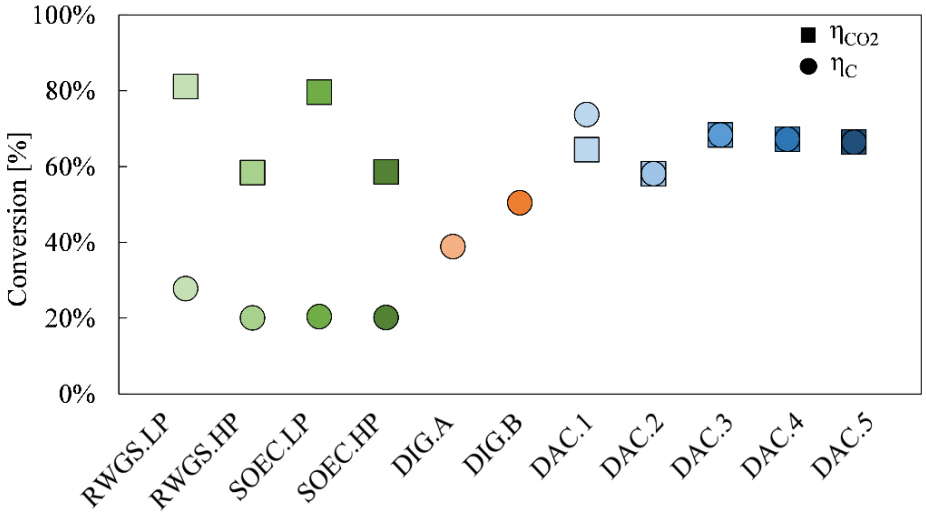

Figure 61. Comparison of the carbon conversion efficiencies.

In terms of process efficiency, a solution utilizing carbon dioxide from a concentrated source seems to be more reliable and efficient. Specifically, configuration SOEC.LP reaches the highest η_{GI}, at 66.5%. The cases utilizing biomass are the second most efficient plants, with their highest value at 56.13% for DIG.B. Finally, extracting CO_2 from the air and converting it into FT material is the least satisfactory solution from an efficiency standpoint.

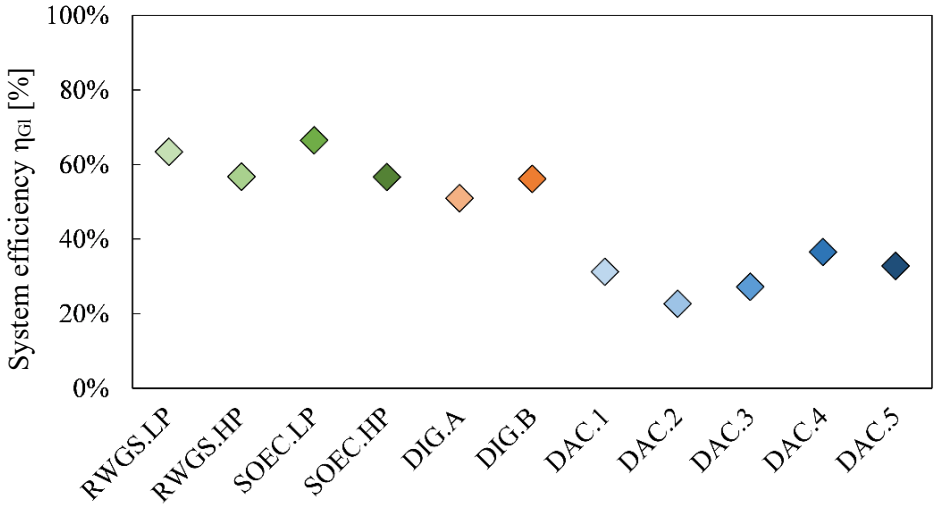

Figure 62. Comparison of the process efficiencies.

Overall, the conversion of carbon dioxide from a flow of biogas in a process scheme employing a low-pressure SOEC device for the syngas generation can be regarded as the best solution from an energy analysis point of view.

Cost of wax production

The analyzed systems can also be compared by looking at the cost of wax production (Figure 63). We assumed a 7.50% discount rate (i.e., realistic case). Overall, converting biogas is the most feasible solution if access to low-price

electricity is viable. Additionally, the most promising configuration corresponds to SOEC.LP. However, converting digestate has the lowest price variation depending on the electricity cost, as the electric input is much lower than in the other configurations. Lastly, the current technology readiness level determines an unfeasible solution if employing the DAC unit.

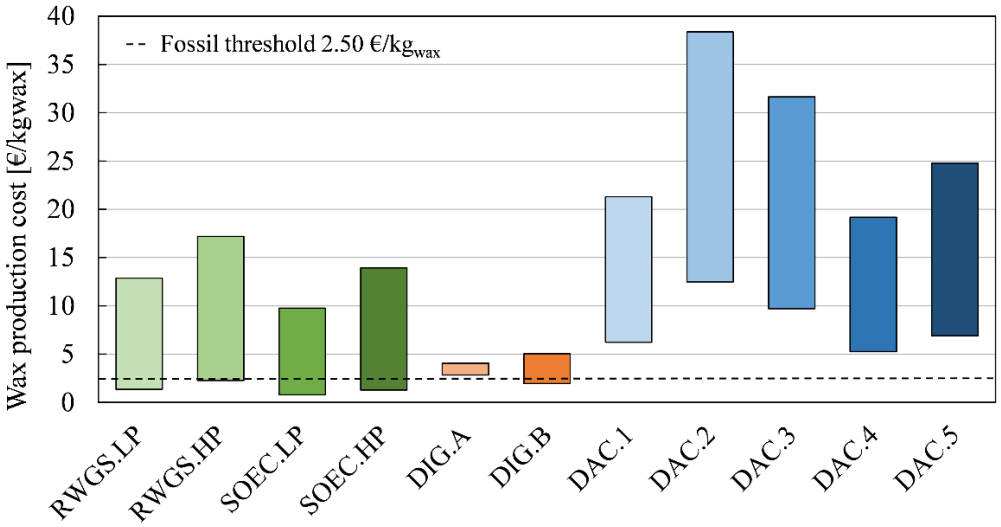

Figure 63. Comparison of wax production costs (discount rate of 7.50%).

Baseload electricity and cost evolution at the years 2030 and 2050

As mentioned, the electric-related OPEX evaluation was accounted for considering global weighted energy costs provided by IRENA [284]. Such electricity purchase costs might not be attainable in the framework of CCU routes that aim to convert non-fossil carbon feedstocks into FT liquids without balancing the electric grid. Indeed, the process schemes proposed in this analysis benefit from steady-state operations. Hence, baseload electricity could be utilized with a direct connection to the electric grid instead of inserting expensive storage solutions for hydrogen and/or carbon dioxide.

Fasihi et al. [285] reported that baseload electricity coming from a mixed PV/wind energy source in Europe would have a cost of 210 €/MWh$_{el}$. However, this cost is expected to drop down to 75 €/MWh$_{el}$ and 60 €/MWh$_{el}$ at the years 2030 and 2050, respectively. Hence, conversion routes with great electricity demand can benefit from this cost reduction in upcoming years.

Parallelly, it is expected that the cost of installation of the devices included in this analysis would reduce over time, as the effect of learning rates derived from the installation of a more significant number of CCU plants. For instance, Fasihi et al. [68] assumed a learning rate of 15% for the DAC unit. Similarly, Zauner et al. [273] reported cost curves for the SOEC and ALK devices at the years 2030 and 2050, decreasing their investment costs. Finally, Albrecht et al. [81] and Martin et al. [301] assumed a 10% learning rate suitable for the other involved technologies (i.e., RWGS, FT reactor, gasifier reactor), with a cost reduction

related to the installation of more than 100 units. Only the biogas upgrading unit was regarded as a mature technology.

With these assumptions, it was possible to determine the evolution of the wax production cost at the years 2030 and 2050 at a 7.5% discount rate, while feeding baseload electricity generated from mixed PV/wind sources in the European area. As visible from Figure 64, there is a sensible reduction in wax production cost from the year 2020 to 2030 and 2050, particularly for those requiring a significant electric input (i.e., major dependency on the electricity cost).

In the year 2050, both biogas and digestate routes deliver FT wax at a price lower than the upper fossil threshold of 2.50 €/kg_{wax}. Contrarywise, the extraction of CO_2 from the air would not be economically feasible even when accounting for learning rates. However, there exists an uncertainty related to the deployment of this relatively new technology. In this regard, no incentive schemes have been implemented for the current economic assessment. However, Herz et al. reported the possible exploitation of a credit solution as high as 300 €/ton_{CO2}, which would make the DAC route highly competitive with the other two, with the advantage of directly reducing the carbon dioxide concentration in the air. A similar consideration can be given at the year 2030, where, however, in the case of biogas, only a solution with SOEC.LP layout would provide a feasible market production of the FT waxes.

Hence, low-price electricity is strongly needed to substitute fossil material with FT synthetic counterparts.

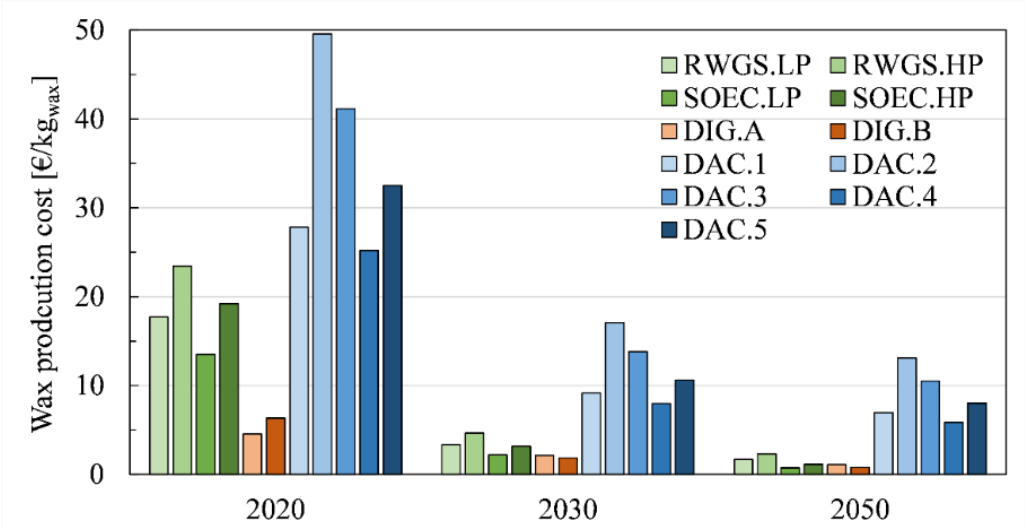

Figure 64. Evolution of the cost of wax production at the year 2030 and 2050 for all the accounted processes (discount rate 7.50%).

Chapter 5

European production potential

The present chapter analyses the possibility of utilizing the full potential of biogas and waste digestate available at the European level to generate Fischer-Tropsch material. The analysis exploits techno-economic considerations presented in the previous chapters, proposing possible preferential locations in Europe to install a carbon conversion plant.

More in detail, it is evaluated the potential out-take of both carbon dioxide and digestate material derived from the process of anaerobic digestion. Biogas and biomethane plants are included, where biomethane plants are intended as biogas plants with a unit for the separation of CO_2 and CH_4 present in the biogas stream. From the CO_2 and digestate stream, the potential production of FT material is evaluated.

5.1 Biogas plants installed in Europe

5.1.1 Biogas and biomethane plants in Europe

As presented in Chapter 1, both the European Biogas Association [58,302] and the International Energy Agency [59] provide information about the total number of biogas plants installed in Europe. Accordingly, the installation of biogas plants is slowly reaching a plateau, with a slowdown for the years 2014-2019 compared to the years 2009-2013. As shown in Figure 6, operating biogas plants in Europe were 6,227 in 2009, and the number increased to 18,966 in 2019. Moreover, the installation of biogas upgrading plants is constantly rising from 187 in 2011 to 742 in 2019. These plants are also presented in the European Biomethane Map, listing the location of all the biomethane plants connected to the EU gas grid [57]. Considering the different States with operating plants as of 2019 (Figure 66), Germany is the country with the highest number of biogas plants (11,084), followed by Italy (1,655), France (837), and the United Kingdom (715). When it comes to the available biomethane plants, Germany is still the country with the highest number, followed by France, the United Kingdom, and Sweden.

In this context, there exists a rising trend in the available *ready-to-use* carbon dioxide, coming from the upgrading of the biogas streams. Thus, CCU application can find an almost pure CO_2 stream available to produce carbon-neutral-products products.

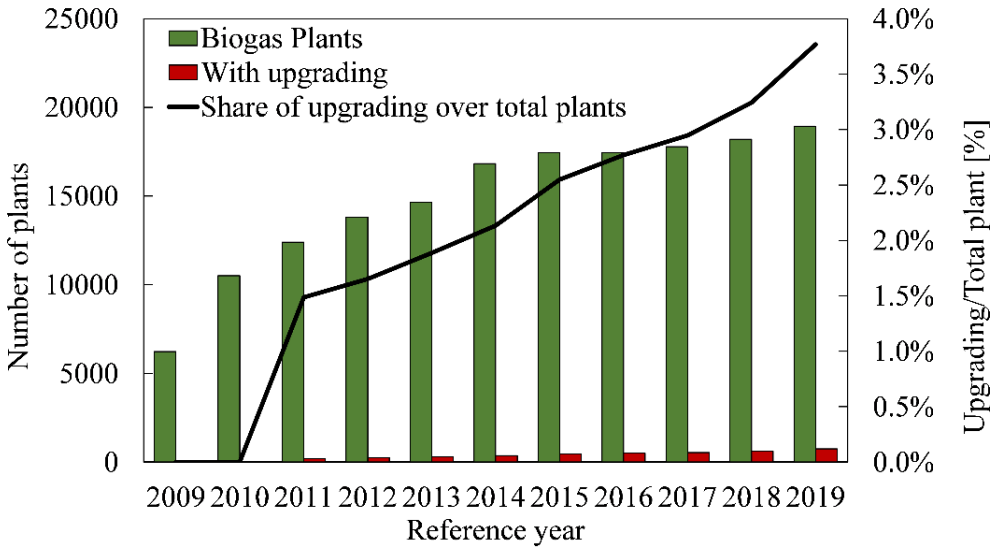

Figure 65. Evolution of the number of installed biogas and biomethane plants in Europe. Adapted from [58,59].

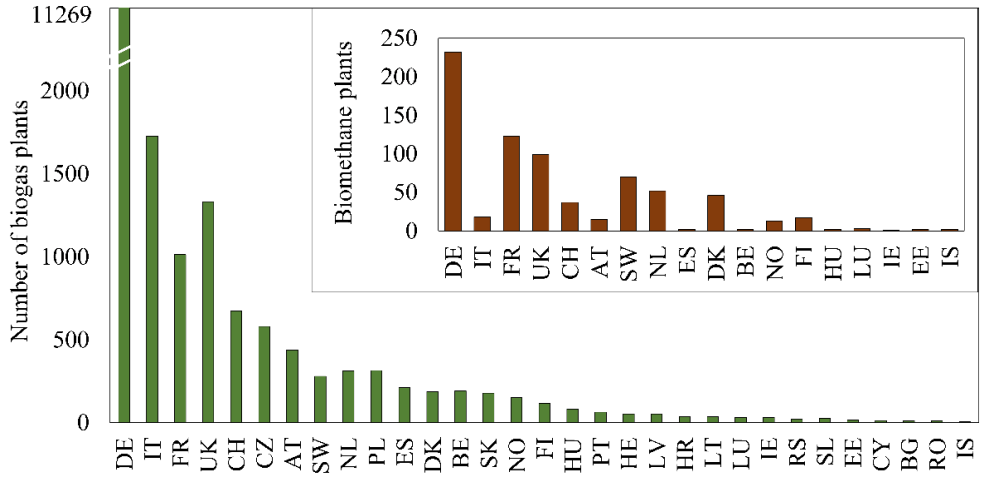

Figure 66. Biogas. Adapted from [58,59].

5.2 CO_2 and digestate potential from biogas plants

In the case of biogas plants (i.e., the plants without upgrading unit already installed at the plant location), the available data from the open literature provides clustered information about the total number of operating plants, the total biogas installed capacity (expressed in MW_{el}), the total production of biomethane (in GWh/y), and the average size of the plants (in MW_{el}) for each of European country assessed [58,303].

The total amount of captured CO_2 was evaluated for these plants according to eq (5.1)-eq.(5.2), starting from the global biogas installed capacity for each country. The generated carbon dioxide from the possible combustion of methane was omitted, assuming CH_4 injection into the gas grid.

$$\dot{V}_{biog}\left[m^3/_h\right] = 3600 \cdot \frac{P_{biog}}{\eta_{el} \cdot LHV_{biog}} \tag{5.1}$$

$$\dot{M}_{CO_2}\left[ton/_h\right] = \dot{V}_{biog} \cdot y_{CO2_{biog}} \cdot \eta_{capt} \cdot PM_{CO_2} \cdot 0.00224 \cdot 10^{-6} \tag{5.2}$$

P_{biog} is the installed capacity of biogas at each country, η_{el} is the electric efficiency assumed at 38% [302], the lower heating value of biogas was considered at 20 MJ/m^3 [59], the capture efficiency η_{capt} was assumed at a mean value of 95% and the concentration of CO_2 in the biogas was of 40%.

Additionally, the potential amount of digestate available to produce FT material was evaluated accordingly to the methodology presented in Chapter 3. Landfill substrate was accounted for only in the production of CO_2 coming from the upgrade of biogas. Digestate corresponding to landfill applications was excluded from evaluating the production potential, being considered a discharged material disposed of in dedicated disposal areas.

Figure 67 shows the biogas installed capacity for each of the countries included in the analysis. Moreover, Figure 68 provides the potential out-take of carbon dioxide and digestate for each State. The total EU potential availability corresponds to 4.23 kton/h and 2.79 kton/h of pure CO_2 and dry digestate, respectively. As visible, Germany dominates the market for installed capacity of biogas – in accordance with the total number of plants installed –, providing the highest potential out-take for both carbon dioxide and biomass material. Remarkably, the UK is the second country in terms of potential *ready-to-use* flow of CO_2, determined by the higher installed capacity than Italy (Italy has a higher number of operating biogas plants than the UK). However, the UK also presents a higher percentage of biogas produced from landfill applications (58% of biogas production from landfill, against 19% for Italy [302]), making Italy the second country in Europe for the availability of digestate material for further processing, followed by France, Czech Republic, and Estonia.

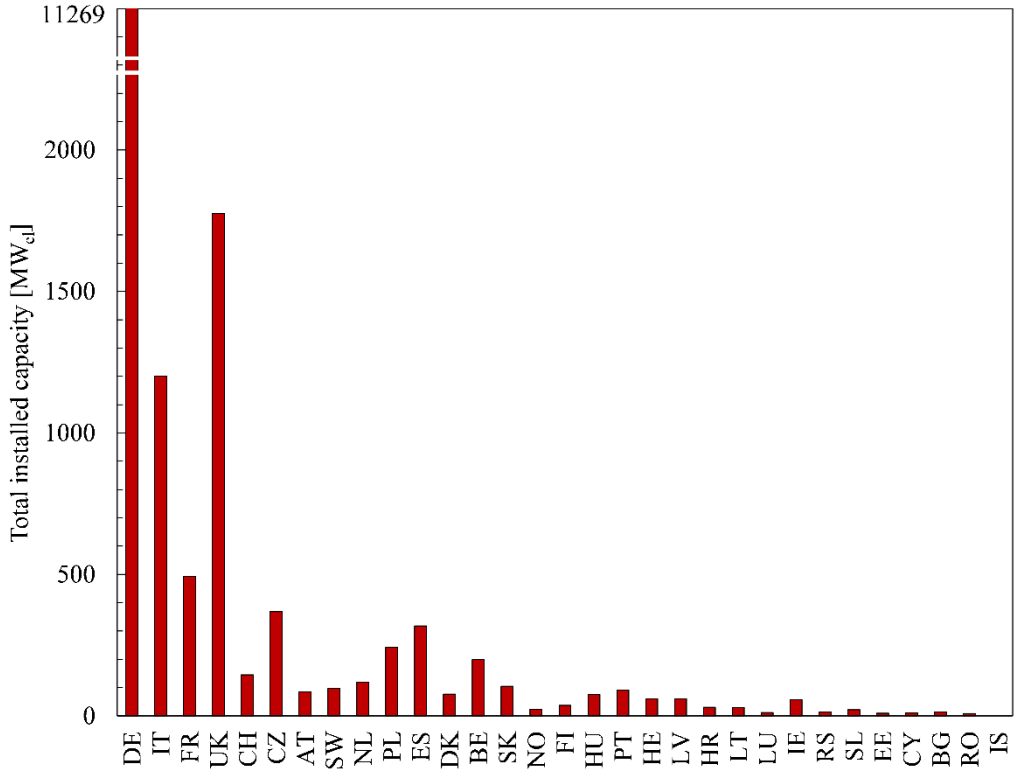

Figure 67. Total installed biogas capacity for each European country (end of the year 2019).

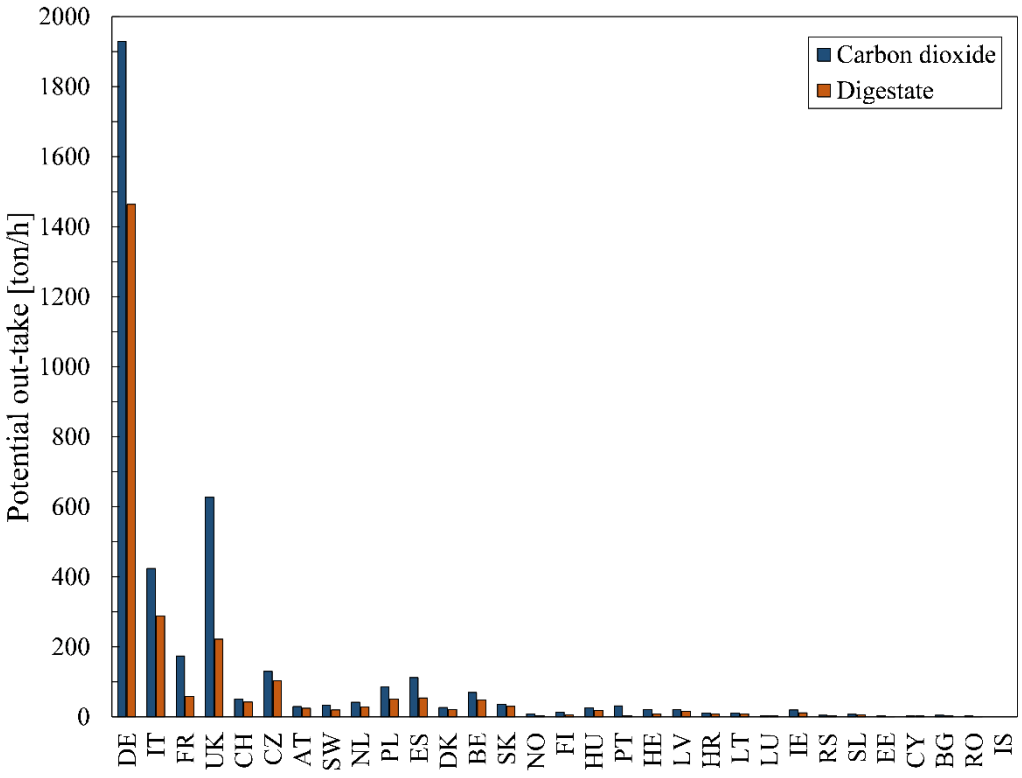

Figure 68. Potential out-take of CO_2 and digestate (dry) from the operating biogas plants in Europe (end of the year 2019).

5.2.1 Potential for Fischer-Tropsch products from biogas plants

Utilizing the streams available from the biogas plants, different amount of FT feedstock can be produced depending on the plant configuration described in Chapter 3 and Chapter 4. The results are listed in Table 49.

Table 49. Potential production of FT compounds utilizing biogas plants CO_2 and digestate flows. Liquid fraction accounts for both naphtha and middle distillate cuts.

DIG.A [ton/h]		**DIG.B** [ton/h]		**RWGS.LP** [ton/h]		**RWGS.HP** [ton/h]		**SOEC.LP** [ton/h]		**SOEC.HP** [ton/h]	
Liq.	Wax	Liq.	Wax	Liq.	Wax	Liq.	Wax	Liq.	Wax	Liq.	Wax
365	69	469	99	731	362	529	250	722	351	531	251

In accordance with the techno-economic analysis results, the configurations that would provide the higher benefit to generate synthetic hydrocarbons are RWGS.LP and SOEC.LP for CO_2 from biogas, and DIG.B for digestate material. Moreover, the biogas-CO_2 configurations outperform the digestate ones, given the lower availability of feedstock material in the second case.

Moreover, data on the exact demand for paraffin waxes worldwide are scarce. However, considering the global demand for waxes, Suaria et al. [304] reported a global production at the year 2018 of 4.79 million tons, with a market value of 6.7 billion $. Such a market size is compliant with the Grand View Research data [45], which forecasted a rise in the global paraffin waxes market from 5.1 billion€ of 2018 to approximately 7.4 billion€ in 2025.

With respect to these data, DIG.B and SOEC.LP configurations (i.e., the two most economically viable routes per feedstock) could provide 831.6 kton/y and 2948.4 kton/y of waxes, respectively. Hence, if we were to exploit the full potential of biogas and digestate, 78.9% of the wax demand could be covered from non-fossil sources.

5.3 CO_2 and digestate potential from biomethane plants

5.3.1 Capture technologies and substrates share

Concerning the data available about biomethane plants (i.e., biogas plants with upgrading unit, connected to the gas grid), the European Biomethane Map provides detail about the type of substrate utilized in the anaerobic digestion process, the technology employed for the carbon dioxide recovery, and the amount of biomethane provided by each plant [57]. Table 50 lists the capture technologies (and their mean capture efficiency [305–309]) and the substrates utilized in the biomethane plants throughout Europe. For these, it was assumed a biogas composition of 60:40 of CH_4:CO_2. Landfill substrate data were accounted for only in the production of biogas and its upgrade to CO_2.

Table 50. Substrates and upgrading technologies utilized for the biogas plants in Europe.

Capture technology		η_{capt}	**Substrate**	
Physical Scrubbing	PHS	*85%*	Agricultural waste	AGR
Chemical Scrubbing	CHS	*95%*	Energy crops	ENC
Membrane	MEM	*95%*	Industrial waste	FAB
Cryogenic Sep	CRY	*98%*	Sewage	SWW
Press Swing Adsorption	PSA	*90%*	Municipal solid waste	MSW
Water Scrubbing	WAS	*85%*	Landfill	LAN

The total number of biomethane plants analysed is 742. With respect to the share of capture technologies, membranes and water scrubbing represent the leading upgrading technologies, followed by chemical scrubbing, pressure swing adsorption, physical scrubbing, and cryogenic separation (Figure 69). Accounting for the different substrates, energy crops and agricultural wastes are the main ones utilized for the anaerobic digestion process (33% and 29% of the biomethane plants, respectively). Only 2% of the plants (i.e., 14 biomethane plants) utilize landfill as the preferential substrate.

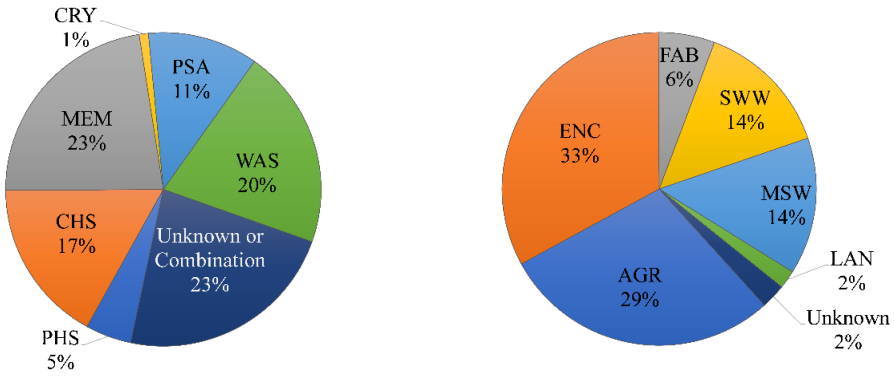

Figure 69. Share of capture technologies (left) and anaerobic digestion substrates (right) utilized in biomethane plants installed in Europe [57].

The total out-take potential of these plants is 419 t/h and 357 t/h of CO_2 and digestate, respectively. The share of production depending on the location is provided in Figure 70. Germany is the country with the highest potential out-take of useful non-fossil streams, followed by the UK, Switzerland, and France.

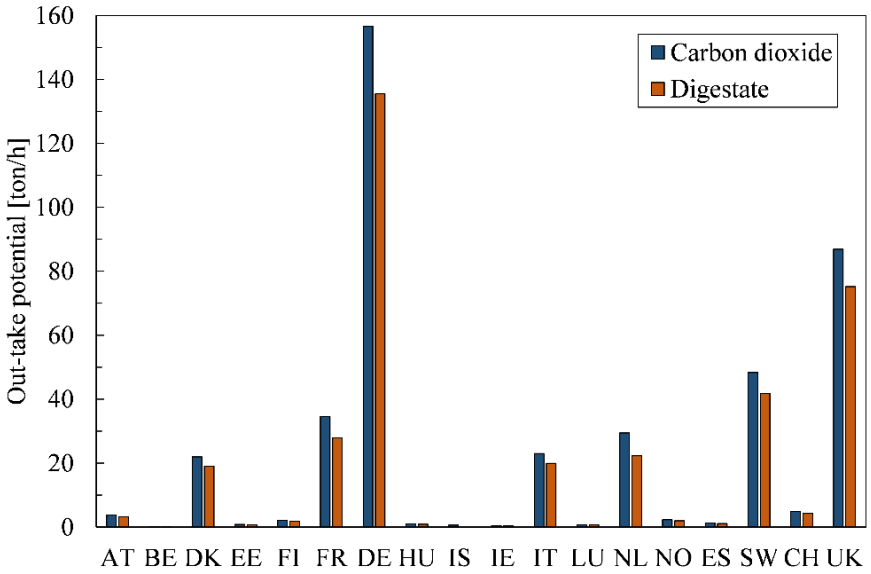

Figure 70. Potential out-take of CO_2 and digestate (dry) from the operating biomethane plants in Europe (end of the year 2019).

5.3.2 Potential for Fischer-Tropsch products from biomethane plants

The production of Fischer-Tropsch material from utilizing the CO_2 stream and digestate available from the biomethane plants is provided in Table 51. The total wax production from DIG.B and SOEC.LP would correspond to 8.29% (39.7 kton/y) of the global paraffin demand.

Table 51. Potential production of FT compounds utilizing biomethane plants CO_2 and digestate flows.

DIG.A [ton/h]		**DIG.B** [ton/h]		**RWGS.LP** [ton/h]		**RWGS.HP** [ton/h]		**SOEC.LP** [ton/h]		**SOEC.HP** [ton/h]	
Liq.	Wax	Liq.	Wax	Liq.	Wax	Liq.	Wax	Liq.	Wax	Liq.	Wax
46.8	8.9	63.5	12.6	72.4	35.8	52.4	24.8	71.5	34.7	52.6	24.8

The FT production trend is the same as the one presented in Table 49 for the biogas plants, with a lower synthesis of FT compounds due to the lower amount of stream available with biomethane plants. However, it is important to point out that this is a *ready-to-use* stream that would otherwise be vented to the atmosphere, specifically for the stream of carbon dioxide. Moreover, the integration of the biogas upgrading unit provided in Chapter 4 with the downstream FT reactor is analysed only in terms of energy integration. Hence, the FT production data are compatible with any biogas upgrading unit in terms of mass balance. However, if the potential production of FT hydrocarbons were narrowed down to only the plants presenting a chemical scrubbing upgrading unit, the production would sensibly reduce (Table 52 – digestate process route could be implemented regardless of the biogas upgrading unit).

Table 52. Potential production of FT compounds utilizing biomethane CO_2 only from the plants with an existing chemical scrubbing unit.

CO_2 Out-take [ton/h]	**RWGS.LP** [ton/h]		**RWGS.HP** [ton/h]		**SOEC.LP** [ton/h]		**SOEC.HP** [ton/h]	
88.7	Liq.	Wax	Liq.	Wax	Liq.	Wax	Liq.	Wax
	15.3	7.58	11.1	5.24	15.1	7.35	11.1	5.25

5.3.3 Matching process modeling results with geographical locations

With the data available from the open literature, it is also possible to identify the plant locations that match the hypotheses of the techno-economic analyses:

- Minimum CO_2 flow available for further processing of 1 ton/h.
- Minimum digestate flow for gasification of 881 kg_{dry}/h.

In this regard, a total number of 73 biomethane plants have been identified across Europe, providing a total CO_2 and digestate out-take potential of 137 ton/h and 119 ton/h, respectively, and a production of waxes of 11.4 t/h and 4.20 t/h with SOEC.LP and DIG.B process routes. These are presented in Figure 71 and Figure 72. The evaluation assumes the installation of both a biogas-to-FT plant and a digestate-to-FT one to avoid any transportation costs and related emissions. However, transportation of digestate material from one plant to another might be more feasible than CO_2 gas transport, making the potential production of FT material from digestate viable from all the biomethane plants in Europe.

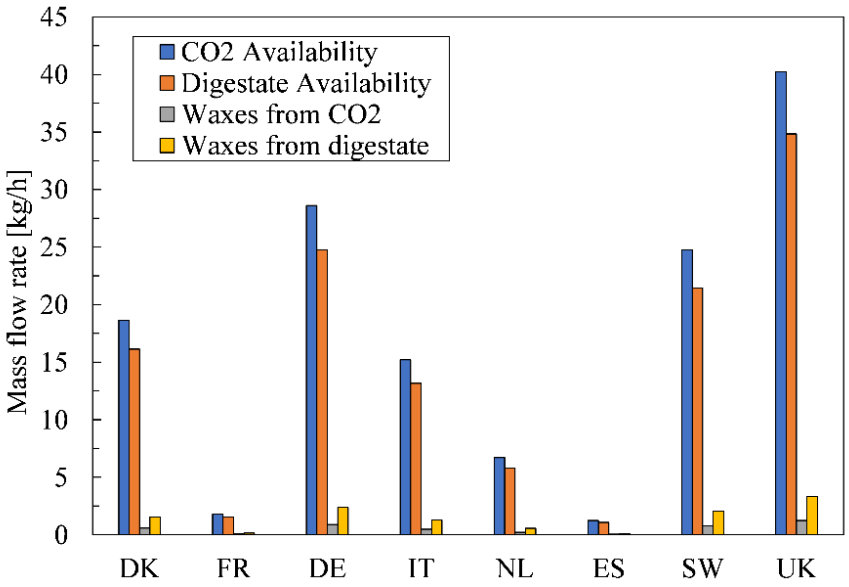

Figure 71. Share of the carbon dioxide and digestate availability, and wax potential production for the countries compliant with the techno-economic results and assumptions.

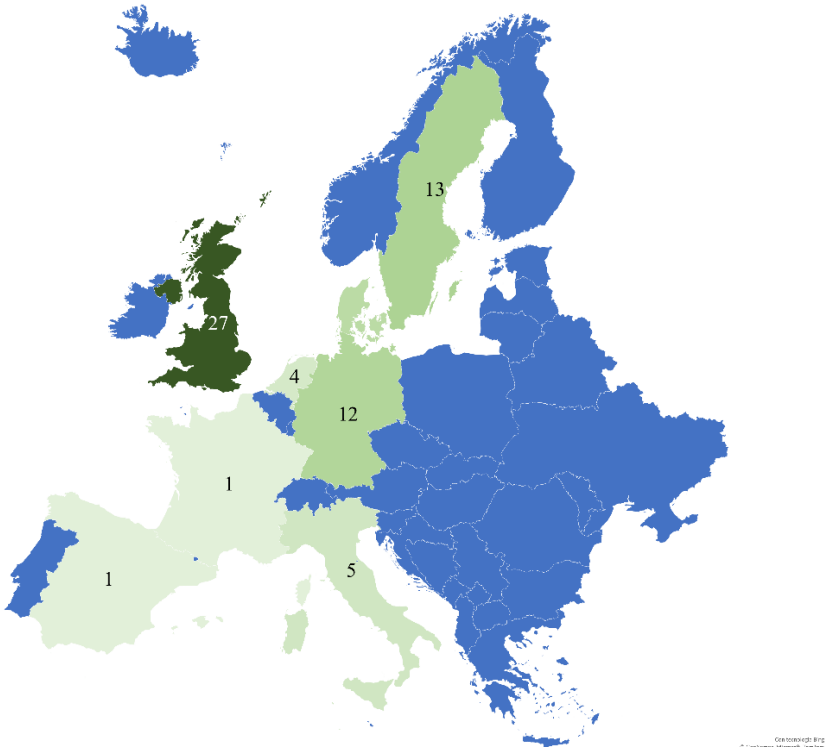

Figure 72. Map of economically feasible locations (green areas) for biomethane plants to produce waxes in Europe.

Lastly, slightly different economic schemes may exist in Spain, the UK, Netherlands, Sweden, and France about incentive solutions for biomethane. Hence, only considering Germany and Italy it is possible to identify 17 plants with feasible market entry characteristics to produce the FT waxes (Table 53).

Table 53. Preferential plant location for Germany and Italy providing at least 1 t/h of carbon dioxide and 881 kg/h of digestate material.

State	**Plant Location**	**CO_2 stream** [t/h]	**Digestate stream** [t/h]	**DIG.B waxes** [t/h]	**SOEC.LP waxes** [t/h]
Germany	Aiterhofen Niederbayern	1.35	1.17	0.041	0.112
Germany	Dargun	1.54	1.34	0.047	0.128
Germany	Güstrow	6.34	5.49	0.194	0.525
Germany	Horn Bad Meinberg	1.38	1.20	0.042	0.114
Germany	Industriepark Hoechst	1.04	0.90	0.032	0.086
Germany	Könnern 2	2.28	1.97	0.070	0.189
Germany	Schwaigern	1.23	1.06	0.038	0.102
Germany	Schwandorf	1.35	1.17	0.041	0.112
Germany	Schwedt	3.80	3.29	0.116	0.315
Germany	Wolnzach	1.36	1.18	0.042	0.113
Germany	Zörbig 1	3.80	3.29	0.116	0.315
Germany	Zörbig 2	3.14	2.72	0.096	0.260
Italy	Montello	4.91	4.25	0.150	0.407
Italy	Este	2.62	2.27	0.080	0.217
Italy	Maniago	3.93	3.40	0.120	0.325
Italy	Faenza	2.62	2.27	0.080	0.217
Italy	Sant'Agata Bolognese	1.12	0.97	0.034	0.093

5.4 Outlook

From the data available in this chapter, it is possible to assess the optimal locations in Europe to produce FT waxes utilizing process schemes like the ones presented in Chapter 3 and Chapter 4. The analysis is influenced by the typology of the plant (i.e., with or without biogas upgrading already installed at the plant location) and by the data available in the open literature, intended as clustered data for each analysed State, or detailed data for each plant.

When assessing the full potential of the biogas plants operating in Europe, it is possible to cover up to 79% of the worldwide paraffin demand, synthetizing waxes from non-fossil sources.

When accounting for the biomethane plants installed in Europe, the potential throughput of synthetic material is slightly lower. However, specific locations can be identified in Europe with *ready-to-use* non-fossil streams that match the techno-economic assumptions and results (i.e., presenting a suitable amount of carbon dioxide and digestate material).

Lastly, accounting for the actual potential of the biogas and biomethane plants in Europe might not be straightforward and might be subjected to specific investigation assumptions. However, the key point is that the carbon dioxide and digestate currently available from the anaerobic digestion processes represent two crucial feedstocks for substituting fossil feedstocks.

Chapter 6

Conclusions

The need to reduce the emissions of carbon dioxide towards the environment has led to the study of a wide variety of process applications that can directly or indirectly impact the concentration of CO_2 in the air. Parallelly, every-day life still highly relies on hydrocarbon materials to produce consumer goods and guarantee societal services like transportation. Hence, it is of paramount importance to identify feasible process solutions that can positively affect the CO_2 released into the atmosphere and secure non-fossil hydrocarbons production. These two conditions can be coupled together into carbon capture and utilization routes promoting the *circular economy* concept. CCU solutions investigate the possibility of transforming waste carbon material into synthetic compounds. Simultaneously, the circular economy allows for the continuous circulation of non-fossil carbon material and avoids fossil fuel consumption.

In this framework, the present analysis investigated the conversion of non-fossil carbon feedstocks into marketable Fischer-Tropsch hydrocarbons. The investigation aimed to identify the most promising and market-ready process routes from both a technical and economic perspective, employing both kinetic and process modelling.

Validated Fischer-Tropsch experimental data have been utilized as the starting point of the analysis. Kinetic modelling activities presented in Chapter 2 provided the performance of a Co-Pt/γ-Al_2O_3 catalyst. Different industrial-like conditions (Fischer-Tropsch operating temperature and pressure) and several inlet syngas compositions have been utilized to collect data about the yield of formation of the FT hydrocarbons. Moreover, these data have been engaged to derive a kinetic model capable of describing the FT product distribution. A combination of global and local optimization steps in non-linear least-squared fitting routes allowed for the definition of product formation rates and reactants consumption rates with a MARR of 41.2%. The selected kinetic model provided detailed information on the synthesis of n-paraffins up to carbon number C_{80} and α-olefins up to C_{40}.

Kinetic information was transferred into process modelling, exploring Fischer-Tropsch hydrocarbons synthesis from non-fossil carbon feedstocks (Chapter 3 and Chapter 4). Specifically, the conversion of the CO_2 content of biogas and air and the carbon content of digestate biomass was investigated.

For each feedstock, several process designs were studied for a total of 11 carbon conversion routes. From the conversion of biogas, configuration RWGS.LP and SOEC.LP were comparable in terms of FT material output and with a similar potential impact on reducing CO_2 emissions towards the environment. From 1000 kg/h of CO_2, RWGS.LP provided 85.7 kg/h of waxes against 83.1 kg/h of SOEC.LP. Furthermore, RWGS.LP had a CO_2 conversion of 81.1%, while SOEC.LP 79.6%. Moreover, it was concluded that low-pressure operations of the syngas generators (i.e., alkaline+RWGS or SOEC) were superior to high-pressure solutions to match the operating condition of the FT reactor. Additionally, from a technical point of view, having a solution with high recirculation rates of the FT off-gas positively impacted the production of Fischer-Tropsch material.

Utilizing digestate as the feedstock of carbon material, DIG.A allowed reaching 24.8 $kg_{wax}/ton_{dry.biom}$ and process efficiency of 50.9%, while DIG.B provided 35.4 $kg_{wax}/ton_{dry.biom}$ and process efficiency of 56.3%. This suggests that is more effective to convert off-gas into FT liquids and waxes (DIG.B) rather than producing electricity for internal consumption (DIG.A).

In the case of air carbon feedstock, it was possible to avoid the use of fossil natural gas to run the capture process with the HT-DAC technology using an electrified DAC or high recirculation of the FT off-gas. With the electrified solution (DAC.4) it was possible to produce up to 73.9 t_{wax}/kt_{CO2}. With recirculation of the FT off-gas (DAC.5) 48.1 t_{wax}/kt_{CO2} were outputted. System efficiencies ranged from 22.6% to 36.5%.

From an economic point of view, the production of FT waxes was assessed at different discount rate values. RWGS.LP, SOEC.LP, SOEC.HP, and DIG.B reached feasible production costs, comparable with the traditional fossil route. Among them, SOEC.LP provided the lowest price of wax production with a discount rate of 7.50% (0.79 €/kg_{wax} when purchasing electricity at 41.1 €/MWh). DAC process configurations had non-market-ready costs to synthesize waxes. Moreover, the most impacting element was represented by the cost of electricity, depending on the source of production. Additionally, it was found out that in the years 2050, all digestate and biogas configurations would reach a well-below fossil threshold wax production cost. The DAC solution would need statal incentives to reach a feasible cost.

The implementation of the biogas-to-FT and digestate-to-FT routes was also assessed at different locations in Europe (Chapter 5). The potential production of FT waxes was investigated based on the current potential availability of CO_2 and digestate material derived from the process of anaerobic digestion in biogas plants. The potential out-take of FT wax from biogas CO_2 corresponds to 362 t/h,

from digestate to 99 t/h, covering almost 80% of the world demand for waxes. The same potential production was studied considering the *ready-to-use* CO_2 and digestate in plants denominated as biomethane plants (i.e., where the upgrading of biogas to CH_4 and CO_2 is existing at the current date). 35.8 t/h and 12.6 t/h can be produced from biogas-CO_2 and digestate, respectively. Finally, 17 plants throughout Europe have been identified as suitable locations for installing the CCU plants converting biogas and digestate proposed with this work.

Outlook

Future applications of the present investigation may range from Fischer-Tropsch kinetic level to on-field verification of the proposed concept routes. Specifically, modifications to the current Fischer-Tropsch kinetic mechanism and methodology should investigate the possibility of directly utilizing CO_2 into the FT reactor and studying the effect of water on the product distribution (i.e., water coming from the syngas generation units). Accordingly, modifications to the process model layouts can be provided. Moreover, to assess the potential benefits of these routes, on-field applications will be needed. In this context, the implementation of pilot plants at selected locations will allow gathering enough experimental data to validate the model results, expand the reliability of the present analysis, and increase the technology readiness level of CCU routes Fischer-Tropsch.

Finally, it is possible to point out how carbon capture and utilization routes can be a feasible solution to tackle the carbon transition issues and reduce the human impact on the environment. Additionally, CCU processes represent a pathway for everyday use hydrocarbons synthesis, among which Fischer-Tropsch can be a means to decarbonize several sectors at once. Hence, depending on the carbon feedstock and process design, marketable production of FT compounds can be reached, substituting fossil counterparts. Lastly, it is of utmost importance to study details of thermochemical and electrochemical processes that can contribute to this production. As such, combining kinetic information with process modelling tools allows identifying the most market-ready configurations to offset fossil compounds and favour the circular economy of the carbon molecule.

References

[1] Iea. Putting CO_2 to Use Creating value from emissions. 2019.

[2] Masson-Delmotte V, Zhai P, Pörtner H-O, Roberts D, Skea J, Shukla PR, et al. Global warming of 1.5°C: An IPCC Special Report on the impacts of global warming of 1.5°C above pre-industrial levels and related global greenhouse gas emission pathways, in the context of strengthening the global response to the threat of climate change,. Intergov Panel Clim Chang 2018.

[3] Crippa M, Oreggioni G, Guizzardi, D., Muntean, Schaaf, et al. Fossil CO2 and GHG emissions of all world countries. Publ Off Eur Union 2019:239. https://doi.org/10.2760/687800.

[4] JRC Data Catalogue - European Commission n.d. https://data.jrc.ec.europa.eu/dataset/488dc3de-f072-4810-ab83-47185158ce2a/resource/a860a0e1-09d2-4690-9191-33fb4aeb9578 (accessed November 26, 2020).

[5] Cormos A-M, Dragan S, Petrescu L, Sandu V, Cormos C-C. Techno-Economic and Environmental Evaluations of Decarbonized Fossil-Intensive Industrial Processes by Reactive Absorption & Adsorption CO_2 Capture Systems. Energies 2020;13:1268. https://doi.org/10.3390/en13051268.

[6] Mikulčić H, Ridjan Skov I, Dominković DF, Wan Alwi SR, Manan ZA, Tan R, et al. Flexible Carbon Capture and Utilization technologies in future energy systems and the utilization pathways of captured CO2. Renew Sustain Energy Rev 2019. https://doi.org/10.1016/j.rser.2019.109338.

[7] Jones CR, Olfe-Kräutlein B, Naims H, Armstrong K, Jones CR. The Social Acceptance of Carbon Dioxide Utilisation : A Review and Research Agenda. Front Energy Res 2017;5:1–13. https://doi.org/10.3389/fenrg.2017.00011.

[8] EC. A new Circular Economy Action Plan. 2020.

[9] Keith DW, Holmes G, St. Angelo D, Heidel K. A Process for Capturing CO_2 from the Atmosphere. Joule 2018;2:1573–94. https://doi.org/10.1016/j.joule.2018.05.006.

[10] Mohammad M, Isaifan RJ, Weldu YW, Rahman MA, Al-Ghamdi SG. Progress on carbon dioxide capture, storage and utilisation. Int J Glob Warm 2020;20:124–44. https://doi.org/10.1504/IJGW.2020.105386.

[11] Mikulčić H, Skov IR, Dominković DF, Rafidah S, Alwi W, Manan ZA, et al. Flexible Carbon Capture and Utilization technologies in future energy systems and the utilization pathways of captured CO 2 2019. https://doi.org/10.1016/j.rser.2019.109338.

[12] Rafiee A, Khalilpour KR, Milani D. CO2 Conversion and Utilization Pathways. Elsevier Inc.; 2018. https://doi.org/10.1016/b978-0-12-813306-4.00008-2.

[13] Alper E, Yuksel Orhan O. CO2 utilization: Developments in conversion processes. Petroleum 2017;3:109–26. https://doi.org/10.1016/j.petlm.2016.11.003.

[14] Panzone C, Philippe R, Chappaz A, Fongarland P, Bengaouer A. Power-to-

Liquid catalytic CO_2 valorization into fuels and chemicals: focus on the Fischer-Tropsch route. J CO_2 Util 2020;38:314–47. https://doi.org/10.1016/j.jcou.2020.02.009.

[15] Salomone F, Giglio E, Ferrero D, Santarelli M, Pirone R, Bensaid S. Techno-economic modelling of a Power-to-Gas system based on SOEC electrolysis and CO_2 methanation in a RES-based electric grid. Chem Eng J 2019;377. https://doi.org/10.1016/j.cej.2018.10.170.

[16] Trieb F, Moser M, Kern J. Liquid Solar Fuel e Liquid hydrocarbons from solar energy and biomass 2018. https://doi.org/10.1016/j.energy.2018.04.027.

[17] Chauvy R, De Weireld G. CO2 Utilization Technologies in Europe: A Short Review. Energy Technol 2020;2000627:1–17. https://doi.org/10.1002/ente.202000627.

[18] Jarvis SM, Samsatli S. Technologies and infrastructures underpinning future CO_2 value chains: A comprehensive review and comparative analysis. Renew Sustain Energy Rev 2018;85:46–68. https://doi.org/10.1016/j.rser.2018.01.007.

[19] Sandalow D, Aines R, Friedmann J, McCormick C, McCoy S. Carbon Dioxide Utilization (CO2U) - Icef Roadmap 2.0. ICEF 2017.

[20] Pérez-Fortes M, Schöneberger JC, Boulamanti A, Tzimas E. Methanol synthesis using captured CO2 as raw material: Techno-economic and environmental assessment. Appl Energy 2016;161:718–32. https://doi.org/10.1016/j.apenergy.2015.07.067.

[21] Zhang Z, Pan SY, Li H, Cai J, Olabi AG, Anthony EJ, et al. Recent advances in carbon dioxide utilization. Renew Sustain Energy Rev 2020. https://doi.org/10.1016/j.rser.2020.109799.

[22] Lehtonen J, Järnefelt V, Alakurtti S, Arasto A, Hannula I, Harlin A, et al. The Carbon Reuse Economy: Transforming CO_2 from a pollutant into a resource. VTT Tech Res Cent Finl 2019. https://doi.org/10.32040/2019.978-951-38-8709-4.

[23] Bos MJ, Kersten SRA, Brilman DWF. Wind power to methanol: Renewable methanol production using electricity, electrolysis of water and CO2 air capture. Appl Energy 2020;264:114672. https://doi.org/10.1016/j.apenergy.2020.114672.

[24] Tian P, Wei Y, Ye M, Liu Z. Methanol to olefins (MTO): From fundamentals to commercialization. ACS Catal 2015;5:1922–38. https://doi.org/10.1021/acscatal.5b00007.

[25] Butera G, Jensen SH, Clausen LR. A novel system for large-scale storage of electricity as synthetic natural gas using reversible pressurized solid oxide cells. Energy 2019:738–54. https://doi.org/10.1016/j.energy.2018.10.079.

[26] Rozzi E, Minuto FD, Lanzini A, Leone P. Green synthetic fuels: Renewable routes for the conversion of non-fossil feedstocks into gaseous fuels and their end uses. Energies 2020;13. https://doi.org/10.3390/en13020420.

[27] Küngas R. Review-Electrochemical CO_2 Reduction for CO Production: Comparison of Low-and High-Temperature Electrolysis Technologies. J Electrochem Soc 2020;167. https://doi.org/10.1149/1945-7111/ab7099.

[28] Marchese M, Giglio E, Santarelli M, Lanzini A. Energy performance of

Power-to-Liquid applications integrating biogas upgrading, reverse water gas shift, solid oxide electrolysis and Fischer-Tropsch technologies. Energy Convers Manag X 2020:100041. https://doi.org/10.1016/j.ecmx.2020.100041.

[29] Hannula I, Kaisalo N, Simell P. Preparation of Synthesis Gas from CO2 for Fischer–Tropsch Synthesis—Comparison of Alternative Process Configurations. C—Journal Carbon Res 2020;6:55. https://doi.org/10.3390/c6030055.

[30] Global CO2 Initiative, CO2 Sciences Inc. Global Roadmap for Implementing CO2 Utilization. Report 2016:20534.

[31] Cuéllar-Franca R, García-Gutiérrez P, Dimitriou I, Elder RH, Allen RWK, Azapagic A. Utilising carbon dioxide for transport fuels: The economic and environmental sustainability of different Fischer-Tropsch process designs. Appl Energy 2019;253:113560. https://doi.org/10.1016/j.apenergy.2019.113560.

[32] European Commission. COMMUNICATION FROM THE COMMISSION TO THE EUROPEAN PARLIAMENT, THE EUROPEAN COUNCIL, THE COUNCIL, THE EUROPEAN ECONOMIC AND SOCIAL COMMITTEE AND THE COMMITTEE OF THE REGIONS: The European Green Deal 2019. https://ec.europa.eu/info/sites/info/files/european-green-deal-communication_en.pdf (accessed November 2, 2020).

[33] Abanades JC, Herzog HJ, Rubin ES, Mazzotti M. Environmental Science On the climate change mitigation potential of CO 2 conversion to fuels. Energy Environ Sci 2017. https://doi.org/10.1039/C7EE02819A.

[34] Chauvy R, Meunier N, Thomas D, De Weireld G. Selecting emerging CO 2 utilization products for short-to mid-term deployment. Appl Energy 2019. https://doi.org/10.1016/j.apenergy.2018.11.096.

[35] Rönsch S, Schneider J, Matthischke S, Schlüter M, Götz M, Lefebvre J, et al. Review on methanation - From fundamentals to current projects. Fuel 2016;166:276–96. https://doi.org/10.1016/j.fuel.2015.10.111.

[36] Kauw M, Benders RM, Visser C. Green methanol from hydrogen and carbon dioxide using geothermal energy and/or hydropower in Iceland or excess renewable electricity in Germany. Energy 2015. https://doi.org/10.1016/j.energy.2015.06.002.

[37] Pérez-Fortes M, Bocin-Dumitriu A, Tzimas E. CO2 utilization pathways: Techno-economic assessment and market opportunities. Energy Procedia, vol. 63, Elsevier Ltd; 2014, p. 7968–75. https://doi.org/10.1016/j.egypro.2014.11.834.

[38] CarbonCure Technologies | From Carbon to Simply Better Concrete n.d. https://www.carboncure.com/ (accessed November 5, 2020).

[39] Patricio J, Angelis-Dimakis A, Castillo-Castillo A, Kalmykova Y, Rosado L. Method to identify opportunities for CCU at regional level - Matching sources and receivers. J CO2 Util 2017;22:330–45. https://doi.org/10.1016/j.jcou.2017.10.009.

[40] Valdovinos-García EM, Barajas-Fernández J, de los Ángeles Olán-Acosta M, Petriz-Prieto MA, Guzmán-López A, Bravo-Sánchez MG. Techno-Economic Study of CO2 Capture of a Thermoelectric Plant Using Microalgae (Chlorella vulgaris) for Production of Feedstock for Bioenergy.

Energies 2020;13:1–19. https://doi.org/10.3390/en13020413.
[41] Hepburn C, Adlen E, Beddington J, Carter EA, Fuss S, Mac Dowell N, et al. The technological and economic prospects for CO2 utilization and removal. Nature 2019;575:87–97. https://doi.org/10.1038/s41586-019-1681-6.
[42] Trippe F, Fröhling M, Schultmann F, Stahl R, Henrich E, Dalai A. Comprehensive techno-economic assessment of dimethyl ether (DME) synthesis and Fischer-Tropsch synthesis as alternative process steps within biomass-to-liquid production. Fuel Process Technol 2013;106:577–86. https://doi.org/10.1016/j.fuproc.2012.09.029.
[43] Herz G, Reichelt E, Jahn M. Techno-economic analysis of a co-electrolysis-based synthesis process for the production of hydrocarbons. Appl Energy 2018;215:309–20. https://doi.org/10.1016/j.apenergy.2018.02.007.
[44] Ail SS, Dasappa S. Investigations into enhanced wax production with combustion synthesized Fischer-Tropsch catalysts. Energy Convers Manag 2016;116:80–90. https://doi.org/10.1016/j.enconman.2016.02.075.
[45] Grand View Research 1. Global Paraffin Wax Market. 2019.
[46] Gutberlet H. FT Waxes – the Next Generation of Candle Fuel. Sasol n.d.
[47] Sasol. Sasol Limited Group Production and sales metrics. 2018.
[48] Korhonen J, Honkasalo A, Seppälä J. Circular Economy: The Concept and its Limitations 2017. https://doi.org/10.1016/j.ecolecon.2017.06.041.
[49] Song C, Zhang C, Zhang S, Lin H, Kim Y, Ramakrishnan M, et al. Thermochemical liquefaction of agricultural and forestry wastes into biofuels and chemicals from circular economy perspectives 2020. https://doi.org/10.1016/j.scitotenv.2020.141972.
[50] Sutter D, Van Der Spek M, Mazzotti M. 10th Anniversary: Evaluation of CO 2-Based and CO 2-Free Synthetic Fuel Systems Using a Net-Zero-CO 2-Emission Framework. Ind Eng Chem Res 2019. https://doi.org/10.1021/acs.iecr.9b00880.
[51] IEA. Energy Technology Perspectives 2020. 2020. https://doi.org/10.1787/ab43a9a5-en.
[52] Dieterich V, Buttler A, Hanel A, Spliethoff H, Fendt S. Power-to-liquid: Via synthesis of methanol, DME or Fischer-Tropsch-fuels: A review. Energy Environ Sci 2020;13:3207–52. https://doi.org/10.1039/d0ee01187h.
[53] Kirsch H, Lochmahr N, Staudt C, Pfeifer P, Dittmeyer R. Production of CO2-neutral liquid fuels by integrating Fischer-Tropsch synthesis and hydrocracking in a single micro-structured reactor: Performance evaluation of different configurations by factorial design experiments. Chem Eng J 2020;393:124553. https://doi.org/10.1016/j.cej.2020.124553.
[54] Vidal Vázquez F, Pfeifer P, Lehtonen J, Piermartini P, Simell P, Alopaeus V. Catalyst Screening and Kinetic Modeling for CO Production by High Pressure and Temperature Reverse Water Gas Shift for Fischer-Tropsch Applications. Ind Eng Chem Res 2017;56:13262–72. https://doi.org/10.1021/acs.iecr.7b01606.
[55] Arning K, Offermann-van Heek J, Sternberg A, Bardow A, Ziefle M. Risk-benefit perceptions and public acceptance of Carbon Capture and Utilization. Environ Innov Soc Transitions 2019. https://doi.org/10.1016/j.eist.2019.05.003.

[56] Rodin V, Lindorfer J, Böhm H, Vieira L. Assessing the potential of carbon dioxide valorisation in Europe with focus on biogenic CO 2. J CO2 Util 2020. https://doi.org/10.1016/j.jcou.2020.101219.
[57] EBA-GIE. European Biomethane MAP – Infrastructure for biomethane production 2020. Gas Infrastruct Eur 2020:1.
[58] European Biogas Association. EBA Statistical Report: 2019 European Overview. 2020.
[59] International Energy Agency (IEA). Outlook for biogas and biomethane. 2020. https://doi.org/10.1787/040c8cd2-en.
[60] Lyng KA, Skovsgaard L, Jacobsen HK, Hanssen OJ. The implications of economic instruments on biogas value chains: a case study comparison between Norway and Denmark. Environ Dev Sustain 2020;22:7125–52. https://doi.org/10.1007/s10668-019-00463-9.
[61] Klackenberg L. Biomethane in Sweden-market overview & policies. Swedish Gas Assoc 2019.
[62] Baena-Moreno FM, Rodríguez-Galán M, Vega F, Alonso-Fariñas B, Vilches Arenas LF, Navarrete B. Energy Sources, Part A: Recovery, Utilization, and Environmental Effects Carbon capture and utilization technologies: a literature review and recent advances. Energy Sources, Part A Recover Util Environ Eff 2018. https://doi.org/10.1080/15567036.2018.1548518.
[63] Corden C, Bougas K, Cunningham E, Tyrer D, Kreißig J, Zetti E, et al. Digestate and compost as fertilisers: Risk assessment and risk management options. 2019.
[64] Antoniou N, Monlau F, Sambusiti C, Ficara E, Barakat A, Zabaniotou A. Contribution to Circular Economy options of mixed agricultural wastes management: Coupling anaerobic digestion with gasification for enhanced energy and material recovery. J Clean Prod 2019;209:505–14. https://doi.org/10.1016/j.jclepro.2018.10.055.
[65] Freda C, Nanna F, Villone A, Barisano D, Brandani S, Cornacchia G. Air gasification of digestate and its co-gasification with residual biomass in a pilot scale rotary kiln. Int J Energy Environ Eng 2019;10:335–46. https://doi.org/10.1007/s40095-019-0310-3.
[66] Giuliano A, Catizzone E, Freda C, Cornacchia G. Valorization of OFMSW digestate-derived syngas toward methanol, hydrogen, or electricity: Process simulation and carbon footprint calculation. Processes 2020;8:526. https://doi.org/10.3390/PR8050526.
[67] Meylan FD, Moreau V, Erkman S. CO2 utilization in the perspective of industrial ecology, an overview. J CO2 Util 2015. https://doi.org/10.1016/j.jcou.2015.05.003.
[68] Fasihi M, Efimova O, Breyer C. Techno-economic assessment of CO_2 direct air capture plants. J Clean Prod 2019;224:957–80. https://doi.org/10.1016/j.jclepro.2019.03.086.
[69] Reverse climate change by removing CO2 from the air. n.d. https://www.climeworks.com/co2-removal/ (accessed January 4, 2021).
[70] Keith DW. Why capture CO_2 from the atmosphere? Science (80-) 2009;325:1654–5. https://doi.org/10.1126/science.1175680.
[71] STORE&GO | STORE&GO n.d. https://www.storeandgo.info/ (accessed November 6, 2020).

[72] Vidal Vázquez F, Koponen J, Ruuskanen V, Bajamundi C, Kosonen A, Simell P, et al. Power-to-X technology using renewable electricity and carbon dioxide from ambient air: SOLETAIR proof-of-concept and improved process concept. J CO_2 Util 2018;28:235–46. https://doi.org/10.1016/j.jcou.2018.09.026.

[73] ICO2CHEM Project CORDIS. From industrial CO2 streams to added value Fischer-Tropsch chemicals: H2020 Eur Comm 2020. https://cordis.europa.eu/project/id/768543/it (accessed December 3, 2020).

[74] Bekker M, Louw NR, Jansen Van Rensburg VJ, Potgieter J. The benefits of Fischer-Tropsch waxes in synthetic petroleum jelly. Int J Cosmet Sci 2013;35:99–104. https://doi.org/10.1111/ics.12011.

[75] Decker M, Schorn F, Samsun RC, Peters R, Stolten D. Off-grid power-to-fuel systems for a market launch scenario – A techno-economic assessment. Appl Energy 2019;250:1099–109. https://doi.org/10.1016/j.apenergy.2019.05.085.

[76] König DH, Freiberg M, Dietrich R-U, Wörner A. Techno-economic study of the storage of fluctuating renewable energy in liquid hydrocarbons. Fuel 2015. https://doi.org/10.1016/j.fuel.2015.06.085.

[77] Fischer N, Clapham B, Feltes T, Claeys M. Cobalt-Based Fischer-Tropsch Activity and Selectivity as a Function of Crystallite Size and Water Partial Pressure. ACS Catal 2015;5:113–21. https://doi.org/10.1021/cs500936t.

[78] Okeson TJ, Keyvanloo K, Lawson JS, Argyle MD, Hecker WC. On the kinetics and mechanism of Fischer-Tropsch synthesis on a highly active iron catalyst supported on silica-stabilized alumina. Catal Today 2016;261:67–74. https://doi.org/10.1016/j.cattod.2015.08.054.

[79] Piermartini P, Boeltken T, Selinsek M, Pfeifer P. Influence of channel geometry on Fischer-Tropsch synthesis in microstructured reactors. Chem Eng J 2017;313:328–35. https://doi.org/10.1016/j.cej.2016.12.076.

[80] Seyednejadian S, Rauch R, Bensaid S, Hofbauer H, Weber G, Saracco G, et al. Power to Fuels: Dynamic Modeling of a Slurry Bubble Column Reactor in Lab-Scale for Fischer Tropsch Synthesis under Variable Load of Synthesis Gas. Appl Sci 2018;8:514. https://doi.org/10.3390/app8040514.

[81] Albrecht FG, König DH, Baucks N, Dietrich RU. A standardized methodology for the techno-economic evaluation of alternative fuels – A case study. Fuel 2017;194:511–26. https://doi.org/10.1016/j.fuel.2016.12.003.

[82] Marchese M, Heikkinen N, Giglio E, Lanzini A, Lehtonen J, Reinikainen M. Kinetic Study Based on the Carbide Mechanism of a Co-Pt/γ-Al_2O_3 Fischer–Tropsch Catalyst Tested in a Laboratory-Scale Tubular Reactor. Catalysts 2019;9:717. https://doi.org/10.3390/catal9090717.

[83] Maitlis PM, de Klerk A. Greener Fischer-Tropsch Processes for Fuels and Feedstocks. 2013. https://doi.org/10.1002/9783527656837.

[84] Dry ME. The Fischer – Tropsch process : 1950 – 2000. Catal Today 2002;71:227–41.

[85] Loosdrecht J Van De, Botes FG, Ciobica IM, Ferreira A, Gibson P, Moodley DJ, et al. Fischer-Tropsch Synthesis : Catalysts and Chemistry. Elsevier Ltd.; 2013.

[86] Velasco JA, Lopez L, Velásquez M, Boutonnet M, Cabrera S, Järås S. Gas to liquids : A technology for natural gas industrialization in Bolivia. J Nat

Gas Sci Eng 2010;2:222–8. https://doi.org/10.1016/j.jngse.2010.10.001.
[87] Saeidi S, Nikoo MK, Mirvakili A, Bahrani S, Saidina Amin NA, Rahimpour MR. Recent advances in reactors for low-temperature Fischer-Tropsch synthesis: Process intensification perspective. Rev Chem Eng 2015;31:209–38. https://doi.org/10.1515/revce-2014-0042.
[88] Klerk A De. Can Fischer-Tropsch Syncrude Be Refined to On-Specification Diesel Fuel ? Energy Fuel 2009;75:4593–604. https://doi.org/10.1021/ef9005884.
[89] De Klerk A. Fischer-Tropsch Refining. Univ Pretoria 2012.
[90] Aresta M, Dibenedetto A, Quaranta E. State of the art and perspectives in catalytic processes for CO 2 conversion into chemicals and fuels : The distinctive contribution of chemical catalysis and biotechnology. J Catal 2016;343:2–45. https://doi.org/10.1016/j.jcat.2016.04.003.
[91] Schmidt P, Batteiger V, Roth A, Weindorf W, Raksha T. Power-to-Liquids as Renewable Fuel Option for Aviation: A Review. Chemie-Ingenieur-Technik 2018;90:127–40. https://doi.org/10.1002/cite.201700129.
[92] Van Dijk HAJ. The Fischer-Tropsch synthesis : A mechanistic study using transient isotopic tracing. PhD Thesis 2001:Appendix 4, 159. https://doi.org/10.6100/IR542426.
[93] Dry ME. Fischer-Tropsch synthesis - Industrial. Encycl Catal 2010:41–88. https://doi.org/10.1007/978-94-009-7040-3_3.
[94] Robota HJ, Richard LA, Deshmukh S, Leviness S, Leonarduzzi D, Roberts D. High Activity and Selective Fischer-Tropsch Catalysts for Use in a Microchannel Reactor. Catal Surv Asia 2014;18:177–82. https://doi.org/10.1007/s10563-014-9175-x.
[95] Rauch R, Kiennemann A, Sauciuc A. Chapter 12 - Fischer-Tropsch Synthesis to Biofuels (BtL Process). vol. #volume#. 2013. https://doi.org/10.1016/B978-0-444-56330-9.00012-7.
[96] Davis BH, Occelli ML. Fischer-Tropsch Synthesis , Catalysts , and Catalysis. CRC Press 2016.
[97] Tucker CL, van Steen E. Activity and selectivity of a cobalt-based Fischer-Tropsch catalyst operating at high conversion for once-through biomass-to-liquid operation. Catal Today 2020;342:115–23. https://doi.org/10.1016/j.cattod.2018.12.049.
[98] Botes FG, Niemantsverdriet JW, Loosdrecht J Van De. A comparison of cobalt and iron based slurry phase Fischer – Tropsch synthesis. Catal Today 2013;215:112–20. https://doi.org/10.1016/j.cattod.2013.01.013.
[99] Luque R, de la Osa AR, Campelo JM, Romero AA, Valverde JL, Sanchez P. Design and development of catalysts for Biomass-To-Liquid-Fischer–Tropsch (BTL-FT) processes for biofuels production. Energy Environ Sci 2012;5:5186–202. https://doi.org/10.1039/C1EE02238E.
[100] Steynberg A, Dry M. Fischer-Tropsch Technology.pdf. Elsevier Ltd 2004;152.
[101] Van der Laan GP, Beenackers AACM. Kinetics and Selectivity of the Fischer-Tropsch Synthesis : A Literature Review. Catal Rev 1999;4940:255–318. https://doi.org/10.1081/CR-100101170.
[102] Home | CatCost n.d. https://catcost.chemcatbio.org/ (accessed December 22, 2020).
[103] Morales BYF, Weckhuysen BM. Promotion Effects in Cobalt-based

Fischer-Tropsch Catalysis – A Review-. Catalysis 2006;19:1–40. https://doi.org/10.1039/9781847555229-00001.

[104] Garces LJ, Hincapie B, Zerger R, Suib SL. The effect of temperature and support on the reduction of cobalt oxide: An in situ x-ray diffraction study. J Phys Chem C 2015;119:5484–90. https://doi.org/10.1021/jp5124184.

[105] Khodakov AY, Chu W, Fongarland P. Advances in the development of novel cobalt Fischer-Tropsch catalysts for synthesis of long-chain hydrocarbons and clean fuels. Chem Rev 2007;107:1692–744. https://doi.org/10.1021/cr050972v.

[106] Rytter E, Tsakoumis NE, Holmen A. On the selectivity to higher hydrocarbons in Co-based Fischer-Tropsch synthesis. Catal Today 2016;261:3–16. https://doi.org/10.1016/j.cattod.2015.09.020.

[107] Parnian MJ, Taheri Najafabadi A, Mortazavi Y, Khodadadi AA, Nazzari I. Ru promoted cobalt catalyst on-Al 2 O 3 : Influence of different catalyst preparation method and Ru loadings on Fischer-Tropsch reaction and kinetics. Appl Surf Sci 2014;313:183–95. https://doi.org/10.1016/j.apsusc.2014.05.183.

[108] Cook KM, Perez HD, Bartholomew CH, Hecker WC. Effect of promoter deposition order on platinum-, ruthenium-, or rhenium-promoted cobalt Fischer-Tropsch catalysts. Appl Catal A Gen 2014;482:275–86. https://doi.org/10.1016/j.apcata.2014.05.013.

[109] Bezemer GL, Bitter JH, Kuipers HPCE, Oosterbeek H, Holewijn JE, Xu X, et al. Cobalt particle size effects in the Fischer-Tropsch reaction studied with carbon nanofiber supported catalysts. J Am Chem Soc 2006;128:3956–64. https://doi.org/10.1021/ja058282w.

[110] Den Breejen JP, Radstake PB, Bezemer GL, Bitter JH, Fr{\o}seth V, Holmen A, et al. On the Origin of the Cobalt Particle Size Effects in. J Am Chem Soc 2009;131:7197–203. https://doi.org/10.1016/j.cattod.2008.10.036.J.

[111] Gavrilović, Save, Blekkan. The Effect of Potassium on Cobalt-Based Fischer–Tropsch Catalysts with Different Cobalt Particle Sizes. Catalysts 2019;9:351. https://doi.org/10.3390/catal9040351.

[112] Eskelinen P, Keskiväli L, Heikkinen N, Franssila S. Cobalt catalyst characterization and modification by atomic layer deposition for Fischer-Tropsch synthesis. Aalto University, 2019.

[113] Oviroh PO, Akbarzadeh R, Pan D, Coetzee RAM, Jen T-C. New development of atomic layer deposition: processes, methods and applications. Sci Technol Adv Mater 2019;20:465–96. https://doi.org/10.1080/14686996.2019.1599694.

[114] Savost AP, Yakovenko RE, Narochnyi GB, Bakun VG, Sulima SI. Industrial Catalyst for the Selective Fischer – Tropsch Synthesis of Long-Chain Hydrocarbons 2017;58:81–91. https://doi.org/10.1134/S0023158417010062.

[115] Kocić S, Corral Valero M, Schweitzer J-M, Raybaud P. Surface speciation of Co based Fischer-Tropsch catalyst under reaction conditions: Deactivation by coke or by oxidation? 2019. https://doi.org/10.1016/j.apcata.2019.117332.

[116] Sadeqzadeh M, Chambrey phane, Hong J, Fongarland P, Luck F, Curulla-Ferre D, et al. Effect of Different Reaction Conditions on the Deactivation

of Alumina-Supported Cobalt Fischer−Tropsch Catalysts in a Milli-Fixed-Bed Reactor: Experiments and Modeling 2014. https://doi.org/10.1021/ie4040303.

[117] Kim YD, Yang CW, Kim BJ, Moon JH, Jeong JY, Jeong SH, et al. Fischer–tropsch diesel production and evaluation as alternative automotive fuel in pilot-scale integrated biomass-to-liquid process. Appl Energy 2016;180:301–12. https://doi.org/10.1016/j.apenergy.2016.07.095.

[118] Griboval-constant A, Lecocq V, Diehl F, Khodakov AY. Influence of operating conditions in a continuously stirred tank reactor on the formation of carbon species on alumina supported cobalt Fischer – Tropsch catalysts 2013;215:43–51. https://doi.org/10.1016/j.cattod.2013.06.014.

[119] Almeida LC, Sanz O, Merino D, Arzamendi G, Gandía LM, Montes M. Kinetic analysis and microstructured reactors modeling for the Fischer – Tropsch synthesis over a Co – Re / Al 2 O 3 catalyst. Catal Today 2013;215:103–11. https://doi.org/10.1016/j.cattod.2013.04.021.

[120] Van Der Laan GP, Beenackers AACM. Kinetics and Selectivity of the Fischer–Tropsch Synthesis: A Literature Review. Catal Rev 1999;41:255–318. https://doi.org/10.1081/CR-100101170.

[121] Lillebø AH, Rytter E, Blekkan EA, Holmen A. Fischer-Tropsch synthesis at high conversions on Al_2O_3 supported Co catalysts with different H_2/CO levels 2017. https://doi.org/10.1021/acs.iecr.7b01801.

[122] Todic B. Kinetic modeling and optimization of fixed-bed reactor for Fischer-Tropsch synthesis. Belgr Univ 2015.

[123] Iglesia E. Design, synthesis, and use of cobalt-based Fischer-Tropsch synthesis catalysts. Appl Catal A, Gen 1997;161:59–78.

[124] Saib AM, Moodley DJ, Ciobîc IM, Hauman MM, Sigwebela BH. Fundamental understanding of deactivation and regeneration of cobalt Fischer – Tropsch synthesis catalysts 2010;154:271–82. https://doi.org/10.1016/j.cattod.2010.02.008.

[125] Tsakoumis NE, Rønning M, Borg Ø, Rytter E, Holmen A. Deactivation of cobalt based Fischer – Tropsch catalysts : A review. Catal Today 2010;154:162–82. https://doi.org/10.1016/j.cattod.2010.02.077.

[126] Storsæter S, Borg, Blekkan EA, Holmen A. Study of the effect of water on Fischer-Tropsch synthesis over supported cobalt catalysts. J Catal 2005;231:405–19. https://doi.org/10.1016/j.jcat.2005.01.036.

[127] Storsæter S, Chen D, Holmen A. Microkinetic modelling of the formation of C_1 and C_2 products in the Fischer–Tropsch synthesis over cobalt catalysts. Surf Sci 2006;600f:2051–63. https://doi.org/10.1016/j.susc.2006.02.048.

[128] Ma W, Jacobs G, Sparks DE, Spicer RL, Davis BH, Klettlinger JLS, et al. Fischer–Tropsch synthesis: Kinetics and water effect study over 25%Co/Al2O3 catalysts. Catal Today 2014;228:158–66. https://doi.org/10.1016/j.cattod.2013.10.014.

[129] Rytter E, Borg Ø, Tsakoumis NE, Holmen A. Water as key to activity and selectivity in Co Fischer-Tropsch synthesis: Γ-alumina based structure-performance relationships. J Catal 2018;365:334–43. https://doi.org/10.1016/j.jcat.2018.07.003.

[130] Todic B, Nowicki L, Nikacevic N, Bukur DB. Fischer-Tropsch synthesis product selectivity over an industrial iron-based catalyst: Effect of process

conditions. Catal Today 2016;261:28–39. https://doi.org/10.1016/j.cattod.2015.09.005.
[131] James OO, Chowdhury B, Mesubi MA, Maity S. Reflections on the chemistry of the Fischer–Tropsch synthesis. RSC Adv 2012;2:7347. https://doi.org/10.1039/c2ra20519j.
[132] Krylova AY. Products of the Fischer – Tropsch Synthesis (A Review). Solid Fuel Chem 2014;48:23–36. https://doi.org/10.3103/S0361521914010030.
[133] Cheng J, Hu P, Ellis P, French S, Kelly G, Lok CM. A DFT study of the chain growth probability in Fischer–Tropsch synthesis. J Catal 2008;257:221–8. https://doi.org/10.1016/J.JCAT.2008.05.006.
[134] Lox ES, Froment GF. Kinetics of the Fischer-Tropsch Reaction on a Precipitated Promoted Iron Catalyst. 2. Kinetic Modeling. Ind Eng Chem Res 1993:71–82. https://doi.org/10.1021/ie00013a011.
[135] Shi B, Davis BH. Fischer–Tropsch synthesis: accounting for chain-length related phenomena. Appl Catal A Gen 2004;277:61–9. https://doi.org/10.1016/J.APCATA.2004.08.032.
[136] Schulz H, Claeys M. Kinetic modelling of Fischer–Tropsch product distributions. Appl Catal A Gen 1999;186:91–107. https://doi.org/10.1016/S0926-860X(99)00166-0.
[137] Iglesia E, Reyes SC, Madon RJ. Transport-Enhanced a-Olefin Readsorption Pathways in Ru-Catalyzed Hydrocarbon Synthesis 1991;6:238–56.
[138] Schulz H, Claeys M. Reactions of α-olefins of different chain length added during Fischer–Tropsch synthesis on a cobalt catalyst in a slurry reactor. Appl Catal A Gen 1999;186:71–90. https://doi.org/10.1016/S0926-860X(99)00165-9.
[139] Cheng J, Song T, Hu P, Lok CM, Ellis P, French S. A density functional theory study of the α-olefin selectivity in Fischer-Tropsch synthesis. J Catal 2008;255:20–8. https://doi.org/10.1016/j.jcat.2008.01.027.
[140] Sonal, Pant KK, Upadhyayula S. Detailed kinetics of Fischer Tropsch synthesis over Fe-Co bimetallic catalyst considering chain length dependent olefin desorption. Fuel 2019;236:1263–72. https://doi.org/10.1016/j.fuel.2018.09.087.
[141] Botes FG. Proposal of a New Product Characterization Model for the Iron-Based Low-Temperature Fischer−Tropsch Synthesis 2007. https://doi.org/10.1021/EF060483D.
[142] Kruit KD, Vervloet D, Kapteijn F, Van Ommen JR. Selectivity of the Fischer-Tropsch process: Deviations from single alpha product distribution explained by gradients in process conditions. Catal Sci Technol 2013;3:2210–3. https://doi.org/10.1039/c3cy00080j.
[143] Kuipers EW, Scheper C, Wilson JH, Vinkenburg IH, Oosterbeek H. Non-ASF Product Distributions Due to Secondary Reactions during Fischer–Tropsch Synthesis. J Catal 1996;158:288–300. https://doi.org/10.1006/JCAT.1996.0028.
[144] Moazami N, Wyszynski ML, Rahbar K, Tsolakis A, Mahmoudi H. A comprehensive study of kinetics mechanism of Fischer-Tropsch synthesis over cobalt-based catalyst. Chem Eng Sci 2017;171:32–60. https://doi.org/10.1016/j.ces.2017.05.022.

[145] Zennaro R, Tagliabue M, Bartholomew CH. Kinetics of Fischer-Tropsch synthesis on titania-supported cobalt. vol. 58. 2000.
[146] Brötz W. Zur Systematik der Fischer-Tropsch-Katalyse. Zeitschrift Für Elektrochemie Und Angew Phys Chemie 1949;53:301–6. https://doi.org/10.1002/BBPC.19490530510.
[147] Yates IC, Satterfield CN. Intrinsic Kinetics of the Fischer-Tropsch Synthesis on a Cobalt Catalyst. Energy and Fuels 1991:168–73.
[148] Ostadi M, Rytter E, Hillestad M. Evaluation of kinetic models for Fischer–Tropsch cobalt catalysts in a plug flow reactor. Chem Eng Res Des 2016;114:236–46. https://doi.org/10.1016/j.cherd.2016.08.026.
[149] Moazami N, Wyszynski ML, Mahmoudi H, Tsolakis A, Zou Z, Panahifar P, et al. Modelling of a fixed bed reactor for Fischer–Tropsch synthesis of simulated N2-rich syngas over Co/SiO2: Hydrocarbon production. Fuel 2015;154:140–51. https://doi.org/10.1016/J.FUEL.2015.03.049.
[150] Botes FG. Kinetic and selectivity modelling of the iron-based low-temperature Fischer-Tropsch synthesis. Eindhoven University of Technology, 2008. https://doi.org/10.6100/IR638544.
[151] Bhatelia T, Li E, Sun Y, Hazewinkel P, Burke N, Sage V. Chain length dependent olefin re-adsorption model for Fischer-Tropsch synthesis over Co-Al_2O_3 catalyst. Fuel Process Technol 2014:277–89. https://doi.org/10.1016/j.fuproc.2014.03.028.
[152] Kondamudi K, Pant KK, Upadhyayula S. Synergistic Effect of Fe−Co Bimetallic Catalyst on FTS and WGS Activity in the Fischer−Tropsch Process : A Kinetic Study. Ind Eng Chem Res 2017. https://doi.org/10.1021/acs.iecr.6b04517.
[153] Davis BH. Fischer-Tropsch synthesis: Current mechanism and futuristic needs. Fuel Process Technol 2001;71:157–66. https://doi.org/10.1016/S0378-3820(01)00144-8.
[154] Fajín J, Cordeiro M, Gomes J, Fajín JLC, Cordeiro MNDS, Gomes JRB. Fischer-Tropsch Synthesis on Multicomponent Catalysts: What Can We Learn from Computer Simulations? Catalysts 2015;5:3–17. https://doi.org/10.3390/catal5010003.
[155] Todic B, Ma W, Jacobs G, Davis BH, Bukur DB. CO-insertion mechanism based kinetic model of the Fischer-Tropsch synthesis reaction over Re-promoted Co catalyst. Catal Today 2014;228:32–9. https://doi.org/10.1016/j.cattod.2013.08.008.
[156] Wojciechowski BW. The Kinetics of the Fischer- Tropsch Synthesis. Catal Re Sci Eng 1988:629–702. https://doi.org/10.1080/01614948808071755 PLEASE.
[157] Turner ML, Long HC, Shenton A, Byers PK, Maitlis PM. The Alkenyl Mechanism for Fischer-Tropsch Surface Methylene Polymerisation; the Reactions of Vinylic Probes with CO/H2 over Rhodium Catalyst. Chem - A Eur J 1995;1:549–56. https://doi.org/10.1002/chem.19950010809.
[158] Fischer F, Tropsch H. The Synthesis of Petroleum at Atmospheric Pressures from Gasification Products of Coal. Brennstoff-Chemie 1926;7:97–104.
[159] Visconti CG, Tronconi E, Lietti L, Zennaro R, Forzatti P. Development of a complete kinetic model for the Fischer – Tropsch synthesis over Co / Al 2 O 3 catalysts. Chem Eng Sci 2007;62:5338–43.

https://doi.org/10.1016/j.ces.2006.12.064.
[160] Visconti CG, Lietti L, Tronconi E, Forzatti P, Zennaro R, Rossini S. Detailed kinetics of the Fischer – Tropsch synthesis over Co-based catalysts containing sulphur. Catal Today 2010;154:202–9. https://doi.org/10.1016/j.cattod.2010.04.007.
[161] Visconti CG, Tronconi E, Lietto L, Forzatti P, Rossini E, Zennaro R. Detailed Kinetics of the Fischer – Tropsch Synthesis on Cobalt Catalysts Based on H-Assisted CO Activation. Top Catal 2011:786–800. https://doi.org/10.1007/s11244-011-9700-3.
[162] Anderson RB. Fischer-Tropsch synthesis. In: Press A, editor. Acad. Press, Academic Press; 1984.
[163] Shivananda Ail S, Dasappa S. Biomass to liquid transportation fuel via Fischer Tropsch synthesis-Technology review and current scenario. Renew Sustain Energy Rev 2016;58:267–86. https://doi.org/10.1016/j.rser.2015.12.143.
[164] Ojeda M, Nabar R, Nilekar AU, Ishikawa A, Mavrikakis M, Iglesia E. CO activation pathways and the mechanism of Fischer–Tropsch synthesis. J Catal 2010;272:287–97. https://doi.org/10.1016/J.JCAT.2010.04.012.
[165] Weststrate CJ, Van Helden P, Van De Loosdrecht J, Niemantsverdriet JW. Elementary steps in Fischer-Tropsch synthesis: CO bond scission, CO oxidation and surface carbiding on Co(0001). Surf Sci 2016;648:60–6. https://doi.org/10.1016/j.susc.2015.10.050.
[166] Todic B, Bhatelia T, Froment GF, Ma W, Jacobs G, Davis BH, et al. Kinetic Model of Fischer−Tropsch Synthesis in a Slurry Reactor on Co−Re/Al2O3 Catalyst. I&EC Res 2013.
[167] Karaca H, Safonova O V., Chambrey S, Fongarland P, Roussel P, Griboval-Constant A, et al. Structure and catalytic performance of Pt-promoted alumina-supported cobalt catalysts under realistic conditions of Fischer-Tropsch synthesis. J Catal 2011;277:14–26. https://doi.org/10.1016/j.jcat.2010.10.007.
[168] Nabaho D, Niemantsverdriet JW (Hans., Claeys M, Steen E van. Hydrogen spillover in the Fischer–Tropsch synthesis: An analysis of gold as a promoter for cobalt–alumina catalysts. Catal Today 2016;275:27–34. https://doi.org/10.1016/j.cattod.2015.12.019.
[169] Rønning M, Tsakoumis NE, Voronov A, Johnsen RE, Norby P, Van Beek W, et al. Combined XRD and XANES studies of a Re-promoted Co/γ-Al 2O3 catalyst at Fischer-Tropsch synthesis conditions. Catal Today 2010;155:289–95. https://doi.org/10.1016/j.cattod.2009.10.010.
[170] Fratalocchi L, Giorgio C, Lietti L, Fischer N, Claeys M. A promising preparation method for highly active cobalt based Fischer- Tropsch catalysts supported on stabilized Al 2 O 3. Appl Catal A, Gen 2018;556:92–103. https://doi.org/10.1016/j.apcata.2018.02.002.
[171] Lögdberg S, Lualdi M, Järås S, Walmsley JC, Blekkan EA, Rytter E, et al. On the selectivity of cobalt-based Fischer–Tropsch catalysts: Evidence for a common precursor for methane and long-chain hydrocarbons. J Catal 2010;274:84–98. https://doi.org/10.1016/j.jcat.2010.06.007.
[172] Boyer C, Gazarian J, Lecocq V, Maury S, Forret A, Schweitzer JM, et al. Development of the Fischer-Tropsch Process: From the Reaction Concept to the Process Book. Oil Gas Sci Technol – Rev d'IFP Energies Nouv

2016;71:44. https://doi.org/10.2516/ogst/2015032.
[173] Botes FG, Dyk B Van, Mcgregor C. The Development of a Macro Kinetic Model for a Commercial Co/Pt/Al2O3 Fischer-Tropsch Catalyst. Ind Eng Chem Res 2009;2:10439–47.
[174] Yang J, Liu Y, Chang J, Wang Y-N, Bai L, Xu Y-Y, et al. Detailed Kinetics of Fischer−Tropsch Synthesis on an Industrial Fe−Mn Catalyst. Ind Eng Chem Res 2003;42:5066–90. https://doi.org/10.1021/ie030135o.
[175] Kasun GT, Gunasooriya K, Van Bavel AP, Kuipers HPCE, Saeys M. Key Role of Surface Hydroxyl Groups in C−O Activation during Fischer−Tropsch Synthesis 2016. https://doi.org/10.1021/acscatal.6b00634.
[176] Chen W, Filot IAW, Pestman R, Hensen EJM. Mechanism of Cobalt-Catalyzed CO Hydrogenation: 2. Fischer− Tropsch Synthesis. ACS Catal 2017;7:8061–71. https://doi.org/10.1021/acscatal.7b02758.
[177] Evans MG, Polanyi M. Inertia and Driving Force of Chemical Reactions. Trans Faraday Soc 1937.
[178] Mandić M, Todić B, Živanić L, Nikačević N, Bukur DB. Effects of Catalyst Activity, Particle Size and Shape, and Process Conditions on Catalyst Effectiveness and Methane Selectivity for Fischer-Tropsch Reaction: A Modeling Study. Ind Eng Chem Res 2017;56:2733–45. https://doi.org/10.1021/acs.iecr.7b00053.
[179] Zohdi-Fasaei H, Atashi H, Farshchi Tabrizi F, Mirzaei AA. Effects of mass transfer on Fischer-Tropsch kinetics over mesoporous silica-supported CoeMneCe nano catalysts in a fixed-bed reactor. J Nat Gas Sci Eng 2016;32:262–72. https://doi.org/10.1016/j.jngse.2016.03.090.
[180] Sánchez-López JRG, Hernández-Ramírez A, Martínez-Hernández A. Modeling of transport phenomena in fixed-bed reactors for the Fischer-Tropsch reaction: a brief literature review. Rev Chem Eng 2017;33:109–42. https://doi.org/10.1515/revce-2015-0044.
[181] Mears DE. Tests for Transport Limitations in Experimental Catalytic Reactors. vol. 10. 1970.
[182] Vervloet D, Kapteijn F, Nijenhuis J, Ruud Van Ommen J. Fischer–Tropsch reaction–diffusion in a cobalt catalyst particle: aspects of activity and selectivity for a variable chain growth probability. Catal Sci Technol 2012;2:1221–33. https://doi.org/10.1039/c2cy20060k.
[183] Fratalocchi L, Visconti CG, Groppi G, Lietti L, Tronconi E. Intensifying heat transfer in Fischer-Tropsch tubular reactors through the adoption of conductive packed foams. Chem Eng J 2018;349:829–37. https://doi.org/10.1016/j.cej.2018.05.108.
[184] Erkey C, Rodden JB, Akgerman A. A correlation for predicting diffusion coefficients in alkanes. Can J Chem Eng 1990;68:661–5. https://doi.org/10.1002/cjce.5450680418.
[185] Park T-Y, Froment GF. A hybrid genetic algorithm for the estimation of parameters in detailed kinetic models. Comput Chem Eng 1998;22:S103–10. https://doi.org/10.1016/S0098-1354(98)00043-X.
[186] Todic B, Olewski T, Nikacevic N, Bukur DB. Modeling of Fischer-Tropsch Product Distribution over Fe-based Catalyst. Chem Enginnering Trans 2013;32.
[187] Mirzaei AA, Shirzadi B, Atashi H, Mansouri M. Modeling and operating conditions optimization of Fischer-Tropsch synthesis in a fixed-bed reactor.

J Ind Eng Chem 2012;18:1515–21. https://doi.org/10.1016/j.jiec.2012.02.013.
[188] Keyser MJ, Everson RC, Espinoza RL. Fischer-Tropsch Kinetic Studies with Cobalt-Manganese Oxide Catalysts 2000. https://doi.org/10.1021/ie990236f.
[189] Nikparsaa P, Mirzaeia AA, Atashib H. Effect of reaction conditions and Kinetic study on the Fischer-Tropsch synthesis over fused Co-Ni/Al2O3 catalyst. J Fuel Chem Technol 2014;42:710–8. https://doi.org/10.1016/S1872-5813(14)60032-3.
[190] Ghouri MM, Afzal S, Hussain R, Blank J, Bukur DB, Elbashir NO. Multi-scale modeling of fixed-bed Fischer Tropsch reactor. Comput Chem Eng 2016;91:38–48. https://doi.org/10.1016/j.compchemeng.2016.03.035.
[191] Nikbakht N, Mirzaei AA, Atashi H. Kinetic modeling of the Fischer-Tropsch reaction over a zeolite supported Fe-Co-Ce catalyst prepared using impregnation procedure. Fuel 2018;229:209–16. https://doi.org/10.1016/J.FUEL.2018.04.132.
[192] Ojeda M, Nabar R, Nilekar AU, Ishikawa A, Mavrikakis M, Iglesia E. CO activation pathways and the mechanism of Fischer–Tropsch synthesis. J Catal 2010;272:287–97. https://doi.org/10.1016/J.JCAT.2010.04.012.
[193] Mansouri M, Atashi H, Mirzaei AA, Jangi R. Kinetics of the Fischer-Tropsch synthesis on silica-supported cobalt-cerium catalyst. Int J Ind Chem 2013:1–10.
[194] Yang R, Zhou L, Gao J, Hao X, Wu B, Yang Y, et al. Effects of experimental operations on the Fischer-Tropsch product distribution. Catal Today 2017;298:77–88. https://doi.org/10.1016/j.cattod.2017.05.056.
[195] Marchese M, Buffo G, Santarelli M, Lanzini A. CO2 from direct air capture as carbon feedstock for Fischer-Tropsch chemicals and fuels : Energy and economic analysis. J CO2 Util 2021;46:101487. https://doi.org/10.1016/j.jcou.2021.101487.
[196] Marchese M, Chesta S, Santarelli M, Lanzini A. Techno-economic feasibility of a biomass-to-X plant : Fischer-Tropsch wax synthesis from digestate gasi fi cation. Energy 2021;228:120581. https://doi.org/10.1016/j.energy.2021.120581.
[197] Dimitriou I, García-Gutiérrez P, Elder RH, Cuéllar-Franca RM, Azapagic A, Allen RWK. Carbon dioxide utilisation for production of transport fuels: Process and economic analysis. Energy Environ Sci 2015;8:1775–89. https://doi.org/10.1039/c4ee04117h.
[198] Sasol Innovation | Gas to Liquids | Technology n.d. https://www.sasol.com/innovation/gas-liquids/technology (accessed January 29, 2021).
[199] Sasol. Sasol Production and Sales metrics for the year ended 30 June 2020 2020:1–11.
[200] Herz G, Reichelt E, Jahn M. Design and evaluation of a Fischer-Tropsch process for the production of waxes from biogas. Energy 2017;132:370–81. https://doi.org/10.1016/j.energy.2017.05.102.
[201] Kärki J, Thomasson T, Melin K, Suomalainen M, Saastamoinen H, Hurskainen M, et al. New business opportunities based on biogenic carbon dioxide utilization. 14th Greenh. Gas Control Technol. Conf. Melb., 2018.
[202] Okeke IJ, Mani S. Techno-economic assessment of biogas to liquid fuels

conversion technology via Fischer-Tropsch synthesis. Biofuels, Bioprod Biorefining 2017;11:472–87. https://doi.org/10.1002/bbb.1758.

[203] Hernandez B, Martin M. Optimization for biogas to chemicals via tri-reforming. Analysis of Fischer-Tropsch fuels from biogas. Energy Convers Manag 2018;174:998–1013. https://doi.org/10.1016/j.enconman.2018.08.074.

[204] Dietrich RU, Albrecht FG, Maier S, König DH, Estelmann S, Adelung S, et al. Cost calculations for three different approaches of biofuel production using biomass, electricity and CO_2 . Biomass and Bioenergy 2018;111:165–73. https://doi.org/10.1016/j.biombioe.2017.07.006.

[205] Hillestad M, Ostadi M, Alamo Serrano G d., Rytter E, Austbø B, Pharoah JG, et al. Improving carbon efficiency and profitability of the biomass to liquid process with hydrogen from renewable power. Fuel 2018;234:1431–51. https://doi.org/10.1016/j.fuel.2018.08.004.

[206] Spyrakis S, Panopoulos KD, Kakaras E. Synthesis, Modeling and Exergy Analysis of Atmospheric Air Blown Biomass Gasification for Fischer-Tropsch Process*. Int J Thermodyn 2009;12:187–92.

[207] Fasihi M, Bogdanov D, Breyer C. Economics of Global Gas-To-Liquids (GtL) Fuels Trading Based on Hybrid Pv-Wind Power Plants; Economics of Global Gas-To-Liquids (GtL) Fuels Trading Based on Hybrid Pv-Wind Power Plants. 2015.

[208] Fasihi M, Bogdanov D, Breyer C. Techno-Economic Assessment of Power-to-Liquids (PtL) Fuels Production and Global Trading Based on Hybrid PV-Wind Power Plants. Energy Procedia, vol. 99, Elsevier Ltd; 2016, p. 243–68. https://doi.org/10.1016/j.egypro.2016.10.115.

[209] Fasihi M, Bogdanov D, Breyer C. Long-term hydrocarbon trade options for the Maghreb region and Europe-renewable energy based synthetic fuels for a net zero emissions world. Sustain 2017;9. https://doi.org/10.3390/su9020306.

[210] Liu CM, Sandhu NK, Mccoy ST, Bergerson JA. A life cycle assessment of greenhouse gas emissions from direct air capture and Fischer-Tropsch fuel production 2020. https://doi.org/10.1039/c9se00479c.

[211] Mansouri M, Atashi H, Mirzaei AA. Hydrogenation of CO on Cobalt Catalyst in Fischer–Tropsch Synthesis. J Thermodyn Catal 2012;03. https://doi.org/10.4172/2157-7544.1000113.

[212] Keith DW, Holmes G, St. Angelo D, Heidel K. A Process for Capturing CO_2 from the Atmosphere. Joule 2018;2:1573–94. https://doi.org/10.1016/j.joule.2018.05.006.

[213] Graves C, Ebbesen SD, Mogensen M, Lackner KS. Sustainable hydrocarbon fuels by recycling CO2 and H 2O with renewable or nuclear energy. Renew Sustain Energy Rev 2011;15:1–23. https://doi.org/10.1016/j.rser.2010.07.014.

[214] Cinti G, Baldinelli A, Di A, Desideri U. Integration of Solid Oxide Electrolyzer and Fischer-Tropsch : A sustainable pathway for synthetic fuel. Appl Energy 2016;162:308–20. https://doi.org/10.1016/j.apenergy.2015.10.053.

[215] Rafiee A, Panahi M, Khalilpour KR. CO_2 utilization through integration of post-combustion carbon capture process with Fischer-Tropsch gas-to-liquid (GTL) processes. J CO_2 Util 2017;18:98–106.

https://doi.org/10.1016/j.jcou.2017.01.016.
[216] Biogas generation | Industriepark Höchst 2020. https://www.industriepark-hoechst.com/en/stp/menu/powered-by-infraserv/services/disposal/biogas-generation/ (accessed September 30, 2020).
[217] Tractebel, Engie, Hinicio. Study on Early Business Cases for H_2 in Energy Storage and More Broadly Power To H_2 Applications. 2017. https://doi.org/fch.europa.eu/sites/default/files/P2H_Full_Study_FCHJU.pdf.
[218] Kasikamphaiboon P, Chungsiriporn J, Bunyakan C, Wiyaratn W. Simultaneous removal of CO2 and H2S using MEA solution in a packed column absorber for biogas upgrading. Songklanakarin J Sci Technol 2013;35:683–91.
[219] Brand CV. CO_2 capture using monoethanolamine solutions: Development and validation of a process model based on the SAFT-VR equation of state. Imperial College London, 2013.
[220] Reino C, Bartrolí A, Prado Ó, Lytras C. Demonstration of water loops with innovative regenerative business models for the Mediterranean region - Hydrousa Project - Deliverable D14. 2020. https://doi.org/H2020-CIRC-2-2017.
[221] Raynal L, Bouillon PA, Gomez A, Broutin P. From MEA to demixing solvents and future steps, a roadmap for lowering the cost of post-combustion carbon capture. Chem Eng J 2011;171:742–52. https://doi.org/10.1016/j.cej.2011.01.008.
[222] Li K, Leigh W, Feron P, Yu H, Tade M. Systematic study of aqueous monoethanolamine (MEA)-based CO_2 capture process: Techno-economic assessment of the MEA process and its improvements. Appl Energy 2016;165:648–59. https://doi.org/10.1016/j.apenergy.2015.12.109.
[223] Moioli S, Nagy T, Langé S, Pellegrini LA, Mizsey P. Simulation Model Evaluation of CO2Capture by Aqueous MEA Scrubbing for Heat Requirement Analyses. Energy Procedia 2017;114:1558–66. https://doi.org/10.1016/j.egypro.2017.03.1286.
[224] Moioli S, Pellegrini LA, Gamba S. Simulation of CO_2 capture by MEA scrubbing with a rate-based model. Procedia Eng 2012;42:1651–61. https://doi.org/10.1016/j.proeng.2012.07.558.
[225] Abu Zahra MRM. Carbon dioxide capture from flue gas: Development and evaluation of existing and novel process concepts. 2009.
[226] Yang J, Ma W, Chen D, Holmen A, Davis BH. Fischer-Tropsch synthesis: A review of the effect of CO conversion on methane selectivity. Appl Catal A Gen 2014;470:250–60. https://doi.org/10.1016/j.apcata.2013.10.061.
[227] ChemSpider | Search and share chemistry n.d. http://www.chemspider.com/ (accessed February 5, 2021).
[228] PubChem n.d. https://pubchem.ncbi.nlm.nih.gov/ (accessed February 5, 2021).
[229] Gamba S, Soave GS, Pellegrini LA. Use of normal boiling point correlations for predicting critical parameters of paraffins for vapour-liquid equilibrium calculations with the SRK equation of state. Fluid Phase Equilib 2009;276:133–41. https://doi.org/10.1016/j.fluid.2008.10.014.
[230] Marano JJ, Holder GD. General Equation for Correlating the Thermophysical Properties of n-paraffins, n-Olefins, and Other

Homologous Series. 2. Asymptotic Behavior Correlations for PVT Properties. Ind Eng Chem Res 1997;36:1895–907. https://doi.org/10.1021/ie960512f.

[231] Luyben WL, Yu CC. Reactive Distillation Design and Control. Wiley; 2008. https://doi.org/10.1002/9780470377741.

[232] Ashraf A Al, Aftab A Al. Distillation Process of Crude Oil. Qatar University, 2012.

[233] Campanario FJ, Gutiérrez Ortiz FJ. Fischer-Tropsch biofuels production from syngas obtained by supercritical water reforming of the bio-oil aqueous phase. Energy Convers Manag 2017;150:599–613. https://doi.org/10.1016/j.enconman.2017.08.053.

[234] Wolf A, Jess A, Kern C. Syngas Production via Reverse Water-Gas Shift Reaction over a Ni-Al 2 O 3 Catalyst : Catalyst Stability , Reaction Kinetics , and Modeling. Chem Eng Technol 2016;298:1040–8. https://doi.org/10.1002/ceat.201500548.

[235] Christensen KO. Steam Reforming of Methane on Different Nickel Catalysts. Norwegian University of Science and Technology, 2005.

[236] Hauch A, Brodersen K, Chen M, Mogensen MB. Ni/YSZ electrodes structures optimized for increased electrolysis performance and durability. Solid State Ionics 2016;293:27–36. https://doi.org/10.1016/j.ssi.2016.06.003.

[237] Wang Y, Liu T, Lei L, Chen F. High temperature solid oxide H2O/CO2 co-electrolysis for syngas production. Fuel Process Technol 2017;161:248–58. https://doi.org/10.1016/j.fuproc.2016.08.009.

[238] Zheng Y, Wang J, Yu B, Zhang W, Chen J, Qiao J, et al. A review of high temperature co-electrolysis of H_2O and CO_2 to produce sustainable fuels using solid oxide electrolysis cells (SOECs): Advanced materials and technology. Chem Soc Rev 2017;46:1427–63. https://doi.org/10.1039/c6cs00403b.

[239] Zhang X, Song Y, Wang G, Bao X. Co-electrolysis of CO_2 and H_2O in high-temperature solid oxide electrolysis cells: Recent advance in cathodes. J Energy Chem 2017;26:839–53. https://doi.org/10.1016/j.jechem.2017.07.003.

[240] Giglio E, Lanzini A, Santarelli M, Leone P. Synthetic natural gas via integrated high-temperature electrolysis and methanation: Part I—Energy performance. J Energy Storage 2015;2:64–79. https://doi.org/10.1016/j.est.2015.06.004.

[241] Chen M, Hauch A, Sun X, Brodersen K, Jørgensen PS, Jonna J, et al. ForskEL 2015-1-12276 Towards Solid Oxide Electrolysis Plants in 2020 2015:1–48.

[242] Dalgaard Ebbesen S, Høgh J, Nielsen KA, Nielsen JU, Mogensen M. Durable SOC stacks for production of hydrogen and synthesis gas by high temperature electrolysis 2011. https://doi.org/10.1016/j.ijhydene.2011.03.130.

[243] Clausen LR, Butera G, Jensen SH. High efficiency SNG production from biomass and electricity by integrating gasification with pressurized solid oxide electrolysis cells. Energy 2019:1117–31. https://doi.org/10.1016/j.energy.2019.02.039.

[244] Graves C, Ebbesen SD, Mogensen M, Lackner KS. Sustainable

hydrocarbon fuels by recycling CO_2 and H_2O with renewable or nuclear energy. Renew Sustain Energy Rev 2011;15:1–23. https://doi.org/10.1016/j.rser.2010.07.014.

[245] Wang L, Pérez-Fortes M, Madi H, Diethelm S, herle J Van, Maréchal F. Optimal design of solid-oxide electrolyzer based power-to-methane systems: A comprehensive comparison between steam electrolysis and co-electrolysis. Appl Energy 2018;211:1060–79. https://doi.org/10.1016/j.apenergy.2017.11.050.

[246] Kazempoor P, Braun RJ. Hydrogen and synthetic fuel production using high temperature solid oxide electrolysis cells (SOECs). Int J Hydrogen Energy 2015;40:3599–612. https://doi.org/10.1016/J.IJHYDENE.2014.12.126.

[247] Carbon Engineering | Direct Air Capture of CO2 | Home n.d. https://carbonengineering.com/ (accessed February 12, 2021).

[248] Baciocchi R, Storti G, Mazzotti M. Process design and energy requirements for the capture of carbon dioxide from air. Chem Eng Process 2006;45. https://doi.org/10.1016/j.cep.2006.03.015.

[249] Göransson K, Söderlind U, He J, Zhang W. Review of syngas production via biomass DFBGs. Renew Sustain Energy Rev 2011:482–92. https://doi.org/10.1016/j.rser.2010.09.032.

[250] Schmid JC, Benedikt F, Fuchs J, Mauerhofer AM, Müller S, Hofbauer H. Syngas for biorefineries from thermochemical gasification of lignocellulosic fuels and residues—5 years' experience with an advanced dual fluidized bed gasifier design. Biomass Convers Biorefinery 2019:1–38. https://doi.org/10.1007/s13399-019-00486-2.

[251] Doherty W, Reynolds A, Kennedy D. Aspen plus simulation of biomass gasification in a steam blown dual fluidised bed. Mater. Process Energy Commun. Curr. Res. Technol. Dev., 2013, p. 212–20.

[252] Blank A, Hoffmann E. Upgrading of a co-digestion plant by implementation of a hydrolysis stage. Waste Manag Res 2011;29:1145–52. https://doi.org/10.1177/0734242X11423954.

[253] Hofbauer H, Rauch R, Bosch K, Koch R, Aichernig C. Biomass CHP plant Güssing-A success story . 2002.

[254] Fernandez-Lopez M, Pedroche J, Valverde JL, Sanchez-Silva L. Simulation of the gasification of animal wastes in a dual gasifier using Aspen Plus®. Energy Convers Manag 2017;140:211–7. https://doi.org/10.1016/j.enconman.2017.03.008.

[255] Rafati M, Wang L, Dayton DC, Schimmel K, Kabadi V, Shahbazi A. Techno-economic analysis of production of Fischer-Tropsch liquids via biomass gasification: The effects of Fischer-Tropsch catalysts and natural gas co-feeding. Energy Convers Manag 2017;133:153–66. https://doi.org/10.1016/j.enconman.2016.11.051.

[256] Tuomi S, Kurkela E, Hannula I, Berg C-G. The impact of biomass drying on the efficiency of a gasification plant co-producing Fischer-Tropsch fuels and heat-A conceptual investigation 2019. https://doi.org/10.1016/j.biombioe.2019.105272.

[257] Tijmensen MJ, Faaij AP, Hamelinck CN, van Hardeveld MR. Exploration of the possibilities for production of Fischer Tropsch liquids and power via biomass gasiÿcation. vol. 23. 2002.

[258] Hamelinck CN, Faaij APC, den Uil H, Boerrigter H. Production of FT transportation fuels from biomass; technical options, process analysis and optimisation, and development potential. Energy 2004;29:1743–71. https://doi.org/10.1016/j.energy.2004.01.002.
[259] Swanson RM, Satrio JA, Brown RC, Platon A, Hsu DD. Techno-Economic Analysis of Biofuels Production Based on Gasification. 2010.
[260] Dutta A, Talmadge M, Hensley J, Worley M, Dudgeon D, Barton D, et al. Process design and economics for conversion of lignocellulosic biomass to ethanol - Thermochemical Pathway by Indirect Gasification and Mixed Alcohol Synthesis. NREL Tech Rep NREL/TP-5100-51400 2011;303:275–3000.
[261] Martín M, Grossmann IE. Energy optimization of bioethanol production via gasification of switchgrass. AIChE J 2011;57:3408–28. https://doi.org/10.1002/aic.12544.
[262] Francois J, Abdelouahed L, Mauviel G, Patisson F, Mirgaux O, Rogaume C, et al. Detailed process modeling of a wood gasification combined heat and power plant. Biomass and Bioenergy 2013;51:68–82. https://doi.org/10.1016/j.biombioe.2013.01.004.
[263] Simell P, Hannula I, Tuomi S, Nieminen M, Kurkela E, Hiltunen I, et al. Clean syngas from biomass-process development and concept assessment. Biomass Conv Bioref 2014. https://doi.org/10.1007/s13399-014-0121-y.
[264] Im-Orb K, Simasatitkul L, Arpornwichanop A. Techno-economic analysis of the biomass gasification and FischereTropsch integrated process with off-gas recirculation 2015. https://doi.org/10.1016/j.energy.2015.11.012.
[265] Dussan K, Monaghan RFD. Integrated Thermal Conversion and Anaerobic Digestion for Sludge Management in Wastewater Treatment Plants. Waste and Biomass Valorization 2018;9:65–85. https://doi.org/10.1007/s12649-016-9812-x.
[266] Tagomori IS, Rochedo PRR, Szklo A. Techno-economic and georeferenced analysis of forestry residues-based Fischer-Tropsch diesel with carbon capture in Brazil. Biomass and Bioenergy 2019;123:134–48. https://doi.org/10.1016/j.biombioe.2019.02.018.
[267] Menin L, Vakalis S, Benedetti V, Patuzzi F, Baratieri M. Techno-economic assessment of an integrated biomass gasification, electrolysis, and syngas biomethanation process. Biomass Convers Biorefinery 2020. https://doi.org/10.1007/s13399-020-00654-9.
[268] Ribeiro AM, Santos JC, Rodrigues AE, Ribeiro AM, Santos · J C, Rodrigues · A E. Pressure swing adsorption for CO 2 capture in Fischer-Tropsch fuels production from biomass. Adsorption 2011;17:443–52. https://doi.org/10.1007/s10450-010-9280-8.
[269] Kemp IC. Pinch Analysis and Process Integration A User Guide on Process Integration for the Efficient Use of Energy. Elsevier Ltd.; 2006. https://doi.org/https://doi.org/10.1016/B978-0-7506-8260-2.X5001-9.
[270] Pinch Analysis and Waste Heat Recovery - NUMEX n.d. https://numex-blog.com/pinch-analysis-and-waste-heat-recovery/.
[271] Campanario FJ, Gutiérrez Ortiz FJ. Techno-economic assessment of bio-oil aqueous phase-to-liquids via Fischer-Tropsch synthesis and based on supercritical water reforming. Energy Convers Manag 2017;154:591–602. https://doi.org/10.1016/j.enconman.2017.10.096.

[272] Proost J. State-of-the art CAPEX data for water electrolysers, and their impact on renewable hydrogen price settings. Int J Hydrogen Energy 2019;44:4406–13. https://doi.org/10.1016/j.ijhydene.2018.07.164.
[273] Zauner A, Böhm H, Rosenfeld DC, Tichler R. Store&Go: Innovative large-scale energy storage technologies and Power-to-Gas concepts after optimization Analysis on future technology options and on techno-economic optimization. 2019.
[274] Bauer F, Persson T, Hulteberg C, Tamm D. Biogas upgrading – technology overview, comparison and perspectives for the future. Biofuels, Bioprod Biorefining 2013;7:499–511. https://doi.org/10.1002/bbb.1423.
[275] McQueen N, Psarras P, Pilorgé H, Liguori S, He J, Yuan M, et al. Cost Analysis of Direct Air Capture and Sequestration Coupled to Low-Carbon Thermal Energy in the United States. Environ Sci Technol 2020;54:7542–51. https://doi.org/10.1021/acs.est.0c00476.
[276] Giarola S, Forte O, Lanzini A, Gandiglio M, Santarelli M, Hawkes A. Techno-economic assessment of biogas-fed solid oxide fuel cell combined heat and power system at industrial scale. Appl Energy 2017;211:689–704. https://doi.org/10.1016/j.apenergy.2017.11.029.
[277] Meerman JC, Knoope MMJ, Ramírez A, Turkenburg WC, Faaij APC. Technical and economic prospects of coal- and biomass-fired integrated gasification facilities equipped with CCS over time. Int J Greenh Gas Control 2013;16:311–23. https://doi.org/10.1016/j.ijggc.2013.01.051.
[278] Comidy LJF, Staples MD, Barrett SRH. Technical, economic, and environmental assessment of liquid fuel production on aircraft carriers. Appl Energy 2019;256:113810. https://doi.org/10.1016/j.apenergy.2019.113810.
[279] Di Marcoberardino G, Vitali D, Spinelli F, Binotti M, Manzolini G. Green hydrogen production from raw biogas: A techno-economic investigation of conventional processes using pressure swing adsorption unit. Processes 2018;6. https://doi.org/10.3390/pr6030019.
[280] Saveyn H, Eder P. End-of-waste criteria for biodegradable waste subjected to biological treatment (compost & digestate): Technical proposals 2014.
[281] Regatrace. Mapping the state of play of renewable gases in Europe. n.d.
[282] Baena-Moreno FM, Sebastia-Saez D, Wang Q, Reina TR. Is the production of biofuels and bio-chemicals always profitable? Co-production of biomethane and urea from biogas as case study 2020. https://doi.org/10.1016/j.enconman.2020.113058.
[283] Barbera E, Menegon S, Banzato D, D'alpaos C, Bertucco A. From biogas to biomethane: A process simulation-based techno-economic comparison of different upgrading technologies in the Italian context 2018. https://doi.org/10.1016/j.renene.2018.12.052.
[284] IRENA. Renewable Power Generation Costs in 2019: Latest Trends and Drivers. 2019.
[285] Fasihi M, Breyer C. Baseload electricity and hydrogen supply based on hybrid PV-wind power plants. J Clean Prod 2020;243:118466. https://doi.org/10.1016/j.jclepro.2019.118466.
[286] Eriksson O, Bisaillon M, Haraldsson M, Sundberg J. Enhancement of biogas production from food waste and sewage sludge e Environmental and economic life cycle performance 2016.

https://doi.org/10.1016/j.jenvman.2016.03.022.
[287] Comidy LJF, Staples MD, Barrett SRH. Technical, economic, and environmental assessment of liquid fuel production on aircraft carriers. Appl Energy 2019;256:113810. https://doi.org/10.1016/j.apenergy.2019.113810.
[288] Hassan A, Patel MK, Parra D. An assessment of the impacts of renewable and conventional electricity supply on the cost and value of power-to-gas. Int J Hydrogen Energy 2018. https://doi.org/10.1016/j.ijhydene.2018.10.026.
[289] Parigi D, Giglio E, Soto A, Santarelli M. Power-to-fuels through carbon dioxide Re-Utilization and high-temperature electrolysis: A technical and economical comparison between synthetic methanol and methane. J Clean Prod 2019;226:679–91. https://doi.org/10.1016/j.jclepro.2019.04.087.
[290] Shehzad MF, Abdelghany MB, Liuzza D, Mariani V, Glielmo L. Mixed Logic Dynamic Models for MPC Control of Wind Farm Hydrogen-Based Storage Systems. Inventions 2019;4:57. https://doi.org/10.3390/inventions4040057.
[291] Daniel-Gromke J, Denysenko V, Liebetrau J, And B, Europe BI. Biogas and biomethane in Europe: lessons from Denmark, Germany, and Italy. 2019.
[292] Verso il biometano. n.d.
[293] Economico MDS. D.M. 19 febbraio 2007 Approvazione. 2007.
[294] Huang Y, Zhang X, Zhang X, Dong H, Zhang S. Thermodynamic Modeling and Assessment of Ionic Liquid-Based CO_2 Capture Processes. Ind Eng Chem Res 2014;53:11805–17. https://doi.org/10.1021/ie501538e.
[295] Zacchello B, Oko E, Wang M, Fethi A. Process simulation and analysis of carbon capture with an aqueous mixture of ionic liquid and monoethanolamine solvent. Int J Coal Sci Technol 2017;4:25–32. https://doi.org/10.1007/s40789-016-0150-1.
[296] Becker WL, Braun RJ, Penev M, Melaina M. Production of Fischer-Tropsch liquid fuels from high temperature solid oxide co-electrolysis units. Energy 2012;47:99–115. https://doi.org/10.1016/j.energy.2012.08.047.
[297] Liu ZK, Ågren J, Hillert M. Application of the Le Chatelier principle on gas reactions. Fluid Phase Equilib 1996;121:167–77. https://doi.org/10.1016/0378-3812(96)02994-9.
[298] Herz G, Reichelt E, Jahn M. Design and evaluation of a Fischer-Tropsch process for the production of waxes from biogas. Energy 2017;132:370–81. https://doi.org/10.1016/j.energy.2017.05.102.
[299] Chiodini A, Bua L, Carnelli L, Zwart R, Vreugdenhil B, Vocciante M. Enhancements in Biomass-to-Liquid processes: Gasification aiming at high hydrogen/carbon monoxide ratios for direct Fischer-Tropsch synthesis applications. Biomass and Bioenergy 2017;106:104–14. https://doi.org/10.1016/j.biombioe.2017.08.022.
[300] Snehesh AS, Mukunda HS, Mahapatra S, Dasappa S. Fischer-Tropsch route for the conversion of biomass to liquid fuels - Technical and economic analysis. Energy 2017;130:182–91. https://doi.org/10.1016/j.energy.2017.04.101.
[301] Martin S, Albrecht FG, Van Der Veer P, Lieftink D, Dietrich RU.

Evaluation of on-site hydrogen generation via steam reforming of biodiesel: Process optimization and heat integration. Int. J. Hydrogen Energy, vol. 41, Elsevier Ltd; 2016, p. 6640–52. https://doi.org/10.1016/j.ijhydene.2016.02.138.
[302] EBA. EBA Statistical Report 2020. 2020.
[303] Association EB. EBA Statistical Report 2018. 2018.
[304] Suaria G, Aliani S, Merlino S, Abbate M. The Occurrence of Paraffin and Other Petroleum Waxes in the Marine Environment: A Review of the Current Legislative Framework and Shipping Operational Practices. Front Mar Sci 2018;5:94. https://doi.org/10.3389/fmars.2018.00094.
[305] Pellegrini LA, De Guido G, Moioli S. Design of the CO2 Removal Section for PSA Tail Gas Treatment in a Hydrogen Production Plant. Front Energy Res 2020;8:77. https://doi.org/10.3389/fenrg.2020.00077.
[306] Riboldi L, Bolland O. Evaluating Pressure Swing Adsorption as a CO 2 separation technique in coal-fired power plants. n.d.
[307] Wesley Awe O, Zhao Y, Nzihou A, Pham Minh D, Lyczko N. A Review of Biogas Utilisation, Purification and Upgrading Technologies A Review of Biogas Utilisation, Purification and Upgrading Technologies: Review. Waste and Biomass Valoriza-tion A Review of Biogas Utilisation, Purification and Upgrading Technologies 2017;8:267–83. https://doi.org/10.1007/s12649-016-9826-4ï.
[308] Huang L, Qing C, Tao H, Wang Y, Liu X. Experimental Study for Biogas Upgrading by Water Scrubbing under Low Pressure. Open Chem Eng J 2015.
[309] Teir S, Suomalainen M, Onarheim K. Pre-evaluation of a new process for capture of CO2 using water. 2014.
[310] van der Giesen C, Kleijn R, Kramer GJ. Energy and Climate Impacts of Producing Synthetic Hydrocarbon Fuels from CO $_2$. Environ Sci Technol 2014;48:7111–21. https://doi.org/10.1021/es500191g.
[311] Falter C, Batteiger V, Sizmann A. Climate Impact and Economic Feasibility of Solar Thermochemical Jet Fuel Production 2015. https://doi.org/10.1021/acs.est.5b03515.
[312] Hombach LE, Doré L, Heidgen K, Maas H, Wallington TJ, Walther G. Economic and environmental assessment of current (2015) and future (2030) use of E-fuels in light-duty vehicles in Germany. J Clean Prod 2019;207:153–62. https://doi.org/10.1016/j.jclepro.2018.09.261.
[313] García A, Monsalve-Serrano J, Villalta D, Sari RL, Gordillo Zavaleta V, Gaillard P. Potential of e-Fischer Tropsch diesel and oxymethyl-ether (OMEx) as fuels for the dual-mode dual-fuel concept 2019. https://doi.org/10.1016/j.apenergy.2019.113622.
[314] Schmidt P, Weindorf W. Power-to-Liquids: Potentials and Perspectives for the Future Supply of Renewable Aviation Fuel. 2016.
[315] Viebahn P, Scholz A, Zelt O. The Potential Role of Direct Air Capture in the German Energy Research Program—Results of a Multi-Dimensional Analysis. Energies 2019;12:1–27. https://doi.org/10.3390/en12183443.
[316] Blanco H, Nijs W, Ruf J, Faaij A. Potential for hydrogen and Power-to-Liquid in a low-carbon EU energy system using cost optimization. Appl Energy 2018;232:617–39. https://doi.org/10.1016/j.apenergy.2018.09.216.
[317] Loewert M, Pfeifer P. Dynamically Operated Fischer-Tropsch Synthesis in

PtL-Part 1: System Response on Intermittent Feed. ChemEngineering 2020;4:21. https://doi.org/10.3390/chemengineering4020021.

[318] Arutyunov V, Nikitin A, Strekova L, Savchenko V, Sedov I. Utilization of renewable sources of biogas for small-scale production of liquid fuels. Catal Today 2020. https://doi.org/10.1016/j.cattod.2020.06.057.

[319] Samavati M, Martin A, Nemanova V, Santarelli M. Integration of solid oxide electrolyser, entrained gasification, and Fischer-Tropsch process for synthetic diesel production: Thermodynamic analysis. Int J Hydrogen Energy 2018;43:4785–803. https://doi.org/10.1016/j.ijhydene.2018.01.138.

[320] Fazeli H, Panahi M, Rafiee A. Investigating the potential of carbon dioxide utilization in a gas-to-liquids process with iron-based Fischer-Tropsch catalyst. J Nat Gas Sci Eng 2018;52:549–58. https://doi.org/10.1016/j.jngse.2018.02.005.

Appendix A – Catalyst testing and kinetic models

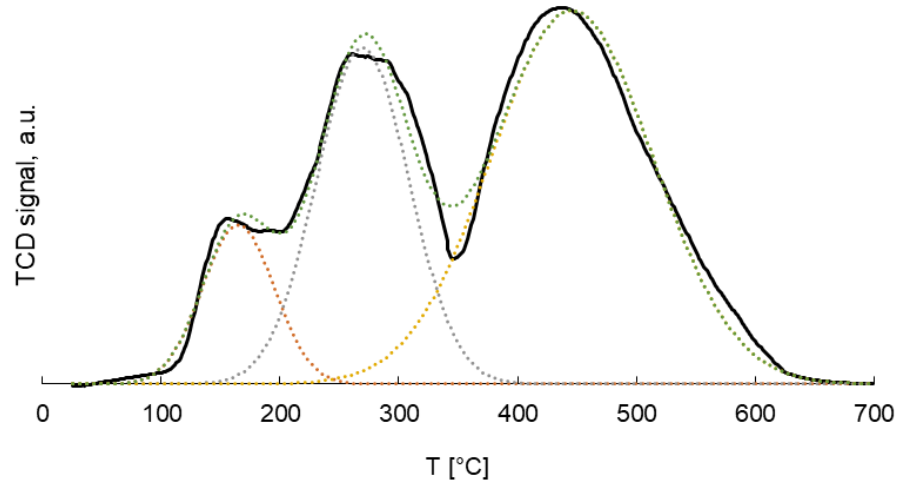

Figure 73. Temperature-programmed reduction results for the studied Co-Pt/γ-Al_2O_3 catalyst. Reproduced from [82].

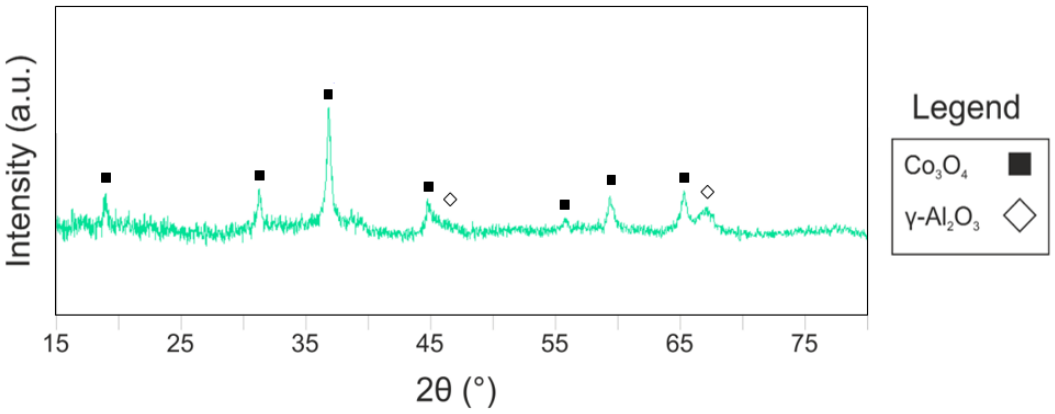

Figure 74. XRD diffractogram for Co-Pt/γ-Al_2O_3 non-reduced catalyst. Reproduced from [82].

Kinetic models

Catalytic site expressed as "*" in the reaction steps

FT-1) reaction paths

MARR=49%

Reaction number	Reaction step	Constant parameter
0	$H_2 + 2^* \leftrightarrow 2H^*$	K0
1 rds	$CO + H^* \rightarrow CO\ H^*$	k1
	$CO + CH_3^* \rightarrow CO\ CH_3^*$	
	$CO + C_NH_{2N+1}^* \rightarrow CO\ C_NH_{2N+1}^*$	
2	$CO\ H^* + H_2 \leftrightarrow H\ C^* + H_2O$	K2
	$CO\ CH_3^* + H_2 \leftrightarrow CH_3\ C^* + H_2O$	
	$C_NH_{2N+1}\ CO^* + H_2 \leftrightarrow C_NH_{2N+1}\ C^* + H_2O$	
3	$H\ C^* + H_2 \leftrightarrow H\ ^*CH_2$	K3
	$CH_3\ C^* + H_2 \leftrightarrow CH_3\ ^*CH_2$	
	$C_NH_{2N+1}\ C^* + H_2 \leftrightarrow C_NH_{2N+1}\ ^*CH_2$	
4	$C_NH_{2N+1}\ ^*CH_2 \leftrightarrow C_NH_{2N+1}\ CH_2^*$	K4
5 rds	$CH_3^* + H_2 \rightarrow CH_4 + H^*$	k5M
	$C_NH_{2N+1}^* + H_2 \rightarrow C_NH_{2N+2} + H^*$	k5
6 rds	$C_2H_5^* \rightarrow C_2H_4 + H^*$	k6E
	$C_NH_{2N+1}^* \rightarrow C_NH_{2N} + H^*$	k6

Resolution of the mechanism to get the Rates expressions. Description of the probability growths as the ratio of the growth over the growth and termination, through alpha values for each of the products.

$R_{CH4} = k_{5M}\,[CH_3^*]\,P_{H2}$

$R_{C2H4} = k_{6E}\,e^{2c}\,[C_2H_5^*]$

$R_{CnH2n+1} = k_5\,[C_nH_{2n+1}^*]\,P_{H2}$ Paraffins n>=2

$R_{CnH2n} = k_6\,e^{nc}\,[C_2H_{2n+1}^*]$ Olefins n>=3

$$\alpha_1 = \frac{k_1 P_{CO}}{k_1 P_{CO} + k_{5M} P_{H_2}}$$

$$\alpha_2 = \frac{k_1 P_{CO}}{k_1 P_{CO} + k_5 P_{H_2} + k_{6E} e^{2c}}$$

$$\alpha_n = \frac{k_1 P_{CO}}{k_1 P_{CO} + k_5 P_{H_2} + k_6 e^{nc}}$$

It is possible to apply the Quasi Steady-State Assumption (QSSA) to derive the formulation of the growth probabilities. For n=1 we apply it on $[CH_3^*]$ species, for n=2 for $[C_2H_5^*]$ and for n>2 we apply it over $[C_NH_{2N+1}^*]$.

$$\frac{d[CH_3^*]}{dt} = 0 = Intermediate\ generation - intermediate\ termination$$
$$= k_1 P_{CO}[H^*] - k_1 P_{CO}[CH_3^*] - k_{5M} P_{H_2}[CH_3^*]$$

$$\frac{d[C_2H_5^*]}{dt} = 0 = k_1 P_{CO}[CH_3^*] - k_1 P_{CO}[C_2H_5^*] - k_5 P_{H_2}[C_2H_5^*] - k_{6E} e^{2c}[C_2H_5^*]$$

$$\frac{d[C_nH^*_{2n+1}]}{dt} = 0 = k_1P_{CO}[C_{n-1}H_{2n-1}{}^*] - k_1P_{CO}[C_nH_{2n+1}{}^*] - k_5P_{H_2}[C_nH_{2n+1}{}^*] - k_6e^{nc}[C_nH_{2n+1}{}^*]$$

From the above formulation, we find the same definition of alphas as previously expressed. Thus, we can express concentrations for the balance of active sites.

$$[\mathrm{CH}^*_3] = \alpha_1[H^*]$$

$$[\mathrm{C_2H}^*_5] = \alpha_2[CH^*_3]$$

$$[\mathrm{C_nH_{2n+1}}{}^*] = \alpha_n[C_{n-1}H_{2n-1}{}^*]$$

From the different reaction steps I can then express values for kinetic and equilibrium constants for the balance of the active sites. The site balance can be expressed as follows:

$$1 = [*] + [H^*] + [CH^*_3] + [C_2H^*_5] + [C_{n-1}H^*_{2n-1}] + [H\ CO^*] + [CH_3\ CO^*] + [C_{n-1}H_{2n-1}\ CO^*] + [H\ C^*] + [CH_3\ C^*] + [C_{n-1}H_{2n-1}\ C^*] + [H^*CH_2] + [CH_3{}^*CH_2] + [C_{n-1}H_{2n-1}{}^*CH_2]$$

The above expression assumes that no active catalytic site decreases over time.

$$[H^*]^2 = K_0P_{H_2}[*]^2 \ \rightarrow\ [H^*] = \sqrt{(K_0P_{H_2})}\,[*]$$

$$[H^*CH_2] = \frac{1}{K_4}\,[CH^*_3] = \frac{1}{K_4}\,\alpha_1\sqrt{(K_0P_{H_2})}\,[*]$$

$$[CH_3{}^*CH_2] = \frac{1}{K_4}\,[C_2H^*_5] = \frac{1}{K_4}\,\alpha_1\alpha_2\sqrt{(K_0P_{H_2})}\,[*]$$

$$[C_{n-1}H_{2n-1}{}^*CH_2] = \frac{1}{K_4}\,[C_nH^*_{2n}] = \frac{1}{K_4}\,\alpha_1\alpha_2\prod_{n=3}^{n}\alpha_n\sqrt{(K_0P_{H_2})}\,[*]$$

$$[HC^*] = \frac{1}{K_3P_{H_2}}\,[H\ CH^*_2] = \frac{1}{K_3K_4P_{H_2}}\,\alpha_1\sqrt{(K_0P_{H_2})}\,[*]$$

$$[CH_3\ C^*] = \frac{1}{K_3P_{H_2}}\,[CH_3\ CH^*_2] = \frac{1}{K_3K_4P_{H_2}}\,\alpha_1\alpha_2\sqrt{(K_0P_{H_2})}\,[*]$$

$$[C_{n-1}H_{2n-1}\ C^*] = \frac{1}{K_3P_{H_2}}\,[C_{n-1}H_{2n-1}\ CH^*_2] = \frac{1}{K_3K_4P_{H_2}}\,\alpha_1\alpha_2\prod_{n=3}^{n}\alpha_n\sqrt{(K_0P_{H_2})}\,[*]$$

$$[H\ CO^*] = \frac{1}{K_2}\frac{P_{H_2O}}{P_{H_2}}\,[H\ C^*] = \frac{1}{K_2K_3K_4}\,\frac{P_{H_2O}}{P^2_{H_2}}\,\alpha_1\sqrt{(K_0P_{H_2})}\,[*]$$

$$[CH_3\ CO^*] = \frac{1}{K_2}\frac{P_{H_2O}}{P_{H_2}}\,[CH_3\ C^*] = \frac{1}{K_2K_3K_4}\,\frac{P_{H_2O}}{P^2_{H_2}}\,\alpha_1\alpha_2\sqrt{(K_0P_{H_2})}\,[*]$$

$$[C_{n-1}H_{2n-1}\ CO^*] = \frac{1}{K_2}\frac{P_{H_2O}}{P_{H_2}}\,[C_{n-1}H_{2n-1}\ C^*] = \frac{1}{K_2K_3K_4}\,\frac{P_{H_2O}}{P^2_{H_2}}\,\alpha_1\alpha_2\prod_{n=3}^{n}\alpha_n\sqrt{(K_0P_{H_2})}\,[*]$$

I can substitute these expression and get all in terms of [*].

$$[*] = \frac{1}{DENOM1}$$

$$DENOM1 = 1 + \sqrt{(K_0 P_{H_2})} + \sqrt{(K_0 P_{H_2})}\left(1 + \frac{1}{K_4} + \frac{1}{K_3 K_4 P_{H_2}} + \frac{1}{K_2 K_3 K_4}\frac{P_{H_2O}}{P_{H_2}^2}\right)(\alpha_1 + \alpha_1\alpha_2 + \alpha_1\alpha_2 \sum_{j=3}^{n_c} \prod_{n=3}^{j} \alpha_n)$$

Substituting the expression of [*] in the expressions of the different active sites and back to the definition of the reactions rates, it is possible to write the latter as follows.

$$R_{CH_4} = k_{5M}\, K_0^{0.5}\, P_{H_2}^{1.5}\, \alpha_1\, [*]$$

$$R_{C_2H_4} = k_{6E}\, e^{2c} \sqrt{(K_0 P_{H_2})}\ \alpha_1\, \alpha_2\, [*]$$

$$R_{C_nH_{2n+2}} = k_5\, K_0^{0.5}\, P_{H_2}^{1.5}\, \alpha_1\, \alpha_2 \prod_{n=3}^{n} \alpha_n\ [*] \qquad \text{Paraffins n>=2}$$

$$R_{C_2H_4} = k_6\, e^{nc} \sqrt{(K_0 P_{H_2})}\ \alpha_1\, \alpha_2 \prod_{n=3}^{n} \alpha_n\ [*] \qquad \text{Olefins n>=3}$$

The same procedure is applied to the definition of all the mechanisms.

FT-2) reaction mechanism

MARR=41.2%

Reaction number	Reaction step	Constant parameter
0	$H_2 + 2* \leftrightarrow 2H*$	K0
1 RDS	$CO + H* \leftrightarrow COH*$	k1
	$CO + CH_3* \leftrightarrow C_2OH_3*$	
	$CO + C_NH_{2N+1}* \leftrightarrow C_{N+1}OH_{2N+1}*$	
2	$COH* + H* \leftrightarrow CH* + OH*$	K2
	$C_2OH_3* + H* \leftrightarrow C_2H_3* + OH*$	
	$C_{N+1}OH_{2N+1}* + H* \leftrightarrow C_NH_{2N-1}* + OH*$	
3	$C_NH_{2N-1}* + H* \leftrightarrow C_NH_{2N}* + *$	K3
4	$C_NH_{2N}* + H* \leftrightarrow C_NH_{2N+1}* + *$	K4
5	$OH* + H* \leftrightarrow H_2O + 2*$	K5
6RDS	$CH_3* + H_2 \rightarrow CH_4 + H*$	k6M
	$C_NH_{2N+1}* + H_2 \rightarrow C_NH_{2N+2} + H*$	k6
7RDS	$C_2H_5* \rightarrow C_2H_4 + H*$	k7E
	$C_NH_{2N+1}* \rightarrow C_NH_{2N} + H*$	k7

Definition of the rates and probability growth values.

$$R_{CH_4} = k_{6M}[CH_3]P_{H2}$$

$$R_{C_2H_4} = k_{7E}\, e^{2c}\, [C_2H_5]$$

$$R_{C_nH_{2n+2}} = k_6[C_NH_{2N+1}]P_{H2}$$

$$R_{C_NH_{2N}} = k_7\, e^{nc}\, [C_NH_{2N+1}]$$

$$\alpha_1 = \frac{k_1P_{CO}}{k_1P_{CO} + k_{6M}P_{H2}}$$

$$\alpha_2 = \frac{k_1P_{CO}}{k_1P_{CO} + k_6P_{H2} + k_{7E}e^{c2}}$$

$$\alpha_N = \frac{k_1P_{CO}}{k_1P_{CO} + k_6P_{H2} + k_7\, e^{cN}}$$

QSSA for the expression of the probability growth.

$$\frac{d[C_nH^*_{2n+1}]}{dt} = 0 = Intermediate\ generation - intermediate\ termination$$

$$= k_1P_{CO}[C_{N-1}H_{2N-1}] - k_1P_{CO}\,[C_NH_{2N+1}] - k_7P_{H2}[C_NH_{2N+1}] - K_7e^{nc}[C_NH_{2N+1}]$$

Same applies to C=1 and C=2 to express alpha1 and alpha2.

$$[CH^*_3] = \alpha_1[H^*]$$

$$[C_2H^*_5] = \alpha_2[CH^*_3]$$

$$[C_nH_{2n+1}{}^*] = \alpha_n[C_{n-1}H_{2n-1}{}^*]$$

Balance:

$$1 = [*] + [H] + [COH] + [CH_3] + [C_2OH_3] + [CH] + [C_2H_3] + [OH] + [C_2H_5] + [CH_2] + [C_2H_4] + \sum_3^N [C_nH^*_{2N+1}] + \sum_3^N [C_nH^*_{2N-1}] + \sum_3^N [C_nH^*_{2N}] + \sum_3^N [C_nOH^*_{2N-1}]$$

$$[H] = \sqrt{(K_0P_{H_2})}\,[*]$$

$$[CH] = \frac{1}{K_3}\frac{[CH_2]}{[H]}\,[*] = \frac{\alpha_1}{K_3\,K_4}\frac{1}{\sqrt{(K_0P_{H_2})}}\,[*]$$

$$[C_2H_3] = \frac{1}{K_3}\frac{[C_2H_4]}{[H]}[*] = \frac{\alpha_1\alpha_2}{K_3\,K_4}\frac{1}{\sqrt{(K_0P_{H_2})}}[*]$$

$$[CH_2] = \frac{1}{K_4}\frac{[CH_3]}{[H]}[*] = \frac{1}{K_4}\frac{\alpha_1\sqrt{(K_0P_{H_2})}}{\sqrt{(K_0P_{H_2})}}[*] = \frac{\alpha_1}{K_4}[*]$$

$$[C_2H_4] = \frac{1}{K_4}\frac{[C_2H_5]}{[H]}[*] = \frac{\alpha_1\alpha_2}{K_4}[*]$$

$$[C_2H_5] = \alpha_1\,\alpha_2\sqrt{(K_0P_{H_2})}\,[*]$$

$$[OH] = P_{H_2O}\frac{[*]^2}{[H]K_5} = \frac{1}{K_5}\frac{P_{H_2O}}{\sqrt{(K_0P_{H_2})}}[*]$$

$$[COH] = \frac{1}{K_2}\frac{[CH][OH]}{[H]} = \frac{\alpha_1}{K_2\,K_3\,K_4\,K_5}\frac{P_{H_2O}}{\left(K_0P_{H_2}\right)^{1.5}}[*]$$

$$[C_2OH_3] = \frac{1}{K_2}\frac{[C_2H_3][OH]}{[H]} = \frac{\alpha_1\alpha_2}{K_2\,K_3\,K_4\,K_5}\frac{P_{H_2O}}{\left(K_0P_{H_2}\right)^{1.5}}[*]$$

$$\sum_3^N[C_nH^*_{2N+1}] = \alpha_1\alpha_2\sum_{j=3}^{n_c}\prod_{n=3}^{j}\alpha_n\sqrt{(K_0P_{H_2})}\,[*]$$

$$\sum_3^N[C_nH^*_{2N-1}] = \alpha_1\alpha_2\sum_{j=3}^{n_c}\prod_{n=3}^{j}\alpha_n\frac{1}{K_3\,K_4\sqrt{(K_0P_{H_2})}}[*]$$

$$\sum_3^N[C_nH^*_{2N}] = \frac{\alpha_1\alpha_2}{K_4}\sum_{j=3}^{n_c}\prod_{n=3}^{j}\alpha_n\,[*]$$

$$\sum_3^N[C_nOH^*_{2N-1}] = \frac{\alpha_1\alpha_2}{K_2\,K_3\,K_4\,K_5}\sum_{j=3}^{n_c}\prod_{n=3}^{j}\alpha_n\frac{P_{H_2O}}{\left(K_0P_{H_2}\right)^{1.5}}[*]$$

From this I can extract [*] and the value of DENOM2.

DENOM2=$1+\sqrt{(K_0P_{H_2})}*\left(1+(\alpha_1+\alpha_1\alpha_2+\alpha_1\alpha_2\sum_{j=3}^{n_c}\prod_{n=3}^{j}\alpha_n)\right)+\left((\alpha_1+\alpha_1\alpha_2+\alpha_1\alpha_2\sum_{j=3}^{n_c}\prod_{n=3}^{j}\alpha_n)\right)\left[\frac{1}{K_4}+\frac{1}{\sqrt{(K_0P_{H_2})}\,K_3K_4}+\frac{P_{H2O}}{(K_0P_{H_2})\text{^}(1.5)\,K_2K_3K_4K_5}\right]+\frac{1}{K_5}\frac{P_{H2O}}{\sqrt{(K_0P_{H_2})}}$

$$R_{CH_4} = k_{7M}\alpha_1\sqrt{(K_9P_{H_2})}\,P_{H2}\,[vac] \qquad \alpha_1 = \frac{k_1P_{CO}}{k_1P_{CO}+k_{7M}P_{H2}}$$

$$R_{C_2H_4} = k_{8E}\,e^{2c}\alpha_1\alpha_2\sqrt{(K_9P_{H_2})}\,[vac] \qquad \alpha_2 = \frac{k_1P_{CO}}{k_1P_{CO}+k_7P_{H2}+k_{8E}e^{c2}}$$

$$R_{C_nH_{2n+2}} = k_7\alpha_1\alpha_2\prod_{n=3}^{n}\alpha_n\sqrt{(K_9P_{H_2})}\,P_{H2}\,[vac]$$

$$\alpha_N = \frac{k_1P_{CO}}{k_1P_{CO}+k_7P_{H2}+k_{8E}\,e^{cN}}$$

$$R_{C_NH_{2N}} = k_8\,e^{nc}\,\alpha_1\alpha_2\prod_{n=3}^{n}\alpha_n\sqrt{(K_9P_{H_2})}\,[vac]$$

FT-3) reaction path

MARR=70%

Reaction number	Reaction step	Constant parameter
0	$H_2 + 2* \leftrightarrow 2H*$	K0
1	$CO + * \leftrightarrow CO*$	K1
2	$CO* + H_2 \leftrightarrow H_2CO*$	K2
3	$H_2CO* + H_2 \leftrightarrow CH_2* + H_2O$	K3
4 RDS	$CH_2* + H* \rightarrow CH_3* + *$	k4
	$CH_2* + CH_3* \rightarrow C_2H_5* + *$	
	$CH_2* + C_NH_{2N+1}* \rightarrow C_{N+1}H_{2N+3}* + *$	
5 RDS	$CH_3* + H* \rightarrow CH_4 + 2*$	k5M
	$C_NH_{2N+1}* + H* \rightarrow C_NH_{2N+2} + 2*$	k5
6 RDS	$C_2H_5* \rightarrow C_2H_4 + H*$	k6E
	$C_NH_{2N+1}* \rightarrow C_2H_{2N} + H*$	k6

$$R_{CH_4} = k_{5M}[CH_3][H] \qquad \alpha_1 = \frac{k_4[CH_2][CH_3]}{k_4[CH_2][CH_3] + k_{5M}[CH_3][H]}$$

$$R_{C_2H_4} = k_{6E}\, e^{2c}\, [C_2H_5] \qquad \alpha_2 = \frac{k_4[CH_2][C_2H_5]}{k_4[CH_2][C_2H_5] + k_5[C_2H_5][H] + k_{6E}e^{c2}\, [C_2H_5]}$$

$$R_{C_nH_{2n+2}} = k_5[C_NH_{2N+1}][H] \quad \text{Paraffins n>=2} \qquad \alpha_n = \frac{k_4[CH_2][C_NH_{2N+1}]}{k_4[CH_2][C_NH_{2N+1}] + k_5[C_NH_{2N+1}][H] + k_6e^{nc}\, [}$$

$$R_{C_2H_4} = k_6\, e^{nc}\, [C_NH_{2N+1}] \quad \text{Olefins n>=3}$$

Application of the QSSA.

$$\frac{d[CH_3^*]}{dt} = 0 = Intermediate\ generation - intermediate\ termination$$
$$= k_4\,[CH_2]\,[H] - [CH_3](k_4[CH_2] + k_{5M}[H])$$

$$\frac{d[C_2H_5^*]}{dt} = 0 = k_4\,[CH_2]\,[CH_3] - [C_2H_5](k_4[CH_2] + k_5[H] + k_{6E}e^{2c})$$

$$\frac{d[C_nH_{2n+1}^*]}{dt} = 0 = k_4\,[CH_2]\,[C_{N-1}H_{2N-1}] - [C_NH_{2N+1}](k_4[CH_2] + k_5[H] + k_6e^{nc})$$

$$[\mathrm{CH_3^*}] = \alpha_1[H^*]$$

$$[\mathrm{C_2H_5^*}] = \alpha_2[CH_3^*]$$

$$[\mathrm{C_nH_{2n+1}^*}] = \alpha_n[C_{n-1}H_{2n-1}^*]$$

Balance:

$$1 = [*] + [H] + [CH_3] + [C_2H_5] + \sum_3^N [C_nH_{2N+1}^*] + [CO] + [H_2CO] + [CH_2]$$

1) $k_{1d}P_{CO}[*] = k_{1r}[CO] \rightarrow [CO] = K_1 P_{CO}[*]$

2) $k_{2d}P_{H_2}[CO] = k_{2r}[H_2CO] \rightarrow [H_2CO] = K_2 P_{H_2}[CO] = K_1K_2\, P_{H_2}P_{CO}[*]$

3) $k_{3d}P_{H_2}[H_2CO] = k_{3r}[CH_2]\, P_{H_2O} \rightarrow [CH_2] = K_3 \frac{P_{H_2}}{P_{H_2O}}[H_2CO] = K_1K_2K_3 \frac{P_{CO}\, P_{H_2}^2}{P_{H_2O}}\,[*]$

4) $[H] = \sqrt{(K_0 P_{H_2})}\,[*]$

And from the definition of the probability growths I can obtain

$$[\mathrm{CH_3^*}] = \alpha_1 \sqrt{(K_0 P_{H_2})}\,[*]$$

$$[\mathrm{C_2H_5^*}] = \alpha_1\, \alpha_2 \sqrt{(K_0 P_{H_2})}\,[*]$$

$$[\mathrm{C_nH_{2n+1}^*}] = \alpha_1\, \alpha_2 \prod_{n=3}^{n} \alpha_n \sqrt{(K_0 P_{H_2})}[*]$$

$$[*] = \frac{1}{DENOM3}$$

$$DENOM3 = 1 + K_1P_{CO} + K_1K_2P_{H_2}P_{CO} + K_1K_2K_3 \frac{P_{CO}\, P_{H_2}^2}{P_{H_2O}} + \sqrt{(K_0 P_{H_2})}(1 + \alpha_1 + \alpha_1\alpha_2 + \alpha_1\alpha_2 \sum_{j=3}^{n_c} \prod_{n=3}^{j} \alpha_n)$$

$$R_{CH_4} = k_{5M}\, K_0\, P_{H_2}\, \alpha_1\, [*]^2$$

$$R_{C_2H_4} = k_{6E}\, e^{2c} \sqrt{(K_0 P_{H_2})}\; \alpha_1\, \alpha_2\, [*]$$

$$R_{C_nH_{2n+2}} = k_5\, K_0\, P_{H_2}\, \alpha_1\, \alpha_2 \prod_{n=3}^{n} \alpha_n\, [*]^2 \qquad \text{Paraffins n>=2}$$

$$R_{C_2H_4} = k_6\, e^{nc} \sqrt{(K_0 P_{H_2})}\; \alpha_1\, \alpha_2 \prod_{n=3}^{n} \alpha_n\; [*] \qquad \text{Olefins n>=3}$$

It is possible to check how the derivation of [*] must pass from an iterative solution.

FT-4) mechanism path

MARR=77.4%

Reaction number	Reaction step	Constant parameter
0	$H_2 + 2* \leftrightarrow 2H*$	K0
1	$CO + * \leftrightarrow CO*$	K1
2	$CO* + H_2 \leftrightarrow H_2CO*$	K2
3	$H_2CO* + H_2 \leftrightarrow CH_2* + H_2O$	K3
4 RDS	$CH_2* + H* \rightarrow CH_3* + *$	k4
	$CH_2* + CH_3* \rightarrow C_2H_5* + *$	
	$CH_2* + C_NH_{2N+1}* \rightarrow C_{N+1}H_{2N+3}* + *$	
5 RDS	$CH_3* + H_2* \rightarrow CH_4 + 2*$	k5M
	$C_NH_{2N+1}* + H_2* \rightarrow C_NH_{2N+2} + 2*$	k5
6 RDS	$C_2H_5* \rightarrow C_2H_4 + H*$	k6E
	$C_NH_{2N+1}* \rightarrow C_2H_{2N} + H*$	k6

$$R_{CH_4} = k_{5M}[CH_3]P_{H_2}$$

$$R_{C_2H_4} = k_{6E}\, e^{2c}\, [C_2H_5]$$

$$R_{C_nH_{2n+2}} = k_5[C_NH_{2N+1}]P_{H_2} \quad \text{Paraffins } n>=2$$

$$R_{C_2H_4} = k_6 e^{nc}\, [C_NH_{2N+1}] \quad \text{Olefins } n>=3$$

$$\alpha_1 = \frac{k_4[CH_2]}{k_4[CH_2] + k_{5M}P_{H_2}}$$

$$\alpha_2 = \frac{k_4[CH_2]}{k_4[CH_2] + k_5P_{H_2} + k_{6E}e^{c2}}$$

$$\alpha_n = \frac{k_4[CH_2]}{k_4[CH_2] + k_5P_{H_2} + k_6e^{nc}}$$

Balance:

$$1 = [*] + [H] + [CH_3] + [C_2H_5] + \sum_3^N [C_nH_{2N+1}^*] + [CO] + [H_2CO] + [CH_2]$$

$$[CO] = K_1P_{CO}[*]$$

$$[H_2CO] = K_2P_{H_2}[CO] = K_1K_2\, P_{H_2}P_{CO}[*]$$

$$[CH_2] = K_3\, \frac{P_{H_2}}{P_{H_2O}}[H_2CO] = K_1K_2K_3\, \frac{P_{CO}\, P_{H_2}^2}{P_{H_2O}}\, [*]$$

$$[H] = \sqrt{(K_0P_{H_2})}\, [*]$$

And from the definition of the probability growths I can obtain

$$[\mathrm{CH_3^*}] = \alpha_1 \sqrt{(K_0P_{H_2})}\, [*]$$

$$[\mathrm{C_2H_5^*}] = \alpha_1\, \alpha_2 \sqrt{(K_0P_{H_2})}\, [*]$$

$$[\mathrm{C_nH_{2n+1}^*}] = \alpha_1\, \alpha_2 \prod_{n=3}^{n} \alpha_n \sqrt{(K_0P_{H_2})}[*]$$

Substituting I can then find the balance value.

$$[*] = \frac{1}{DENOM4}$$

$$DENOM4 = 1 + K_1 P_{CO} + K_1 K_2 P_{H_2} P_{CO} + K_1 K_2 K_3 \frac{P_{CO} P_{H_2}^2}{P_{H_2O}} + \sqrt{(K_0 P_{H_2})}(1 + \alpha_1 + \alpha_1\alpha_2 + \alpha_1\alpha_2 \sum_{j=3}^{n_c} \prod_{n=3}^{j} \alpha_n)$$

$$R_{CH_4} = k_{5M} \sqrt{(K_0 P_{H_2})}\ P_{H_2}\ \alpha_1\ [*]$$

$$R_{C_2H_4} = k_{6E}\ e^{2c} \sqrt{(K_0 P_{H_2})}\ \alpha_1\ \alpha_2\ [*]$$

$$R_{C_nH_{2n+2}} = k_5 \sqrt{(K_0 P_{H_2})}\ P_{H_2}\ \alpha_1\ \alpha_2 \prod_{n=3}^{n} \alpha_n\ [*] \qquad \text{Paraffins n>=2}$$

$$R_{C_2H_4} = k_6\ e^{nc} \sqrt{(K_0 P_{H_2})}\ \alpha_1\ \alpha_2 \prod_{n=3}^{n} \alpha_n\ [*] \qquad \text{Olefins n>=3}$$

It is possible to check how the derivation of [*] must pass from an iterative solution.

FT-5) reaction mechanism

MARR=98%

Reaction number	Reaction step	Constant parameter
1	$CO + * \leftrightarrow CO*$	K1
2	$CO* + H_2 \leftrightarrow H_2CO*$	K2
3	$H_2CO* + H_2 \leftrightarrow CH_2* + H_2O$	K3
4	$H_2 + 2* \leftrightarrow 2H*$	K4
5 RDS	$CH_2* + CH_2* \rightarrow C_2H_4* + *$	k5
	$CH_2* + C_NH_{2N}* \rightarrow C_{N+1}H_{2N+2}* + *$	
6	$CH_2* + H* \rightarrow CH_3* + *$	k6
	$C_NH_{2N}* + H* \rightarrow C_NH_{2N+1}* + *$	
7 RDS	$CH_3* + H* \rightarrow CH_4 + *$	k7M
	$C_NH_{2N+1}* + H* \rightarrow C_NH_{2N+2} + *$	k7
8 RDS	$C_2H_5* \rightarrow C_2H_4 + H*$	k8E
	$C_NH_{2N+1}* \rightarrow C_2H_{2N} + H*$	k8

$$R_{CH_4} = k_{7M}[CH_3][H]$$

$$\alpha_1 = \frac{k_5[CH_2]^2}{k_5[CH_2]^2 + k_{7M}P_{H_2}}$$

$$R_{C_2H_4} = k_{8E}\, e^{2c}\, [C_2H_5]$$

$$\alpha_2 = \frac{k_5[CH_2][C_2H_4]}{k_5[CH_2][C_2H_4] + k_7[C_2H_5][H] + k_{8E}e^{c2}[C_2H_5]}$$

$$R_{C_nH_{2n+2}} = k_7[C_NH_{2N+1}][H]$$

Paraffins n>=2

$$\alpha_N = \frac{k_5[CH_2][C_NH_{2N}]}{k_5[CH_2][C_NH_{2N}] + k_7[C_NH_{2N+1}][H] + k_{8E}e^{c2}[C_2H_5]}$$

$$R_{C_2H_4} = k_8\, e^{nc}\, [C_NH_{2N+1}]$$

Olefins n>=3

Balance from other reactions, we obtain

$$[CO] = K_1P_{CO}[*]$$

$$[H_2CO] = K_2P_{H_2}[CO] = K_1K_2\, P_{H_2}P_{CO}[*]$$

$$[CH_2] = K_3\, \frac{P_{H_2}}{P_{H_2O}}[H_2CO] = K_1K_2K_3\, \frac{P_{CO}\, P_{H_2}^2}{P_{H_2O}}\, [*]$$

$$k_{4d}P_{H_2}[*]^2 = k_{4r}[H]^2 \;\rightarrow\; [H] = \sqrt{(K_4P_{H_2})}\, [*]$$

$$[CH_3] = K_6\, \frac{[CH_2][H]}{[*]} = K_1K_2K_3\, K_6\sqrt{(K_4)}\, \frac{P_{CO}\, P_{H_2}^{2,5}}{P_{H_2O}}\, [*]$$

$$[C_NH_{2N+1}] = K_1K_2K_3\, \frac{P_{CO}\, P_{H_2}^2}{P_{H_2O}}\, [*] \prod_{n=2}^{n} \alpha_n$$

Balance:

$$1 = [*] + [H] + [CH_3] + \sum_{2}^{N}[C_NH_{2N+1}^*] + \sum_{2}^{N}[C_NH_{2N}^*] + [CO] + [H_2CO] + [CH_2]$$

With substitution of the previous expressions we can then get a value of

$$1 = [*] + P_{CO}[*]\left(K_1 + K_1K_2\,P_{H_2} + K_1K_2K_3\,\frac{P_{H_2}^2}{P_{H_2O}}\right) + \sqrt{(K_4P_{H_2})}\,[*] + K_1K_2K_3\,K_6\sqrt{(K_4)}\,\frac{P_{CO}\,P_{H_2}^{2.5}}{P_{H_2O}}\,[*] + K_1K_2K_3\,K_6\sqrt{(K_4)}\,\frac{P_{CO}\,P_{H_2}^{2.5}}{P_{H_2O}}\,[*]\prod_{n=2}^{n}\alpha_n + K_1K_2K_3\,\frac{P_{CO}\,P_{H_2}^2}{P_{H_2O}}\,[*]\prod_{n=2}^{n}\alpha_n$$

$$[*] = \frac{1}{DENOM5}$$

$$DENOM5 = 1 + P_{CO}\left(K_1 + K_1K_2\,P_{H_2} + K_1K_2K_3\,\frac{P_{H_2}^2}{P_{H_2O}}\right) + \sqrt{(K_4P_{H_2})} + K_1K_2K_3\,K_6\sqrt{(K_4)}\,\frac{P_{CO}\,P_{H_2}^{2.5}}{P_{H_2O}} + K_1K_2K_3\,K_6\sqrt{(K_4)}\,\frac{P_{CO}\,P_{H_2}^{2.5}}{P_{H_2O}}\,\prod_{n=2}^{n}\alpha_n + K_1K_2K_3\,\frac{P_{CO}\,P_{H_2}^2}{P_{H_2O}}\,\prod_{n=2}^{n}\alpha_n$$

Application of the QSSA.

$$\frac{d[CH_2^*]}{dt} = 0 = Intermediate\ generation - intermediate\ termination = -k_5\,[CH_2]^2 + k_5[CH_2]^2 + k_{7M}[CH_3][H])\ (would\ actually\ get\ a\ null\ value)$$

$$\frac{d[C_2H_4^*]}{dt} = 0 = -k_5\,[CH_2]\,[C_2H_4] + k_5[CH_2][C_2H_4] + k_7[C_2H_5][H] + k_{8E}e^{2c}[C_2H_5]$$

$$\frac{d[C_nH_{2n}^*]}{dt} = 0 = -k_5\,[CH_2]\,[C_NH_{2N}] + k_5[CH_2][C_NH_{2N}] + k_7[C_NH_{2N+1}][H] + k_8e^{nc}[C_NH_{2N+1}]$$

$$R_{CH_4} = k_{7M}K_1K_2K_3\,K_6K_4\,\frac{P_{CO}\,P_{H_2}^3}{P_{H_2O}}\,[*]^2$$

$$R_{C_2H_4} = k_{8E}\,e^{2c}\,K_1K_2K_3\,\frac{P_{CO}\,P_{H_2}^2}{P_{H_2O}}\,\alpha_2$$

$$R_{C_nH_{2n+2}} = k_7K_1K_2K_3\,K_6K_4\,\frac{P_{CO}\,P_{H_2}^3}{P_{H_2O}}\,[*]^2\prod_{n=2}^{n}\alpha_n \qquad \text{Paraffins n>=2}$$

$$R_{C_nH_{2n}} = k_8\,e^{nc}\,K_1K_2K_3\,\frac{P_{CO}\,P_{H_2}^2}{P_{H_2O}}\prod_{n=2}^{n}\alpha_n \qquad \text{Olefins n>=3}$$

There is the need of an iterative procedure in order to get values of [*] and of the different alphas.

FT-6) reaction mechanism

MARR=77.8%

Reaction number	Reaction step	Constant parameter
0	$H_2 + 2* \leftrightarrow 2H*$	K0
1	$CO + * \leftrightarrow CO*$	K1
2	$CO* + H* \leftrightarrow HCO* + *$	K2
3	$HCO* + H* \leftrightarrow C* + H_2O*$	K3
4	$H_2O* \leftrightarrow H_2O + *$	K4
5	$C* + H* \leftrightarrow CH* + *$	K5
6	$CH* + H* \leftrightarrow CH_2* + *$	K6
7 RDS	$CH_2* + H* \rightarrow CH_3* + *$	k7
	$CH_2* + CH_3* \rightarrow C_2H_5* + *$	
	$CH_2* + C_NH_{2N+1}* \rightarrow C_{N+1}H_{2N+3}* + *$	
8 RDS	$CH_3* + H* \rightarrow CH_4 + 2*$	k8M
	$C_NH_{2N+1}* + H* \rightarrow C_NH_{2N+2} + 2*$	k8
9 RDS	$C_2H_5* \rightarrow C_2H_4 + *$	k9E
	$C_NH_{2N+1}* \rightarrow C_NH_{2N} + 2*$	k9

Definition of the rates and probability growth values.

$$R_{CH_4} = k_{8M}[CH_3][H]$$

$$R_{C_2H_4} = k_{9E}\, e^{2c}\, [C_2H_5]$$

$$R_{C_nH_{2n+2}} = k_8[C_NH_{2N+1}][H]$$

$$R_{C_2H_4} = k_9\, e^{nc}\, [C_NH_{2N+1}]$$

$$\alpha_1 = \frac{k_7[CH_2]}{k_7[CH_2] + k_{8M}[H]}$$

$$\alpha_2 = \frac{k_7[CH_2]}{k_7[CH_2] + k_8[H] + k_{9E}e^{c2}}$$

$$\alpha_N = \frac{k_7[CH_2]}{k_7[CH_2] + k_8[H] + k_9e^{cn}}$$

Application of the QSSA.

$$\frac{d[CH_3^*]}{dt} = 0 = Intermediate\ generation - intermediate\ termination$$
$$= k_7[CH_2]\,[H] - [CH_3](k_7[CH_2] + k_{8M}[H])$$

$$\frac{d[C_2H_5^*]}{dt} = 0 = k_7[CH_2]\,[CH_3] - [C_2H_5](k_7[CH_2] + k_8[H] + k_{9E}e^{2c})$$

$$\frac{d[C_nH_{2n+1}^*]}{dt} = 0 = k_7[CH_2]\,[C_{N-1}H_{2N-1}] - [C_NH_{2N+1}](k_7[CH_2] + k_8[H] + k_9e^{nc})$$

$$[CH_3^*] = \alpha_1[H^*]$$
$$[C_2H_5^*] = \alpha_2[CH_3^*]$$
$$[C_nH_{2n+1}^*] = \alpha_n[C_{n-1}H_{2n-1}^*]$$

Balance:

$$1 = [*] + [H] + [CO] + [HCO] + [H_2O] + [C] + [CH] + [CH_2] + [CH_3] + [C_2H_5] + \sum_{3}^{N} [C_nH^*_{2N+1}]$$

$$[H] = \sqrt{(K_0 P_{H_2})}\,[*]$$

$$[CO] = K_1 P_{CO}[*]$$

$$[HCO] = K_2 \frac{[CO][H]}{[*]} = K_1 K_2 P_{CO} \sqrt{(K_0 P_{H_2})}\,[*]$$

$$[C] = K_3 \frac{[HCO][H]}{[H_2O]} = K_1\, K_2\, K_3\, K_4\, K_0\, \frac{P_{H_2}\, P_{CO}}{P_{H_2O}}\,[*]$$

$$[H_2O] = \frac{1}{K_4}\, P_{H_2O}\,[*]$$

$$[CH] = K_5 \frac{[C][H]}{[*]} = K_1\, K_2\, K_3\, K_4\, K_5\, K_0^{1.5}\, \frac{P_{H_2}^{1.5}\, P_{CO}}{P_{H_2O}}\,[*]$$

$$[CH_2] = K_6 \frac{[CH][H]}{[*]} = K_1\, K_2\, K_3\, K_4\, K_6\, K_5\, K_0^{2}\, \frac{P_{H_2}^{2}\, P_{CO}}{P_{H_2O}}\,[*]$$

Substitute all in the balance of sites to get the expression for the free site fraction/concentration.

$$1 = [*] + \sqrt{(K_0 P_{H_2})}\,[*] + K_1 P_{CO}[*] + K_1 K_2 P_{CO} \sqrt{(K_0 P_{H_2})}\,[*] + \frac{1}{K_4}\, P_{H_2O}\,[*] + K_1\, K_2\, K_3\, K_4\, K_0\, \frac{P_{H_2}\, P_{CO}}{P_{H_2O}}\,[*] + K_1\, K_2\, K_3\, K_4\, K_5\, K_0^{1.5}\, \frac{P_{H_2}^{1.5}\, P_{CO}}{P_{H_2O}}\,[*] + K_1\, K_2\, K_3\, K_4\, K_6\, K_5\, K_0^{2}\, \frac{P_{H_2}^{2}\, P_{CO}}{P_{H_2O}}\,[*] + \alpha_1 \sqrt{(K_0 P_{H_2})}\,[*] + \alpha_1 \alpha_2 \sqrt{(K_0 P_{H_2})}\,[*] + \alpha_1 \alpha_2 \sum_{j=3}^{n_c} \prod_{n=3}^{j} \alpha_n \sqrt{(K_0 P_{H_2})}\,[*]$$

From this I can extract [*] and the value of DENOM6.

There is the need of an iterative process to find the solution.

FT-7) reaction mechanism

MARR=52.38%

Reaction number	Reaction step	Constant parameter
0	$H_2 + 2^* \leftrightarrow 2H^*$	K0
1	$CO + H^* \leftrightarrow COH^*$	K1
	$CO + CH_3^* \leftrightarrow C_2OH_3^*$	
	$CO + C_NH_{2N+1}^* \leftrightarrow C_{N+1}OH_{2N+1}^*$	
2 RDS	$COH^* + H_2 \rightarrow CH^* + H_2O$	k2
	$C_2OH_3^* + H_2 \rightarrow C_2H_3^* + H_2O$	
	$C_NOH_{2N-1}^* + H_2 \rightarrow C_NH_{2N-1}^* + H_2O$	
3	$CH^* + H_2 \rightarrow CH_3^*$	K3
	$C_2H_3^* + H_2 \rightarrow C_2H_5^*$	
	$C_NH_{2N-1}^* + H_2 \rightarrow C_NH_{2N+1}^*$	
5 rds	$CH_3^* + H_2 \rightarrow CH_4 + H^*$	k5M
	$C_NH_{2N+1}^* + H_2 \rightarrow C_NH_{2N+2} + H^*$	k5
6 rds	$C_2H_5^* \rightarrow C_2H_4 + H^*$	k6E
	$C_NH_{2N+1}^* \rightarrow C_NH_{2N} + H^*$	k6

Definition of the rates and probability growth values.

$$R_{CH_4} = k_{5M}[CH_3]P_{H_2}$$

$$R_{C_2H_4} = k_{6E}\, e^{2c}\, [C_2H_5]$$

$$R_{C_nH_{2n+2}} = k_5[C_NH_{2N+1}]P_{H_2}$$

$$R_{C_NH_{2N}} = k_6\, e^{nc}\, [C_NH_{2N+1}]$$

$$\alpha_1 = \frac{k_2[C_2OH_3]}{k_2[C_2OH_3] + k_{5M}[CH_3]}$$

$$\alpha_2 = \frac{k_2[C_3OH_4]}{k_2[C_3OH_4] + k_5[C_2H_5] + k_{6E}e^{c2}}$$

$$\alpha_N = \frac{k_2[C_NOH_{2N-1}]}{k_2[C_NOH_{2N-1}] + k_5[C_NH_{2N+1}] + k_6e^{cn}}$$

QSSA application.

$$\frac{d[CH_3^*]}{dt} = 0 = generation - termination = k_{5m}[CH_3]\,P_{H_2} - P_{H_2}k_2[COH] + P_{H_2}k_2[C_2OH_3])$$

$$\frac{d[C_2H_5^*]}{dt} = 0 = = K_5[C_2H_5]P_{H_2} + K_6e^{2c}[C_2H_5] + K_2K_1P_{CO}[C_2H_5]P_{H_2} - K_2K_1P_{CO}[CH_3]P_{H_2}$$

$$\frac{d[C_nH_{2n+1}^*]}{dt} = 0 = K_5[C_NH_{2N+1}]P_{H_2} + K_6e^{nc}[C_NH_{2N+1}] + K_2K_1P_{CO}[C_NH_{2N+1}]P_{H_2} - K_2K_1P_{CO}[C_{N-1}H_{2N-1}]P_{H_2}$$

$$[CH_3^*] = \alpha_1[H^*]$$

$$[C_2H_5^*] = \alpha_2[CH_3^*]$$

$$[C_nH_{2n+1}^*] = \alpha_n[C_{n-1}H_{2n-1}^*]$$

$$\alpha_1 = \frac{k_2K_1P_{CO}}{k_2K_1P_{CO}+k_{5M}}$$

$$\alpha_2 = \frac{k_2K_1P_{CO}P_{H_2}}{k_2K_1P_{CO}P_{H_2} + k_5P_{H_2} + k_{6E}e^{c2}}$$

$$\alpha_N = \frac{k_2 K_1 P_{CO} P_{H_2}}{k_2 K_1 P_{CO} P_{H_2} + k_5 P_{H_2} + k_6 e^{cn}}$$

Balance:

$$1 = [*] + [H] + [CO] + [CH_3] + [C_2OH_3] + [C_2H_5] + \sum_3^N [C_n H^*_{2N+1}] + \sum_3^N [C_n OH^*_{2N-1}] + [CH] + [C_2H_3] + \sum_3^N [C_n H^*_{2N-1}]$$

$$[H] = \sqrt{(K_0 P_{H_2})}\,[*]$$

$$[COH] = K_1 P_{CO}[H] = K_1 P_{CO}\sqrt{(K_0 P_{H_2})}\,[*]$$

$$[CH_3] = \alpha_1[H^*] = \alpha_1\sqrt{(K_0 P_{H_2})}\,[*]$$

$$[C_2OH_3] = K_1 P_{CO}[CH_3] = K_1 P_{CO}\,\alpha_1\sqrt{(K_0 P_{H_2})}\,[*]$$

$$[C_2H_5] = \alpha_1\alpha_2[CH_3] = \alpha_1\,\alpha_2\sqrt{(K_0 P_{H_2})}\,[*]$$

$$[CH] = \frac{1}{K_3\,P_{H_2}}[CH_3] = \frac{1}{K_3\,P_{H_2}}\,\alpha_1\sqrt{(K_0 P_{H_2})}\,[*]$$

$$[C_2H_3] = \frac{1}{K_3\,P_{H_2}}[C_2H_5] = \frac{1}{K_3\,P_{H_2}}\,\alpha_1\,\alpha_2\sqrt{(K_0 P_{H_2})}\,[*]$$

$$\sum_3^N [C_n H^*_{2N-1}] = \frac{1}{K_3\,P_{H_2}}\sqrt{(K_0 P_{H_2})}\,[*]\,\alpha_1\,\alpha_2\sum_{j=3}^{n_c}\prod_{n=3}^{j}\alpha_n$$

$$\sum_3^N [C_n OH^*_{2N-1}] = K_1 P_{CO}\sqrt{(K_0 P_{H_2})}\,[*]\,\alpha_1\alpha_2\sum_{j=3}^{n_c}\prod_{n=3}^{j}\alpha_n$$

$$\sum_3^N [C_n H^*_{2N+1}] = \sqrt{(K_0 P_{H_2})}\,[*]\,\alpha_1\alpha_2\sum_{j=3}^{n_c}\prod_{n=3}^{j}\alpha_n$$

From this I can extract [*] and the value of DENOM7.
NO iteration needed.

FT-8) reaction mechanism

MARR=60.7%

Reaction number	Reaction step	Constant parameter
0	$H_2 + 2^* \leftrightarrow 2H^*$	0
1	$CO + H^* \leftrightarrow COH^*$	K1
	$CO + CH_3^* \leftrightarrow C_2OH_3^*$	
	$CO + C_NH_{2N+1}^* \leftrightarrow C_{N+1}OH_{2N+1}^*$ (As C_NOH_{2N-1})	
2	$COH^* + H_2 \rightarrow CH^* + H_2O$	K2
	$C_2OH_3^* + H_2 \rightarrow C_2H_3^* + H_2O$	
	$C_NOH_{2N-1}^* + H_2 \rightarrow C_NH_{2N-1}^* + H_2O$	
3 RDS	$CH^* + H_2 \rightarrow CH_3^*$	k3
	$C_2H_3^* + H_2 \rightarrow C_2H_5^*$	
	$C_NH_{2N-1}^* + H_2 \rightarrow C_NH_{2N+1}^*$	
5 rds	$CH_3^* + H_2 \rightarrow CH_4 + H^*$	k5M
	$C_NH_{2N+1}^* + H_2 \rightarrow C_NH_{2N+2} + H^*$	k5
6 rds	$C_2H_5^* \rightarrow C_2H_4 + H^*$	k6E
	$C_NH_{2N+1}^* \rightarrow C_NH_{2N} + H^*$	k6

Definition of the rates and probability growth values.

$$R_{CH_4} = k_{5M}[CH_3]P_{H_2} \qquad \alpha_1 = \frac{k_3[C_2H_3]\,P_{H_2}}{k_3[C_2H_3]\,P_{H_2} + k_{5M}[CH_3]\,P_{H_2}}$$

$$R_{C_2H_4} = k_{6E}\,e^{2c}\,[C_2H_5] \qquad \alpha_2 = \frac{k_3[C_3H_5]\,P_{H_2}}{k_3[C_3H_5]\,P_{H_2} + k_5[C_2H_5]P_{H_2} + k_{6E}e^{c2}[C_2H_5]}$$

$$R_{C_nH_{2n+2}} = k_5[C_NH_{2N+1}]P_{H_2} \qquad \alpha_N = \frac{k_3[C_NH_{2N-1}]\,P_{H_2}}{k_3[C_NH_{2N-1}]\,P_{H_2} + k_5[C_NH_{2N+1}+1]P_{H_2} + k_6e^{cN}[C_NH_{2N+1}]}$$

$$R_{C_NH_{2N}} = k_6\,e^{nc}\,[C_NH_{2N+1}]$$

By substitution of the different species expressions, based on the reactions

$$[C_2H_3] = K_2\frac{P_{H_2}}{P_{H_2O}}\,[C_2OH_3]\,;\,[C_2OH_3] = K_1P_{CO}\,[CH_3]\,;\,[C_3H_5] = K_1K_2P_{CO}P_{H_2}\,[C_2H_5]$$

$$\alpha_1 = \frac{K_1\,K_2\,k_3\frac{P_{CO}P_{H_2}^2}{P_{H_2O}}}{K_1\,K_2\,k_3\frac{P_{CO}P_{H_2}^2}{P_{H_2O}} + k_{5M}\,P_{H_2}}$$

$$\alpha_2 = \frac{K_1\,K_2\,k_3\frac{P_{CO}P_{H_2}^2}{P_{H_2O}}}{K_1\,K_2\,k_3\frac{P_{CO}P_{H_2}^2}{P_{H_2O}} + k_5P_{H_2} + k_{6E}e^{c2}}$$

$$\alpha_N = \frac{K_1\,K_2\,k_3\frac{P_{CO}P_{H_2}^2}{P_{H_2O}}}{K_1\,K_2\,k_3\frac{P_{CO}P_{H_2}^2}{P_{H_2O}} + k_5P_{H_2} + k_6e^{cN}}$$

QSSA application.

$$\frac{d[C_nH^*_{2n+1}]}{dt} = 0 = -k_5[C_NH_{2N+1}]\,P_{H_2} - k_6 e^{nc}\,[C_NH_{2N+1}] - k_{1D}P_{CO}[C_NH_{2N+1}] + K_3[C_NH_{2N-1}]$$

$$\frac{d[C_nH^*_{2n+1}]}{dt} = -k_5[C_NH_{2N+1}]\,P_{H_2} - k_6 e^{nc}\,[C_NH_{2N+1}] - k_3K_2K_1\,[C_NH_{2N+1}]\,\frac{P_{CO}P_{H_2}^2}{P_{H_2O}} + k_3K_2K_1P_{CO}\,[C_{N-1}H_{2N-1}]\,\frac{P_{H_2}}{P_{H_2O}}$$

Same applies to C=1 and C=2 to express alpha1 and alpha2. Considering always

$$[\mathrm{CH}_3^*] = \alpha_1[H^*]$$

$$[\mathrm{C_2H}_5^*] = \alpha_2[CH_3^*]$$

$$[\mathrm{C_nH}_{2n+1}{}^*] = \alpha_n[C_{n-1}H_{2n-1}{}^*]$$

Balance:

$$1 = [*] + [H] + [CO] + [CH_3] + [C_2OH_3] + [C_2H_5] + \sum_3^N [C_nH^*_{2N+1}] + \sum_3^N [C_nOH^*_{2N-1}] + [CH] + [C_2H_3] + \sum_3^N [C_nH^*_{2N-1}]$$

$$[H] = \sqrt{(K_0P_{H_2})}\,[*]$$

$$[COH] = K_1P_{CO}[H] = K_1P_{CO}\sqrt{(K_0P_{H_2})}\,[*]$$

$$[CH_3] = \alpha_1[H^*] = \alpha_1\sqrt{(K_0P_{H_2})}\,[*]$$

$$[C_2OH_3] = K_1P_{CO}[CH_3] = K_1P_{CO}\,\alpha_1\sqrt{(K_0P_{H_2})}\,[*]$$

$$[C_2H_5] = \alpha_2[CH_3] = \alpha_1\,\alpha_2\sqrt{(K_0P_{H_2})}\,[*]$$

$$[CH] = K_2\frac{P_{H_2}}{P_{H_2O}}\,[COH] = K_1K_2\,\frac{P_{H_2}}{P_{H_2O}}\,\sqrt{(K_0P_{H_2})}\,[*]$$

$$[C_2H_3] = \alpha_1K_1K_2\,\frac{P_{CO}P_{H_2}}{P_{H_2O}}\,\sqrt{(K_0P_{H_2})}\,[*]$$

$$\sum_3^N [C_nH^*_{2N-1}] = K_1K_2\,\frac{P_{CO}P_{H_2}}{P_{H_2O}}\sqrt{(K_0P_{H_2})}\,[*]\,\alpha_1\,\alpha_2\sum_{j=3}^{n_c}\prod_{n=3}^{j}\alpha_n$$

$$\sum_3^N [C_nOH^*_{2N-1}] = K_1P_{CO}\,\sqrt{(K_0P_{H_2})}\,[*]\,\alpha_1\alpha_2\sum_{j=3}^{n_c}\prod_{n=3}^{j}\alpha_n$$

$$\sum_3^N [C_nH^*_{2N+1}] = \sqrt{(K_0P_{H_2})}\,[*]\,\alpha_1\alpha_2\sum_{j=3}^{n_c}\prod_{n=3}^{j}\alpha_n$$

From this I can extract [*] and the value of DENOM8.

This time I have NO iteration needed.

FT-9) reaction mechanism

MARR=85.1%

Reaction number	Reaction step	Constant parameter
1	CO + * ↔ CO*	K1
2	CO* + * ↔ C* + O*	K2
3	C* + H_2 ↔ CH_2*	K3
4	O* + H_2 ↔ H_2O + *	K4
5	H_2 + 2* ↔ 2H*	K5
6 rds	CH_2* + H* → CH_3* + *	k6
	CH_2* + CH_3* → C_2H_5* + *	
	CH_2* + C_NH_{2N-1}* → $C_{N+1}H_{2N+3}$* + *	
7RDS	CH_3* + H* → CH_4 + 2*	k7M
	C_NH_{2N+1}* + H* → C_NH_{2N+2} + 2*	k7
8RDS	C_2H_5* → C_2H_4 + H*	k8E
	C_NH_{2N+1}* → C_NH_{2N} + H*	k8

Definition of the rates and probability growth values.

$$R_{CH_4} = k_{7M}[CH_3][H]$$

$$R_{C_2H_4} = k_{8E}\, e^{2c}\, [C_2H_5]$$

$$R_{C_nH_{2n+2}} = k_7[C_NH_{2N+1}][H]$$

$$R_{C_NH_{2N}} = k_8\, e^{nc}\, [C_NH_{2N+1}]$$

$$\alpha_1 = \frac{k_6[CH_2]}{k_6[CH_2] + k_{7M}[H]}$$

$$\alpha_2 = \frac{k_6[CH_2]}{k_6[CH_2] + k_{7M}[H] + k_{8E}e^{c2}}$$

$$\alpha_N = \frac{k_6[CH_2]}{k_6[CH_2] + k_7[H] + k_{8E}\, e^{cN}}$$

$$[CH_2] = K_3[C]P_{H_2}\,;\, [C] = K_2\frac{[CO][*]}{[O]};\, [O] = \frac{P_{H_2O}[*]}{K_4P_{H_2}};\, [CO] = K_1P_{CO}[*];[H] = \sqrt{(K_5P_{H_2})}[*]$$

$$\alpha_1 = \frac{K_1\,K_2\,K_3\,K_4\,k_6\frac{P_{CO}P_{H_2}^2}{P_{H_2O}}}{K_1\,K_2\,K_3\,K_4\,k_6\frac{P_{CO}P_{H_2}^2}{P_{H_2O}} + k_{7M}\sqrt{(K_5P_{H_2})}}$$

$$\alpha_2 = \frac{K_1\,K_2\,K_3\,K_4\,k_6\frac{P_{CO}P_{H_2}^2}{P_{H_2O}}\,[*]}{K_1\,K_2\,K_3\,K_4\,k_6\frac{P_{CO}P_{H_2}^2}{P_{H_2O}}[*] + k_7\sqrt{(K_5P_{H_2})}\,[*] + k_{8E}e^{c2}}$$

$$\alpha_N = \frac{K_1\,K_2\,K_3\,K_4\,k_6\frac{P_{CO}P_{H_2}^2}{P_{H_2O}}\,[*]}{K_1\,K_2\,K_3\,K_4\,k_6\frac{P_{CO}P_{H_2}^2}{P_{H_2O}}\,[*] + k_7\sqrt{(K_5P_{H_2})}\,[*] + k_8e^{cn}}$$

QSSA for the expression of the probability growth.

$$\frac{d[C_nH_{2n+1}^*]}{dt} = 0 = k_6[CH_2][C_{N-1}H_{2N-1}] - k_6[CH_2]\,[C_NH_{2N+1}] - k_7[H][C_NH_{2N+1}] - K_8e^{nc}[C_NH_{2N+1}]$$

Same applies to C=1 and C=2 to express alpha1 and alpha2. Considering always

$$[\mathrm{CH}_3^*] = \alpha_1[H^*]$$

$$[\mathrm{C_2H}_5^*] = \alpha_2[CH_3^*]$$

$$[\mathrm{C_nH}_{2n+1}{}^*] = \alpha_n[C_{n-1}H_{2n-1}{}^*]$$

Balance:

$$1 = [*] + [H] + [CO] + [CH_3] + [C_2H_5] + [C] + [0] + [CH_2] + \sum_3^N [C_nH_{2N+1}^*]$$

$$[H] = \sqrt{(K_5 P_{H_2})}\,[*]$$

$$[CO] = K_1 P_{CO}[*]$$

$$[C] = K_2 \frac{[CO][*]}{[O]} = K_1\, K_2\, K_4\, \frac{P_{CO}P_{H_2}}{P_{H_2O}}\,[*]$$

$$[CH_2] = K_1\, K_2\, K_3\, K_4\, \frac{P_{CO}P_{H_2}^2}{P_{H_2O}}\,[*]$$

$$[O] = \frac{P_{H_2O}}{K_4 P_{H_2}}\,[*]$$

$$[CH_3] = \alpha_1\,[H] = \alpha_1\sqrt{(K_5 P_{H_2})}\,[*]$$

$$[C_2H_5] = \alpha_1\,\alpha_2\sqrt{(K_7 P_{H_2})}\,[*]$$

$$\sum_3^N [C_nH_{2N+1}^*] = \sqrt{(K_7 P_{H_2})}\,[*]\,\alpha_1\alpha_2 \sum_{j=3}^{n_c}\prod_{n=3}^{j}\alpha_n$$

From this I can extract [*] and the value of DENOM9.

Iteration needed.

FT-10) reaction mechanism

MARR=74%

Reaction number	Reaction step	Constant parameter
0	$H_2 + 2^* \leftrightarrow 2H^*$	K0
1 RDS	$CO + H^* \leftrightarrow COH^*$	k1
	$CO + CH_3^* \leftrightarrow C_2OH_3^*$	
	$CO + C_NH_{2N+1}^* \leftrightarrow C_{N+1}OH_{2N+1}^*$	
2	$COH^* + H^* \leftrightarrow CH^* + OH^*$	K2
	$C_2OH_3^* + H^* \leftrightarrow C_2H_3^* + OH^*$	
	$C_{N+1}OH_{2N+1}^* + H^* \leftrightarrow C_NH_{2N-1}^* + OH^*$	
3	$C_NH_{2N-1}^* + H^* \leftrightarrow C_NH_{2N}^* + ^*$	K3
4	$C_NH_{2N}^* + H^* \leftrightarrow C_NH_{2N+1}^* + ^*$	K4
5	$OH^* + H^* \leftrightarrow H_2O + 2^*$	K5
6RDS	$CH_3^* + H^* \rightarrow CH_4 + 2^*$	k6M
	$C_NH_{2N+1}^* + H^* \rightarrow C_NH_{2N+2} + 2^*$	k6
7RDS	$C_2H_5^* \rightarrow C_2H_4 + H^*$	k7E
	$C_NH_{2N+1}^* \rightarrow C_NH_{2N} + H^*$	k7

Definition of the rates and probability growth values.

$$R_{CH_4} = k_{6M}[CH_3][H]$$

$$R_{C_2H_4} = k_{7E}\, e^{2c}\, [C_2H_5]$$

$$R_{C_nH_{2n+2}} = k_6[C_NH_{2N+1}][H]$$

$$R_{C_NH_{2N}} = k_7\, e^{nc}\, [C_NH_{2N+1}]$$

$$\alpha_1 = \frac{k_1P_{CO}}{k_1P_{CO} + k_{6M}[H]}$$

$$\alpha_2 = \frac{k_1P_{CO}}{k_1P_{CO} + k_6[H] + k_{7E}e^{c2}}$$

$$\alpha_N = \frac{k_1P_{CO}}{k_1P_{CO} + k_6[H] + k_{7E}\, e^{cN}}$$

QSSA for the expression of the probability growth.

$$\frac{d[C_nH_{2n+1}^*]}{dt} = 0 = k_1P_{CO}[C_{N-1}H_{2N-1}] - k_1P_{CO}\,[C_NH_{2N+1}] - k_7[H][C_NH_{2N+1}] - K_8e^{nc}[C_NH_{2N+1}]$$

Same applies to C=1 and C=2 to express alpha1 and alpha2.

$$[\mathrm{CH_3^*}] = \alpha_1[H^*]$$

$$[\mathrm{C_2H_5^*}] = \alpha_2[CH_3^*]$$

$$[\mathrm{C_nH_{2n+1}}^*] = \alpha_n[C_{n-1}H_{2n-1}{}^*]$$

Balance:

$$1 = [*] + [H] + [COH] + [CH_3] + [C_2OH_3] + [CH] + [C_2H_3] + [OH] + [C_2H_5] + [CH_2] + [C_2H_4] + \sum_3^N [C_nH_{2N+1}^*] + \sum_3^N [C_nH_{2N-1}^*] + \sum_3^N [C_nH_{2N}^*] + \sum_3^N [C_nOH_{2N-1}^*]$$

$$[H] = \sqrt{(K_0P_{H_2})}\,[*]$$

$$[CH] = \frac{1}{K_3}\frac{[CH_2]}{[H]}[*] = \frac{\alpha_1}{K_3\,K_4}\frac{1}{\sqrt{(K_0P_{H_2})}}[*]$$

$$[C_2H_3] = \frac{1}{K_3}\frac{[C_2H_4]}{[H]}[*] = \frac{\alpha_1\alpha_2}{K_3\,K_4}\frac{1}{\sqrt{(K_0P_{H_2})}}[*]$$

$$[CH_2] = \frac{1}{K_4}\frac{[CH_3]}{[H]}[*] = \frac{1}{K_4}\frac{\alpha_1\sqrt{(K_0P_{H_2})}}{\sqrt{(K_0P_{H_2})}}[*] = \frac{\alpha_1}{K_4}[*]$$

$$[C_2H_4] = \frac{1}{K_4}\frac{[C_2H_5]}{[H]}[*] = \frac{\alpha_1\alpha_2}{K_4}[*]$$

$$[C_2H_5] = \alpha_1\,\alpha_2\sqrt{(K_0P_{H_2})}\,[*]$$

$$[OH] = P_{H_2O}\frac{[*]^2}{[H]K_5} = \frac{1}{K_5}\frac{P_{H_2O}}{\sqrt{(K_0P_{H_2})}}[*]$$

$$[COH] = \frac{1}{K_2}\frac{[CH][OH]}{[H]} = \frac{\alpha_1}{K_2\,K_3\,K_4\,K_5}\frac{P_{H_2O}}{\left(K_0P_{H_2}\right)^{1.5}}[*]$$

$$[C_2OH_3] = \frac{1}{K_2}\frac{[C_2H_3][OH]}{[H]} = \frac{\alpha_1\alpha_2}{K_2\,K_3\,K_4\,K_5}\frac{P_{H_2O}}{\left(K_0P_{H_2}\right)^{1.5}}[*]$$

$$\sum_3^N[C_nH^*_{2N+1}] = \alpha_1\alpha_2\sum_{j=3}^{n_c}\prod_{n=3}^{j}\alpha_n\sqrt{(K_0P_{H_2})}\,[*]$$

$$\sum_3^N[C_nH^*_{2N-1}] = \alpha_1\alpha_2\sum_{j=3}^{n_c}\prod_{n=3}^{j}\alpha_n\frac{1}{K_3\,K_4\sqrt{(K_0P_{H_2})}}[*]$$

$$\sum_3^N[C_nH^*_{2N}] = \frac{\alpha_1\alpha_2}{K_4}\sum_{j=3}^{n_c}\prod_{n=3}^{j}\alpha_n\,[*]$$

$$\sum_3^N[C_nOH^*_{2N-1}] = \frac{\alpha_1\alpha_2}{K_2\,K_3\,K_4\,K_5}\sum_{j=3}^{n_c}\prod_{n=3}^{j}\alpha_n\frac{P_{H_2O}}{\left(K_0P_{H_2}\right)^{1.5}}[*]$$

From this I can extract [*] and the value of DENOM10.

This time I have iteration needed.

FT-11) reaction mechanism

MARR=93.9%

Reaction number	Reaction step	Constant parameter
0	$H_2 + 2* \leftrightarrow 2H*$	K0
1	$CO + H* \leftrightarrow COH*$	k1
	$CO + CH_3* \leftrightarrow C_2OH_3*$	
	$CO + C_NH_{2N+1}* \leftrightarrow C_{N+1}OH_{2N+1}*$	
2 rds	$COH* + H* \leftrightarrow CH* + OH*$	k2
	$C_2OH_3* + H* \leftrightarrow C_2H_3* + OH*$	
	$C_NOH_{2N-1}* + H* \leftrightarrow C_NH_{2N-1}* + OH*$	
3	$C_NH_{2N-1}* + H* \leftrightarrow C_NH_{2N}* + *$	K3
4	$C_NH_{2N}* + H* \leftrightarrow C_NH_{2N+1}* + *$	K4
5	$OH* + H* \leftrightarrow H_2O + 2*$	K5
6RDS	$CH_3* + H* \rightarrow CH_4 + 2*$	k6M
	$C_NH_{2N+1}* + H* \rightarrow C_NH_{2N+2} + 2*$	k6
7RDS	$C_2H_5* \rightarrow C_2H_4 + H*$	k7E
	$C_NH_{2N+1}* \rightarrow C_NH_{2N} + H*$	k7

Definition of the rates and probability growth values.

$$R_{CH_4} = k_{6M}[CH_3][H] \qquad \alpha_1 = \frac{k_2[C_2OH_3]}{k_2[C_2OH_3] + k_{7M}[CH_3]}$$

$$R_{C_2H_4} = k_{7E}\, e^{2c}\, [C_2H_5] \qquad \alpha_2 = \frac{k_2[C_3OH_5][H]}{k_2[C_3OH_5][H] + k_6[C_2H_5][H] + k_{7E}e^{c2}[C_2H_5]}$$

$$R_{C_nH_{2n+2}} = k_6[C_NH_{2N+1}][H] \qquad \alpha_N = \frac{k_2[C_{N+1}OH_{2N+1}][H]}{k_2[C_{N+1}OH_{2N+1}][H] + k_6[C_NH_{2N+1}][H] + k_7e^{cN}[C_NH_{2N+1}]}$$

$$R_{C_NH_{2N}} = k_7\, e^{nc}\, [C_NH_{2N+1}]$$

Given that I can express the intermediates as

$$[C_2OH_3] = K_1[CH_3]P_{CO}\,;\, [C_3OH_5] = K_1[C_2H_5]P_{CO}\,;\, [H] = \sqrt{(K_9P_{H_2})}\,[*]$$

QSSA for the expression of the probability growth.

$$\frac{d[C_nH^*_{2n+1}]}{dt} = 0 = -k_{1D}P_{CO}[C_{N+1}H_{2N+1}] + k_2[C_{N-1}OH_{2N-1}][H] - k_6[H][C_NH_{2N+1}] - K_7e^{nc}[C_NH_{2N+1}]$$

Same applies to C=1 and C=2 to express alpha1 and alpha2. Considering always

$$CH_3 = \alpha 1[H*]$$

$$C_2H_5* = \alpha 2[CH3*]$$

$C_nH_{2n+1}* = \alpha n[C_{n-1}H_{2n-1}*]$

Balance:

$$1 = [*] + [H] + [COH] + [CH_3] + [C_2OH_3] + [CH] + [C_2H_3] + [OH] + [C_2H_5] + [CH_2] + [C_2H_4] + \sum_{3}^{N}[C_nH^*_{2N+1}] + \sum_{3}^{N}[C_nH^*_{2N-1}] + \sum_{3}^{N}[C_nH^*_{2N}] + \sum_{3}^{N}[C_nOH^*_{2N-1}]$$

Get values of other intermediates concentration with respect to the reactions

$$[H] = \sqrt{(K_0 P_{H_2})}\,[*]$$

$$[CH] = \frac{1}{K_3}\frac{[CH_2]}{[H]}[*] = \frac{\alpha_1}{K_3\,K_4}\frac{1}{\sqrt{(K_0 P_{H_2})}}[*]$$

$$[C_2H_3] = \frac{1}{K_3}\frac{[C_2H_4]}{[H]}[*] = \frac{\alpha_1\alpha_2}{K_3\,K_4}\frac{1}{\sqrt{(K_0 P_{H_2})}}[*]$$

$$[CH_2] = \frac{1}{K_4}\frac{[CH_3]}{[H]}[*] = \frac{\alpha_1}{K_4}\,[*]$$

$$[C_2H_4] = \frac{1}{K_4}\frac{[C_2H_5]}{[H]}[*] = \frac{\alpha_1\alpha_2}{K_4}\,[*]$$

$$[C_2H_5] = \alpha_1\,\alpha_2\sqrt{(K_0 P_{H_2})}\,[*]$$

$$[OH] = P_{H_2O}\frac{[*]^2}{[H]K_5} = \frac{1}{K_5}\frac{P_{H_2O}}{\sqrt{(K_0 P_{H_2})}}[*]$$

$$[COH] = K_1 P_{CO}[H] = K_1 P_{CO}\sqrt{(K_0 P_{H_2})}\,[*]$$

$$[C_2OH_3] = K_1[CH_3]P_{CO} = K_1 P_{CO}\,\alpha_1\sqrt{(K_0 P_{H_2})}\,[*]$$

$$\sum_{3}^{N}[C_nH^*_{2N+1}] = \alpha_1\alpha_2\sum_{j=3}^{n_c}\prod_{n=3}^{j}\alpha_n\sqrt{(K_0 P_{H_2})}\,[*]$$

$$\sum_{3}^{N}[C_nH^*_{2N-1}] = \alpha_1\alpha_2\sum_{j=3}^{n_c}\prod_{n=3}^{j}\alpha_n\frac{1}{K_3\,K_4\sqrt{(K_0 P_{H_2})}}[*]$$

$$\sum_{3}^{N}[C_nH^*_{2N}] = \frac{\alpha_1\alpha_2}{K_4}\sum_{j=3}^{n_c}\prod_{n=3}^{j}\alpha_n\,[*]$$

$$\sum_{3}^{N}[C_nOH^*_{2N-1}] = K_1 P_{CO}\,\alpha_1\alpha_2\sum_{j=3}^{n_c}\prod_{n=3}^{j}\alpha_n\sqrt{(K_0 P_{H_2})}\,[*]$$

From this I can extract [*] and the value of DENOM11. This time I have iteration needed.

Appendix B – Literature studies

Ref.	Carbon Feedstock	Study Obj.
[72]	Air	Results of a pilot plant within the Finnish national project SOLETAIR, integrating DAC with RWGS, low-T electrolysis, and FT
[310]	Air, concentrated CO_2 source, biomass	Life cycle assessment (LCA) for Liquid FT diesel, using different carbon sources, with RWGS and FT technologies
[311]	Air	LCA and economic assessment for FT jet fuels, including low-T DAC and fixed syngas-to-FT conversion, with solar electricity feed
[312]	Air	LCA and economic assessment for FT fuels for light-duty vehicles in 2015/2030. Low-T DAC for cost analysis, and literature-based FT description
[313]	Air	Evaluation of the combustion processes and of FT and OMEx synthetic fuels, with LCA considerations when feeding CO_2 from DAC
[210]	Air	LCA study over the conversion of CO_2 from air to FT diesel, with sensitivity over the carbon intensity of different electricity sources. High-T DAC model and literature-based FT distribution, with no mass/energy integration
[91,314]	Air, concentrated CO_2 source	Review of the Power-To-Liquid routes to Fischer-Tropsch and MeOH liquid fuels, with additional environmental and TEA formulations
[315]	Air	Integration of the DAC technology (both high and low temperature) in the German technology horizon, with inclusion of productivity data for the FT synthesis
[213]	Air	Review of CO_2 utilization pathways, with TEA for the production of synthetic diesel from air CO_2, solid oxide co-electrolysis, and Fischer-Tropsch, with energy integration solution
[207,209]	Air	Forecast scenarios with economic considerations for the production of transportation fuels using carbon dioxide from the air. Low-T DAC design and Fischer-Tropsch description based on clustered data depending on the mass share. Energy and mass integration solutions included
[316]	Air, biomass	Production of FT syncrude based on different carbon sources and with intermittent RES feeding coupled with CO_2 storage unit. Fischer-Tropsch data based on experimental activities on commercial catalyst [317]
[316]	Air, concentrated CO_2 source, biomass	Review on power-to-liquid routes and evaluation of the production costs of synthetic diesel based on the carbon feedstock and production chain
[14]	Air, concentrated CO_2 source, biomass, biogas	Review of power-to-liquid production routes aimed at Fischer-Tropsch synthetic fuels
[28]	Biogas	Energy analysis and system integration for the capture of carbon dioxide from biogas, and its conversion to FT products with interposed RWGS+alkaline electrolysis or SOEC co-electrolysis of steam and CO_2
[202]	Biogas	TEA evaluation for the production of Fischer-Tropsch diesel, with direct use of biogas, with steam and partial oxidation reforming for syngas generation
[200]	Biogas	TEA evaluation for the synthesis of Fischer-Tropsch waxes from biogas, exploiting reforming reaction for the production of intermediate syngas
[318]	Biogas	Direct use of biogas, with oxidation of methane for syngas production, and two-steps Fischer-Tropsch synthesis
[215]	CO_2 concentrated source	Energy analysis derived from the integration of the capture of carbon dioxide from flue gases to Fische-Tropsch products synthesis.
[29]	CO_2 concentrated source	Energy and mass integration of CO_2 to FT process, with low and high temperature electrolysis fro hydrogen production. Comparison of different solution for the heat generation required by the syngas production step.
[214]	CO_2 concentrated source	Production of FT fuels with experimental SOEC co-electrlysis data and fixed probability growth value for the FT distribution derived from the ASF theory
[43]	CO_2 concentrated	TEA analysis for the synthesis of Fischer-Tropsch waxes and liquid

	source	fuels with connection of the SOEC technology in co-electrolysis to the FT reactor. Analysis on different temperature and pressure values of the SOEC unit
[319]	CO_2 concentrated source	Thermodynamic analysis for the conversion of concentrated carbon dioxide and biomass carbon material to Fischer-Tropsch liquid diesel with direct connection to RES power
[320]	CO_2 concentrated source	Thermodynamic analysis for the conversion of concentrated carbon dioxide to FT fuels with autothermal reforming and high-temperature (Fe-based catalyst) technology with FT experimental data
[201]	CO_2 concentrated source	TEA analysis for the conversion of carbon dioxide into Fischer-Tropsch wax fraction
[296]	CO_2 concentrated source	TEA analysis for the conversion of carbon dioxide into Fischer-Tropsch diesel fraction, including heavy waxes hydrocracking and syngas generation in a SOEC co-electrolyser
[75]	CO_2 concentrated source	Economic considerations for the production of FT diesel in off-grid applications directly connected to renewable energy sources located in Germany
[256]	Biomass (Forest residues, wood straws)	Energy and thermodynamic analysis of the conversion of biomass to FT products, with effect of different biomass drying levels
[264]	Biomass (rice straw)	TEA evalution for the production of FT liquid fuels with integrated recirculation of FT off-gas, with ASF description and selectivity of C_{5+} compounds depending on reactancts partial pressure and temperature
[255]	Biomass (wood)	TEA assessment for the conversion of biomass to FT liquid fuels, with both low and high temperature FT reaction and co-feeding of natural gas for syngas generation
[204]	Biomass, concentrated CO_2 source	Economic analysis for the conversion of carbon feedstock to FT diesel material, under routes configurations coprising of power-to-liquid (BtL), biomass-to-liquid (PtL), and Power/Biomass-to-Liquid (PBtL)
[205]	Biomass (wood)	TEA evaluation for the conversion of wood biomass into FT diesel, with interposed SOEC for hydrogen generation
[266]	Biomass (forest residues)	TEA analysis for the conversion of residues of forestry activities into FT diesel, located in the country of Brazil
[42]	Biomass (wood residues/straw)	TEA analysis comparis the conversion of biomass into either FT diesel of DME liquid fuels
[206]	Biomass (wood)	Thermodynamic analysis of a small-scale route converting biomass to FT fuels exploiting literature data for the FT distribution
[300]	Biomass (wood chips)	TEA analysis for the conversion of biomass to FT diesel, with experimental activities of the entire process route

Appendix C – Fortran code

Code -

```
C$ #2 BY: PATNAIK DATE: 14-NOV-1998 INCLUDE COMMONS FOR RADFRAC/RATEFRAC
C$ #1 BY: ANAVI DATE:  1-JUL-1994 NEW FOR USER MODELS
C
C     User Kinetics Subroutine for RCSTR, RPLUG, RBATCH, PRES-RELIEF,
C     RADFRAC and RATEFRAC (USER type Reactions)
C
      SUBROUTINE USRFT1 (SOUT,   NSUBS,  IDXSUB,   ITYPE,  NINT,
     2                   INT,    NREAL,  REAL,     IDS,    NPO,
     3                   NBOPST, NIWORK, IWORK,    NWORK,  WORK,
     4                   NC,     NR,     STOIC,    RATES,  FLUXM,
     5                   FLUXS,  XCURR,  NTCAT,    RATCAT, NTSSAT,
     6                   RATSSA, KCALL,  KFAIL,    KFLASH, NCOMP,
     7                   IDX,    Y,      X,        X1,     X2,
     8                   NRALL,  RATALL, NUSERV,   USERV,  NINTR,
     9                   INTR,   NREALR, REALR,    NIWR,   IWR,
     *                   NWR,    WR,     NRL,      RATEL,  NRV,
     1                   RATEV)
C
      IMPLICIT NONE
C
C     DECLARE VARIABLES USED IN DIMENSIONING
C
      INTEGER NSUBS, NINT,  NPO,   NIWORK,NWORK,
     +        NC,    NR,    NTCAT, NTSSAT,NCOMP,
     +        NRALL, NUSERV,NINTR, NREALR,NIWR,
     +        NWR
C
C     DECLARE ARGUMENTS
C
      INTEGER IDXSUB(NSUBS),ITYPE(NSUBS), INT(NINT),
     +        IDS(2),NBOPST(6,NPO),IWORK(NIWORK),
     +        IDX(NCOMP),   INTR(NINTR),  IWR(NIWR),
     +        NREAL, KCALL, KFAIL, KFLASH, NRL,
     +        NRV
      REAL*8 SOUT(1),      WORK(NWORK),
     +       STOIC(NC,NSUBS,NR),  RATES(NC),
     +       FLUXM(1),     FLUXS(1),     RATCAT(NTCAT),
     +       RATSSA(NTSSAT),      Y(NCOMP),
     +       X(NCOMP),     X1(NCOMP),    X2(NCOMP)
      REAL*8 RATALL(NRALL), USERV(NUSERV),
     +       REALR(NREALR), WR(NWR),      RATEL(1),
     +       RATEV(1),     XCURR
C
C     DECLARE LOCAL VARIABLES
      INTEGER NCP, NCO
      PARAMETER(NCP=70)
      PARAMETER(NCO=40)
      INTEGER IMISS, I, J, DMS_KCCIDC, ICO, IH2, IH2O, ICO2,
     +        IC_P(NCP), IC_O(NCO)
      REAL*8 REAL(NREAL),  RMISS,  T, P,
     +       VFRAC, BETA,  VVAP,  VLIQ, VLIQS
      REAL*8 CATMASS, BED_VOID, XLEN, DIAM, AXCRD
      REAL*8 k1, K2, K3, K4, K5, k6, k6M, k70, k7E0, K8,
     +       ALPHA(NCP), DE, ADSORP, ALPH, ALP, B(1),
     +       ALPHTERM, AREA, CAT_RHO
      REAL*8 PCO, PH2, PH2O
      REAL*8 KF_P(NCP), DRIVE_P,
     +       KF_O(NCO), DRIVE_O
C
#include "ppexec_user.cmn"
      EQUIVALENCE (RMISS, USER_RUMISS)
      EQUIVALENCE (IMISS, USER_IUMISS)
#include "dms_maxwrt.cmn"
```

```
 9000 FORMAT('**FT** ONE =',I4,'  TWO =',I4,'  THREE =',G12.5)
 9020 FORMAT('**FT** ONE=',I4,' TWO=',I4,' THREE=',I4)
 9030 FORMAT('**FT** FOUR=',G12.5,' FIVE=',G12.5,' SIX=',G12.5)
#include "dms_plex.cmn"
      EQUIVALENCE (B(1), IB(1))
C
C.....RCSTR...
#include "rplg_rplugr.cmn"
      EQUIVALENCE (CATMASS, RPLUGR_CATWT)
      EQUIVALENCE (BED_VOID, RPLUGR_BED_VOID)
      EQUIVALENCE (XLEN, RPLUGR_UXLONG)
      EQUIVALENCE (DIAM, RPLUGR_UDIAM)
      EQUIVALENCE (AXCRD, RPLUGR_AXPOS)
C
C.....REACTOR (OR PRES-RELIEF VESSEL OR STAGE) PROPERTIES...
#include "rxn_rprops.cmn"
      EQUIVALENCE (T, RPROPS_UTEMP)
      EQUIVALENCE (P, RPROPS_UPRES)
      EQUIVALENCE (VFRAC, RPROPS_UVFRAC)
      EQUIVALENCE (BETA, RPROPS_UBETA)
      EQUIVALENCE (VVAP, RPROPS_UVVAP)
      EQUIVALENCE (VLIQ, RPROPS_UVLIQ)
      EQUIVALENCE (VLIQS, RPROPS_UVLIQS)
C
C     BEGIN EXECUTABLE CODE
C
      AREA = (3.14D0/4.D0)*DIAM**2
      CAT_RHO = BED_VOID*CATMASS/(AREA*XLEN)
C
      IC_P(1) = DMS_KCCIDC('CH4')
      IC_O(1) = 0
      IC_P(2) = DMS_KCCIDC('C2H6')
      IC_O(2) = DMS_KCCIDC('C2H4')
      IC_P(3) = DMS_KCCIDC('C3H8')
      IC_O(3) = DMS_KCCIDC('C3H6')
      IC_P(4) = DMS_KCCIDC('C4H10')
      IC_O(4) = DMS_KCCIDC('C4H8')
      IC_P(5) = DMS_KCCIDC('C5H12')
      IC_O(5) = DMS_KCCIDC('C5H10')
      IC_P(6) = DMS_KCCIDC('C6H14')
      IC_O(6) = DMS_KCCIDC('C6H12')
      IC_P(7) = DMS_KCCIDC('C7H16')
      IC_O(7) = DMS_KCCIDC('C7H14')
      IC_P(8) = DMS_KCCIDC('C8H18')
      IC_O(8) = DMS_KCCIDC('C8H16')
      IC_P(9) = DMS_KCCIDC('C9H20')
      IC_O(9) = DMS_KCCIDC('C9H18')
      IC_P(10) = DMS_KCCIDC('C10H22')
      IC_O(10) = DMS_KCCIDC('C10H20')
      IC_P(11) = DMS_KCCIDC('C11H24')
      IC_O(11) = DMS_KCCIDC('C11H22')
      IC_P(12) = DMS_KCCIDC('C12H26')
      IC_O(12) = DMS_KCCIDC('C12H24')
      IC_P(13) = DMS_KCCIDC('C13H28')
      IC_O(13) = DMS_KCCIDC('C13H26')
      IC_P(14) = DMS_KCCIDC('C14H30')
      IC_O(14) = DMS_KCCIDC('C14H28')
      IC_P(15) = DMS_KCCIDC('C15H32')
      IC_O(15) = DMS_KCCIDC('C15H30')
      IC_P(16) = DMS_KCCIDC('C16H34')
      IC_O(16) = DMS_KCCIDC('C16H32')
      IC_P(17) = DMS_KCCIDC('C17H36')
      IC_O(17) = DMS_KCCIDC('C17H34')
      IC_P(18) = DMS_KCCIDC('C18H38')
      IC_O(18) = DMS_KCCIDC('C18H36')
      IC_P(19) = DMS_KCCIDC('C19H40')
      IC_O(19) = DMS_KCCIDC('C19H38')
      IC_P(20) = DMS_KCCIDC('C20H42')
      IC_O(20) = DMS_KCCIDC('C20H40')
      IC_P(21) = DMS_KCCIDC('C21H44')
      IC_O(21) = DMS_KCCIDC('C21H42')
      IC_P(22) = DMS_KCCIDC('C22H46')
      IC_O(22) = DMS_KCCIDC('C22H44')
```

```
      IC_P(23) = DMS_KCCIDC('C23H48')
      IC_O(23) = DMS_KCCIDC('C23H46')
      IC_P(24) = DMS_KCCIDC('C24H50')
      IC_O(24) = DMS_KCCIDC('C24H48')
      IC_P(25) = DMS_KCCIDC('C25H52')
      IC_O(25) = DMS_KCCIDC('C25H50')
      IC_P(26) = DMS_KCCIDC('C26H54')
      IC_O(26) = DMS_KCCIDC('C26H52')
      IC_P(27) = DMS_KCCIDC('C27H56')
      IC_O(27) = DMS_KCCIDC('C27H54')
      IC_P(28) = DMS_KCCIDC('C28H58')
      IC_O(28) = DMS_KCCIDC('C28H56')
      IC_P(29) = DMS_KCCIDC('C29H60')
      IC_O(29) = DMS_KCCIDC('C29H58')
      IC_P(30) = DMS_KCCIDC('C30H62')
      IC_O(30) = DMS_KCCIDC('C30H60')
      IC_P(31) = DMS_KCCIDC('C31H64')
      IC_O(31) = DMS_KCCIDC('C31H62')
      IC_P(32) = DMS_KCCIDC('C32H66')
      IC_O(32) = DMS_KCCIDC('C32H64')
      IC_P(33) = DMS_KCCIDC('C33H68')
      IC_O(33) = DMS_KCCIDC('C33H66')
      IC_P(34) = DMS_KCCIDC('C34H70')
      IC_O(34) = DMS_KCCIDC('C34H68')
      IC_P(35) = DMS_KCCIDC('C35H72')
      IC_O(35) = DMS_KCCIDC('C35H70')
      IC_P(36) = DMS_KCCIDC('C36H74')
      IC_O(36) = DMS_KCCIDC('C36H72')
      IC_P(37) = DMS_KCCIDC('C37H76')
      IC_O(37) = DMS_KCCIDC('C37H74')
      IC_P(38) = DMS_KCCIDC('C38H78')
      IC_O(38) = DMS_KCCIDC('C38H76')
      IC_P(39) = DMS_KCCIDC('C39H80')
      IC_O(39) = DMS_KCCIDC('C39H78')
      IC_P(40) = DMS_KCCIDC('C40H82')
      IC_O(40) = DMS_KCCIDC('C40H80')
      IC_P(41) = DMS_KCCIDC('C41H84')
      IC_P(42) = DMS_KCCIDC('C42H86')
      IC_P(43) = DMS_KCCIDC('C43H88')
      IC_P(44) = DMS_KCCIDC('C44H90')
      IC_P(45) = DMS_KCCIDC('C45H92')
      IC_P(46) = DMS_KCCIDC('C46H94')
      IC_P(47) = DMS_KCCIDC('C47H96')
      IC_P(48) = DMS_KCCIDC('C48H98')
      IC_P(49) = DMS_KCCIDC('C49H100')
      IC_P(50) = DMS_KCCIDC('C50H102')
      IC_P(51) = DMS_KCCIDC('C51H104')
      IC_P(52) = DMS_KCCIDC('C52H106')
      IC_P(53) = DMS_KCCIDC('C53H108')
      IC_P(54) = DMS_KCCIDC('C54H110')
      IC_P(55) = DMS_KCCIDC('C55H112')
      IC_P(56) = DMS_KCCIDC('C56H114')
      IC_P(57) = DMS_KCCIDC('C57H116')
      IC_P(58) = DMS_KCCIDC('C58H118')
      IC_P(59) = DMS_KCCIDC('C59H120')
      IC_P(60) = DMS_KCCIDC('C60H122')
      IC_P(61) = DMS_KCCIDC('C61H124')
      IC_P(62) = DMS_KCCIDC('C62H126')
      IC_P(63) = DMS_KCCIDC('C63H128')
      IC_P(64) = DMS_KCCIDC('C64H130')
      IC_P(65) = DMS_KCCIDC('C65H132')
      IC_P(66) = DMS_KCCIDC('C66H134')
      IC_P(67) = DMS_KCCIDC('C67H136')
      IC_P(68) = DMS_KCCIDC('C68H138')
      IC_P(69) = DMS_KCCIDC('C69H140')
      IC_P(70) = DMS_KCCIDC('C70H142')
C
      k1 = REALR(1)*EXP(-REALR(2)/T/8314.472)
      K2 = REALR(3)*EXP(-REALR(4)/T/8314.472)
      K3 = REALR(5)*EXP(-REALR(6)/T/8314.472)
      K4 = REALR(7)*EXP(-REALR(8)/T/8314.472)
      K5 = REALR(9)*EXP(-REALR(10)/T/8314.472)
      k6 = REALR(11)*EXP(-REALR(12)/T/8314.472)
```

```
      k6M = REALR(13)*EXP(-REALR(14)/T/8314.472)
      k70 = REALR(15)*EXP(-REALR(16)/T/8314.472)
      k7E0 = REALR(17)*EXP(-REALR(18)/T/8314.472)
      K8 = REALR(19)*EXP(-REALR(20)/T/8314.472)
      DE = REALR(21)
      ICO = DMS_KCCIDC('CO')
      IH2 = DMS_KCCIDC('H2')
      IH2O = DMS_KCCIDC('H2O')
      PCO = Y(ICO)*P
      PH2 = Y(IH2)*P
      PH2O = Y(IH2O)*P
C
C           DO 150 I = NCO+1,NCP
C           ALPHA(I) = k1*PCO/(k1*PCO+k6*PH2+k70*EXP(I*(-DE)/T/8314.472))
C       150 CONTINUE

      ALPHA(1) = k1*PCO/(k1*PCO+k6M*PH2)
      ALPHA(2) = k1*PCO/(k1*PCO+k6*PH2+k7E0*EXP(2*(-DE)/T/8314.472))
      DO 100 I = 3,NCO
        ALPHA(I) = k1*PCO/(k1*PCO+k6*PH2+k70*EXP(I*(-DE)/T/8314.472))
  100 CONTINUE
      DO 150 I = NCO+1,NCP
          ALPHA(I) = k1*PCO/(k1*PCO+k6*PH2+k70*EXP(I*(-DE)/T/8314.472))
  150 CONTINUE
      ALPHTERM = 1
      ALP = 1
      DO 200 I = 1,NCP
          ALP = ALP*ALPHA(I)
          ALPHTERM = ALPHTERM + ALP
  200 CONTINUE
C
      ADSORP = (1+((K8*PH2)**0.5)*(1+ALPHTERM)+
     +         ALPHTERM*(1/K4+1/(((K8*PH2)**0.5)*K3*K4)+
     +         PH2O/(((K8*PH2)**1.5)*K2*K3*K4*K5))+
     +         (1/K5)*PH2O/((K8*PH2)**0.5))

C
C
      KF_P(1) = k6M*ALPHA(1)
      KF_P(2) = k6*ALPHA(1)*ALPHA(2)
      KF_O(1) = 0.D0
      KF_O(2) = k7E0*EXP(2*(-DE)/T/8314.472)*ALPHA(1)*ALPHA(2)
      ALPH = ALPHA(1)*ALPHA(2)
      DO 300 I = 3,NCO
          ALPH = ALPH*ALPHA(I)
          KF_P(I) = k6*ALPH
          KF_O(I) = k70*EXP(I*(-DE)/T/8314.472)*ALPH
  300 CONTINUE
      DO 350 I = NCO+1,NCP
          ALPH = ALPH*ALPHA(I)
          KF_P(I) = k6*ALPH
  350 CONTINUE
      DRIVE_P = (K8**0.5)*(PH2**1.5)
      DRIVE_O = (K8*PH2)**0.5
      DO 400 I = 1,NC
          RATES(I) = 0.D0
  400 CONTINUE
      DO 500 I = 1,NCP
          J = IC_P(I)
          RATES(J) = (KF_P(I)*DRIVE_P/ADSORP)*CAT_RHO*AREA
  500 CONTINUE
      DO 600 I = 2,NCO
          J = IC_O(I)
          RATES(J) = (KF_O(I)*DRIVE_O/ADSORP)*CAT_RHO*AREA
  600 CONTINUE
C
      RATES(ICO) = -(RATES(4)+2*RATES(5)+2*RATES(6)+
     +             3*RATES(7)+3*RATES(8)+4*RATES(9)+
     +             4*RATES(10)+5*RATES(11)+5*RATES(12)+6*RATES(13)+
     +             6*RATES(14)+7*RATES(15)+7*RATES(16)+8*RATES(17)+
     +             8*RATES(18)+9*RATES(19)+9*RATES(20)+10*RATES(21)+
     +             10*RATES(22)+11*RATES(23)+11*RATES(24)+12*RATES(25)+
     +             12*RATES(26)+13*RATES(27)+13*RATES(28)+14*RATES(29)+
```

```
     +             14*RATES(30)+15*RATES(31)+15*RATES(32)+16*RATES(33)+
     +             16*RATES(34)+17*RATES(35)+17*RATES(36)+18*RATES(37)+
     +             18*RATES(38)+19*RATES(39)+19*RATES(40)+20*RATES(41)+
     +             20*RATES(42)+21*RATES(43)+21*RATES(44)+22*RATES(45)+
     +             22*RATES(46)+23*RATES(47)+23*RATES(48)+24*RATES(49)+
     +             24*RATES(50)+25*RATES(51)+25*RATES(52)+26*RATES(53)+
     +             26*RATES(54)+27*RATES(55)+27*RATES(56)+28*RATES(57)+
     +             28*RATES(58)+29*RATES(59)+29*RATES(60)+30*RATES(61)+
     +             30*RATES(62)+31*RATES(63)+31*RATES(64)+32*RATES(65)+
     +             32*RATES(66)+33*RATES(67)+33*RATES(68)+34*RATES(69)+
     +             34*RATES(70)+35*RATES(71)+35*RATES(72)+36*RATES(73)+
     +             36*RATES(74)+37*RATES(75)+37*RATES(76)+38*RATES(77)+
     +             38*RATES(78)+39*RATES(79)+39*RATES(80)+40*RATES(81)+
     +             40*RATES(82)+41*RATES(83)+42*RATES(84)+43*RATES(85)+
     +             44*RATES(86)+45*RATES(87)+46*RATES(88)+47*RATES(89)+
     +             48*RATES(90)+49*RATES(91)+50*RATES(92)+51*RATES(93)+
     +             52*RATES(94)+53*RATES(95)+54*RATES(96)+55*RATES(97)+
     +             56*RATES(98)+57*RATES(99)+58*RATES(100)+59*RATES(101)
     +            +60*RATES(102)+61*RATES(103)+62*RATES(104)
     +            +63*RATES(105)+64*RATES(106)+65*RATES(107)
     +            +66*RATES(108)+67*RATES(109)+68*RATES(110)
     +            +69*RATES(111)+70*RATES(112))
      RATES(IH2)=-(3*RATES(4)+5*RATES(5)+4*RATES(6)+7*RATES(7)+6*RATES(8
     +            )+9*RATES(9)+8*RATES(10)+11*RATES(11)+10*RATES(12)+
     +             13*RATES(13)+12*RATES(14)+15*RATES(15)+14*RATES(16)+
     +             17*RATES(17)+16*RATES(18)+19*RATES(19)+18*RATES(20)+
     +             21*RATES(21)+20*RATES(22)+23*RATES(23)+22*RATES(24)+
     +             25*RATES(25)+24*RATES(26)+27*RATES(27)+26*RATES(28)+
     +             29*RATES(29)+28*RATES(30)+31*RATES(31)+30*RATES(32)+
     +             33*RATES(33)+32*RATES(34)+35*RATES(35)+34*RATES(36)+
     +             37*RATES(37)+36*RATES(38)+39*RATES(39)+38*RATES(40)+
     +             41*RATES(41)+40*RATES(42)+43*RATES(43)+42*RATES(44)+
     +             45*RATES(45)+44*RATES(46)+47*RATES(47)+46*RATES(48)+
     +             49*RATES(49)+48*RATES(50)+51*RATES(51)+50*RATES(52)+
     +             53*RATES(53)+52*RATES(54)+55*RATES(55)+54*RATES(56)+
     +             57*RATES(57)+56*RATES(58)+59*RATES(59)+58*RATES(60)+
     +             61*RATES(61)+60*RATES(62)+63*RATES(63)+62*RATES(64)+
     +             65*RATES(65)+
     +             64*RATES(66)+67*RATES(67)+66*RATES(68)+69*RATES(69)+
     +             68*RATES(70)+71*RATES(71)+70*RATES(72)+73*RATES(73)+
     +             72*RATES(74)+75*RATES(75)+74*RATES(76)+77*RATES(77)+
     +             76*RATES(78)+79*RATES(79)+78*RATES(80)+81*RATES(81)+
     +             80*RATES(82)+83*RATES(83)+85*RATES(84)+87*RATES(85)+
     +             89*RATES(86)+91*RATES(87)+93*RATES(88)+95*RATES(89)+
     +             97*RATES(90)+99*RATES(91)+101*RATES(92)+103*RATES(93)
     +            +105*RATES(94)+107*RATES(95)+109*RATES(96)
     +            +111*RATES(97)+113*RATES(98)+115*RATES(99)
     +            +117*RATES(100)+119*RATES(101)+121*RATES(102)
     +            +123*RATES(103)+125*RATES(104)+127*RATES(105)
     +            +129*RATES(106)+131*RATES(107)+133*RATES(108)
     +            +135*RATES(109)+137*RATES(110)+139*RATES(111)
     +            +141*RATES(112) )
      RATES(IH2O) = - RATES(ICO)
C
      END SUBROUTINE USRFT1
```

Appendix D – Data employed for pinch analysis evaluation

Biogas feedstock processes

RWGS.LP 90%			
Component	T_{in} [°C]	T_{out} [°C]	[W_{th}/K]
Stripper Cond.	88	88	-227062
Stripper Reb.	115.6	115.6	1313190
H1	34.7	40	703.2
HX1-b	-3	20	454.0
HX2-b	20	40	1485
C1	88.5	15	-3033.6
CX1-b	40	10	-1416.7
CX2-b	207	-3	-532.4
CX3-b	78	40	-22324.4
RWGS reactor	800	800	1089690
FT reactor	228	228	-1436060
Col1 Cond.	28	28	-44992
Col1 Reb.	398	398	22458
Col1. Side strip.	183	183	5000
Col2 Cond.	383	383	-12530
Col2 Reb.	520	520	6598
C2	800	25	1460.8
C3	149.1	100	-1162.9
C4	252.9	100	-1174.6
C5	252.9	228	-1190.5
C6	228	25	-3021.8
C7	1000	50	786.6
C8	28	25	-15
C9	225	25	-63.5
C10	383	25	-47.8
C11	520	25	-19.8
H2	21.4	560	824.6
H3	19.6	250	242.4
H4	398	455	144.8
H5	25	200	672.4
H6	18.7	560	6598

SOEC.LP			
Component	T_{in} [°C]	T_{out} [°C]	[W_{th}/K]
Stripper Cond.	88	88	-227062
Stripper Reb.	115.6	115.6	1313190
H1	34.7	40	703.2
HX1-b	-3	20	454.0
HX2-b	20	40	1485
C1	88.5	15	-3033.6
CX1-b	40	10	-1416.7
CX2-b	207	-3	-532.4
CX3-b	78	40	-22324.4
HX2-s	785	800	2189.8
H7 (before evap)	20	101.5	1610.3
H7 (during evap)	101.5	101.5	828963
H7 (after evap)	101.5	800	714.7
FT reactor	228	228	-1431940
Col1 Cond.	28	28	-44588
Col1 Reb.	398	398	22285
Col1. Side strip.	186	186	5000
Col2 Cond.	383	383	-12162
Col2 Reb.	520	520	6399
C2	800	25	-1618.9
C3	170.6	100	-1206.5
C4	279.3	100	-1222.1
C5	279.3	228	-1230.5
C6	228	25	-3072.9
C7	1000	50	799.6
C8	28	25	-14.2
C9	225	25	-63.3
C10	383	25	-46.6
C11	520	25	-19.0
CX2-s	145.6	25	-2210.3
H2 1	15	500	283
H2 2	600	800	1711
H3	19.4	250	281
H4	398	455	141.1
H5	25	200	213.7
H6	18.5	800	504.5

RWGS.HP 90%			
Component	T_{in} [°C]	T_{out} [°C]	[W_{th}/K]
Stripper Cond.	88	88	-227062
Stripper Reb.	115.6	115.6	1313190
H1	34.7	40	703.2
HX1-b	-3	20	454.0
HX2-b	20	40	1485
C1	88.5	15	-3033.6
CX1-b	40	10	-1416.7
CX2-b	207	-3	-532.4
CX3-b	78	40	-22324.4
RWGS reactor	800	800	1296480
FT reactor	228	228	-1252920
Col1 Cond.	28	28	-33484
Col1 Reb.	398	398	16319
Col1. Side strip.	183	183	5000
Col2 Cond.	383	383	-8822
Col2 Reb.	520	520	4541
C2	800	25	-3465.2
C6	228	25	-3169.3
C7	1000	50	1562.1
C8	28	25	-10.8
C9	225	25	-49.1
C10	383	25	-33.9
C11	520	25	-12.9
H2	168.1	560	804.8
H3	17.8	250	171.9
H4	398	455	101.7
H5	25	200	1314.9
H6	25.7	560	1155.5
H1-HP	25	228	1729.5
H-Cdep (before evap)	26.7	233.6	1118.3
H-Cdep (during evap)	233.6	233.6	434916
H-Cdep (after evap)	233.6	800	299.9

SOEC.HP			
Component	T_{in} [°C]	T_{out} [°C]	[W_{th}/K]
Stripper Cond.	88	88	-227062
Stripper Reb.	115.6	115.6	1313190
H1	34.7	40	703.2
HX1-b	-3	20	454.0
HX2-b	20	40	1485
C1	88.5	15	-3033.6
CX1-b	40	10	-1416.7
CX2-b	207	-3	-532.4
CX3-b	78	40	-22324.4
HX2-s	785	800	2193.6
H7 (before evap)	20	223.9	2785.6
H7 (during evap)	223.9	223.9	1126191
H7 (after evap)	223.9	800	1292.6
FT reactor	228	228	-1256112
Col1 Cond.	28	28	-37850
Col1 Reb.	398	398	20266
Col1. Side strip.	186	186	5000
Col2 Cond.	383	383	-8819
Col2 Reb.	520	520	4536
C2	800	25	3503.2
C6	228	25	-3167.8
C7	1000	50	1256.5
C8	28	25	-7.9
C9	225	25	-46.1
C10	383	25	-33.9
C11	520	25	-12.9
CX2-s	586	25	-744.6
H2 1	15	500	146.1
H2 2	600	800	3071.2
H3	16.7	250	172.8
H4	398	455	101.6
H5	25	200	1189.8
H6	25.4	800	1211.8
H1-HP	25	228	1724.6

Air feedstock processes

	DAC.1			DAC.2			DAC.3		
Component	Tin	Tout	kW	Tin	Tout	kW	Tin	Tout	kW
Hx-1	99.6	99.6	1974.0	99.6	99.6	2535.8	99.6	99.6	2707.3
Hx-10	20.7	20.7	60.9	19.4	19.4	60.9	19.5	19.5	60.9
Hx-11	20.6	550	54324.8	20.6	550	54311.9	21.1	550	55993.3
Hx-13	150.1	100	-10672.7	144	100	-3179.7	146.2	100	-4418.4
Hx-14	254.3	100	-33177.8	245.7	100	-10661.4	248.8	100	-14401.7
Hx-15	254.4	228.1	-5727.8	245.9	228.1	-1325.4	248.9	228.1	-2047.4
Hx-16	800	29.4	-173865.4	800	65.7	-73870.8	800	59.7	-90852.4
Hx-17	29.4	25	-3695.2	65.7	25	-32257.1	59.7	25	-29740.4
Hx-18	21.1	550	58462.5			0.0	15.4	550	8956.0
Hx-19	228.1	25	-100129.6	228.1	25	-36187.2	228.1	25	-48823.2
Hx-2	99.6	99.6	-94350.7	99.6	99.6	-105215.6	99.6	99.6	-105215.6
Hx-3	99.6	50	-8656.3	99.6	50	-9653.1	99.6	50	-9653.1
Hx-4	57.5	100.7	120015.9	57.2	100.7	120087.8	57.7	100.7	120216.5
Hx-5	100.7	300	30506.0	100.7	300	30508.2	100.7	300	30507.9
Hx-6	235.7	253.3	56305.2	212.6	253.3	70162.1	212.5	253.3	70162.1
Hx-7	253.3	300	3195.3	253.3	300	3765.9	253.3	300	3765.9
Hx-8	64.5	45	-605.7	63.8	45	-750.9	59.6	45	-700.8
Hx-9	45	15	-920.7	45	15	-1186.6	45	15	-1111.3
Hx-air	24.8	200	11147.4	24.8	200	9481.8	24.8	200	4623.9
HX-DS	25	250	7038.9	11	250	2945.9	15	250	4071.8
BURNER	1000		-71252.2	1000		-63248.2	1000		-30049.2
CALCIN	900	901	0.0	900	901	0.0	900	901	0.0
FT	228	227	-210361.7	228	227	-80937.7	228	227	-111296.5
PELLET	25	24	-13142.5	25	24	-6774.8	25	24	-6930.2
RWGS	800	801	182117.1	800	801	41135.0	800	801	69525.4
SLAKER	300	299	-46310.9	300	299	-41885.8	300	299	-41885.8
Col – a C_5	72.6	71.6	-4104.4	72.6	71.6	-3729.7	72.6	71.6	-4366.0
Col – a C_5	387	388	1993.4	387	388	2343.6	387	388	2606.4
Col – b C_{11}	29	28	-2500.5	29	28	-2973.7	29	28	-3234.4
Col – b C_{11}	229	230	2901.9	229	230	3322.3	229	230	3668.4
Col – c C_{20}	25	24	-536.7	25	24	-2116.9	25	24	-2107.6
Col – c C_{20}	62.9	63.9	826.4	62.9	63.9	2127.2	62.9	63.9	2154.6
C-HX-1[a]			31409.5			32079.4			32079.4
C-HX-2			3985.5			4771.2			4525.1
C-HX-3			10405.0			12462.2			11817.3
C-HX-4			13877.5			16623.1			15761.3
C-HX-5			7503.3			7503.2			7503.3
hrsg			-37459.9			-36599.4			-36599.4
CX-C5+	63	25	-314.5	63	25	-93.2	63	25	-136.9
CX-C11+	229	25	-1950.2	229	25	-728.4	229	25	-1025.6
CX-C20+	387	35	-2524.2	387	35	-1001.6	387	35	-1404.1

	DAC.4			DAC.5		
Component	**Tin**	**Tout**	**kW**	**Tin**	**Tout**	**kW**
Hx-1	99.6	99.6	3428.1	99.6	99.6	2861.9
Hx-10	17.8	17.8	60.9	17.8	17.8	60.9
Hx-11	21.7	550	41642.1	21.4	550	58016.8
Hx-13	149.8	100	-6219.8	148.5	100	-6869.2
Hx-14	253.9	100	-19397.2	252.1	100	-21761.1
Hx-15	254.1	228.1	-3311.3	100	228.1	-3495.5
Hx-16	800	37.8	-103634.4	800	48.8	-123177.6
Hx-17	37.8	25	-7670.4	48.8	25	-21720.1
Hx-18	19.8	550	26289.0	18.6	550	26543.1
Hx-19	228.1	25	-65776.9	228.1	25	-71126.2
Hx-2	99.6	99.6	-67897.3	99.6	99.6	-80021.8
Hx-3	99.6	50	-6229.3	99.6	50	-7341.7
Hx-4	47.5	100.7	122529.7	57	100.6	120138.1
Hx-5	100.7	300	30508.5	100.6	300	30514.9
Hx-6	235.7	253.3	56305.2	212.6	253.3	70162.0
Hx-7	253.3	300	3195.3	253.3	300	3765.9
Hx-8	53.3	45	-194.3	63.5	45	-663.8
Hx-9	45	15	-731.3	45	15	-1061.9
Hx-air	24.8	200	7366.9	24.8	200	7039.8
HX-DS	20.5	250	5728.0	19.7	250	5649.0
BURNER	1000		-46460.7	1000		-45264.0
CALCIN	900	901	128465.0	900	901	0.0
FT	228	227	-154795.0	228	227	-159810.6
PELLET	25	24	-5471.9	25	24	-5471.9
RWGS	800	801	123667.0	800	801	117860.4
SLAKER	300	299	-46310.9	300	299	-41885.8
Col – a C_5	106.5	105.5	-4104.4	107	106	-4733.5
Col – a C_5	388	389	1533.2	388	389	2656.0
Col – b C_{11}	63	62	-2577.5	62.5	61.5	-2992.7
Col – b C_{11}	229	230	3059.7	229.7	230.7	3467.2
Col – c C_{20}	25	24	-1031.2	25	24	-1443.3
Col – c C_{20}	62.9	63.9	1179.9	62.9	63.9	1592.1
C-HX-1[a]			31409.5			32079.4
C-HX-2			2296.6			4355.9
C-HX-3			6013.4			11367.3
C-HX-4			8033.2			15150.8
C-HX-5	900	674	-7503.3			7503.4
hrsg	42	421	37459.9	42	421	38542.5
CX-C5+	63.5	25	-203.0	65.7	25	-214.6
CX-C11+	231	25	-1487.5	230.7	25	-1478.0
CX-C20+	389.1	35	-2024.1	389.1	35	-1992.3

Digestate feedstock processes

	DIG.A			DIG.B		
	T_{in} [°C]	T_{out} [°C]	[kWth]	T_{in} [°C]	T_{out} [°C]	[kWth]
Air hx	37	450	87.6	37	450	105
Flue-gas cx	855	200	162.6	855	200	200.7
Steam pre-hx	20	189	43.1	20	188	45.4
Steam hx	188	189	122.1	188	189	128.8
Steam post-hx	173	450	32.5	173	450	34.2
Intercooler	262	35	69.5	248	35	89.1
FT	228	227	527.1	228	227	742.7
FT prod CX	228	35	221.7	228	35	478.07
Flash tank MT	199	200	21.97	199	200	26.7
Flash tank HT	319	320	9.42	319	320	15.26
Naphtha cx	200	35	13.8	200	35	13.98
Middle cx	320	35	12.2	320	35	21.25
Heavy cx	320	35	4.7	320	35	5.85
TG gases cx	431	100	379.1	616	100	0
Steam Heat	20	188	0	20	188	0
Steam Evap	188	189	0	188	189	0
Hx to FT	193	228	11.8	185	228	14.7
Reformer	800	801	239.7	800	801	639
Ref. Hx in gas	25	500	69.56	25	500	429
Ref. steam hx 1	20	224	13.9	20	224	26.8
Ref. steam hx 2	224	225	27.56	224	225	53
Ref. steam hx 3	224	450	7.13	224	450	13.7
Ref. cx	800	228	134.06	800	228	617

List of Publications

List of publications derived from this research work.

Scientific Publications

- **M. Marchese**, S. Chesta, M. Santarelli, and A. Lanzini, "Techno-economic feasibility of a biomass-to-X plant: Fischer-Tropsch wax synthesis from digestate gasification," *Energy*, p. 120581, Apr. 2021. doi.org/10.1016/j.energy.2021.120581
- **M. Marchese**, G. Buffo, M. Santarelli, and A. Lanzini, "CO_2 from direct air capture as carbon feedstock for Fischer-Tropsch chemicals and fuels: Energy and economic analysis," *J. Of CO_2 Util.*, p. 101487, Febr. 2021. doi.org/10.1016/j.jcou.2021.101487
- **M. Marchese**, E. Giglio, M. Santarelli, and A. Lanzini, "Energy performance of Power-to-Liquid applications integrating biogas upgrading, reverse water gas shift, solid oxide electrolysis and Fischer-Tropsch technologies," Energy Convers. Manag. X, p. 100041, Apr. 2020. doi.org/10.1016/j.ecmx.2020.100041
- **M. Marchese**, N. Heikkinen, E. Giglio, A. Lanzini, J. Lehtonen, and M. Reinikainen, "Kinetic Study Based on the Carbide Mechanism of a Co-Pt/γ-Al_2O_3 Fischer–Tropsch Catalyst Tested in a Laboratory-Scale Tubular Reactor," Catalysts, vol. 9, no. 9, p. 717, Aug. 2019. doi.org/10.3390/catal9090717

Conferences

- "Conversion of Carbon Dioxide and Hydrogen to Hard Aliphatic Waxes". **Marchese, M.**, Giglio, E., Santarelli, M., Lanzini, A. 4th Energy for Sustainability International Conference – Designing a Sustainable Future, Turin, 24-26 July 2019. www.efs2019.uc.pt
- "Integrated CO_2 Absorption Capture, Solid Oxide Electrolyser, Fischer-Tropsch Synthesis Unit: Process Modelling of an Industrial CCU System for Making High Molecular Weight Synthetic Hydrocarbons". **Marchese, M.**, Lanzini, A., Santarelli, M. –14th Greenhouse Gas Control Technologies Conference Melbourne 21-26 October 2018 (GHGT-14). ssrn.com/abstract=3365757

Awards

Best Oral Presentation Silver Award: excellence in Oral Presentation at the Energetics 2020 PhD Days – Turin, Italy, December 2020